Asteroseismology of cool stars: testing scaling laws and detecting signatures of rapid structure variation.

University of Birmingham

Hugo R. Coelho

March 2017

Abstract

Asteroseismology is the study of resonant oscillations in stars, and a revolution in this field is taking place thanks to data from the *Kepler* Space Telescope. Asteroseismology is now a rapidly growing field of astrophysics thanks to the long and precise photometric data obtained for thousands of stars. Analysis of this high-quality time-series reveals wide and detailed spectra of oscillations. Such oscillations carry detailed information about the internal structure of stars. Therefore, stellar frequencies can reveal crucial information from the unseen interior of the stars. Furthermore, it is possible to use these oscillations to infer global stellar parameters, such as mass, radius and age, which helps studying populations of stars in our galaxy.

First, we investigated the $\nu_{\rm max}$ scaling relation, a widely-used equation that states that the frequency of maximum amplitude in a power spectrum scales with a combination of surface gravity and effective temperature. We tested how well the oscillations of cool main-sequence and sub-giant stars follow this relation, using a ensemble of asteroseismic targets observed by *Kepler*. Our results, which come from a grid-based analysis, rule out departures to a level of $\simeq 1.5$ percent from the classic scaling dependence $\nu_{\rm max} \propto gT_{\rm eff}^{-1/2}$ in the range of temperatures that we tested.

We then tested seismic scaling relations in a small group of 10 bright red-giant stars observed by *Kepler*. These giants, some of the brightest observed in the *Kepler* field, have precise values of parallaxes. We compared the measured distances with inferences made using asteroseismic parameters. We also combined high-quality spectroscopic data with seismic constraints to determine their evolutionary phase. We compared the observed surface abundances of lithium and carbon with models that account for additional mixing processes in red-giants.

Finally, we then shifted our focus to a group of 13 stars observed by *Kepler*, and use asteroseismic tools to extract model-independent information about their internal regions. Our objective is to detect the so-called acoustic glitches, characterized as departures from the uniform frequency spacings predicted by the asymptotic relation. Such departures originate in regions where there is an abrupt change in the stratification of the star. Analysis of the glitch signal can be used to estimate the acoustic location of the base of the convective zone and the second helium ionization zone, providing stringent constraints to predictions of stellar models.

Contributions from collaborators

The following figures were produced by some of our collaborators: figure 2.10, figure 3.2, figure 3.3 and figure 3.4. A few parts of sections 3.2 and 3.5 were written with the help of collaborators.

Acknowledgements

First and foremost, I would like to thank my supervisors, Andrea Miglio and William Chaplin. Since I have arrived at Birmingham, they have both supported and guided me in the most varied situations, and have always been available for discussions and questions of any kind. They are inspirational figures that showed me how to conduct proper work in the field of professional science. The tremendous amount of information they have shared with me over the past years has proven to be invaluable.

I would also like to thank Daniel Reese for helping me in my research during several moments, and Diego Bossini for our little chats that helped me to better understand the wonderful (and highly complex) world of stellar modelling.

Throughout my Ph.D., I have collaborated with a large group of international astronomers on different projects. It would take too long to mention each one of them here individually, but the Kepler Asteroeismic Science Consortium has been immensely helpful to keeping people in close contact and always ready to share knowledge. Particular thanks to Sarbani Basu and Aldo Serenelli, both of which I have the pleasure of meet in person during several occasions. The Kepler Science Team has provided all of us with outstanding asteroseismic data. I am very grateful for the work of all people involved on it.

I have been fortunate to have been supported financially with an Brazilian Postgraduate Scholarship provided by CAPES. I am grateful for the support of all the personal that helped me with all kinds of logistics.

Finally, I would like to thank my family. They have always encouraged me to take whatever path I wished for me. Their support and love have been of one of my main driving forces.

Contents

List of Figures

List of Tables

Chapter 1

Introduction

1.1 Motivation and Outline

If one desires to understand the nature of the universe, then understanding stars would be extremely important, for they are one of the most basic and interesting building blocks of the observable universe, for a variety of reasons. The current cosmological models predict that the primordial composition of the early universe was mostly light elements such as hydrogen and helium, with small amounts of lithium. Stars are dynamical objects with a source of energy that converts light elements into heavier elements inside their cores, making them the main source of chemical evolution in the galaxy. Therefore, they are responsible for the chemical species needed to create rocky, dense planets and any possible lifeforms that might inhabit their surface. This chemical nucleosynthesis will also gradually alter the stellar structure through time, with transport of energy by convection playing an important role in the internal chemical mixing. Each star is unique, as its initial mass and chemical composition will largely define how it will evolve. Certain stars with periodic variations of brightness can be used to estimate distances beyond the limits where trigonometric parallaxes can be measured. In the same line, type Ia supernova can be used to estimate distances of faraway galaxies, which is crucial for cosmological studies. By observing stars like our Sun, we can infer how it looked like in the past and how it will evolve in the future. Additionally, to characterize exoplanets, it is necessary to better understand their parent stars, specially in the context of planets located inside the so-called habitable zone, a region around the parent star where the planet receives the necessary amount of radiation for water to exist in the liquid form on their surface. Of course, several other factors are important in this context, such the planetary density, atmospheric composition, orbital eccentricity, and many more. Indeed, stellar astrophysics is of vital importance to various aspects of astronomy in general.

In order to study stars we have to gather as much information as possible from their light, such as surface temperature, chemical composition, mass and radius. Broad-band

photometry can be used to estimate surface temperatures, while high-resolution spectroscopy can obtain the photospheric chemical composition. Those two parameters, when combined with information about luminosity, distances and precise $\log g$, can be used to constrain models of stellar evolution in order to infer stellar mass and radius. This appears to be a great approach on the first sight, however, it implies one basic assumption: that our models are perfect. This assumption is not true, for stars are highly complex objects. Modelling stellar atmospheres is particularly difficult, and both broad-band photometry and spectroscopy, for instance, rely heavily on such models. Meanwhile, stellar evolution models make simplified assumptions when describing mixing of chemical and transport processes that are not well understood yet. Ideally, the best way to do this is to obtain direct, models-independent measurements of fundamental stellar parameters and compare them with predictions made by models. If there is not an agreement between them, the models need to be modified to reproduce the observed results. However, even the closest star is located more than 4 light-years away from our solar system (one light-year is roughly ~ 9.5 trillion of kilometres). Therefore, such immense distances make direct estimations of global stellar parameters very difficult. Direct estimation of mass and radii can be obtained from eclipsing binaries, but those are only a small fraction of the observed stars (e.g. Torres et al., 2010).

But even in the best case scenario of direct, model-independent measurements of global stellar parameters, they can only give us information about the surface of the stars. Sir Arthur Eddington, in his book *The Internal Constitution of the Stars* (Eddington, 1926), had mentioned that "At first sight it would seem that the deep interior of the Sun and stars is less accessible to scientific investigation than any other region of the universe. Our telescopes may probe farther and farther into the depths of space; but how can we ever obtain certain knowledge of that which is hidden behind substantial barriers? What appliance can pierce through the outer layers of a star and test the conditions within?". According to Eddington, all we could ever hope to do was to use our knowledge of physics and try to model the inside of the star. By incorporating nuclear reaction rates and how the energy is transported thorough the star, it is possible to use computers to create an evolutionary model. But still, as mentioned before, there are various unknowns. The size of the convective zone in solar-like stars, for example, can only be estimated roughly depending on the stellar mass and evolutionary stage. However, having this information is a crucial factor in learning about several types of chemical-mixing near the surface, and also for the generation of the dynamo effect responsible for creating the local and global magnetic field.

It is possible to use asteroseismology to bypass the stellar surface and obtain information on the internal structure. The concept of asteroseismology is based on the study of standing sound waves travelling through the stellar interior that can make the star pulsate. We can observe small variations of stellar brightness and measure the time-scale of such

oscillations. The amplitude of the oscillations in cool, low-mass stars is very small, with usually a few parts per million in the case of solar oscillation detected in photometry, for example. However, such oscillations now can be observed in thousands of stars thanks to advances in space-based observations and improvements on the technology of CCD-detectors. Those frequencies of oscillation are heavily dependent on internal structure and can be used to obtain direct information about the internal layers of the observed star. This makes asterosiesmology remarkable in obtaining sensitive data that can be used to improve and refine our models of stellar structure and evolution. The main topic of this thesis is the use of asteroseismology to study cool, low-mass stars in different stages of evolution to help us to put tight constraints on predictions made by stellar models. We conduct tests on precision and accuracy of the seismic scaling laws used to estimate global stellar parameters. Such scaling laws are commonly used for a great number of stars and it is vital to ascertain their effectiveness. We also use departures from the predicted frequency spacing in solar like stars to detect and characterize local features in the deep stellar interior such as the base of the convective zone and the second helium ionization zone. Such information can be used to better understand mixing processes.

This thesis is organized as follows. The remainder of this chapter will give an introduction to the basic astrophysical concepts of stellar structure and evolution, as relevant for all later chapters. Chapter 2 presents results from asteroseismology for a large sample of stars, where we conducted tests on one of the main scaling laws used to obtain global stellar parameters. Chapter 3 presents the analysis of a sample of bright nearby red-giant stars for which we combined high-quality information from asteroseismology and spectroscopy to better constrain stellar models. Chapter 4 presents the study of acoustic glitches in main-sequence stars for which we where able to obtain good estimations for the acoustic depth of the base of the convective envelope. Finally, Chapter 5 provides a summary of all results and a discussion of future work related to the main topics of this thesis.

1.2 Stellar Structure and Evolution

We begin with a quick summary on the theory of stellar structure and evolution of cool, low-mass stars. Much of what is written in this section can be found in much more detail on several other sources. For a more complete reading, we suggest the standard work of Kippenhahn and Weigert (1994), on which the majority of the contents in this section are based on. We only focus on the evolution of single stars.

The study of stellar evolution consists in understating how the variations of luminosity and surface temperature through the life of stars are related to physical processes occurring in the stellar interior. This is better visualised in an Hertzsprung-Russell (H-

R) diagram, as shown in Figure 1.1. The main critical stages of stellar evolution to be discussed bellow are marked as coloured symbols.

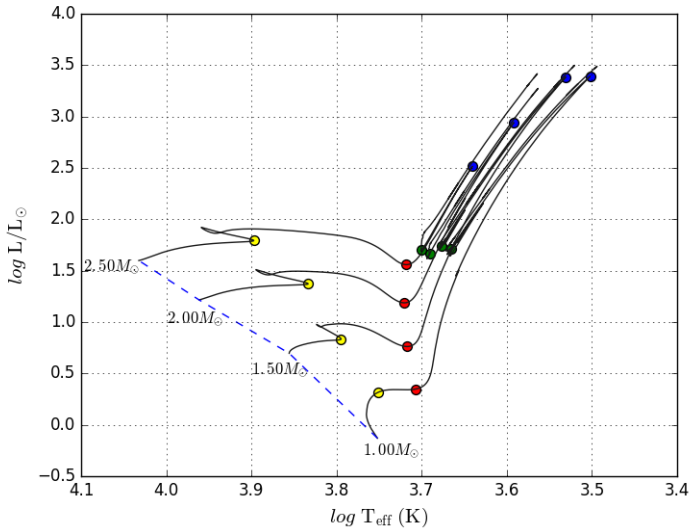

Figure 1.1: H-R diagram showing the main stages of stellar evolution for low-mass stars. The tracks were computed using MESA (Paxton et al., 2011) for four different masses with solar composition (solid grey lines). The dashed blue line shows the position of the zero- age main sequence (ZAMS). The different colours of the symbols mark four distinct points of stellar evolution along each track: yellow - hydrogen exhaustion in the core; red - Bottom of the red-giant branch; green - Ignition of helium-core burning; blue - helium-core burning main-sequence.

1.2.1 Main Sequence

Stars are formed from interstellar clouds through a process of gravitational instability that results in the contraction of material. This collapse continues until the central regions of the proto-star reach temperatures and densities that are high enough to start nuclear reactions. The zero-age main sequence (ZAMS, blue dashed line on Figure 1.1) is characterized by the ignition of hydrogen burning through nuclear fusion in the central regions of the star, where it is converted into helium. Stars will stay in the main-sequence for approximately 90% of the stellar lifetime, transforming hydrogen into helium in the core. A basic condition for maintaining structural stability through the stellar lifetime is to keep hydrostatic equilibrium, where the gravitational collapse of the outer layers is balanced by the energy liberated from the nuclear reactions occurring in the core.

The two main nuclear reactions that convert hydrogen into helium are the proton-proton (p-p) chain and the CNO cycle. In the p-p chain, protons are converted into deuterium, which is then converted into helium-3 shortly after. From helium-3 to helium-2

the chain can follow different paths. This reaction is the dominant form of hydrogen production in low mass stars. In the CNO cycle, hydrogen burning is catalysed by carbon, nitrogen and oxygen. The CNO cycle is more efficient at higher temperatures, and is therefore dominant in stars with a mass greater than approximately 1.3 solar masses ($M_\odot$).

The internal structure of a main sequence star can be divided into three key regions: the core, the radiative zone and the convective envelope. In the core, the energy released by fusion reactions can be transported to outer layers by either radiative or convective processes, depending on the conditions of the gas, with opacity playing a important factor.

Stars with a mass lower than ~0.35 $M_\odot$ are entirely convective all the way to the core. Stars with mass between ~0.35 $M_\odot$ and ~1.10 $M_\odot$ have external convective layers on top of radiative region that includes the core. When stellar mass is greater than ~1.10 $M_\odot$, a convective core appears and the convective zone near the surface diminishes in size as the stellar mass increases. For masses greater than ~1.50 $M_\odot$, the internal structure is characterized by an internal convective region surrounded by an external radiative zone.

On Figure 1.1, it is possible to see a 'hook' feature on the evolutionary path of low mass stars that are slightly more massive than the Sun. This is a consequence of the mixing of enhanced helium content produced by the convective core in higher mass stars ($M \gtrsim 1.30 M_\odot$). This forms a discontinuity in molecular weight and, as a consequence, an abrupt decrease in density at the boundary with the outer radiative regions. In order to keep the hydrostatic equilibrium, a decrease in density corresponds to a decrease in the pressure gradient. Since the pressure gradient from the core to the surface must be continuous, this causes the pressure to reach zero at a larger radial distance than before, and hence the star increases in radius. At the same time, the central temperature during hydrogen burning dominated by the CNO cycle changes only slowly, and hence the increase in radius shifts the star to the right in the HR diagram. When hydrogen is finally exhausted in the core, the star rapidly contracts, which causes an increase in temperature, shifting the star to the left in the HR diagram.

For low mass stars, the core is radiative and there is no mixing of enhanced helium content. Hydrogen is burned gradually and mean molecular weight decreases continuously from the center to surface. Since there is no discontinuity in the pressure gradient, the 'hook' feature is absent on the evolutionary track.

The amount of time that a star will be in the main sequence will heavily depends upon its mass. High mass stars have much higher pressure and temperatures in their cores when compared with low mass stars, and will burn hydrogen at faster rates as a result. Stars with a mass similar to our Sun, for example, have an estimated main sequence lifetime of ~10 billion years. Meanwhile, a star with 10 $M_\odot$ will stay in the main sequence for 10 million years.

1.2.2 Subgiant Phase

The subgiant phase begins when hydrogen is depleted at the core and the only mean of generation of energy is done in a thin hydrogen burning shell surrounding the inert helium core. For low mass stars, the core is an electron-degenerate gas supported by degeneracy pressure. The subgiant phase for sun-like stars will take up to ~5% of the main-sequence lifetime.

The picture is a bit different for higher-mass stars. Their core will have higher temperature and lower density when compared to low mass stars, and they do not become degenerate. The helium produced by the hydrogen burning shell will be deposited in the core, gradually increasing its mass. This process continues until the mass fraction $q_c = M_c/M$ reaches the Schönberg-Chandrasekhar limit ($q_{SC} \simeq 0.1$). After the limit is exceeded, the core can no longer support the outer layers and it suffers a rapid contraction. The contraction of the core is accompanied of a expansion of the outer layers. Those effects will make the stars move quickly to the right of the H-R diagram. The timescale of this process is relatively small and there is a low chance to observe a star going thought this stage of evolution. This is translated into the observational phenomenon known as the Hertzsprung gap. It is important to note that high mass stars may have helium cores already beyond the Schönberg-Chandrasekhar mass.

1.2.3 Red Giant Branch and Red Clump

The core continues to increase its mass and to contract. Meanwhile, the surface envelope continues to expand and the stellar radius increases by roughly ~200 times the main sequence size. This will make the surface temperatures decrease to a range of ~ 3500 - 5500K. At the same time, the enormous increase in stellar radius will create a increase in luminosity, making the star shift towards the upper right part of the H-R diagram. This characterizes the ascending red giant phase. Stars in this stage usually have similar surface temperatures regardless of mass.

The core will continue to increase in temperature until it reaches ~ 100 million Kelvin, where ignition of helium begins through the triple alpha process, where three nuclei of helium (three alpha particles) are combined into a carbon nucleon. This process occurs at the tip of the red giant branch. The mass of the star will affect the critical core mass that is needed to begin the fusion of helium. Stars with $M \leq 2M_\odot$ will have a degenerate core. In these conditions, the hydrogen burning shell will continue to deposit helium into the degenerate core. The temperature in the core increases until it reaches 100 million Kelvin, and helium burning begins at a common luminosity and critical core mass of $M_c \sim 0.45M_\odot$. For non-degenerate conditions, the core helium burning begins at $M_c \sim 0.35M_\odot$. This is the minimum core mass required to ignite helium in non-degenerate conditions. When the stellar mass is $M \gtrsim 3M_\odot$, the mass of the core at the end of the

main sequence is already greater than 0.35 $M_{\odot}$

The energy liberated by the triple alpha process raises the core temperature quickly. In higher-mass stars with non-degenerate cores, this leads to an increase in pressure, making the core expand until the temperature drops to reach an equilibrium state, characterizing the helium burning main sequence. However, in low mass stars with a degenerate helium core, the electron degeneracy pressure will make the temperature increase without expansion. The temperature in the degenerate core will keep rising, increasing the rate of fusion reactions that will in turn leads to an even greater increase in temperature. This runaway process only ends when the core temperature is so high that the energy liberated by the helium fusion turns explosive in a process known as the helium flash. This event takes only a few minutes, but liberates an enormous amounts of energy that will be responsible to lift the degeneracy of the electrons in the center of the star.

Once the helium fusion begins, the core expansion and subsequent envelope contraction will shift the star in the HR diagram towards lower luminosities. The star will settle in their main helium-burning phase with the surrounding hydrogen burning shell still active. This stage of evolution is also known as the horizontal branch and the star will stay in this phase for a considerable time, but still substantially shorter when compared to the main-sequence lifetime. For stars that went through the helium flash, they have a similar value of core mass at the moment of helium ignition and still have a similar core and luminosity after the flash. This will create a region in the H-R diagram where these stars can be found gathered in a similar position, referred as the red clump. Stars with slightly higher masses that did not pass through the flash, having instead a gradual ignition of helium on lower luminosities, will occupy a similar region at lower luminosities named as the secondary clump (Girardi, 1999).

In the core, the triple alpha process will create a substantial amount of carbon that will then combine with helium to form oxygen nuclei. The central region begins to become reach in carbon and oxygen. As the amount of helium in the core drops, the central region contracts and temperature increases again, leaving a shell where fusion of helium continues around a inert core of oxygen and carbon. The external layers expand, lowering surface temperature and increasing the luminosity. The star moves again to the upper part of the H-R diagram in the asymptotic giant branch.

The physical and chemical profile in the core are difficult to measure directly, as we are limited to observe surface condition only in most situations. The description detailed above is backed by numerical results obtained through stellar models that reasonably reproduce the observations.

The final stages of evolution are characterized by thermal pulses where the external layers of the star are ejected and mass loss occurs. Such processes, however, are beyond the scope of this thesis.

1.3 Asteroseismology of Solar-Like Oscillations

This section presents an introduction on asteroseismology with focus on solar-like oscillations found in cool, low-mass stars. The contents of this section follow mainly the work done by Aerts et al. (2010) and reviews by Bedding (2011), Christensen-Dalsgaard & Thompson (2011) and Chaplin and Miglio (2013), which we suggest to the reader for a detailed description.

If we listen to a concert, an average person can identify individual instruments even if they are al playing the same note. The particular shape and material of the instrument will define the amount of power placed in each of their natural harmonics. The combination of frequencies, amplitudes and phase of each harmonic will define the overtone of the instrument.

Sound is a pressure wave. The compression and expansion of the gas propagate the wave. Assuming an ideal gas, changes in pressure will translate into variations of density and temperature. If the temperature increases, the molecules are moving faster, collide more frequency, and the sound speed is higher. For an isothermal configuration, molecules in lighter gases move faster, and the sound speed will be also high. On the same way, if we manage to measure the sound speed inside stars, we can determine the internal density and, consequently, the temperature and chemical composition.

1.3.1 Fundamentals

Stars that show periodic changes of luminosity have been known for centuries, the oldest case being of Mira (α Ceti), with its variability recorded by David Fabricius in 1596. By the end of the 19th century, a significant number of variable stars were discovered, most of those being associated with a binary companion. However, many stars with no evidence of binarity still showed abrupt and periodic changes in brightness. It was only in the 20th century that such variability was linked to intrinsic stellar pulsations (Shapley, 1914).

For some stars slightly more massive then the Sun ($M \geq 2M_{\odot}$), such as the Cepheid variables, the oscillations are driven by layers of partial ionization of elements. Within this layer, the gas is in a state with high opacity, and it absorbs most of the radiation that comes from the inner layers. The temperature of the layer continues to increase until it begins to expand. During expansion, the opacity of the gas decreases, liberating the energy that was trapped inside. The temperature then drops and the layer contracts, raising the opacity again. This layer functions similar to a heat engine, converting thermal energy into movement. This phenomenon is known as the κ mechanism and drives global oscillations in other types of stars as well, such as δ Scuti, RR Lyrae, β Cephei, slowing pulsating B stars and some types of white dwarfs. In asteroseismology, they constitute a group of stars commonly called ‘classical pulsators’ or ‘heat-engine pulsators’.

In 1962, Leighton et al. (1962) published the first detection of oscillatory motion in solar atmosphere. They used the Doppler shift on absorption lines in the spectra of the Sun, and determined a period of 5 minutes. Those shifts in the lines are interpreted as vertical oscillations of large regions of fluid with a speed of 1 km/s. A few years later, Ulrich (1970) suggested that those shifts where caused by global oscillations of the solar sphere, and the first detection and identification of these oscillations as global modes is attributed to Claverie et al. (1979). Since then, helioseismology has helped to improve our understanding of the internal structure of the Sun (see e.g. Christensen-Dalsgaard, 2002, for a review).

Before we move to a description of the driving mechanisms of solar-like oscillations, we should lay out the basic mathematical description of oscillatory motion in a symmetric three-dimensional sphere. In this case, the solutions to the equations of motion have displacements in radius r, co-latitude θ and longitude ϕ given by (see section 1.4 for more details):

$$\xi_r(r,\theta,\phi,t) = a(r)Y_l^m(\theta,\phi)\exp(-2\pi i\nu t) \tag{1.1}$$

$$\xi_\theta(r,\theta,\phi,t) = b(r)\frac{\partial Y_l^m(\theta,\phi)}{\partial\theta}\exp(-2\pi i\nu t) \tag{1.2}$$

$$\xi_\phi(r,\theta,\phi,t) = \frac{b(r)}{\sin\theta}\frac{\partial Y_l^m(\theta,\phi)}{\partial\phi}\exp(-2\pi i\nu t) \tag{1.3}$$

where ξ_r , ξ_θ , ξ_ϕ are the complex displacements, $a(r)$ and $b(r)$ are amplitudes, ν is the (complex) oscillation frequency, and $Y_l^m(\theta,\phi)$ are the spherical harmonics given by:

$$Y_l^m(\theta,\phi) = (-1)^m c_{lm} P_l^m(\cos\theta)\exp(im\phi), \tag{1.4}$$

where $P_l^m(\cos\theta)$ are the Legendre polynomials and c_{lm} is a normalization constant given by:

$$c_{lm} = \sqrt{\frac{2l+1}{4\pi}\frac{(l-m)!}{(l+m)!}}, \tag{1.5}$$

The quantum numbers l and m are the spherical degree and the azimuthal number, respectively. The number of surface nodes on the surface is characterized by l, and can assume integer values ($l = 0, 1, 2, ...$). The azimuthal order is expressed by m, and $|m|$ specifies the number of surface node lines in the longitudinal direction. The azimuthal number m takes values ranging from $-l$ to $+l$, and there are $2l + 1$ azimuthal modes for each spherical degree l. There is a third equally important quantum number, the radial order n, that defines the number of nodes between the center and the surface of the star.

The spherical degree $l = 0$ characterizes radial pulsations responsible for making the star expand and contract in its entirety. Non-radial pulsations are associated with

spherical modes where $l > 0$. Figure 1.2 shows some of the first harmonics, with $l = 1$ being a dipole mode where half of the star contracts while the other half expands, $l = 2$ are quadrupole modes and $l = 3$ are octupole modes. It is important to note that modes with $l > 3$ are not observed in stars other than the Sun, since they are viewed as point sources and cancellation effects will prevent their visualization. Line profile variations can be used to detect (high-amplitude) modes with $l > 3$ (Aerts et al., 2010).

The negative and positive values of m are associated with the travelling direction of the mode, so that azimuthal modes travelling in the direction of rotation are positive and modes going in the opposite direction of rotations have negative values of m. For the case of spherically symmetric star, the $2l + 1$ azimuthal modes m of a multiplet (such as $l = 3, m = -3, -2, -1, 0, +1, +2, +3$) are the same. This degeneracy is destroyed when there are deviations from spherical symmetry, such as in rotating stars. Even if the effects of rotation are non negligible, we use frequencies with only $m = 0$ modes, which are not affected by velocity fields, so we focus our work in radial and spherical modes, n and l, respectively.

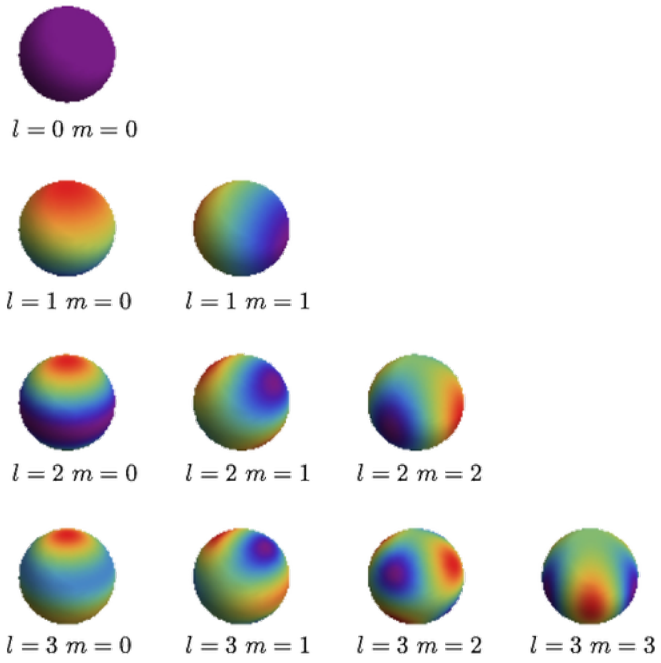

Figure 1.2: The first ten spherical harmonics. The quantum numbers l and m range from 0 to 3. The movement of the stellar surface is represented by colours, with blue and red being the maximum and minimum displacement, respectively.

1.3.2 Excitation and Propagation of Oscillation Modes

In the previous section, we explained the first class of variable stars as being relatively massive stars that oscillate though the κ mechanism. This form of oscillation is classified as 'self-excited', and has large amplitudes, being relatively easy to observe. On the

other hand, oscillations in cool, low mass stars like the Sun are stochastically excited and intrinsically damped by the turbulent motion of gas in the sub-surface convective layer. These so called 'solar-like oscilations' have low surface amplitude and will be present in any star that has a convective envelope near the surface, including more evolved stars such as subgiants and red giants. The exact nature of the excitation and damping of these modes is still relatively poorly understood, due to our restricted understanding of stellar convection (see, e.g. Houdek et al., 1999; Houdek, 2006). Fig 1.3 shows some pulsating stars across the Hertzsprung-Russell diagram.

There are two main types of pulsation modes in stars: pressure modes (p modes) and gravity modes (g modes). The p modes are acoustic waves propagating inside a star by successive compression and decompression of gas, having the pressure gradient acting as the restoring force. The g modes arise from the combined effect of buoyancy of the gas and gravity, where the buoyancy acts as the restoring force. In the frequency range of g modes, no radial ($l = 0$) modes exist and the radial order n is considered to be negative by convention.

The p modes, excited by convection, propagate down into the interior of the star (see Figure 1.4). Generally, the sound speed increases with depth, which has the effect of bending the acoustic ray paths of non-radial modes. Eventually p modes of $l > 0$ will reach their inner turning point and be refracted towards the surface. At the surface the rays will again be reflected, this time by the rapid decrease in density. High degree modes do not propagate as deeply as those of lower degree. The frequency of each mode depends upon the sound travel time along its ray path. As different modes have different 'acoustic cavities', they will exhibit different properties. Using these differences to infer stellar structure is one of the aims of asteroseismology. In a main-sequence Sun-like star, the g modes are confined to the radiative region beneath the convective envelope, as shown in Figure 1.4. Where convection exists g modes are evanescent. It is therefore difficult to detect them in stars like the Sun as their surface amplitudes are small (Appourchaux et al. 2000; Elsworth et al. 2006; Garcia et al. 2007; Appourchaux et al. 2010). However, in more evolved stars, modes of a mixed character are observed arising from the coupling of p and g modes of the same degree, l, and similar frequency. These mixed modes have great potential as seismic indicators because their g mode-like behaviour is sensitive to the core, while their p mode-like behaviour near the surface allows them to be observed. Unfortunately, for main sequence stars like the Sun, the frequencies of p and g modes are vastly different and no mixed modes are observed.

The period spacing of consecutive gravity modes with the same value of angular degree l is given by (Tassoul 1980, Christensen-Dalsgaard 2011):

$$\Delta\Pi_l = \frac{2\pi^2}{\sqrt{l(l+1)}}\left(\int_g N\frac{dr}{r}\right) \tag{1.6}$$

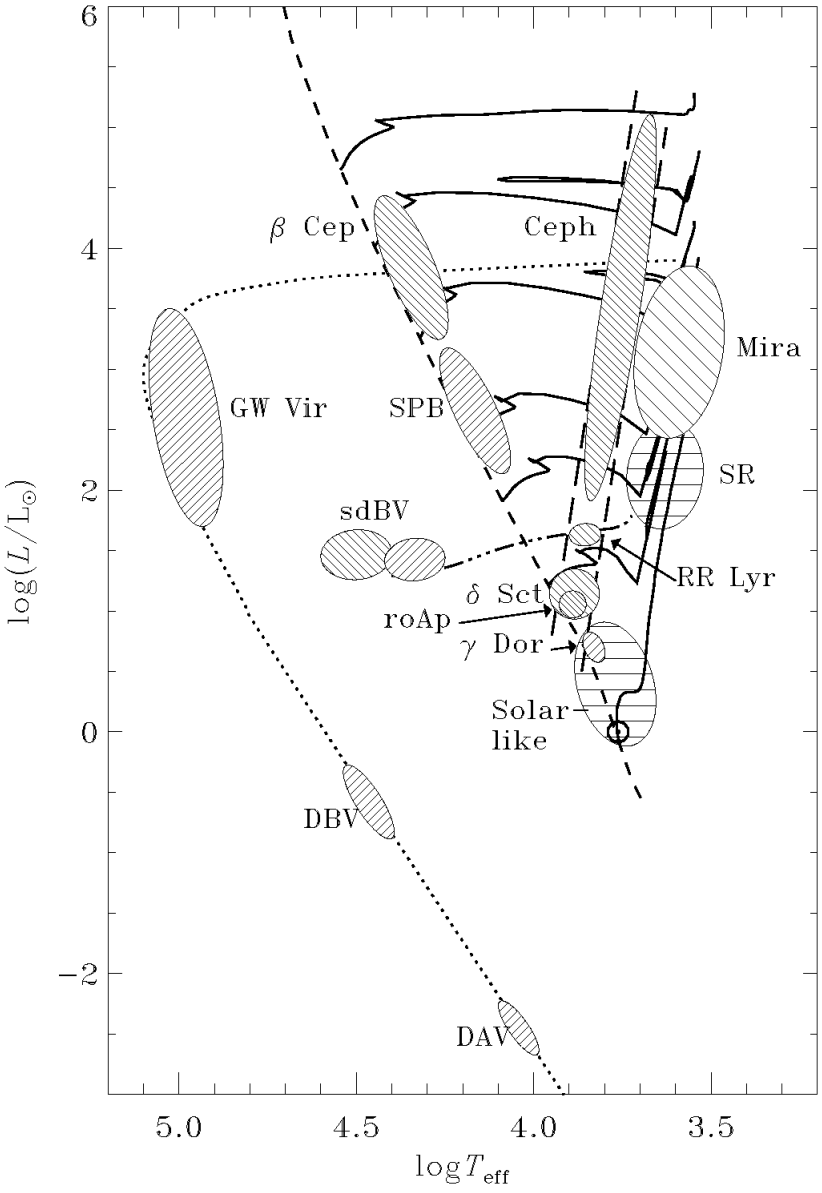

Figure 1.3: H-R diagram with regions where stellar oscillations can occur. The zero age main-sequence (ZAMS) is indicated by the dashed line. The solid curves are stellar tracks for different masses (1, 2, 3, 4, 7, 12 and 20 solar masses). The triple-dot-dashed line represents the horizontal branch and the dotted curve is the white dwarf cooling phase. The instability strip is indicated by parallel long-dashed lines. Figure taken from J. Christensen-Dalsgaard lecture notes on stellar oscillation (http://astro.phys.au.dk/ jcd/oscilnotes/contents.html).

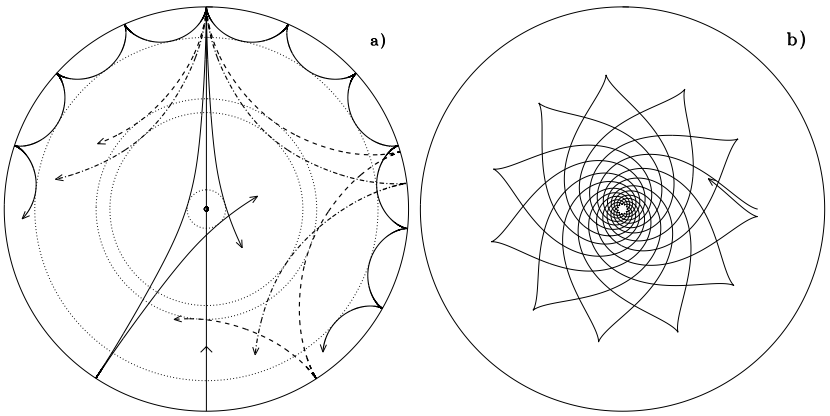

Figure 1.4: Propagation of rays of sound or gravity waves in a cross-section of the solar interior. The acoustic ray paths (a) are bent by the increase in sound speed with depth until they reach the inner turning point (indicated by the dotted circles) where they are refracted towards the surface. At the surface the acoustic waves are reflected by the rapid decrease in density. Rays are shown corresponding to modes with frequency 3000 μHz and degrees (in order of increasing penetration depth) l = 75, 25, 20 and 2; the line passing through the centre schematically illustrates the behaviour of a radial mode. The gravity-mode ray path (b) corresponds to a mode of frequency 190 μHz and degree 5. From Cunha et al. (2007)

where N is the Bruntt-Väisälä frequency, which depends on the density stratification (we will define this quantity later), and the integration is done on the g mode cavity.

Observing mean mixed mode spacing provide unique information for distinguishing red-giants with similar luminosities but different stages of evolution (Bedding et al. 2011, Stello et al. 2013). Asymptotic period spacings are derived from the precise fit of the mixed mode patterns with an asymptotic expansion (Mosser et al. 2012, Vrard et al. 2016). Ascending red giants, characterized by a hydrogen-burning shell around an inert He-core, have a low value of $\Delta\Pi$ ($\sim$ 60s) when compared to core Helium-burning clump stars ($\Delta\Pi$ = $\sim$ 300s), e.g. Mosser et al. (2014).

1.4 Mathematical description

The set of equations that describes the dynamical behaviour of a fluid are the Poisson equation for gravitational potential, the continuity equation and the equation of motion, defined as:

$$\nabla^2\Phi = 4\pi G\rho, \tag{1.7}$$

$$\frac{\partial\rho}{\partial t} + \nabla\cdot(\rho\mathbf{v}) = \mathbf{0}, \tag{1.8}$$

$$\rho(\frac{\partial}{\partial t} + \mathbf{v} \cdot \nabla)\mathbf{v} = -\nabla P - \rho\nabla\Phi, \tag{1.9}$$

where $\mathbf{v} = \mathbf{v}(\mathbf{r}, t)$ is the velocity of the fluid, $\mathbf{\Phi}$ is the gravitational potential related to the local gravity vector $g = -\nabla\Phi$, P is the pressure, G is the gravitational constant and ρ is the density. Those equations produce an *Eulerian* description of movement (denoted as $'$) where the referential is placed in a particular region, $\mathbf{r}$, inside the star as we observe how $\mathbf{v}(\mathbf{r}, t)$, $\rho(\mathbf{r}, t)$, etc. change over time. For a non-rotating star in hydrostatic equilibrium, the velocity $\mathbf{v}$ is zero in all points.

We assume here that we know the values of the physical variables of the non-perturbed star as a function of $r = |\mathbf{r}|$. Then, imagine that each fluid element in the star is dislocated from its equilibrium position in $\mathbf{r}$ by a infinitesimal, arbitrary vectorial distance, $\xi(\mathbf{r}, t)$. This type of displacement, taking an certain element of fluid and moving it to another place, is a *Lagrangian* displacement, that we will denote here as δ. When $\mathbf{v} = 0$ on a model in equilibrium, the Eulerian and Lagrangian perturbations of $\mathbf{v}$, described respectively as $\mathbf{v}'$ and $\delta\mathbf{v}$, are equal and are given by:

$$\mathbf{v}' = \delta\mathbf{v} = \frac{d\xi}{dt}, \tag{1.10}$$

where d/dt is the Stokes derivative:

$$\frac{d}{dt} = \frac{\partial}{\partial t} + \mathbf{v} \cdot \nabla. \tag{1.11}$$

When there is a fluid displacement, the other physical parameters are perturbed accordingly. For example, the pressure $P(\mathbf{r})$ originally associated with a fluid element in $\mathbf{r}$ becomes $P(\mathbf{r}) + \delta P(\mathbf{r}, t)$ when the fluid element moves to $\mathbf{r} + \xi(\mathbf{r}, t)$. Something similar occurs for other quantities and their perturbations.

If the adiabatic approximation is adopted, i.e., there is no heat exchange during movement, the relation between δP and $\delta\rho$ are the same as the radial case:

$$\frac{\delta P}{P} = \Gamma_1 \frac{\delta\rho}{\rho}. \tag{1.12}$$

We cannot use a similar relation for the Eulerian perturbations, $P'(\mathbf{r}, t)$ and $\rho'(\mathbf{r})$, because they are used to find the new pressures and densities in a *given* point $\mathbf{r}$ without informing the original position of the fluid. However, the Eulerian and Lagrangian variations can be related though the first order expression:

$$\delta\rho = \rho' + \xi \cdot \nabla\rho. \tag{1.13}$$

Now let's exchange P, ρ, Φ and $\mathbf{v}$, for $P + P'$, $\rho + \rho'$, $\Phi + \Phi'$ and $\mathbf{v}'$ into the previous equations, keeping only the first order approximation. For example, the equation of force becomes:

$$\rho\frac{\partial^2\xi}{\partial t^2} = -\nabla\mathbf{P} - \rho\nabla\mathbf{\Phi} - \nabla\mathbf{P}' - \rho\nabla\mathbf{\Phi}' - \rho'\nabla\mathbf{\Phi}. \tag{1.14}$$

However, $-\nabla\mathbf{P}-\rho\nabla\mathbf{\Phi} = \mathbf{0}$ due to the condition of maintaining hydrostatic equilibrium. The final result is a equation containing only the perturbing quantities. Similarly, the continuity equation and the Poisson equation, when perturbed, becomes:

$$\rho' + \nabla\cdot(\rho\xi) = \mathbf{0}, \tag{1.15}$$

$$\nabla^2\Phi' = 4\pi G\rho'. \tag{1.16}$$

On the continuity equation, the integration was done in relation to time and the integration constant was eliminated by demanding $\rho' = 0$ when $\xi = 0$.

Even after we tried to keep everything linear, we now have a set of partial differential equations that are second order in time and fourth order in space. In order to transform the partial derivatives into ordinary differential equations, we assume that the pulsations are periodic and can be analysed by a Fourier series. This hypothesis allow us to assume that all variables have some form of temporal dependency proportional to $e^{i\omega t}$, where ω is the complex angular frequency. For example, we assume for ξ:

$$\xi(\mathbf{r}, t) = \xi(\mathbf{r})e^{i\omega t}. \tag{1.17}$$

By doing this, we separate the time variable from the function of position in radial coordinates (r, θ, ϕ).

We can model the angular portion of the pulsations by using the spherical harmonics (Equation 1.4). Hence, the solution for $\xi(\mathbf{r})$ and $P'(\mathbf{r})/\rho$ is:

$$\begin{aligned}\xi(r,\theta,\phi) = \xi_r(r,\theta,\phi)\mathbf{e_r} + \xi_\theta(r,\theta,\phi)\mathbf{e}_\theta + \xi_\phi(r,\theta,\phi)\mathbf{e}_\phi = \\ [\xi_r(r)\,\mathbf{e_r} + \xi_t(r)\,\mathbf{e_\theta}\frac{\partial}{\partial\theta} + \xi_t(r)\,\mathbf{e_\phi}\frac{1}{\sin\theta}\frac{\partial}{\partial\phi}]\,Y_{\ell m}(\theta,\phi),\end{aligned} \tag{1.18}$$

where

$$\xi_\theta(r,\theta,\phi) = \xi_t(r)\frac{\partial Y_{lm}}{\partial\theta}. \tag{1.19}$$

Before we continue, it is important to define a couple of important frequencies. The first being the *Brunt-Väisälä frequency N*:

$$N^2 = -Ag = -g\left[\frac{d\ln\rho}{dr} - \frac{1}{\Gamma_1}\frac{d\ln P}{dr}\right], \tag{1.20}$$

where g is the gravitational acceleration. N, in its most simple interpretation, is the frequency of oscillation associated with a perturbation of a fluid element in a situation of

stable convection ($N^2 > 0$), in other words, associated with buoyancy. This buoyancy frequency was derived independently by Yrjö Väisälä (1891-1971) in 1925, and Sir David Brunt (1886-1965), in 1927.

The second frequency is the *Lamb frequency*, S_l, defined in 1910 by Sir Horace Lamb (1849-1934) as:

$$S_\ell^2 = \frac{\ell(\ell+1)}{r^2}\frac{\Gamma_1 P}{\rho} = \frac{\ell(\ell+1)}{r^2}v_s^2. \tag{1.21}$$

We also define the transversal wave number, k_t, (units being cm^{-1}):

$$k_t^2 = \frac{\ell(\ell+1)}{r^2} = \frac{S_\ell^2}{v_s^2}. \tag{1.22}$$

If we relate the transversal length $\lambda_t = 2\pi/k_t$ to k_t, then S_ℓ^{-1} is the time that a sound wave takes to travel a distance of $\lambda_t/2\pi$.

We can learn a lot from the solution of the ordinary differential equation for ξ_r and ξ_t by doing an local analysis of the system. We assume that ξ_r and ξ_t have faster spatial variations than other physical quantities that appear in the equations. Other physical variables can therefore be considered constant in a limited region of radius.

In order to quantify this, we assume that both ξ_r and ξ_t change spatially as $e^{ik_r r}$, where the wave number k_r is large when compared to r. When we insert this complex exponential into equations 1.13, 1.14 and 1.15, we obtain a set of homogeneous equations in ξ_r and ξ_t. The determinant of the coefficients need to be zero to obtain non-trivial solutions. If we keep only terms dominant in k_r, we obtain the *dispersion relation*:

$$k_r^2 = \frac{k_t^2}{\omega^2 S_\ell^2}(\omega^2 - N^2)(\omega^2 - S_\ell^2), \tag{1.23}$$

where we assume that ω^2 is positive. This equation shows that, if ω^2 is larger (or lower) then both N^2 and S_ℓ^2, it means that $k_r^2 > 0$, has a real value, and sinusoidal solution are present. However, if ω^2 had an intermediary value between N^2 and S_ℓ^2, then k_r is an imaginary number, and the realistic solutions will decay exponentially. Those are evanescent waves.

Both N^2 and S_ℓ^2 are critical frequencies for wave propagation and we can solve the dispersion relation for ω^2 in two limits of wave propagation. To make things easy, we define the total wave number K, as $K^2 = k_r^2 + k_t^2$ (see Unno et al. 1979). The wave can travel in a combination of radial and transversal directions. In a local analysis, K must be large. Therefore, if ω^2 is much larger than both N^2 and S_ℓ^2, and $|N^2|$ is less than S_ℓ^2, then we have:

$$\omega_p^2 \approx \frac{K^2}{k_t^2}S_\ell^2 = (k_r^2 + k_t^2)v_s^2 \quad (\omega^2 \gg N^2, S_\ell^2), \tag{1.24}$$

where the subscript 'p' in ω^2 denote 'pressure', since only the sound speed in present in this expression. This characterize the pressure modes described in the previous section. The other expression obtained from equation 1.23 occurs if ω^2 is much lower than both N^2 and S_ℓ^2 and is given by:

$$\omega_g^2 \approx \frac{k_t^2}{k_r^2 + k_t^2} N^2 \quad (\omega^2 \ll N^2, S_\ell^2), \tag{1.25}$$

which describe the gravity waves.

If each mode is orthogonal in relation to each other, then the eigenfunctions that correspond to each eigenvalue ω^2 has to differ from each other. In our approximation, k_r and ℓ should be able to measure this difference. Since k_r is a wave number, the corresponding wavelength is $\lambda_r = 2\pi/k_r$. The total number of nodes in the radial direction (basically the n value) in the eigenfunction is given by $n \approx 2\int_0^R dr/\lambda_r$ where the factor '2' count for the two nodes for wavelength. Hence, $n \approx \int_0^R k_r\, dr/\pi$. If we integrate equation 1.24 and assuming that ℓ is small enough so that k_t^2 can be ignored (for simplicity), we obtain the following estimation:

$$\omega_p \approx n\pi \left[\int_0^R \frac{dr}{v_s}\right]^{-1}. \tag{1.26}$$

For large values of n, the frequencies of the p modes are equally spaced. Note that the spacing of the frequencies depend only of the sound speed variation and, for a ideal gas, depends mainly on temperature. Therefore, for sun-like stars, p modes are effective way to obtain information on the internal temperature profile.

The corresponding estimation for g modes is:

$$\Pi_g = \frac{2\pi}{\omega_g} \approx n \frac{2\pi^2}{[\ell(\ell+1)]^{1/2}} \left[\int_0^R \frac{N}{r}\, dr\right]^{-1}. \tag{1.27}$$

For g modes, the period is equally spaced in n, and are sensible to the value of ℓ. Additionally, the period rises with n, in contrast to p modes.

1.4.1 Properties of Solar-like Oscillations

Let us focus now on the properties of pressure modes exited by subsurface convection in cool, low-mass stars. Tassoul (1980, 1990) and Gough (1993) have shown that the eigenfrequencies of low-degree p modes satisfy the following relation:

$$\nu_{n,l} = \frac{\omega_{n,l}}{2\pi} \simeq \left(n + \frac{l}{2} + \frac{1}{4} + \alpha\right)\Delta\nu - [Al(l+1) - \delta]\frac{\Delta\nu^2}{\nu_{n,l}}, \tag{1.28}$$

where δ and α are related to sub-surface effects and:

$$A = \frac{1}{4\pi^2\Delta\nu}\left[\frac{c(R)}{R} - \int_0^R \frac{dc}{dr}\frac{dr}{r}\right]. \tag{1.29}$$

The quantity $\Delta\nu$ is the average large separation and it is related to the time that a sound wave takes to travel from core to surface (Christensen-Dalsgaard 2003):

$$\Delta\nu = \left(2 \int_0^R \frac{dr}{c}\right)^{-1}, \tag{1.30}$$

where c is the sound speed defined as (assuming adiabatic approximation):

$$c = \sqrt{\frac{\Gamma_1 P}{\rho}} \tag{1.31}$$

where Γ_1 the first adiabatic index, P is the pressure and ρ is the density. For an ideal gas, $\rho \propto \mu P/T$, and the best estimates for the central temperature give $T \propto \mu M/R$ (Kippenhahn and Weigert 1994). We therefore arrive at:

$$\Delta\nu \propto \sqrt{\frac{M}{R^3}}. \tag{1.32}$$

Therefore, the average large frequency separation is a proxy for the mean density of a star (Ulrich 1986).

If we look at the solar oscillation spectrum in figure 1.5, we note that the amplitudes of the modes follow a broad envelope which can be described by a Gaussian function. The central frequency is denoted $\nu_{\max}$, the frequency of maximum power. The shape and position of this envelope is dictated by the mechanisms of mode excitation and damping, making it dependent on fundamental stellar properties. Brown et al.(1991) suggested that $\nu_{\max}$ scales with the acoustic cut-off frequency, ν_{ac}, which is the frequency above which acoustic modes are not reflected at the surface:

$$\nu_{\max} \propto \nu_{ac} \propto \frac{c}{2H_p}, \tag{1.33}$$

where H_p is the pressure scale height, which for an isothermal atmosphere is given by (Kippenhahn and Weigert 1994):

$$H_p = \frac{PR^2}{GM\rho}. \tag{1.34}$$

If we assume an ideal gas and that the temperature may be approximated by the effective temperature, we obtain:

$$\nu_{\max} \propto \frac{g}{\sqrt{T_{\rm eff}}} \propto \frac{M}{R^2\sqrt{T_{\rm eff}}}, \tag{1.35}$$

where g is the surface gravity (Kjeldsen and Bedding 1995). The validity of this scaling relation for $\nu_{\max}$ is on less solid theoretical grounds than its counterpart for $\Delta\nu$, Equation 1.30. We will discuss the scaling $\nu_{\max}$ scaling relation in more detail in Chapter 2.

If we decide to ignore the last second order term in equation 1.28, we will obtain an uniform spacing between two modes with the same value of angular degree l and

consecutive value of n, as can be seen in figure 1.5. This defines the large frequency separation as:

$$\Delta\nu_{nl} = \nu_{n+1,l} - \nu_{n,l}. \tag{1.36}$$

This quantity can be equal to $\Delta\nu$ if we assume a first order approximation. Modes with the same value of $n + l/2$ will be grouped together in the power spectrum:

$$\nu_{n,l} \simeq \nu_{n-1,l+2}. \tag{1.37}$$

The small frequency separation will measure departures from equation 1.37:

$$d_{l,l+2} = \nu_{n,l} - \nu_{n-1,l+2}. \tag{1.38}$$

The small frequency separation can be related to the second-order term in equation 1.28:

$$d_{l,l+1} = \nu_{n,l} - \frac{1}{2}(\nu_{n-1,l+1} + \nu_{n,l+1}) \simeq -(2l+2)\frac{\Delta\nu}{4\pi^2\nu_{n,l}}\int_0^R \frac{dc}{dr}\frac{dr}{r}. \tag{1.39}$$

We can see in the equations above that the small separation is related to the gradient of sound speed near the core and, as a consequence, sensible to the composition profile in the central regions of the star. Therefore, the small frequency separation is an important tool to obtain valuable information on stellar age.

The structure in frequencies that appears in equation 1.28 can be visualized in figure 1.6 in the so-called echelle diagram, where the axis with the frequencies is separated in pieces with length of $\Delta\nu$ and then stacked in top of each other. By doing this, we obtain the characteristic vertical lines with different values of l, each one being separated by the corresponding small separation. We can see by the curvature of the vertical lines that the observed frequencies show departures from the asymptotic relation. This is mainly due to our poor knowledge of near-surface effects in δ and α. Another important effect are departures from a smooth internal structure, translated in the so-called acoustic glitches. Such glitches can be used to obtain estimations of acoustic location of the base of the convective zone and helium ionization zones. We will analyse the details of the glitch signature during Chapter 4.

It is possible to retrieve information about specific regions of the star by using other combinations of frequencies.

The amplitude of modes with spherical degree l = 0,1 are much larger than modes with l = 2,3. For some stars, this may cause problems when trying to obtain small separations that need consecutive modes. However, the *Kepler* space telescope obtained a high number of modes for many solar-like stars. We will here focus in frequency combinations with modes where l = 0,1 and 2, but it is important to note that detection of l = 3 modes was possible for the brightest stars in the *Kepler* field.

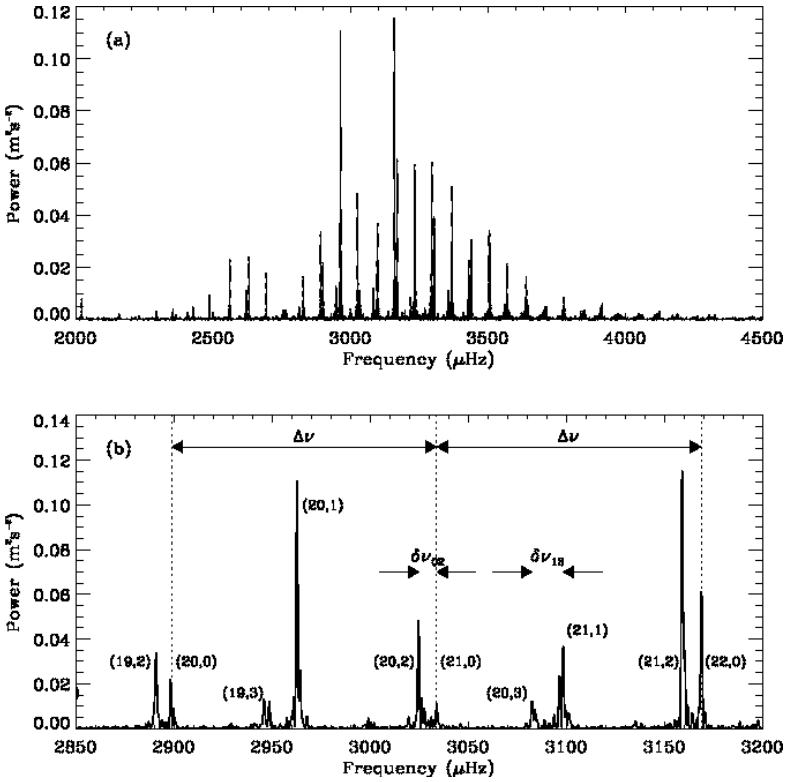

Figure 1.5: (a) Power spectrum of 10 days of velocity observations of the Sun taken with the BiSON instrument (Chaplin et al. 1997b). (b) Close-up of panel (a) near the frequency of maximum power, indicating the spherical degree l and radial order n for each mode. Dotted lines mark the radial modes, and the large and small separations are indicated. From Bedding (2011).

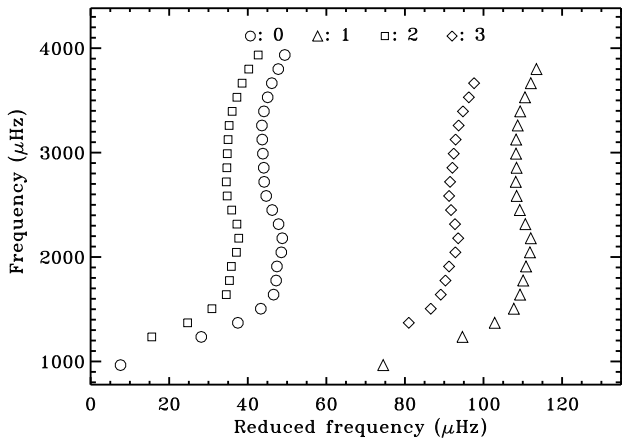

Figure 1.6: Echelle diagram for observed solar frequencies obtained with the BiSON network (Chaplin et al. 2002a), plotted with $\Delta\nu = 135\mu$HZ. Circles, triangles, squares and diamonds are used for modes of degree $l = 0, 1, 2$ and 3, respectively. From Cunha et al. (2007)

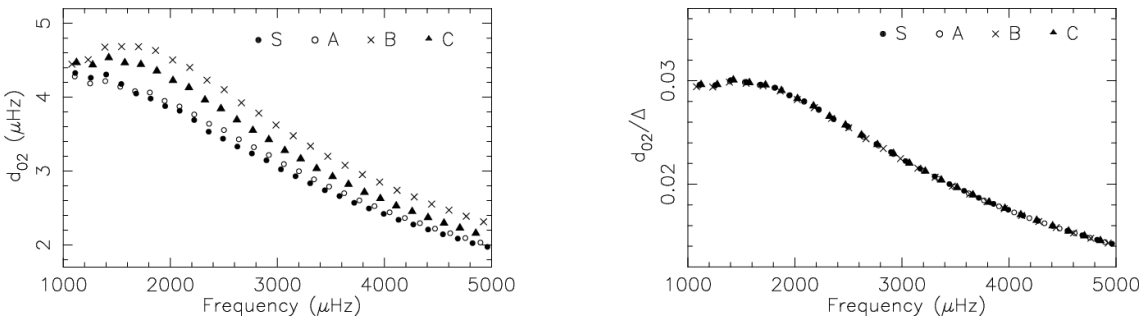

(a) (b)

Figure 1.7: Small separations d_{02} and ratios r_{02} for four solar models with different outer envelopes. Figures were extracted from Roxburgh & Vorontsov (2003).

One combination in particular is the ratio of small to large separation, showed in Roxburgh and Vorontsov(2003) to be independent of the outer layers in the stellar structure. First we define the small separations d_{01} and d_{10}, also know as the three point difference:

$$d_{01,n} = \frac{1}{2}(2\nu_{n,0} - \nu_{n-1,1} - \nu_{n,1}), \tag{1.40}$$

$$d_{10,n} = -\frac{1}{2}(2\nu_{n,1} - \nu_{n,0} - \nu_{n+1,0}), \tag{1.41}$$

and the corresponding ratios:

$$r_{01,n} = \frac{d_{01,n}}{\Delta\nu_{1,n}}, \tag{1.42}$$

$$r_{10,n} = \frac{d_{10,n}}{\Delta\nu_{0,n+1}}. \tag{1.43}$$

By using these variables, the near-surface effects are effectively cancelled when the ratio is computed, as can be seem in figure 1.7.

On the equation 1.36, we defined the large separations as an approximation for the derivative of $\nu_{n,l}$ as function of n for each spherical degree l. It is possible to obtain higher derivatives, such as the second differences:

$$\Delta_2\nu_{n,l} = \nu_{n-1,l} - 2\nu_{n,l} + \nu_{n+1,l} \tag{1.44}$$

In chapter 4, we will make use of second differences and frequency ratios as a tool to isolate and amplify the signatures of rapid variation that induce a departure of the asymptotic relation.

1.5 The *Kepler* Space Telescope

1.5.1 Motivation

In the past few decades, the discovery of thousands of planets orbiting other stars, also known as extrasolar planets or exoplanets, has brought attention to one of the most fundamental questions of humanity: what are the prospects of finding life in other planets? Many believe that such discovery would indeed have strong influence in modern philosophy and society. The search for life on an exoplanet has been one of the greatest challenges of modern astronomy.

However, finding exoplanets themselves is a difficult task. The amount of light emitted by the parent star is orders of magnitudes higher than the light reflected by the exoplanet. This effect can be mitigated by using a coronograph to block the light from the parent star. However, there are technological limitations to the technique. As a result, very few extrasolar planets have been observed directly.

In 1995, Michel Mayor and Didier Queloz made the first indirect discovery of a planet orbiting a main-sequence star (Mayor and Queloz 1995). They used the technique of Doppler shift in the spectra of 51 Peg to find a planet pulling the star away and toward us as it completes a full orbit. The Doppler shift was applied to several other stars and the number of exoplanets quickly rose. However, such technique induces a heavy observational bias: it is much easier to detect massive planets in short orbits. Such class of objects are classified today as 'Hot-Jupiters' and have an orbit of only a few days. In order to detect a planet with a mass similar to Earth around a Sun-like star in a orbital period of ~ 1 year requires a precision in radial velocity measurements of $\sim 1\ m/s$, which is in the order of magnitude of the small variability induced by solar-like oscillations.

Another indirect method that has great success in finding smaller planets in the so-called transit method. When a exoplanet passes in front of the parent star (with respect to the line of sight), it will block a fraction of the light and produce a characteristic dip in the stellar light-curve. This signature can be used to obtain an estimation of the ratio between the size of the exoplanet and the size of the parent star. However, the fraction of the stellar light that is blocked by a planet is incredibly small, and requires an continuous observations with high photometric precision. This can be achieved from ground based observations, and there are some networks of telescope dedicated to observe photometric transits, such as WASP (Pollacco et al. 2006), HATnet (Bakos et al. 2004) and TrES (Alonso et al. 2004). Even so, gaps in the data will be produced due to daylight and bad weather, and the signal from a Earth-like planet around a sun-like star at 1 AU will produce a dip of only 0.01%, and this level of precision will be masked by perturbations caused by earth's atmosphere, leaving transit observation made by ground-based telescopes to find mostly giant planets and super earth. In this context, a spaced based

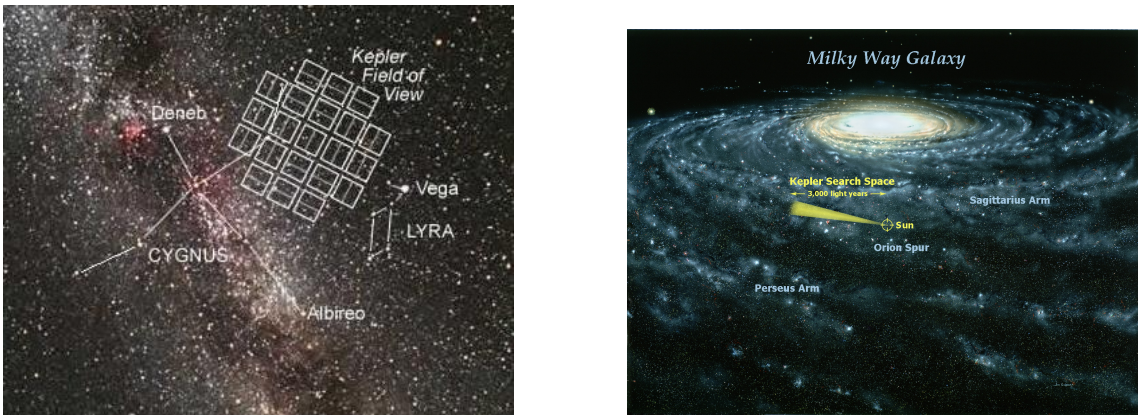

(a) (b)

Figure 1.8: Left: Projection of the field of view of *Kepler* onto the sky. The field of the 42 CCD detectors are represented by each individual rectangle. The constellations Cygnus and Lyra are also indicated. Right: Artists impression of the Milky Way galaxy indicating the the approximate search cone of Kepler. Image Credits: Carter Roberts and Jon Lomberg.

observatory dedicated to detect planetary transits is the best option to find a planet similar to Earth. This level of precision is also ideally suited to detect intrinsic pulsations in low mass stars.

The first space observatory partially dedicated to search for exoplanet transits was the French-led *CoRoT* mission (Baglin et al. 2009), launched in 2006. In 2009, NASA launched the *Kepler* space telescope (named after the German astronomer Johannes Kepler). The telescope was designed to continuously stare at a single patch of sky near the constellations of Cygnus and Lyra, with a nominal duration of $\approx$ 3 years to search for Earth-like planets around Sun-like stars (e.g. Borucki et al. 2010).

1.5.2 Design and Mission Objectives

Kepler was launched in an Earth-trailing, heliocentric orbit with an orbital period of 373 days. In order to maximize the efficiency of detecting planetary transits, Kepler was designed to monitor a fixed patch in the sky for its entire mission length. This is achieved by observing a field of the ecliptic plane while rotating the spacecraft by 90 degrees every three months in order to keep the solar panels directed towards the Sun. The *Kepler* field of view is centred towards the galactic plane in the constellations of Cygnus and Lyra (see Figure 1.8), corresponding to a line-of-sight along the Orion arm of the Milky Way galaxy. *Kepler* simultaneously monitored the brightnesses of roughly 170 000 stars of spectral types F-K in a magnitude range down to V $\sim$ 16.

The telescope is a modified Schmidt design and the scientific instrument is the photometer, with a 0.95 m correcting lens and 1.4 m primary mirror. The detector at the

primary focus is an array of 42 CCD detectors. Observations are taken in two cadence modes. Long cadence data have a sample rate of one data point every 29.4 minutes, and is good enough to detect the majority of transits that typically last several hours. The majority of stars in the *Kepler* field of view are observed in long cadence. Short cadence allows for more rapid observations in a smaller number of targets, taking a data point every 58.85 s. This mode can measure transit duration with more precision (possibly revealing transit time variations that indicate the presence of additional planets), observe the ingress and egress of the transit in more detail, and to observe stellar variations on periods shorter than 30 minutes, such as solar-like oscillations in main sequence stars. *Kepler* does not return images of its entire field-of-view because the amount of data to be sent back to Earth would be too large. In order to reduce the amount of data to be downlinked, 'pixel masks' are used around target stars to select specific pixels containing the majority of the stellar flux.

Since the spacecraft needs to be rotated once every three months, *Kepler* data is therefore naturally split into quarters. *Kepler* observations began with a commissioning period of 10 days, between 2–11 May of 2009, constituting the quarter zero (Q0). This was followed by the short, month-long Quarter 1 (Q1) before the first rotation of the spacecraft, and all other following quarters lasted three months.

One of the four reaction wheels, responsible for fine pointing, failed in July 2012. However, the spacecraft remained operational, since only three reaction wheels are necessary to maintain fine pointing. A second reaction wheel failed in May 2013, making impossible for *Kepler* to continue the observations as was it initially designed. However, the telescope was not completely lost and the mission was renamed K2 and continues to obtain data by using solar wind to compensate for the failure of two reaction wheels. However, the spacecraft is not as stable as before and the dataset of K2 has a much shorter period compared to a full functional *Kepler*. On the other hand, K2 has the opportunity to observe different regions of the sky.

1.5.3 Main results

Despite the failure of these parts, the *Kepler* mission has been considered as a great success, producing fifteen quarters of data. It discovered hundreds of planets, and there are still thousands of candidates awaiting confirmation, with great amounts of data yet to be analysed. *Kepler* observed many multiple planet systems (e.g. Lissauer et al. 2011), planets orbiting binary stars (e.g. Doyle et al. 2011), many rocky planets (e.g. Batalha et al. 2011) and several super-Earth size planets orbiting in their stars' habitable zones (Borucki et al. 2012, 2013; Barclay et al. 2013a). Since *Kepler* can obtain such high precision in photometry, the same data that can be used to detect transiting exoplanets can also be used to study stars asteroseismically. By analysing stars with asteroseismolgy,

fundamental properties such as the mass, age, and radius can be determined with great precision. An accurate estimation for stellar radius is specially crucial in the context of planetary transits, since the dip produced in the light curves is only proportional to the ratio between the size of the planet and the size of the parent star. Estimations of stellar age translate into the age of the planets, revealing clues as to whether life may potentially have had time to evolve in the case of planets located at the habitable zone.

The potential of the relationship between exoplanets and asteroseismology led to the creation of the Kepler Asteroseismic Science Consortium (KASC). Members of the KASC carry out investigations of all types of variable stars present in the *Kepler* data, ranging from high-amplitude classical pulsators, such as Cepheid, Mira and RR Lyrae variables, through to the lower amplitude solar-like oscillations observable in cooler stars. *Kepler* has altered the way we do asteroseismology of Sun-like stars. With so many stars observed by *Kepler* it is no longer possible to study every star in detail. We therefore need to develop and exploit tools that allow us to perform asteroseismic analyses of stars in a large scale.

Chapter 2

Testing the asteroseismic $\nu_{\rm max}$ scaling relation

In this chapter, we describe our work to test the scaling relation for the global asteroseismic parameter $\nu_{\rm max}$, the frequency of maximum amplitude in a power spectrum. This relation assumes that $\nu_{\rm max}$ scales with surface gravity and surface temperature, that also describes the behaviour of the acoustic cut-off frequency $\nu_{\rm ac}$ when assuming an isothermal atmosphere. This scaling relation has been widely used to derive global stellar parameters, and it is therefore important to test the validity of this relation. The majority of the content in this chapter was directly extracted from Coelho et al. (2015), with the difference that we added here a brief discussion of the theoretical relation between $\nu_{\rm max}$ and $\nu_{\rm ac}$.

The work of this chapter is structured as follows: in section 2.1 we make a general introduction where we describe the usefulness of the asteroseismic relations. In section 2.2 we summarise the theoretical understanding of the $\nu_{\rm max} - \nu_{\rm ac}$ relation. Section 2.3 describes the methodology we used to run our tests. Section 2.4 describes both the artificial and *Kepler* data used in our analysis, as well as the grid of stellar models used to run the analysis. In section 2.5, we describe the results for both the artificial data and *Kepler* stars, and section 2.6 summarises our conclusions.

2.1 Introduction

Data on global (or average) asteroseismic parameters associated with the observed oscillations spectra provide important diagnostics of fundamental stellar properties. Extracting these global parameters from oscillation spectra is usually very straightforward, meaning a large number of stars can easily be analysed. This can be particularly advantageous when low S/N ratios either obstruct or prevent a more detailed analysis of individual modes in the spectrum. Moreover, detailed analysis of stars with high S/N or complicated

oscillation spectra can be very time consuming.

Two global asteroseismic parameters have received particular attention, and wide use. One parameter is the average large frequency separation, $\Delta\nu$, defined as the average of the observed frequency spacings between consecutive overtones n of the same angular (spherical) degree, l. The average large frequency separation,$\Delta\nu$, scales to a very good approximation as $\rho^{1/2}$, where $\rho \propto M/R^3$ is the mean density of a star of mass M and surface radius R (e.g. see Tassoul 1980, Ulrich 1986, Christensen-Dalsgaard 1993). This scaling has physical justification (e.g., see Reese et al. 2012).

The second parameter, $\nu_{\rm max}$, is the frequency at which detected modes of a star show the strongest amplitude. However, one of the main conditions for the existence of p-modes is that acoustic waves are trapped in cavities inside the star, where they are reflected in the interior and exterior walls of such cavity. In regions near the stellar surface, the reflection occurs in an atmospheric layer due to abrupt changes in physical conditions, such as variations of sound speed and density. In such conditions, reflection occurs for waves with frequencies smaller than a critical value $\nu_{\rm ac}$. This critical value is known as the atmospheric cut-off frequency, since acoustic waves with frequencies higher than $\nu_{\rm ac}$ propagate through the stellar atmosphere.

Brown et al. (1991) speculated that $\nu_{\rm max}$ might scale with the cut-off frequency, $\nu_{\rm ac}$. Adopting an isothermal approximation to the full equation describing the cut-off frequency, one derives the scaling $\nu_{\rm ac} \propto \nu_{\rm max} \propto gT_{\rm eff}^{-1/2}$ (Brown et al. 1991, Kjeldsen & Bedding 1995). Numerous studies have shown empirically that $\nu_{\rm max}$ appears to follow this relation to reasonable approximation (e.g., Chaplin & Miglio 2013 and references therein). While some headway has been made on understanding the exact form of the scaling (e.g., Belkacem et al., 2013), a full theoretical justification remains elusive. Additions to the scaling, for example a dependence on the changing Mach number of the near-surface turbulent flow (Belkacem et al. 2013), have also been proposed. This will be discussed in more detain in section 2.2.

Information encoded in $\Delta\nu$ and $\nu_{\rm max}$ is commonly exploited by using the above scaling dependencies normalized to observed solar parameters or properties, i.e.,

$$\Delta\nu \simeq \left(\frac{M}{\mathrm{M}_\odot}\right)^{1/2}\left(\frac{R}{\mathrm{R}_\odot}\right)^{-3/2}\Delta\nu_\odot \tag{2.1}$$

and

$$\nu_{\rm max} \simeq \left(\frac{M}{\mathrm{M}_\odot}\right)\left(\frac{R}{\mathrm{R}_\odot}\right)^{-2}\left(\frac{T_{\rm eff}}{\mathrm{T}_{\rm eff\,\odot}}\right)^{-1/2}\nu_{\rm max\,\odot}. \tag{2.2}$$

Typical solar values for the seismic parameters (e.g., see Chaplin et al. 2014) are $\Delta\nu_\odot = 135.1\,\mu$Hz and $\nu_{\rm max\,\odot} = 3090\,\mu$Hz. These solar-calibrated scaling relations represent two equations in two unknowns when an estimate of $T_{\rm eff}$ is also available, allowing us to solve directly for M and R to give so-called "direct" estimates of the stellar properties.

Moreover, each relation can be used independently to provide direct estimates of the mean stellar density ρ (Equation 2.1) or the surface gravity g (Equation 2.2). Alternatively, the relations may be utilized (together or separately) as part of a grid-based search code. Here, one searches amongst a grid of stellar evolutionary models to find those models whose predicted asteroseismic or atmospheric parameters match the actual observed parameters (at the level of the observational uncertainties). The solar-calibrated relations provide the means to translate model properties (R, M, $T_{\rm eff}$) to expected values for $\Delta\nu$ and $\nu_{\rm max}$, thereby allowing a comparison to be made with the observations.

These global asteroseismic parameters and their associated scaling relations are now being employed in analyses of large samples of solar-like oscillators to, for example, generate catalogues of asteroseismic stellar properties (e.g., see Huber et al. 2013, Chaplin et al. 2014, Casagrande et al. 2014, Pinsonneault et al. 2014). Tests in the literature of the scaling relations for solar-type stars have, by and large, returned encouraging results. Studies have most commonly looked at data on estimated stellar radii, and include comparisons with very accurate properties from binaries, parallaxes and long baseline interferometry (e.g., Bruntt et al. 2010, Bedding 2011, Miglio 2012, Huber et al. 2012, Silva Aguirre et al. 2012, White et al. 2013). Results have tested the combination of the two scaling relations to levels of around 4 per cent in inferred radii, and 10 per cent in inferred masses (Chaplin et al. 2014).

Results on red giants are more complicated. For example, He-core burning and H-shell burning giants with the same mass and radius can have a different $\Delta\nu$, due to differences in the sound-speed profile in the outer layers (Miglio et al. 2012), which implies a different absolute scaling for Equation 2.1. Meanwhile, other studies have looked at open clusters in the *Kepler* field, comparing results on red giants inferred from asteroseismology and from turnoff eclipsing binaries (Brogaard et al. 2012, Sandquist et al. 2013).

Our approach is to test, empirically, the accuracy of the classic $\nu_{\rm max}$ scaling relation for oscillations seen in solar-type stars, i.e., cool main-sequence and sub-giant stars (we leave a study of giants to future work). There is actually very little in the literature on the $\nu_{\rm max}$ scaling alone, which partly reflects the difficulty of obtaining the data needed to test the one relation in isolation. A recent example made use of interferometric data on a few very bright *Kepler* targets: White et al. (2013) concluded that results on the F-type star θ Cyg may point to problems for the $\nu_{\rm max}$ scaling in the hottest solar-type stars.

Our basic approach is as follows. We use data on a sample of around 500 stars observed by the NASA *Kepler* Mission (the same sample as in Chaplin et al. 2014). Each star in our sample has a measured $\nu_{\rm max}$, which comes from analysis of the *Kepler* data. Throughout the rest of the paper we shall refer to these actual, measured values as $\nu_{\rm max}$(data). Now, the classic scaling relation (Equation 2.2) gives $\nu_{\rm max}$ in terms of g and $T_{\rm eff}$, or, to be more specific, the combination $g\,T_{\rm eff}^{-1/2}$. We can therefore test the scaling if

we have independent measures of

$$\nu_{\rm max}({\rm grid}) \equiv \left(\frac{g}{\rm g_\odot}\right)\left(\frac{T_{\rm eff}}{\rm T_{eff\,\odot}}\right)^{-1/2} \nu_{\rm max\,\odot}, \tag{2.3}$$

to which the observed $\nu_{\rm max}$(data) may be compared. The $\nu_{\rm max}$(grid) are so-named because we adopt a grid-based search technique to estimate them, using as inputs the asteroseismic average large separations, $\Delta\nu$, of the stars along with photometric temperatures, $T_{\rm eff}$, derived using the Infrared Flux Method (IRFM) and, where available, metallicities [Fe/H] from spectroscopy. We search grids of stellar evolutionary models to find those models whose predicted $\{\Delta\nu, T_{\rm eff}, [{\rm Fe/H}]\}$ match the actual observed inputs. Each model in the grid also has a computed $\nu_{\rm max}$(grid), which comes from its M, R and $T_{\rm eff}$. The best-matching models will have the most likely values of $\nu_{\rm max}$(grid). A suitable, likelihood-weighted average therefore provides an estimate of $\nu_{\rm max}$(grid) for every star (see Section 2.4.2), which may then be compared directly to the observed $\nu_{\rm max}$(data). Any departures from a one-to-one correspondance of the values would point to problems with the classic scaling relation, and allow us to quantify departures from the scaling. In sum, we leverage the potential of using asteroseismic results on a large number of solar-type stars to follow a statistical (ensemble) approach to the analysis and to thereby beat-down the errors. The approach is not dissimilar to that adopted by Morel et al. (2014) for part of their analysis of red giants observed by the CNES/ESA CoRoT Mission, which compared values of the surface gravity estimated using $\Delta\nu$ on the one hand and $\nu_{\rm max}$ on the other.

2.2 Theoretical background for the $\nu_{\rm max}$ scaling relation

The acoustic cut-off frequency $\nu_{\rm ac}$ (see equation 1.33) is defined as the frequency above which there is no more complete reflection of acoustic modes at the surface. The acoustic cut-off frequency also correspond to time-scales related with the stellar atmosphere. Therefore, a direct relation between $\nu_{\rm ac}$ and $\nu_{\rm max}$ has been proposed (Brown et al., 1991; Kjeldsen & Bedding, 1995). The theoretical relations followed by the acoustic cut-off are (Balmforth & Gough, 1990):

$$\omega_{\rm ac} = \frac{c_s}{2H_\rho} \propto \frac{g}{\sqrt{T_{\rm eff}}} \propto \frac{M}{R^2\sqrt{T_{\rm eff}}}, \tag{2.4}$$

where g is the gravitational acceleration, M is the stellar mass, R is the stellar radius, $T_{\rm eff}$ is the effective temperature, c_s is the sound speed and H_ρ is the density scale height. Equation 2.4 is valid when assuming all quantities to be in the photosphere and using the relations $c_s \propto T_{\rm eff}$ and $H_p \propto T_{\rm eff}/g$ If we take equation 2.4 and adopt an isothermal approximation where we can, as consequence, consider H_ρ as $H_P = P/\rho g$ (with P denoting pressure), and then normalize everything to solar values, we obtain:

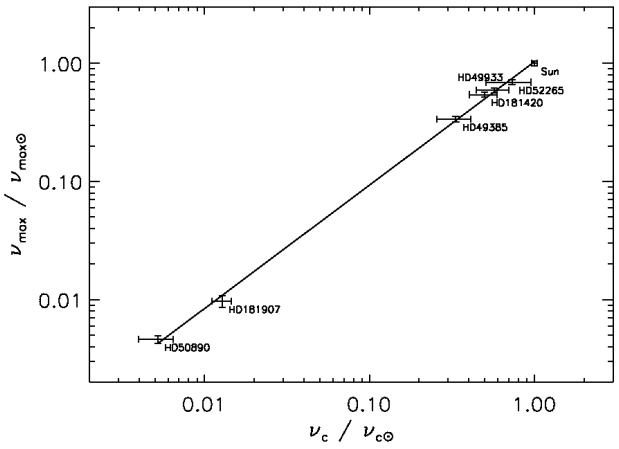

Figure 2.1: Frequency of the maximum of oscillation power for a group of main-sequence and red-giant stars as a function of the acoustic cut-off frequency (denoted here as ν_c). The fitted slope is 1.01 ± 0.02. Figure from Belkacem et al. (2013)

$$\nu_{\rm ac} = \nu_{\rm ac\odot} \frac{M}{M_\odot} \left(\frac{R}{R_\odot}\right)^{-2} \left(\frac{T_{\rm eff}}{T_{\rm eff\odot}}\right)^{-1/2} . \tag{2.5}$$

By obtaining surface temperatures using, e.g, spectroscopy, and stellar models to obtain M and R, one can use equation 2.5 to obtain $\nu_{\rm ac}$ an compare it with values of $\nu_{\rm max}$ extracted directly from the power spectrum. This can be done to ascertain the relation $\nu_{\rm ac} \propto \nu_{\rm max} \propto g T_{\rm eff}^{-1/2}$, as shown in Figure 2.1. Numerous studies have shown empirically that $\nu_{\rm max}$ appears to follow this relation to reasonable approximation (e.g., Bedding & Kjeldsen, 2003; Mosser et al., 2010; Chaplin and Miglio, 2013, and references therein).

The theoretical foundations of the relationship between $\nu_{\rm max}$ and $\nu_{\rm ac}$ and have been explored by Belkacem et al. (2011) and are not very intuitive. The relation between the two quantities can be explained by using two consecutive relations:

$$\nu_{\rm max} \propto \tau_{\rm th}^{-1} \rightarrow \tau_{\rm th}^{-1} \propto \nu_{\rm ac}, \tag{2.6}$$

where $\tau_{\rm th}^{-1}$ is the thermal adjustment timescale defined as:

$$\tau_{\rm th} = \frac{1}{L} \int_{m_{\rm tr}}^{M} c_\nu T dm, \tag{2.7}$$

where M is the total mass of the star, c_ν is specific heat capacity at a fixed volume, and $m_{\rm tr}$ is the mass at the transition region. We will come back to this quantity later. For now, let us discuss the nature of $\nu_{\rm max}$ and the relation $\nu_{\rm max} \propto \tau_{\rm th}^{-1}$. The frequency of maximum power in a power spectrum is defined by the maximum frequency height H defined as (after background noise is properly removed):

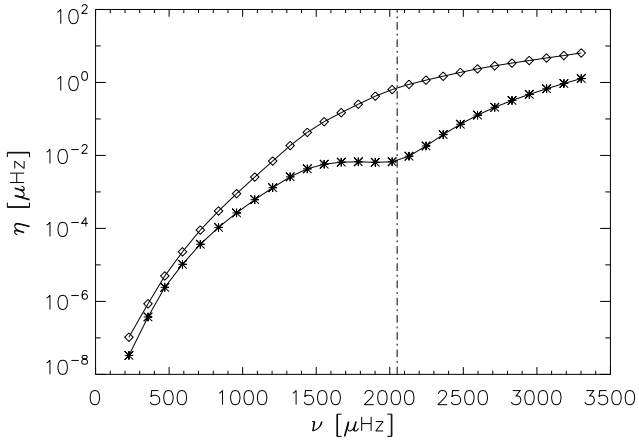

Figure 2.2: Mode damping rates versus mode frequencies computed for a model of one solar mass on the main-sequence, using the Grigahcène et al. (2005) formalism as described by Belkacem et al. (2012). The star symbols correspond to the full computation while the diamond symbols correspond to the computations for which $\delta\kappa/\kappa = 0$ was imposed. The vertical dashed-dotted line corresponds to the frequency $\nu_{\max}$ computed using scaling relations. Figure extracted from Belkacem et al. (2011)

$$H = \frac{P}{2\eta^2 \mathcal{M}}, \tag{2.8}$$

where P is the excitation rate, η is the damping rate and $\mathcal{M}$ is defined as the mode mass:

$$\mathcal{M} = \int_0^M \frac{|\xi|^2}{|\xi(M)|^2} dm, \tag{2.9}$$

with ξ being the mode displacement.

The maximum value of H is determined by the squared value of the damping rate η^2 in equation 2.8 (see Chaplin et al., 2008; Belkacem et al., 2013; Appourchaux et al., 2012). More specifically, $\nu_{\max}$ arises from the plateau in the damping rates (see figure 2.2). The plateau in η happens when the modal period is almost equal to the thermal adjustment time-scale ($\tau_{\rm th}$) in the superadiabatic layers (see Balmforth, 1992; Belkacem et al., 2013). For classical pulsators (Chepheids, δ Scuti stars, etc..), this happens in the so-called transition region (e.g. Cox, 1974) and its occurrence in the ionization layers is one of the conditions for a mode to be exited by the κ-mechanism (e.g. Cox, 1980; Cox & Giuli, 1968).For solar-like oscillations, the situation is similar, with the major difference that the damping rates will never be dominated by the destabilizations induced by perturbations of opacity, and convective movement make the situation more complicated by modifying the thermal adjustment timescale (see Belkacem et al., 2013, 2012, for a more detailed description). Figure 2.2 shows the damping rates for models with and without perturbations on opacity, confirming that $\delta\kappa/\kappa$ is of vital importance in the relation between modal

period and the thermal adjustment timescale.

Now that we established the linear relation between $\nu_{\rm max}$ and $\tau_{\rm th}$, let us explore the relation between $\tau_{\rm th}$ and $\nu_{\rm ac}$. Belkacem et al. (2013) used mixing-length formalism to obtain a linear relation between $\nu_{\rm ac}$ and $\tau_{\rm th}$. The quantity $1/\tau$ can be written as:

$$\frac{1}{\tau} = \frac{F_{\rm conv}}{\rho c_v T H_p}\left[1 + \frac{F_{\rm rad}}{F_{\rm conv}}\right], \tag{2.10}$$

where $F_{\rm conv}$ and $F_{\rm rad}$ are the convective and radiative fluxes, respectively. The solutions for the convective flux and velocity predicted by mix-length theory can be written as (Cox & Giuli, 1968):

$$F_{\rm conv} = \frac{1}{2}\rho c_p \mathrm{v}_{\rm conv} T \frac{\Lambda}{H_p}(\nabla - \nabla'), \tag{2.11}$$

$$\mathrm{v}_{\rm conv} = \frac{\alpha c_s \Sigma^{1/2}}{2\sqrt{2}\Gamma_1^{1/2}}(\nabla - \nabla')^{1/2}, \tag{2.12}$$

where $\Lambda = \alpha H_p$ is the mixing length, α is the mixing length parameter, $\nabla = (d\ln T/\ln P)$, $\nabla' = (d\ln T'/\ln P)$ is the gradient of the rising convective element, $\Sigma = (\partial\ln\rho/\partial\ln T)_{\mu,P}$, where μ is the mean molecular weight, and $\Gamma_1 = (\partial\ln P/\partial\ln\rho)_{\rm ad}$. Inserting equations 2.11 and 2.12 into equation 2.10, we have:

$$\frac{1}{\tau} = 8\left(\frac{\Gamma_1^2}{\chi_\rho \Sigma}\right)\left(\frac{\mathcal{M}_a^3}{\alpha}\right)\left(\frac{c_s}{2H_p}\right)\left[1 + \frac{F_{\rm rad}}{F_{\rm conv}}\right] \tag{2.13}$$

where $\chi_\rho = (\partial\ln P/\partial\ln\rho)_T$ and $\mathcal{M}_a$ is the Mach number defined as the ratio between the velocity of convective material and the sound speed. The ratio $F_{\rm rad}/F_{\rm conv}$ is generally the same in all models considered in the super-adiabatic layer. Therefore, using equation 2.13 together with the resonance condition $\nu_{\rm max} = 1/2\pi\tau$ (equation 10 in Belkacem et al., 2013):

$$\nu_{\rm max} \propto \frac{1}{\tau} \propto \left(\frac{\Gamma_1^2}{\chi_\rho \Sigma}\right)\left(\frac{\mathcal{M}_a^3}{\alpha}\right)\nu_{\rm ac}. \tag{2.14}$$

The thermodynamic variables in equation 2.14 do not change significantly in the super-adiabatic regime. Hence, equation 2.14 corresponds to the observed relation between $\nu_{\rm max}$ and $\nu_{\rm ac}$.

However, mixing-length theory suffers from questionable approximations, and has several problems when dealing with near surface effects. Belkacem et al. (2011) used a set of 3D hydrodynamical numerical simulations to better constrain the relation $\nu_{\rm ac} \propto \tau_{\rm th}$. The numerical 3D models are representative of the observations of main sequence and red giants observed by *Kepler* and CoRoT. Figure 2.3 shows that the linear relation proposed in Belkacem et al. (2013) is confirmed by the 3D simulations, even with a dispersion for high values of $\nu_{\rm max}$ related to main sequence stars (see right panel in Fig. 2.3). Belkacem

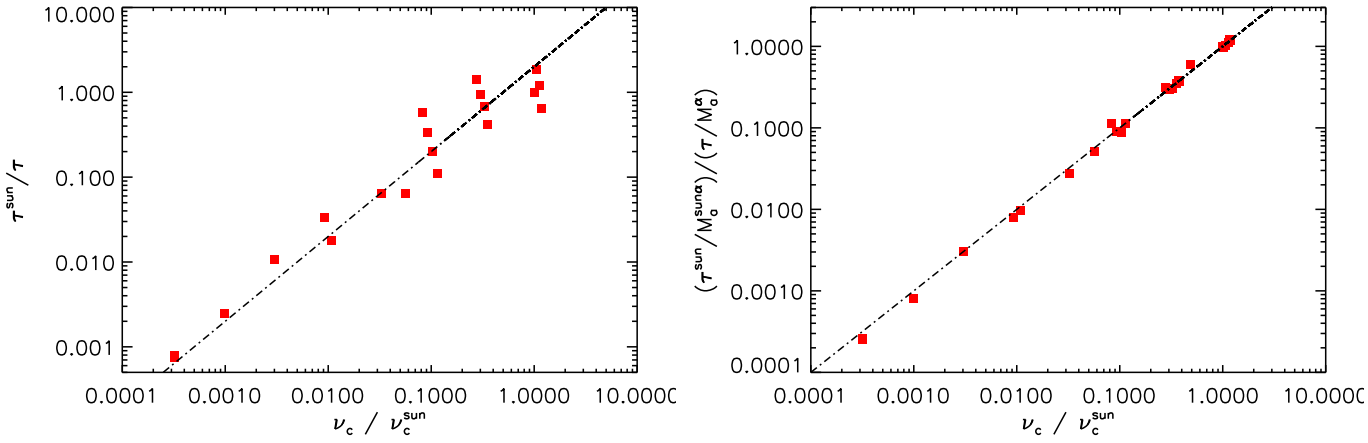

Figure 2.3: Left panel: thermal adjustment timesace $\tau_{\rm th}^{-1}$ as a function of the acoustic cut-off frequency (here indicated by $\nu_{\rm c}$). All the quantities are normalized by the values derived from the Solar 3D simulation. The filled red squares correspond estimations obtained from 3D models. The dashed-dotted line is a linear fit. Right panel: Same as the left panel, except that the thermal timescae is corrected by the mach number with $\alpha = 2.78$. Figure extracted from Belkacem et al.(2013).

et al. (2011) shows that the main source of uncertainty is the Mach number $\mathcal{M}_a$. If we assume the relation:

$$\tau_{\rm th}^{-1} \propto \mathcal{M}_a^{\alpha} \nu_{\rm ac}, \tag{2.15}$$

so that it possible to obtain a value f α to minimize the dispersion. They find a value of $\alpha = 2.78$, agreeing well with results obtained by using mixing legth theory ($\alpha = 3$). This is a powerful result, since the dependence to the Mach number can be derived from energetic assumptions that have little dependence on the arguments made when using mixing length theory. The scaling relation that accounts for the dependence on the Mach number is shown in the left panel of figure 2.3, confirming that the expected dispersions of the $\tau_{\rm th} \propto \nu_{\rm ac}$ relation (and, as consequence, $\nu_{\rm max} \propto \nu_{\rm ac}$) comes from this extra dependence on the Mach number $\mathcal{M}_a$.

2.2.1 Mach Number in Stellar Models

We used a set of 331 models computed using the MESA code (Paxton et al. 2011) to calculate the Mach number and use equation 2.14 to compute values of $\nu_{\rm max}$. Details regarding the models and their computation will be described in detail in section 2.4.

First, we define the super-adiabatic layers in our models and compute the Mach number there, using the sound speed and the convective velocity. The super-adiabatic layers was defined as the peak found in the difference between the total temperature gradient

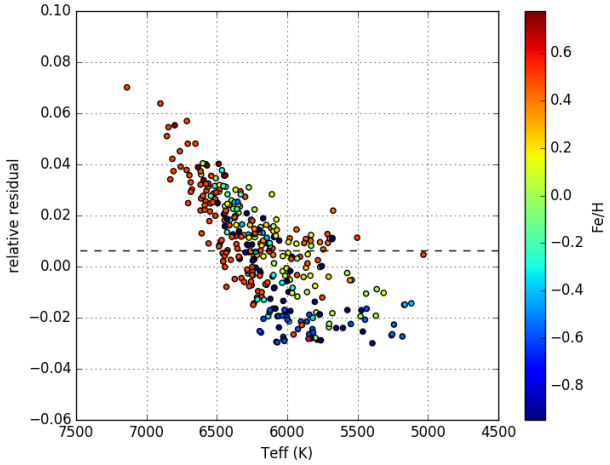

Figure 2.4: Relative residual between values of $\nu_{\max}$ computed using the classic scaling relation (equation 2.2) and values obtained from equation 2.14, plotted as function of temperature. The black dashed line represent the weighted average of the residuals. Metalicity values are represented by the colour code indicated in the bar on the right side of the figure.

and the adiabatic temperature gradient ($\nabla - \nabla_{ad}$). The other quantities present in equation 2.14 are also evaluated in the super-adiabatic layers. Γ_1^2 and χ_ρ are already present in the model outputs, and we computed Σ using density and temperature. The acoustic cut-off frequency was computed using the pressure scale height and the sound speed (see equation 2.4). Figure 2.4 shows the residual values between $\nu_{\max}$ computed using the classic scaling relation (equation 2.2) and values obtained using equation 2.14. The residual has an average of 0.0063 (black dashed line in figure 2.4). The colour code indicates the metallicity of the models. There is a clear trend towards higher temperatures. This trend seems to have a relation with relatively high metallicity as well. This may be due to higher values of sound speed in hotter stars with an increased value of mean molecular weight μ. Sound speed plays an important role during calculation of the Mach number and the acoustic cut-off frequency $\nu_{\rm ac}$. Since we used equation 2.2 to calculate values of $\nu_{\max}$, the stellar mass may also have a significant effect. More in-depth investigations of this trends, including models of red-giant stars and a wider range of masses, shall be conducted in more details on future projects.

2.3 Method

We may in principle use some suitable grid-based results to test the $\nu_{\max}$ scaling relation, albeit with caveats that we will discuss and address below. Let us suppose for the moment

that grid-based searches using the set of inputs

$$\{\Delta\nu, T_{\rm eff}, [{\rm Fe/H}]\}$$

provide robust, unbiased estimates of the combination $gT_{\rm eff}^{-1/2}$, as calibrated to give $\nu_{\rm max}({\rm grid})$ defined by Equation 2.3 above. Assuming the temperatures and metallicities to be unbiased, at least to a level that will not influence significantly estimation of the combination $gT_{\rm eff}^{-1/2}$, the fractional differences

$$[\nu_{\rm max}({\rm data})/\nu_{\rm max}({\rm grid})] - 1,$$

will provide a direct estimate of the bias in the $\nu_{\rm max}$ scaling, i.e., the fractional amount by which the $\nu_{\rm max}({\rm data})$ values are over or underestimated relative to $(g/{\rm g}_\odot)\,(T_{\rm eff}/{\rm T}_{{\rm eff}\,\odot})^{-1/2}\,\nu_{{\rm max}\,\odot}$.

Crucial to the approach is the accuracy of $\nu_{\rm max}({\rm grid})$. First, we know to expect a small bias if the grid-based search pipelines employ the $\Delta\nu$ scaling relation, as we now go on to explain. When the scaling relation is used in the grid-based searches, the fundamental properties of models in the grid are used as inputs to Equation 2.1 to yield model estimates of $\Delta\nu$ for comparison with the observed separations. Alternatively, one may circumvent use of the scaling by computing for each model a set of theoretical oscillation frequencies (e.g., radial-mode frequencies spanning the same orders as those observed in the real data), from which one may then estimate the required $\Delta\nu$ from a suitable fit to those frequencies.

It is now well known that predictions made by the calibrated scaling-relation (Equation 2.1) have small, systematic differences with respect to predictions from frequencies computed by models (e.g., see Ulrich 1986, White et al. 2011; Mosser et al. 2013). For solar-type stars, these differences can be up to $\simeq 2$ percent in size, and become more pronounced at effective temperatures progressively further away from $T_{\rm eff} \simeq 5700\,{\rm K}$ (e.g., see Figures 5 and 6 of White et al. 2011; and figures in Chaplin et al. 2014). Here, we have employed grid-based search pipelines that can run with or without the $\Delta\nu$ scaling relation. We use one pipeline that may be run either using individual model-calculated frequencies or the $\Delta\nu$ scaling relation; and, for comparison, two other pipelines that used the $\Delta\nu$ scaling only.

Second, we must consider the impact of the poor modelling of the near-surface layers of stars. In the case of the Sun it is now well established that this gives rise to a frequency-dependent offset between observed and model-calculated oscillation frequencies (e.g., see Chaplin & Miglio 2013, and references therein). This so-called "surface term" increases in magnitude with increasing overtone number, n. The amount by which $\Delta\nu$ is affected will depend on the variation of the surface term with n. Tests of the grid-based method (Basu et al. 2010) indicate that the impact of the solar surface term on $\Delta\nu$ – which decreases the observed solar $\Delta\nu$ by just under 1 per cent compared to model predictions – leads only to very small errors in the inferred solar properties, certainly well within the

observational uncertainties associated with the *Kepler* data used in this paper. Stellar surface terms would need to be substantially larger than the solar term to produce significant bias in our results. However, the nature of the term in other stars remains rather poorly understood, and so this caveat should be borne in mind.

Our tests with artificial data do nevertheless provide some insights on the sensitivity of the results to such offsets. The artificial data come from models computed using a different stellar evolutionary code and different input physics to those of the grids to which the grid-based pipelines are coupled. This can give rise to "surface-term" like offsets between models in the artificial sample in the grids that share the same fundamental properties (in particular from differences in boundary conditions, matching to model atmospheres etc.).

2.4 Data and grid pipelines

2.4.1 Real and artificial data

The observational data for our study come from Chaplin et al. (2014). This study produced an asteroseismic catalogue from an extensive grid-based analysis of more than 500 solar-like oscillators, which were observed by *Kepler* as part of an asteroseismic survey that was conducted over the first 10 months of science operations. Stellar properties were estimated from a grid-based analysis using the global asteroseismic parameters $\Delta\nu$ and $\nu_{\rm max}$ together with complementary photometric and spectroscopic data as the inputs. Homogeneous sets of effective temperatures $T_{\rm eff}$ were available for the full sample of stars, courtesy of complementary ground-based photometry. A homogeneous set of spectroscopic parameters ($T_{\rm eff}$ and [Fe/H]) was also available from Bruntt et al. (2012), but only for a subset of 87 stars in the sample.

Here, we make use of the global asteroseismic parameters and the complementary data to perform the new grid-based analysis needed to test the $\nu_{\rm max}$ scaling relation. The Chaplin et al. (2014) sample is dominated by cool main-sequence and sub-giant stars but does contain a small fraction of stars at the base of the red-giant branch that were serendipitously observed as part of the short-cadence asteroseismic survey. We have removed the more evolved stars from the sample (which will be the subject of a separate study). The selected sample contains 426 solar-type stars.

As noted above, complementary photometry was available on the entire sample. This allowed us to perform a new, homogenous grid-based analysis on all the selected solar-type stars, but at the cost of not having robust, well-constrained estimates of [Fe/H] for each star since the complementary photometry available to us in the *Kepler* Input Catalogue (KIC; see Brown et al. 2011) does not provide strong constraints on metallicity. Just like Chaplin et al. (2014), we therefore adopted an average [Fe/H] value as input for every star when we analysed the 426-star sample. We actually tried two different val-

ues: One set of results came from using the average of the 87 metallicities measured by Bruntt et al. (2012), i.e., [Fe/H] = −0.05 dex; while the other results came from using [Fe/H] = −0.20 dex for all stars (e.g., see Silva Aguirre et al. 2011), the value adopted in Chaplin et al. (2014). In both cases we adopted large input uncertainties of ±0.3 dex.

In spite of the weak constraints on [Fe/H], we still obtained more precise results from the larger 426-star sample having complementary photometric data than we did from the smaller sample with complementary spectroscopic data because the larger sample size compensated for the inferior precision in [Fe/H]. Results obtained were similar, and hence in what follows we present detailed results from the photometric sample. This sample also provided much better coverage in the domain where $T_{\rm eff} > 6000$ K.

Finally with regards to the input data, we note that the photometric temperatures were the Infrared Flux Method (IRFM) estimates from Chaplin et al. (2014), which were calculated using multi-band photometry in the Two Micron All Sky Survey (2MASS; see Skrutskie et al. 2006) JHK bands, and in the Sloan Digital Sky Survey (SDSS) *griz* bands (both available in the KIC).

Panel (a) of Fig. 2.5 plots the locations of the sample of selected *Kepler* solar-type stars on a Hertzsprung-Russell diagram. The lines mark evolutionary tracks computed by the Modules for Experiments in Stellar Astrophysics (MESA) code (Paxton et al. 2011; see below), for models having solar composition and masses ranging from 0.8 to 1.5 $M_\odot$ (in steps of 0.1 $M_\odot$). Panel (b) of the same figure shows the measured $\nu_{\rm max}$(data) of the *Kepler* sample, from analysis of the oscillation spectra of the stars, indicating the parameter range tested by the analysis.

We also used artificial data to test and validate our methodology. The artificial sample of stars was comprised of models drawn from an evolutionary grid, computed using MESA. The grid spanned the range $0.8 \leq M/M_\odot \leq 1.5$ and $-0.8 \leq$ [Fe/H] ≤ 0.8 (both in steps of 0.1), with tracks computed from the pre-main sequence to the base of the red-giant branch.

The Grevesse & Noels (1993) value of $Z_\odot/X_\odot = 0.0245$ was used to translate between model values of [Fe/H] and Z/X. The OPAL equation of state (Rogers & Nayfonov 2002) and OPAL opacities (Iglesias & Rogers 1996) were used, augmented by low-temperature opacities from Ferguson et al. (2005). Nuclear reaction rates were from NACRE (Angulo et al. 1999), with updates for the $^{14}{\rm N}(p,\gamma)^{15}{\rm O}$ (Imbriani et al. 2004, 2005) reaction. Convection was treated according to mixing-length theory, using the solar-calibrated mixing length parameter. Diffusion and effects of rotational mixing were not included. The primordial Helium abundance was fixed to $Y_{\rm p} = 0.2484$ (Cyburt et al. 2003), and the helium enrichment set to $\Delta Y/\Delta Z = 2$ (e.g., Chiosi & Matteucci 1982, Carigi & Peimbert 2008). We refer the reader to Paxton et al. (2011) for further details.

Artificial stars were drawn from the grid by seeking a "best matching" model for each of the solar-type stars in the *Kepler* sample (via a χ^2 minimization). We found that a

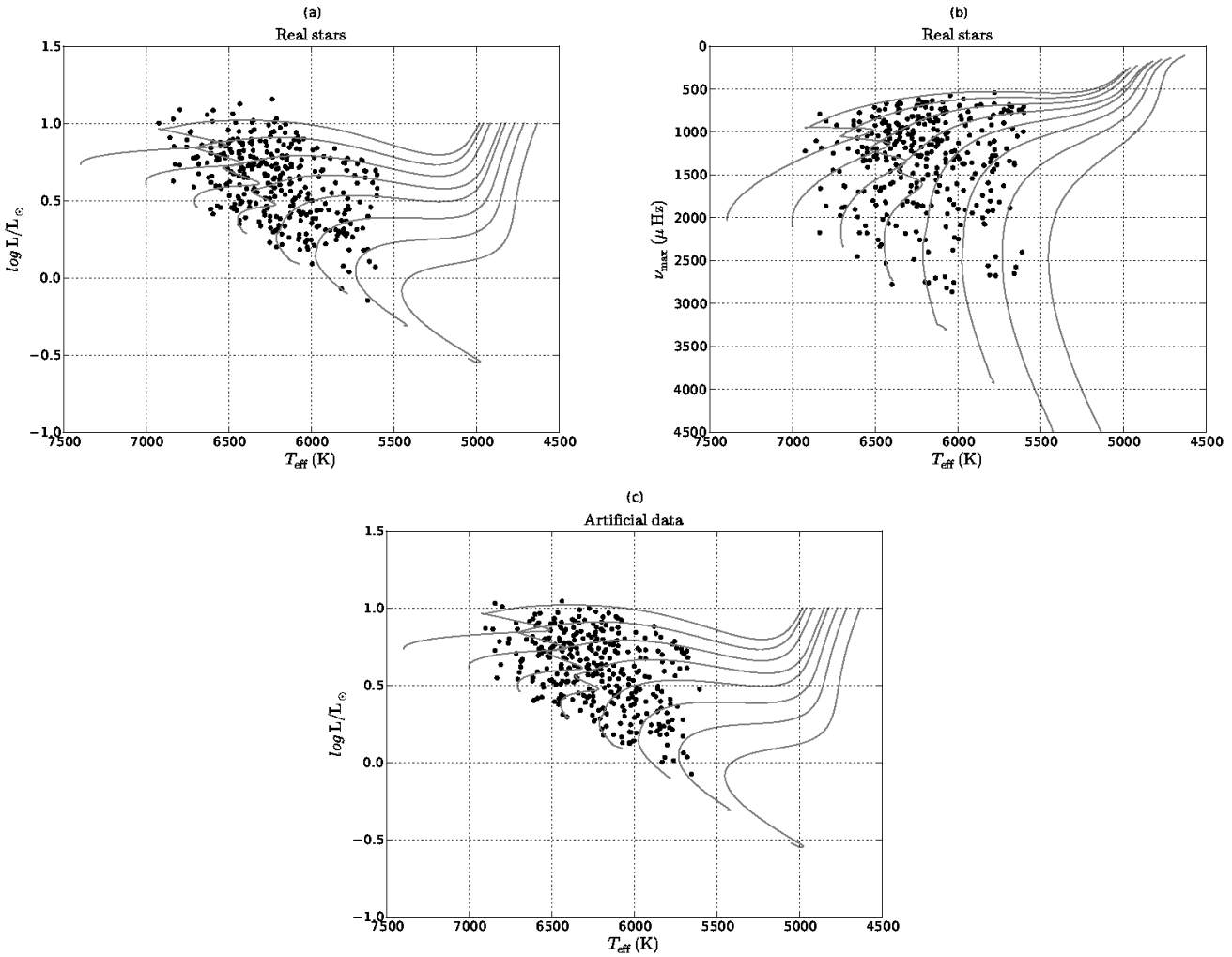

Figure 2.5: Panel (a): Hertzsprung-Russell diagram of the asteroseismic sample of *Kepler* solar-type stars. Panel (b): measured values, $\nu_{\rm max}$(data), from analysis of the oscillation spectra of the real stars, also as a function of effective temperature. Panel (c): Hertzsprung-Russell diagram of the sample of artificial targets, computed from MESA models. The lines in the panels show evolutionary tracks computed by the MESA code (see text), for models having solar composition and masses ranging from 0.8 to 1.5 $M_\odot$ (in steps of 0.1 $M_\odot$).

selection based solely on a comparison of the observed (*Kepler*) and model (grid) values of $T_{\rm eff}$ and $\Delta\nu$ (the latter using the calibrated scaling relation) was sufficient to produce an artificial sample that had distributions in each of the fundamental properties that were a reasonable match to those for the real sample. Panel (c) of Fig. 2.5 marks the locations of the selected models in our artificial sample of stars (using the pristine model parameters). Owing to the limited resolution of the grid, we found that some real stars had the same best-matching artificial model. This meant that our final sample of selected artificial stars was comprised of 306 unique models.

Next, we computed adiabatic oscillation frequencies for each of the 306 selected models, using the GYRE (Townsend & Teitler 2013) stellar oscillations code. The $\Delta\nu$ of each artificial star was then given by the best-fitting gradient of a linear fit to the radial order, n, of the five $l = 0$ frequencies centred on the estimated $\nu_{\rm max}$ (see below) of the model. This approach gives values that are representative of the average values extracted from the real data. We also tested the impact of calculating $\Delta\nu$ using a different number of orders (to reflect the varying data quality and S/N levels in the real sample of stars) and from adopting a weighted fit of the frequencies (to reflect the impact of the changing S/N in any given observed spectrum). Neither change had a significant impact on our results.

We computed three different sets of $\nu_{\rm max}$ for the artificial sample. One set was computed assuming perfect adherence to the solar-calibrated scaling relation, i.e., by using Equation 2.2. We made two other sets by applying a temperature-dependent fractional offset to the solar-calibrated scaling relation, i.e., a computation that took the form

$$\nu_{\rm max} = \mathcal{F}(T_{\rm eff})\left(\frac{M}{\rm M_\odot}\right)\left(\frac{R}{\rm R_\odot}\right)^{-2}\left(\frac{T_{\rm eff}}{\rm T_{eff\,\odot}}\right)^{-1/2}\nu_{\rm max\,\odot}, \tag{2.16}$$

with $\mathcal{F}(T_{\rm eff})$ being the fractional temperature-dependent offset. We applied a linear and quadratic offset, respectively, both of which are shown in panel (a) of Fig. 2.8 (in the figure that also shows results from the data; see below for further discussion). Use of the first set of "perfect" values allowed us to test the impact of biases not associated with the $\nu_{\rm max}$ scaling relation; while the other sets allowed us to test whether we could recover information on a known bias in the $\nu_{\rm max}$ scaling.

Finally, with each artificial star then having calculated values of $\Delta\nu$ and $\nu_{\rm max}$, and a model $T_{\rm eff}$, it remained to add noise and to assign uncertainties to those parameters for input to the grid pipelines. This meant that in our analysis we would treat the artificial data in exactly the same way as the real data. Here, we simply used the relevant parameter uncertainties of the real *Kepler* star to which each artificial star was associated. To make a given realization of the artificial datasets, we added Gaussian noise to each pristine input parameter, multiplied by the relevant parameter uncertainty, to give $\nu_{\rm max}$(data), $\Delta\nu$(data), and $T_{\rm eff}$(data) for each artificial star.

2.4.2 Grid pipelines

We utilized three different grid-based pipeline codes to return estimates of the parameter $\nu_{\rm max}$(grid) for all stars in the real and artificial samples:

- the Bellaterra Stellar Properties Pipeline (BeSPP) (Serenelli et al. 2013, extended for asteroseismic modelling);
- the Yale-Birmingham (YB) (Basu et al. 2010, 2012, Gai et al. 2011); and
- PARAM (da Silva et al. 2006; Miglio et al. 2013; Rodrigues et al. 2014);

The BeSPP pipeline was run with a grid comprised of models constructed with the GARSTEC code (Weiss & Schlattl 2008). The parameters of the grid are described in Silva Aguirre et al. (2012). BeSPP was run in two different modes of operation: one where grid-model estimates of $\Delta\nu$ were computed using adiabatic oscillation frequencies (frequency mode); and one where the estimates were instead computed using the solar-calibrated scaling relation (Equation 2.1; scaling-relation mode). The other two pipelines were run only in the latter, scaling-relation mode. PARAM was run using a grid comprising models made by the Padova group (Marigo et al. 2008). Further details may be found in Miglio et al. (2013). The YB pipeline returned results using five different sets of stellar models: grids computed by the Dartmouth (Dotter et al. 2008) and Padova groups (Bressan et al. 2012); the set of YY isochrones (Demarque et al. 2004); a grid comprised of the BASTI models of Pietrinferni et al. (2004), computed for use in asteroseismic studies (see Silva Aguirre et al 2013); and, finally, a grid constructed using the YREC Code (Demarque et al. 2008), which is described by Basu et al. (2012). This grid has been used in other papers, and we retain the YREC2 name here.

We also report results from YB which are labelled ALL. This set of results was generated by combining the YB analysis over all five grids to compute what are in essence averages from a composite "super distribution". This is a new addition to the YB code that has not previously been documented in the literature, and so we provide further details here.

The YB pipeline determines the properties of a star using the given observational input (central) parameter set. A key step in the method is to generate 10,000 input parameter sets by adding different random realisations of Gaussian noise (commensurate with the input uncertainties) to the actual (central) observational input parameter set. For each realisation, we find all models in a grid within 3σ of the input uncertainties, and use these models to define a likelihood function (e.g., see Gai et al. 2011, Basu et al. 2012 for details). The estimated property, e.g., $\nu_{\rm max}$(grid), is then the likelihood-weighted average of the property of the selected models. The 10001 values of any given property estimated from the central value and the 10000 realisations, form the probability distribution function for that parameter. In the YB pipeline we adopt the median of the distribution as the

estimated value of the property, and we use 1σ limits from the median as a measure of the uncertainties. The ALL results were obtained by constructing a consolidated probability distribution for a given star by adding together the five different distribution functions obtained using the five different grids. Then we determined the median of this consolidated or "super" distribution function, to determine the average $\nu_{\rm max}$(grid).

All three pipelines were employed in the grid-based analysis described in Chaplin et al. (2014), where summary details of the physics employed in the grids may also be found.

2.5 Results

2.5.1 Results from artificial data

We begin with results from analysing the first set of artificial data. Recall that in this case $\nu_{\rm max}$(data) for each artificial star – essentially the proxy for what would be the observed $\nu_{\rm max}$ of each real star – was computed assuming strict adherence to the solar-calibrated scaling relation. The top two panels of Fig. 2.6 show results from the BeSPP pipeline, run in both frequency mode [panel (a)] and scaling-relation mode [panel (b)], on a representative noise realization of the artificial set. Both panels show fractional differences $\nu_{\rm max}$(data)/$\nu_{\rm max}$(grid) − 1, i.e., fractional differences between the simulated measurements, $\nu_{\rm max}$(data), and the grid-based estimates, $\nu_{\rm max}$(grid). Here, grid-based estimates were calculated assuming an input [Fe/H] pegged to the Bruntt et al. average, i.e., [Fe/H] = −0.05 dex. Results are shown both for the individual artificial stars (symbols) and for averages computed over 130-K bins in $T_{\rm eff}$ (lines). The error bars mark uncertainties on each average. The scatter in the fractional differences is entirely consistent with the formal uncertainties on the differences (which are propagated from the individual formal uncertainties on $\nu_{\rm max}$(data) and $\nu_{\rm max}$(grid)).

The results on the whole show the expected trends. The scaling-relation-mode results in panel (b) are not flat. The differences show an upward trend with increasing $T_{\rm eff}$, which is due to the known offsets in the $\Delta\nu$ scaling. This tells us that if there were no $\nu_{\rm max}$ bias in the real data we should expect to see trends like these when using a scaling-relation-based grid pipeline.

With regards to the frequency-mode results in the panel (a) of Fig. 2.6, as expected the upward trend from the $\Delta\nu$ scaling is absent, and we see a flat trend in the comparison at the level of precision of the data. The frequency-mode results therefore allow us to conclude, correctly, that the artificial data follow a $gT_{\rm eff}^{-1/2}$ like scaling. That said, the differences do show a small absolute offset, albeit one that does not change significantly with $T_{\rm eff}$. The absolute offset has more than one contribution.

First, there is a contribution due to the uncertainty in [Fe/H] we adopted for the input

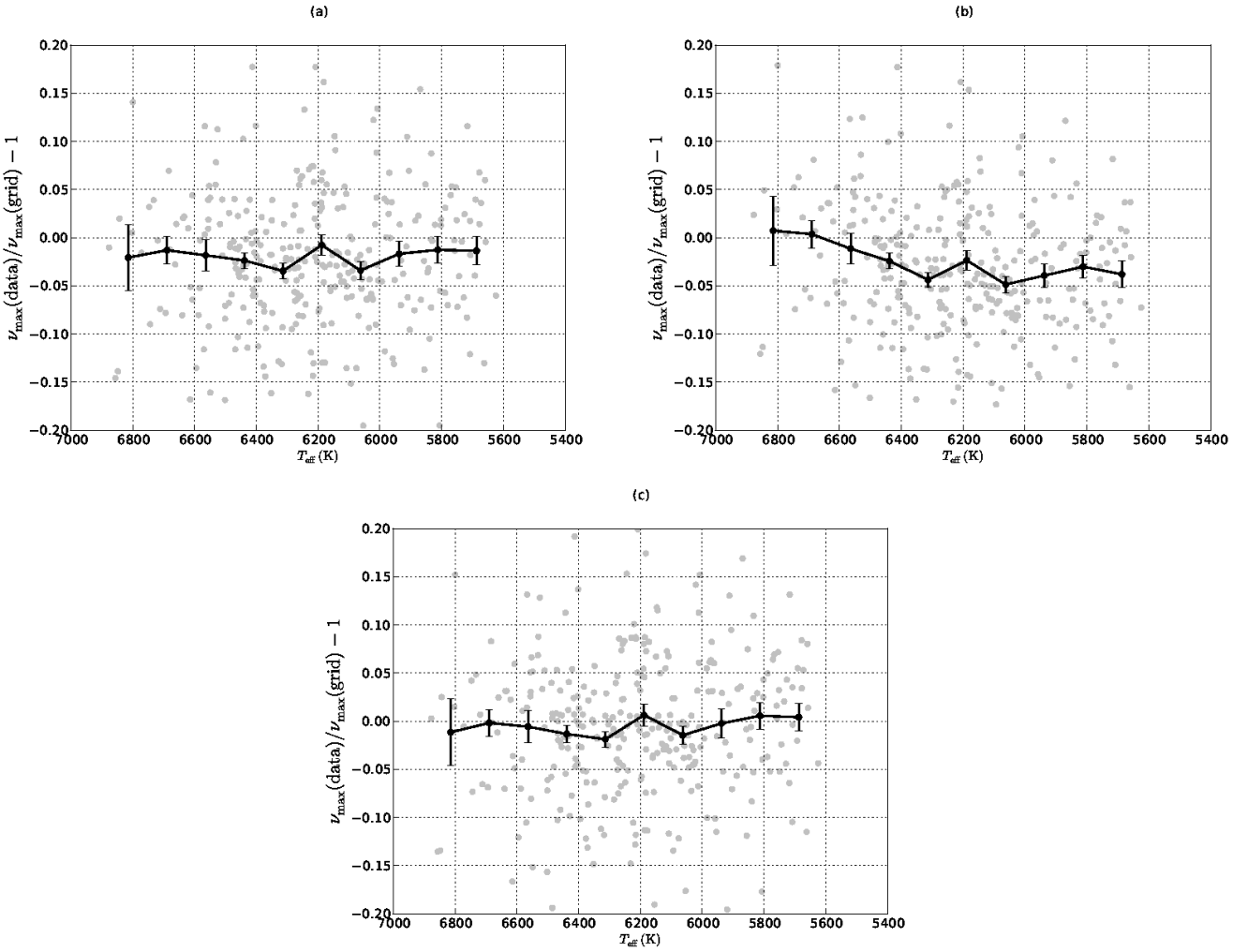

Figure 2.6: Results from BeSPP grid pipeline, for artificial data following perfect adherence to the $\nu_{\rm max}$ scaling relation. Panel (a) shows results from when BeSPP is run in frequency mode; while panel (b) shows results when the pipeline is run in scaling-relation mode (see text). Plotted are fractional differences $\nu_{\rm max}({\rm data})/\nu_{\rm max}({\rm grid}) - 1$, with grid-based estimates calculated assuming an input [Fe/H] of −0.05 dex for every artificial star. Results are plotted for individual artificial stars (symbols) and for averages computed over 130-K bins in $T_{\rm eff}$ (lines). The error bars mark uncertainties on each average. Panel (c): Frequency-mode results from analysing the same artificial data, but now with an input [Fe/H] of −0.20 dex.

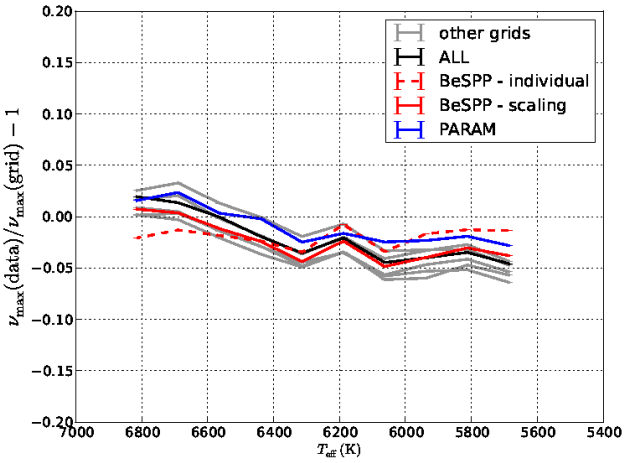

Figure 2.7: Fractional differences $\nu_{\rm max}$(data)/$\nu_{\rm max}$(grid) − 1 returned by all three grid pipelines, for artificial data following perfect adherence to the solar-calibrated $\nu_{\rm max}$ scaling relation (Equation 2.2). Different lines show 130-K averages in $T_{\rm eff}$ for different pipeline-grid combinations (see annotation), all of which used an input [Fe/H] of −0.05 dex.

data (to mimic that for the real 426-star sample). Panel (c) of Fig. 2.6 shows results from BeSPP run in frequency mode, but with [Fe/H] = −0.20 dex now used as input for all stars. This change to the input [Fe/H] produces a shift in the absolute offset of just under 1 per cent. Second, there will be a contribution to the absolute offset arising from differences between the models on which the artificial stars are based and those used in the BeSPP grid. These differences can give rise to what looks like a "surface term" offset (see discussion in Section 2.3 above). We conclude that we should expect there to be some uncertainty over the *absolute* calibration of the relation for results on the real *Kepler* data. We shall come back in Section 2.5.2 to attempt an estimate of the relative contributions of the above effects to the uncertainty in the absolute calibration.

Fig. 2.7 also includes results from the YB and PARAM pipelines, which were coupled to a variety of grids with [Fe/H] = −0.05 dex used as input. The YB ALL results are plotted in black, the YB results from individual grids in grey, and the PARAM results in blue. Recall that these pipelines were run only in scaling-relation mode. To aid the clarity of the plots we present just the $T_{\rm eff}$-binned averages. Results from the other pipelines follow the BeSPP scaling-relation results from the top panels of Fig. 2.6, which we plot again here (in red) for direct comparison. The shapes of the scaling-relation trends for each grid-pipeline combination are similar – showing an upward trend with increasing $T_{\rm eff}$, again due to the known offsets in the $\Delta\nu$ scaling – with an extreme spread of approximately 3.5 per cent in the fractional differences.

Fig. 2.8 presents results for the artificial sets which have known biases in $\nu_{\rm max}$. Panel (a) shows the linear and quadratic biases, $\mathcal{F}(T_{\rm eff})$ (Equation 2.16), which we imposed

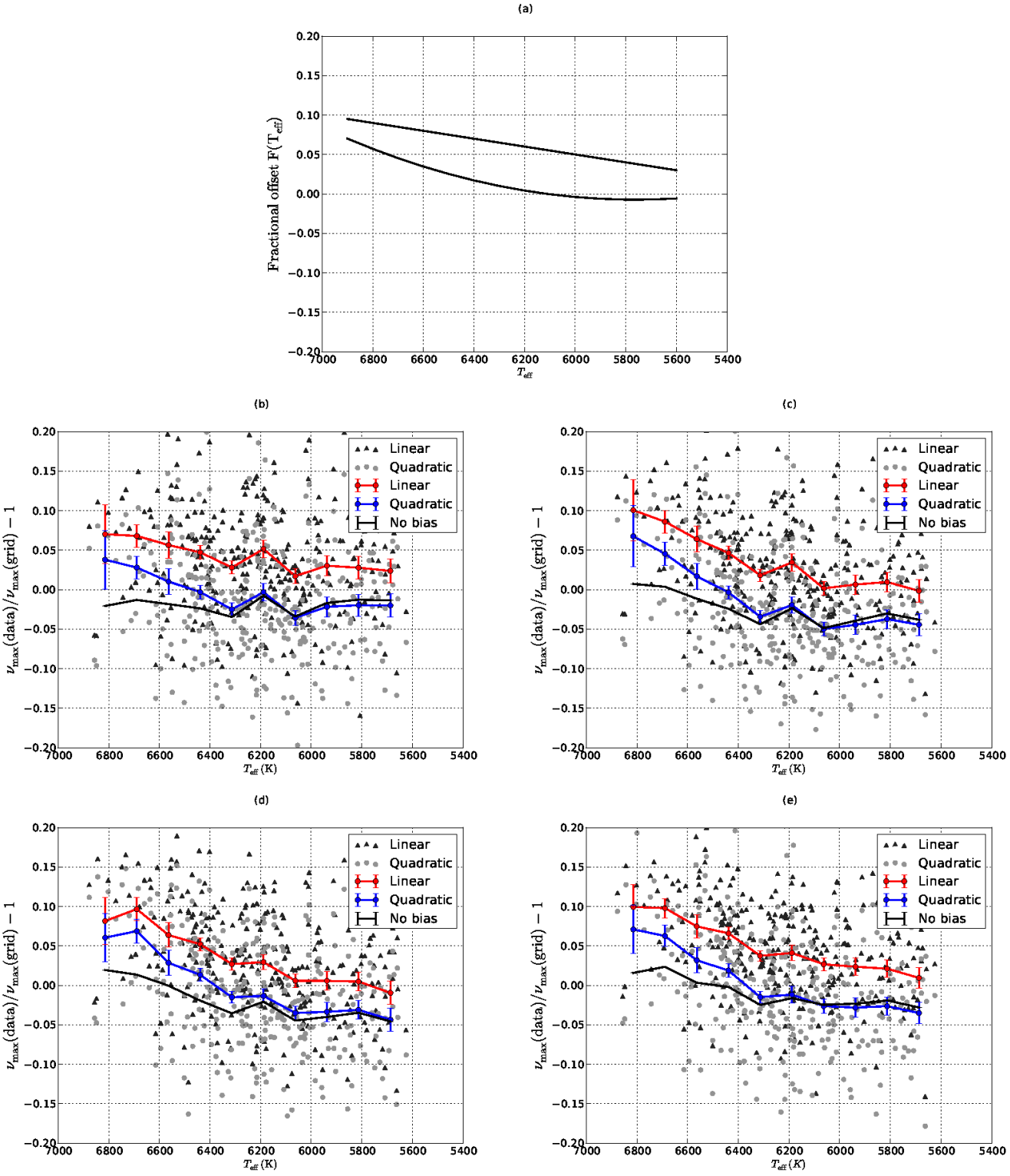

Figure 2.8: Results from all grid pipelines, using an input [Fe/H] of −0.05 dex, for artificial datasets having a $T_{\rm eff}$-dependent bias imposed on the solar-calibrated $\nu_{\rm max}$ scaling relation. Panel (a): Linear and quadratic biases, $\mathcal{F}(T_{\rm eff})$ (Equation 2.16), imposed on the artificial data. Other panels: results of testing the biased artificial data. Plotted are the fractional differences $\nu_{\rm max}({\rm data})/\nu_{\rm max}({\rm grid}) - 1$ for each biased set, returned by: BeSPP in frequency mode (b); BeSPP run in scaling mode (c); YB ALL (d); and PARAM (e). Each panel also shows for comparison the result from the unbiased data (see Figs. 2.6 and 2.7).

on the artificial data. The other panels show results of testing the biased artificial data, with fractional differences plotted for each biased set (see figure legends). Also plotted for reference (black lines) are the recovered trends from the unbiased data (see Figs. 2.6 and 2.7). The panels show returned fractional differences from: BeSPP in frequency mode (b); BeSPP run in scaling mode (c); YB ALL (d); and PARAM (e).

The results are again encouraging. Evidence of the injected bias is clearly present in the results. We also see the offset between the two bias trends, although we would not be able to tell the difference between the shapes of the trends. Nevertheless, we are able to conclude that for the level of bias tested here, it would be possible to discriminate between the no-bias and bias cases.

2.5.2 Results from *Kepler* data

Fig. 2.9 shows results from analysing the selected sample of *Kepler* solar-type stars, which all have complementary photometric data. The fractional differences $\nu_{\rm max}$(data)/$\nu_{\rm max}$(grid)$-$1 are plotted for the different pipelines, including results obtained using BeSPP in both modes of operation. The top four panels show results with [Fe/H] = -0.05 dex used as input, as returned by: BeSPP in frequency mode (a); BeSPP run in scaling mode (b); YB ALL (c); and PARAM (d).

The trends observed here bear a striking resemblance to those given by the results on the artificial data that follow the classic $\nu_{\rm max}$ scaling relation. The trend in the BeSPP frequency-mode *Kepler* results on the real data is flat in $T_{\rm eff}$, and consistent with a $gT_{\rm eff}^{-1/2}$ like scaling at the level of precision of the data.

The scatter in the fractional differences of the real data in Fig. 2.9 is entirely consistent with statistical scatter, given the formal uncertainties. The histograms in Fig. 2.10 show the normalized distributions of fractional differences for the real (red) and artificial no-bias (blue) BeSPP frequency-mode results. Here, each $\nu_{\rm max}$(data)/$\nu_{\rm max}$(grid) $-$ 1 was subtracted from the respective mean trend-line of its sample, and then normalized by its formal uncertainty, that uncertainty having been propagated from the individual formal uncertainties on $\nu_{\rm max}$(data) and $\nu_{\rm max}$(grid). The lines show the cumulative distributions of the histogram data. The real and artificial data histograms follow one another very closely.

We may quantify further the adherence of the BeSPP frequency-mode results to a $gT_{\rm eff}^{-1/2}$ like scaling, i.e., a flat trend. If we fit a simple linear model to *all* the data, the best-fitting gradient implies a linear bias of 0.16 ± 0.10 per cent per 100 K. We may therefore rule out departures from a $gT_{\rm eff}^{-1/2}$ scaling at the level of $\simeq 1.5$ percent over the full $\Delta T \simeq$ 1560 K range tested in $T_{\rm eff}$.

As noted in Section 2.1, the scaling relations (Equations 2.1 and 2.2) may be manipulated to give expressions for the stellar radius, R, and mass, M. The dependencies of the resulting expressions imply that any bias in $\nu_{\rm max}$ propagates to give bias in the inferred

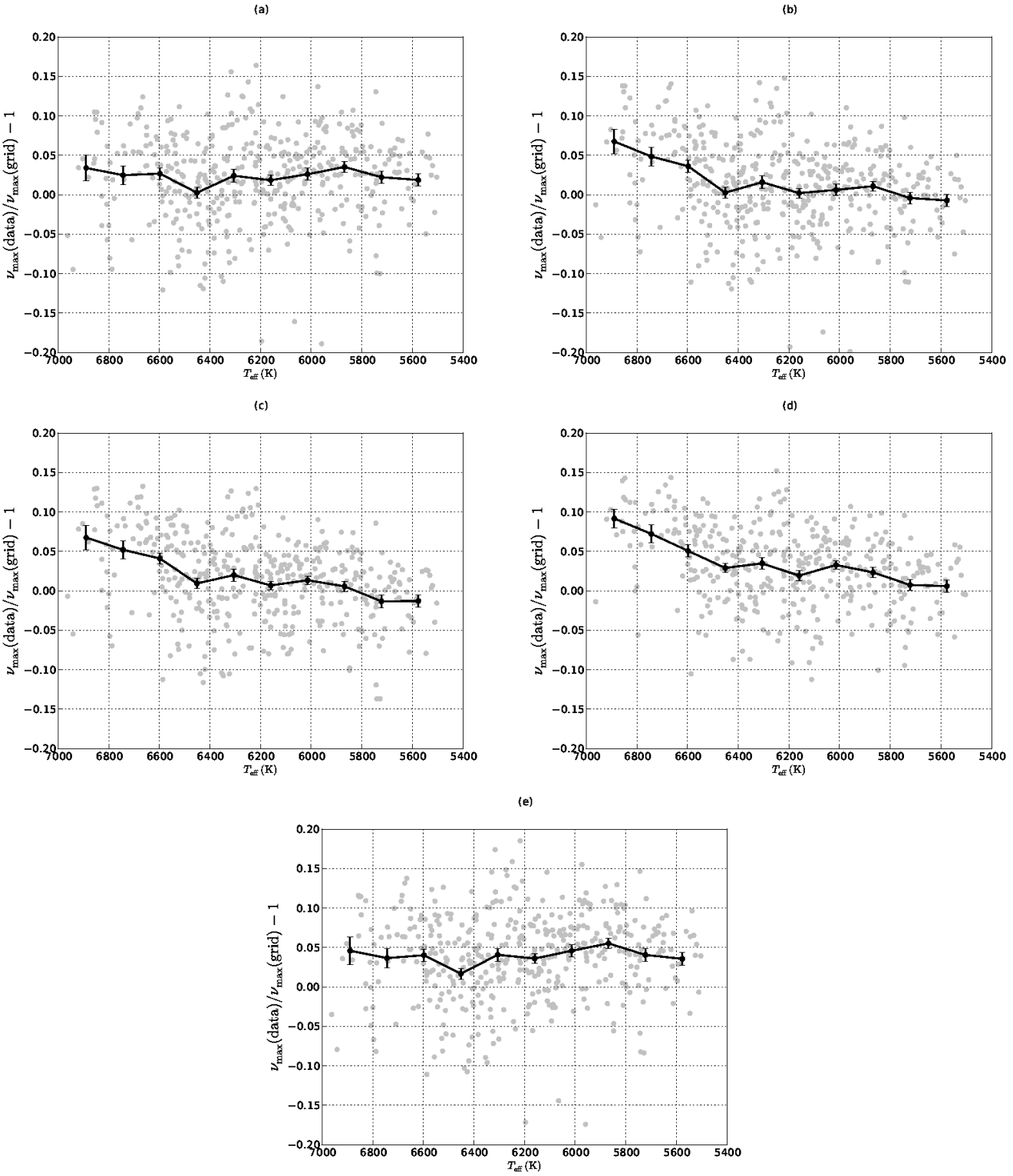

Figure 2.9: Results from analysis of the real *Kepler* sample of solar-type stars, showing the fractional differences $\nu_{\rm max}({\rm data})/\nu_{\rm max}({\rm grid}) - 1$ returned by the different pipelines. The top four panels show results with [Fe/H] $= -0.05$ dex used as input, as returned by: BeSPP in frequency mode (a); BeSPP run in scaling mode (b); YB ALL (c); and PARAM (d). Panel (e): BeSPP frequency-mode results form using an input [Fe/H] of -0.20 dex for every star.

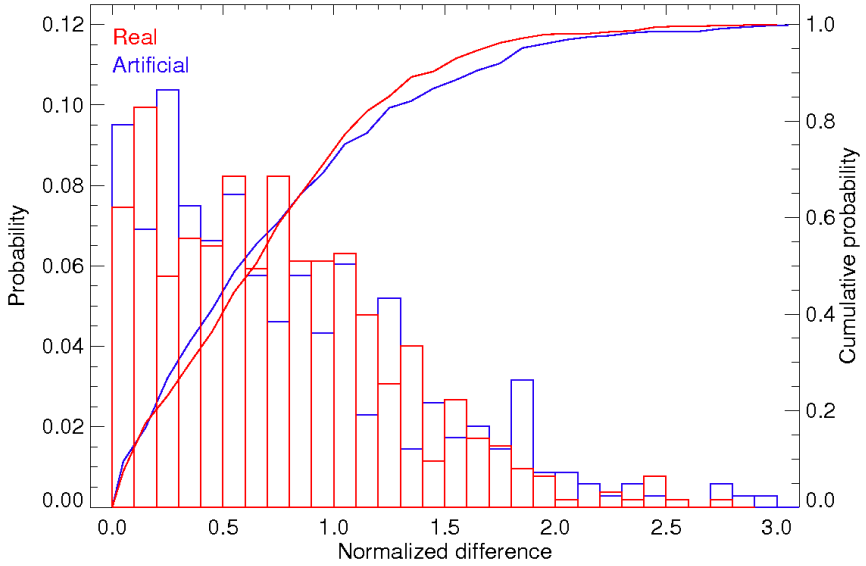

Figure 2.10: Bar plots (associated to left-hand ordinate scale): histograms of the normalized distribution of fractional differences $\nu_{\max}(\text{data})/\nu_{\max}(\text{grid}) - 1$ for the artificial no-bias (blue) and real (red) BeSPP frequency-mode results, which were plotted in Figs. 2.6 and 2.9 respectively. Each fractional difference was subtracted from the respective mean trend-line of its sample, and then normalized by its formal uncertainty, that uncertainty having been propagated from the individual formal uncertainties on $\nu_{\max}(\text{data})$ and $\nu_{\max}(\text{grid})$. Lines (associated to right-hand ordinate scale): the cumulative distributions of the histogram data.

properties of

$$\left(\frac{\delta R}{R}\right) = \left(\frac{\delta \nu_{\rm max}}{\nu_{\rm max}}\right),$$

and

$$\left(\frac{\delta M}{M}\right) = 3\left(\frac{\delta \nu_{\rm max}}{\nu_{\rm max}}\right).$$

Departures from the classic scaling of $\simeq$ 1.5 percent across the full range (see above) therefore fix 1-σ upper limits on changes in any bias in inferred properties with changing $T_{\rm eff}$ of $\delta R/R \leq 1.5$ percent and $\delta M/M \leq 4.5$ percent. Since the $\nu_{\rm max}$ scaling relation implies

$$\left(\frac{\delta g}{g}\right) = \left(\frac{\delta \nu_{\rm max}}{\nu_{\rm max}}\right),$$

bias in surface gravities inferred from use of the relation will be similar to that for the radii above (which corresponds to a bias in $\log g$ of $\simeq 0.006$ dex).

We also fitted data in overlapping $\Delta T_{\rm eff} = 500\,K$-wide bins, moving systematically through the full range to test the temperature dependence of any departures from the scaling. Throughout most of the range we obtain 1-σ uncertainties on the best-fitting gradients of $\simeq$ 0.4 per cent per 100 K. The limits increase to $\simeq$ 0.5 per cent per 100 K at temperatures above about 6200 K, rising to $\simeq$ 1 per cent per 100 K in the highest range we fitted, which started at 6450 K.

Our results neverthless imply some uncertainty over the *absolute* calibration of the $\nu_{\rm max}$ scaling. Panel (e) in Fig. 2.9 shows the impact on the BeSPP frequency-mode results of using a different input [Fe/H] for each star, here -0.20 dex instead of the value of -0.05 dex used for the top left-hand panel. Just like the artificial data in Fig. 2.6, we see a systemetic shift in the absolute offset, from just over 3 per cent for an input [Fe/H] of -0.05 dex to around 4 per cent for an input [Fe/H] of -0.20 dex. Assuming that the overall shift results from the quadratic addition of uncorrelated effects, this implies a systematic shift due to the uncertainty in [Fe/H] of around 2.5 per cent. It is worth noting that if we analyse the smaller sample of real stars having spectroscopic data from Bruntt et al. (2012) – which have much more tightly constrained input [Fe/H] – we get the same $\approx$ 3 per cent offset as the -0.05 dex full-sample case.

Accounting for the above still leaves us with an uncertainty in the absolute calibration of around 3 per cent (again, assuming that the contributions are uncorrelated). We recall from discussions in previous sections that we would expect this to reflect differences between the physics and structures of the real stars (including near-surface effects) and those of the grid models.

An analysis performed on $\Delta T_{\rm eff} = 500\,K$-wide bins finds no evidence for any significant deviation of the offset with $T_{\rm eff}$. The results imply that if there are any absolute errors in the calibration, all inferred properties will be biased by the *same* fractional amount. For the solar-calibrated Equation 2.2 the calibration is provided by the value

$\nu_{\max\odot} = 3090\,\mu$Hz. Guided by the results above, a 3 per cent uncertainty in the overall calibration translates to an error in the the calibrating frequency of around $100\,\mu$Hz.

2.6 Conclusion

We have tested the scaling relation for the global asteroseismic parameter $\nu_{\max}$, the frequency at which a solar-like oscillator presents its strongest observed pulsation amplitude. The classic scaling relation assumes that $\nu_{\max}$ scales with surface gravity and effective temperature according to $gT_{\rm eff}^{-1/2}$. We have tested how well the detected oscillations in a large sample of solar-type stars observed by the NASA *Kepler* Mission adhere to this relation by comparing the observed $\nu_{\max}$ of the stars with independent estimates of the combination $g\,T_{\rm eff}^{-1/2}$.

Our results rule out departures from the classic $\nu_{\max}$ scaling at the level of $\simeq 1.5$ percent over the full $\simeq 1560$ K range in $T_{\rm eff}$ that we tested. There is some uncertainty over the absolute calibration of the scaling, but any variation with $T_{\rm eff}$ is evidently small, with limits similar to those above.

Chapter 3

Combining spectroscopic and seismic constraints on red giant stars

In this chapter, we describe the spectroscopic and seismic study of 10 nearby *Kepler* red giant stars. These red giants are some of the brightest stars observed by *Kepler* and have accurate values of parallaxes, making this sample ideal for testing seismic estimations of radii and distances. The high S/N ratio of the data allowed us to obtain high quality photometry and detailed light curves, from which we extracted period spacing of gravity-dominated mixed modes for 7 of them, helping us to discern their evolutionary status. We used the average seismic parameters $\Delta\nu$ and $\nu_{\rm max}$, along with the scaling relations, to obtain estimations of mass, radius, density, surface gravity and distance for each star. We compare our seismic estimations of global parameters with predictions from theoretical stellar evolution models. We also discuss the data obtained from spectroscopy, with emphasis on elements known to be signatures of extra mixing on advanced stages of stellar evolution, such as surface abundances of carbon isotopic ratio and lithium. Seismic gravities are available to all stars, and were used to constrain the spectroscopic analysis.

3.1 Introduction

Asteroseismology is able to place model independent constraints directly related to internal stellar structure. In red giants, p-modes and g-modes can be coupled into mixed modes, behaving like p-modes near the surface and g-modes when near the core, carrying out direct information related to internal stellar structure (see section 1.3.2). The analysis of such mixed modes can be specially useful for red giants, since it is then possible to infer the size of the core in order to distinguish between the Hydrogen shell burning phase in the ascending RGB and the Helium-burning core in the clump phase (e.g. Mosser et al., 2014; Bedding et al., 2011).

Ideally, one would conduct an analysis of individual frequencies on a star-by-star ba-

sis, since the study of period spacing and the analysis of the combination of certain modes of oscillation would give the best information on the internal stellar structure. However, the incredibly large number of stars observed by *CoRoT* and *Kepler* makes this impractical with current analysis procedures. At the same time, the star must have a high signal to noise ratio to obtain individual frequencies, and this is not the case for most stars with available photometry. Even so, it is still possible to obtain average seismic parameters in low S/N data. Such parameters are related to global stellar properties and can be combined with estimations of surface temperature in the so-called scaling relations to infer masses and radii for a large sample of field stars. Scaling relations and the Stefan-Boltzmann law can be combined to derive seismic estimation for distances. This is particularly useful for targets without a good estimation of parallaxes, which is the case for the vast majority of field stars observed by *CoRoT* and *Kepler*. It has become increasingly important to test the scaling relations and the seismic inferred distances by using bright giants with accurate parallaxes and good estimations of surface temperature.

At the same time, bright giants with high quality spectra offer the opportunity to measure the surface abundance of individual elements. Red giant stars, in general, are luminous stars with a wide range of mass, age and chemical composition, making them an useful set of data for the study of the evolution of our galaxy (e.g. Miglio et al 2012). However, the evolution of the surface chemical abundances in low mass red-giant stars is not entirely understood. Spectroscopic studies have shown a large number of cases where the observed surface abundances don't match the estimations made using theoretical models of stellar evolution. Various extra-mixing mechanisms were proposed to explain this unexpected chemical profile (e.g see Charbonnel, 2006; Denissenkov , 2010; Lagarde et al., 2011).

One of the most important mixing processes, that causes a noticeable change of the surface composition of low-mass stars, takes place at the so-called bump in the luminosity function on the red giant branch (RGB), which occurs when the hydrogen-burning shell encounters the sharp discontinuity in molecular weight left by the receding convective envelope ('first dredge up'). The net result is a decrease of the surface abundance of elements such as Lithium and Carbon (e.g see Gilroy & Brown al., 1991; Mikolaitis et al., 2012; Tautvaisiene, 2013).

Thermohaline mixing has been proposed to play an important role to explain the observed chemical surface profile of low mass RGB stars (Charbonnel & Lagarde, 2010). Such instability is the direct effect of the inversion of mean molecular weight caused by the ^{3}He(^{3}He, 2p)^{4}He reaction that occurs in the layers between the hydrogen-burning shell and the convective envelope. This mixing process is relevant both on the ascending red giant branch and during Helium-burning phase.

Mixing induced by rotation has an effect during the main sequence and the ascending RGB phase, and it provides an explanation for certain abundance patterns observed at

the surface of RGB stars (Charbonnel, 1995). However, rotational-induced mixing alone does not account for enough mixing of chemicals to explain the abundance profile of low-mass, low-metallicity RGB stars observed around the luminosity bump (e.g. Palacios et al. (2006)).

The combination of seismic and spectroscopic constraints can be used to quantify the efficiency of the extra-mixing processes that occur inside red giant stars. Spectroscopy provides information about surface chemical properties and temperatures, while asteroseismology can give us information on stellar interiors and accurate estimations of stellar mass, radius, and evolutionary state. Lagarde et al. (2015) conducted a study of this kind for *CoRoT* stars using stellar models that incorporate the effects of rotation and thermohaline mixing. Despite the small size of the sample, results for estimations of mass and radius show a good agreement within standard errors. However, in most stars in the *CoRoT* sample, seismic constraints were not stringent enough to, e.g., constrain the evolutionary state.

In this work we present the seismic and spectroscopic study of 10 bright red giant stars observed by the *Kepler* space telescope. The data obtained for the target stars have a high signal to noise ratio, allowing a detailed study of chemical abundances coupled with high quality seismic data. Seismic gravities are available for all stars and period spacing was extracted from the mixed modes for all but three stars on our sample, allowing us to discern their evolutionary status.

This chapter is organized as follows: in Section 3.2, we discuss the methodology used in obtaining the spectroscopic properties. In Section 3.3 we discuss the seismic/frequency analysis, and some of the non-seismic properties as well. Global stellar parameters obtained by grid-modelling are discussed on Section 3.4. In section 3.5, we combine the spectroscopic and seismic results to test current models of extra internal mixing episodes in the red-giant phase.

3.2 Spectroscopic analysis

The spectra were collected on October 2014 by the NARVAL (Aurière 2003) spectrograph located at the 2-meter Bernard Lyot Telescope at Pic du Midi. The spectral coverage was from $\sim$ 370 to 1048 nm. The spectra were collected in "star only" mode which allows us to have a high resolution of R $\sim$ 75 000. Long exposure times were used to obtain high signal-to-noise ratio for all the targets ($\geq$ 200).

We obtained a first set of effective temperature ($T_{\rm eff}$), metallicity ([Fe/H]) and surface gravity ($\log g$) using three different methods to conduct an unconstrained analysis:

- Spectral synthesis software SME (Spectroscopy Made Easy) (Valenti & Piskunov, 1996): Using the wavelength ranges of 5160-5190 Å, 6000-6030 Å, 6050-6070

Å, 6100-6118 Å, 6121-6140 Å, 6142-6159 Å and 6160-6180 Å(Valenti & Fischer, 2005). The spectral regions used were re-normalized and the software was run several times using different starting values in order to be sure of the reliability of the results. Different stellar models (ATLAS9, ATLAS12 and MARCS) were used to insure that SME results are model independent: all the values found are usually in good agreement with each other.

- The 2010 version of MOOG (Sneden 1973): The spectrum of the star Arcturus was used to calibrate the code. Determination of spectroscopic parameters where obtained using the atmospheric models of Kurucz and 44 Spectral lines (species: 26.0, 26.1).

- MOOG was also used by a different collaborator using Kurucz plane-parallel atmospheric models computed using ATLAS9 code ported into Linux (see Morel et al.2014 for more details).

We decided to adopt the values of temperature and metallicity from the set with $\log g$ that are closest to the corresponding seismic value, obtained by using MOOG (Morel et al.2014). The seismic surface gravities were obtained using $\nu_{\rm max}$ and $T_{\rm eff}$ using scaling relations (see chapter 1 and section 3.3 below)

In principle, we had no plans to conduct a second iteration of the spectroscopic parameters using the seismic values of surface gravity to do a constrained analysis. However, from previous studies of the *CoRoT* Red Giants (Morel et al., 2014), it is likely that adopting the seismic *logg* values would, in most cases, lead to small adjustments in $T_{\rm eff}$ (below 30 K) and [Fe/H] (below 0.1 dex), with a larger difference for stars with high values of surface temperature and surface gravity.

To investigate possible systematic uncertainties on $T_{\rm eff}$, and to account for any discrepancies in our results, we decided to compare the surface temperatures from the unconstrained spectroscopic analysis with photometric temperatures estimated using MARCS models from Casagrande et al. (2014b). We used values of seismic surface gravitates, metallicities, E(B-V) and observed B-V colors to obtain the desired value of photometric temperature through iteration of the parameters. Results showed that the spectroscopic temperatures for the three hottest stars in our sample are higher by roughly $\sim$ 60 K when compared to the photometric temperatures, when using E(B-V) values obtained from the dust maps of Green et al. (2015) as input in the MARCS models. The use of different values of E(B-V) produced by different dust maps yields similar results. Also, determination of period spacing and the placement of such stars in the HR diagram suggest that the spectroscopic temperatures are overestimated also when compared to the predictions from stellar models (see Figure 3.1), although we do not consider this as a strong argument, given the uncertainties in predicting temperatures for stellar models.

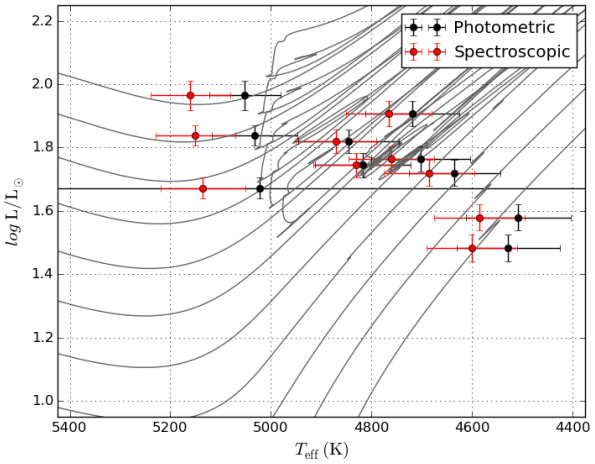

Figure 3.1: HR diagram comparing the photometric temperatures (black) and the spectroscopic temperatures from the unconstrained analysis (red). The luminosities are calculated using *Hipparcos* parallaxes. One of the stars has a very high error on the B-V colour used to compute the photometric temperature. The tracks showed here are the same as Figure 3.7.

In order to correct those effects, we conducted a new constrained analysis of the spectroscopic parameters by fixing the values of seismic surface gravities. Once the seismic $\log g$ are fixed, it is possible to estimate surface temperatures using iron lines through two distinct methods: excitation balance and iron ionization balance.

Excitation balance consists of nulling the slope between the Fe I abundances and the lower excitation potentials. This method has been used to obtain surface temperatures for red giant stars observed by *CoRoT* (Morel et al., 2014) and *Kepler* (Thygesen et al., 2012). When this is enforced for one cool star (HIP 96396) and one warm star (HIP 96706) with the largest discrepancy between the spectroscopic and seismic $\log g$, we obtain a value of $T_{\rm eff}$ higher by $\sim 35K$. Since this increases the temperatures even further, we decided not adopt this approach.

The alternative method, iron ionisation balance, requires that the mean Fe I and Fe II abundances to be identical. As consequence, excitation equilibrium of the Fe I lines is no longer fulfilled).

When this is done for HIP 96396, we obtain the following results: $\Delta T_{\rm eff} = -60$K (new $T_{\rm eff}$ = 4705 K instead of 4765 K) Δ[Fe/H] = -0.04 dex. When the same is done for HIP 96706, we obtain: $\Delta T_{\rm eff} = -100$ K (new $T_{\rm eff}$ = 5050 K instead of 5150 K) Δ[Fe/H] = -0.07 dex.

The temperature scale becomes cooler (which is in better agreement with the photometric $T_{\rm eff}$) and the metallicities are slightly lower. However, those examples are for the two stars with the largest discrepancy in $\log g$, so for the other stars the corrections are

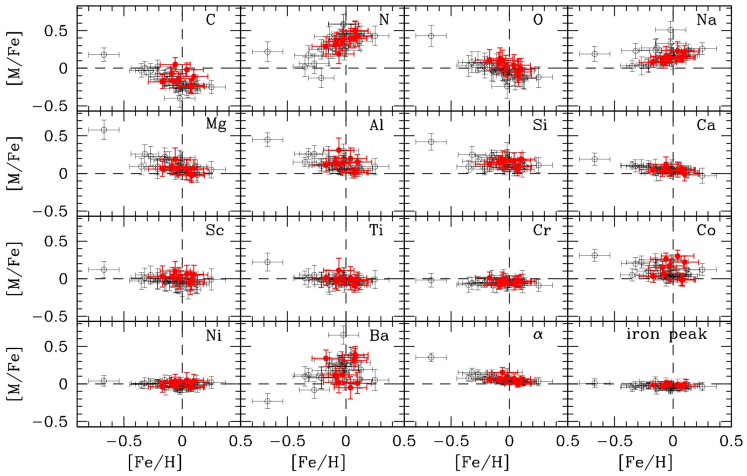

Figure 3.2: Abundance ratios with respect to iron as a function of [Fe/H]. The results have been obtained using the seismic gravities. The mean abundance ratio of the synthesised elements is defined as the unweighed mean of the Mg, Si, Ca, and Ti abundances. For the mean abundance of the iron-peak elements, we considered Cr and Ni. The red giants observed by *CoRoT* and analysed in Morel et al. (2014) are shown in black and the stars in our sample are over-plotted in red.

smaller.

In principle, there is no particular preference between temperatures obtained with excitation balance or ionization balance, judging from a spectroscopic point of view. Therefore, we decided to adopt the iron ionisation equilibrium coupled with seismic surface gravities to obtain estimations of surface temperature that will be used in grid-modelling.

The normalisation of the spectra to the continuum was performed in the same way for all stars to ensure the highest consistency possible. The analysis is identical to that carried out for *CoRoT* red giants by Morel et al. (2014) to which the reader is referred to for more details. However, although this leads to differences in the parameters and abundances that remain within the uncertainties, a number of improvements have been implemented here:

- Two Fe II lines (at ~ 5991 and 6416 Å) were discarded from the analysis because they turn out to give slightly discrepant results.

- A modification of the atomic data for some CN features around ~ 6707.6 Å, which leads to a better fit of the blend formed by Li I λ 6708 Å and a nearby Fe I line at ~6707.4 Å.

- A better removal of the telluric features affecting the CN lines around ~ 8003 Å (and occasionally [O I] λ6300), as well as a more precise assessment of the effect of telluric subtraction on the $^{12}C/^{13}C$ isotopic ratio.

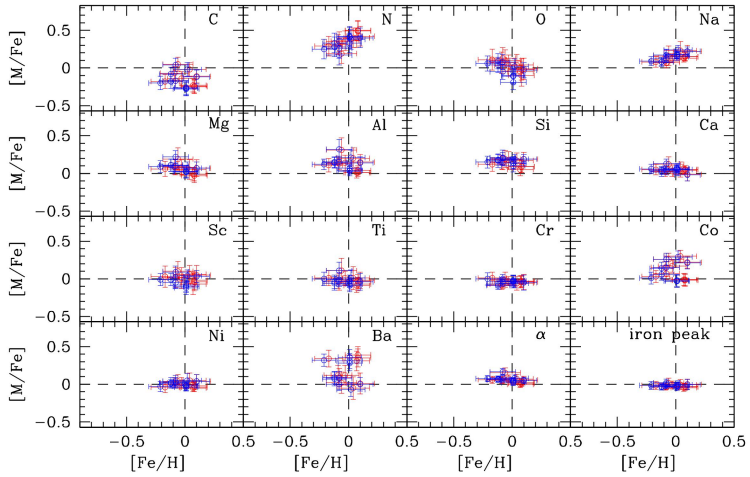

Figure 3.3: Same as figure 3.2, but now the red dots are the old sample and blue dots are the new abundances determined using seismic log g.

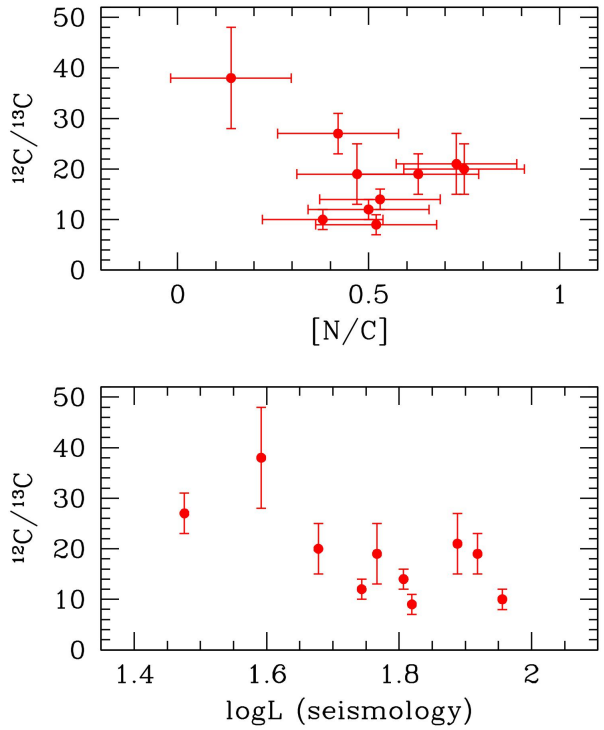

Figure 3.4: The behaviour of $^{12}C/^{13}C$ as a function of [N/C] and log L .

Table 3.1. Seismic properties for the stars in our sample.

KIC	HIP	$\nu_{\max}$ (μHz)	$\Delta\nu$ (μHz)	$\Delta\Pi$ (s)	Status
1720554	95480	55.73 ± 0.48	5.81 ± 0.07	66	RGB
4049174	94799	41.51 ± 0.29	4.48 ± 0.05	319.7	clump
7680115	95352	68.87 ± 2.65	5.49 ± 0.05	undetected[1]	clump[3]
8752618	95534	38.78 ± 0.25	4.43 ± 0.06	298.9	clump
9411865	96706	77.83 ± 0.41	6.45 ± 0.05	268.6	clump2[2]
10323222	92885	46.28 ± 0.35	4.85 ± 0.06	undetected[1]	RGB
10425397	98013	32.13 ± 0.26	3.92 ± 0.05	324.5	clump
11408263	96572	44.23 ± 0.37	4.58 ± 0.05	289.4	clump
11808639	94623	97.99 ± 0.56	7.93 ± 0.07	226.6	clump2[2]
11918397	96396	32.13 ± 0.31	3.51 ± 0.04	undetected[1]	RGB

[1]For KIC 7680115, the period spacing could not be extracted due to limitations on the photometric data. The other two stars without a detection of period spacing are assumed to be RGB (see discussion on section 3.3.2 for more details)

[2]clump2 indicate stars in the secondary clump (see section 1.2.3)

[3]Intermediate-mass stars spend more time in the helium-burning phase, with the ascending red giant branch having a small time-scale. Therefore, it is very unlikely that such star ($M \sim 3$) is on the ascending red-giant phase.

The full set of parameters and abundances can be found in tables 2 and 3. Note that the Li feature is only detected in three stars. For all other stars, the analysis provides an upper limit to the Li abundance only.

3.3 Data analysis

Our sample is made of 10 red giants whose main seismic characteristics are listed in Table 3.1. Given the high quality of the photometric data, we can expect to have good estimations of $\nu_{\max}$ and $\Delta\nu$, as well as the asymptotic period spacing of gravity modes. One of the stars in our sample (KIC 10323222) has a measurement of interferometric angular diameter (θ_{LD}) presented in Huber et al. (2012).

Table 3.2. Chemical abundances for several elements. Obs: NLTE values are preferred over LTE

KIC	HIP	$^{12}C/^{13}C$	A(Li)(LTE)	A(Li)(NLTE)	σ A(Li)	[C/Fe]	[N/Fe]	[O/Fe]	[Na/Fe]
1720554	95480	38 ± 15	−1.89	−1.68	9999	0.04 ± 0.09	0.17 ± 0.13	0.08 ± 0.10	0.17 ± 0.08
4049174	94799	14 ± 3	−1.49	−1.27	9999	−0.12 ± 0.09	0.40 ± 0.13	−0.03 ± 0.10	0.22 ± 0.06
7680115	95352	21 ± 9	−0.14	−0.02	0.12	−0.27 ± 0.09	0.41 ± 0.13	−0.10 ± 0.10	0.18 ± 0.06
8752618	95534	12 ± 3	−1.39	−1.21	9999	−0.17 ± 0.09	0.26 ± 0.13	−0.05 ± 0.10	0.13 ± 0.06
9411865	96706	21 ± 7	−0.89	−0.77	9999	−0.28 ± 0.09	0.42 ± 0.13	−0.19 ± 0.10	0.17 ± 0.05
10323222	92885	27 ± 6	−2.09	−1.86	9999	−0.02 ± 0.09	0.38 ± 0.13	0.02 ± 0.10	0.24 ± 0.06
10425397	98013	10 ± 3	−1.49	−1.30	9999	−0.08 ± 0.09	0.28 ± 0.13	0.04 ± 0.10	0.08 ± 0.06
11408263	96572	9 ± 3	−1.13	−0.97	9999	−0.18 ± 0.09	0.33 ± 0.13	0.09 ± 0.10	0.08 ± 0.05
11808639	94623	19 ± 7	−0.27	−0.16	0.12	−0.26 ± 0.09	0.33 ± 0.13	−0.11 ± 0.10	0.15 ± 0.05
11918397	96396	19 ± 8	−0.59	−0.41	0.12	−0.20 ± 0.09	0.25 ± 0.13	0.06 ± 0.10	0.09 ± 0.06

Table 3.3. Continuation of Table 3.2.

KIC	HIP	[Mg/Fg]	[Al/Fe]	[Si/Fe]	[Ca/Fe]	[Sc/Fe]	[Ti/Fe]	[Cr/Fe]	[Co/Fe]
1720554	95480	0.22 ± 0.08	0.32 ± 0.13	0.20 ± 0.08	0.13 ± 0.06	0.09 ± 0.08	0.11 ± 0.11	0.00 ± 0.06	0.26 ± 0.08
4049174	94799	0.07 ± 0.08	0.14 ± 0.08	0.19 ± 0.06	−0.02 ± 0.08	0.03 ± 0.08	−0.04 ± 0.11	−0.05 ± 0.10	0.21 ± 0.08
7680115	95352	0.03 ± 0.08	0.07 ± 0.05	0.14 ± 0.08	0.07 ± 0.05	−0.08 ± 0.09	−0.03 ± 0.08	−0.02 ± 0.07	−0.03 ± 0.08
8752618	95534	0.10 ± 0.08	0.15 ± 0.08	0.21 ± 0.10	0.04 ± 0.06	−0.05 ± 0.08	−0.01 ± 0.09	−0.04 ± 0.06	0.15 ± 0.08
9411865	96706	0.02 ± 0.08	0.04 ± 0.05	0.14 ± 0.08	0.06 ± 0.05	−0.10 ± 0.08	−0.07 ± 0.08	−0.03 ± 0.07	−0.03 ± 0.08
10323222	92885	0.07 ± 0.08	0.21 ± 0.10	0.19 ± 0.06	0.05 ± 0.08	0.04 ± 0.08	0.01 ± 0.11	−0.06 ± 0.05	0.29 ± 0.08
10425397	98013	0.11 ± 0.08	0.15 ± 0.07	0.18 ± 0.07	0.02 ± 0.06	9999 ± 999	−0.06 ± 0.09	−0.09 ± 0.05	0.14 ± 0.08
11408263	96572	0.11 ± 0.08	0.14 ± 0.07	0.17 ± 0.09	0.04 ± 0.05	−0.01 ± 0.08	−0.04 ± 0.09	−0.07 ± 0.05	0.06 ± 0.08
11808639	94623	0.02 ± 0.08	0.03 ± 0.06	0.100 ± 0.08	0.05 ± 0.05	−0.12 ± 0.09	−0.09 ± 0.08	−0.04 ± 0.08	−0.02 ± 0.08
11918397	96396	0.09 ± 0.08	0.12 ± 0.07	0.15 ± 0.08	0.06 ± 0.06	−0.01 ± 0.08	0.00 ± 0.09	0.00 ± 0.08	0.01 ± 0.08

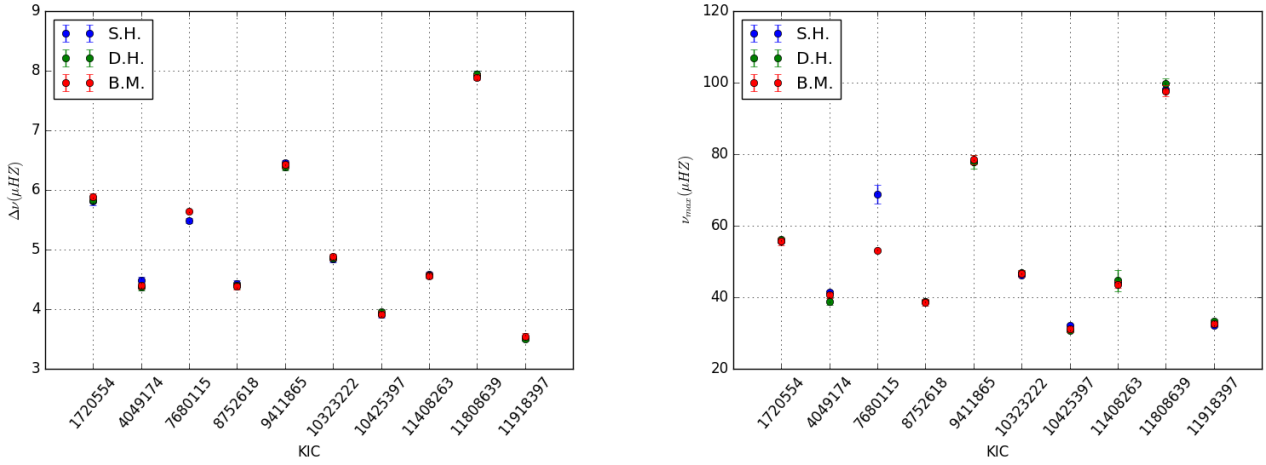

Figure 3.5: Left panel: Comparison between estimations of $\Delta\nu$ obtained by three different collaborators. Right panel: same as left panel, but for $\nu_{\max}$.

3.3.1 Light curve preparation

The raw data we had available for all giants comes from the Pre-search Data Conditioning (PDC) pipeline, one of the main *Kepler* data analysis pipelines. It uses a Bayesian approach to remove the systematic trends and some discontinuities in the raw data that comes directly from the spacecraft. The PDC pipeline is applied to the light curves extracted using an algorithm that attempts to optimize the signal-to-noise for planet detection. Most of the time, the PDC data can be used to derive the power spectra, but it can, in some situations, make an undesired filtering in the data.

The methodology adopted by the PDC pipeline is indeed a great tool for finding planetary transits. For asteroseismology of Red Giants, however, it seems that PDC is perturbing the signals below a $\nu_{\max}$ of $\sim$100 μHz. For extraction of average seismic parameters, $\Delta\nu$ and $\nu_{\max}$, the effects might be negligible, but for parameters such as g-mode period spacing, the impact would be more significant.

In order to make a better version of the light curve than those provided by the PDC pipeline, we recreated the mask and filtered the data in another way that is more optimized for asteroseismology. The custom masks are created based at an estimate of the pixel response function for the star (Bryson et al., 2010), in such manner that brighter targets will have appropriately larger masks, yielding light curves that are more suited for asteroseismic analysis.

3.3.2 Extraction of global seismic indices

Several different methods have been used to detect oscillations and extract global seismic parameters $\Delta\nu$, $\nu_{\max}$ and the period spacing $\Delta\Pi$ from the light curves. Three collaborators

helped us with this task, and shall be referenced as B.M., D.H. and S.H. from here on. The methods used by B.M. for the data analysis are described in extensive detail in Mosser & Appourchaux (2009) for the global analysis, Mosser et al. (2011) for the precise $\Delta\nu$ measurement from the universal red giant oscillation pattern, Mosser et al. (2012) for extraction of period spacing and Mosser et al. (2014) for the determination of evolutionary status. However, B.M. could not provide errorbars for KIC 7680115 because this star has a very short time-series. D.H. used the methodology described in Huber et al. (2009) to extract $\Delta\nu$ and $\nu_{\rm max}$, and was unable to find strong evidence for oscillations using the available quarter for KIC 7680115, however it should be noted that he used his own detrending for the light curves, rather than the data available at the KASOC database. Finally, S.H. was able to provide estimations of $\Delta\nu$ and $\nu_{\rm max}$ for all stars, including errorbars, by using the methodology described in Hekker et al. (2010).

There is no significant differences between the global oscillation parameters obtained from the different methods, except for KIC 7680115 (see figure 3.5). We decided to adopt the values provided by S.H. since it has errorbars in $\Delta\nu$ and $\nu_{\rm max}$ for all stars. Those values are presented in table 3.1.

As for the period spacing, B.M. was able to provide estimations of $\Delta\Pi$. We show the period spacing of our stars on Figure 3.6 and the observed values and evolutionary status are shown in Table 3.1. B.M. was able to obtain the asymptotic period spacing for seven of our stars, six of those are confirmed as clump stars and one star is ascending (Hydrogen-shell burning phase) the red giant branch. The period spacing of KIC 7680115 could not be extracted due to the limited time series. The period spacings of the two other stars, KIC 10323222 and KIC 11918397 could not be measured. This indicates that these stars very certainly lie on the RGB, with a low value of $\Delta\Pi_1$ and a high mixed mode density. Otherwise, they would be clump stars, with a clear mixed mode pattern (Grosjean et al. 2014, Vrard et al. 2016).

3.3.3 Stellar properties using seismic scaling relations

To calculate the bolometric luminosities, we used the relations found in Alonso et al. (1999). The bolometric corrections are used together with the *Hipparcos* parallaxes, and the apparent magnitudes in V-band. We accounted for the effects of stellar extinction and reddening by using the dust maps presented in Green et al. (2015). More detail about the effects of stellar extinction and the choice for dust map can be found in the Appendix B. The set of spectroscopic and other non-seismic parameters can be found in Table 3.4.

To obtain the luminosities based on seismology, we first need to derive global stellar parameters using seismic constraints. It is possible to combine the information carried by $\Delta\nu$ and $\nu_{\rm max}$ into the scaling relations to obtain seismic estimates of mass and radius:

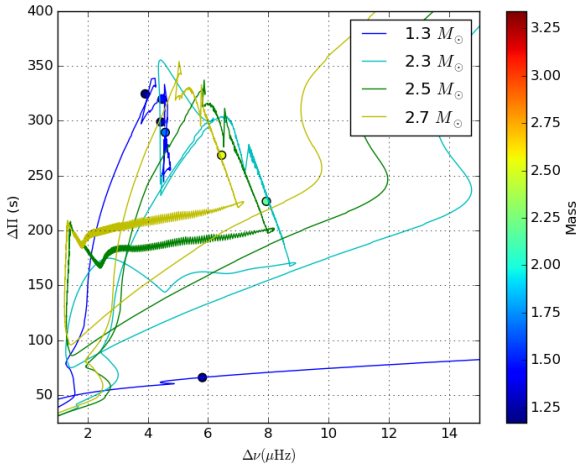

Figure 3.6: Period spacing ($\Delta\Pi$) versus Large separation $\Delta\nu$. The coloured solid lines indicate evolutionary tracks computed by the Modules for Experiments in Stellar Astrophysics (MESA) code (Paxton et al., 2011) with the convective overshooting mixing scheme described in Bossini et al. (2015). The models have solar composition and four different masses (1.30, 2.30, 2.50 and 2.70 $M_\odot$). The colour code of the dots are related to the stellar masses through the color bar on the right of the plot.

Table 3.4. Spectroscopic properties for the stars in our sample. The masses are obtained through the use of scaling relations.

KIC	HIP	$M/M_\odot$	$T_{\rm eff}$ (K)	[Fe/H]	$\log g$	π (mas)
1720554	95480	1.21 ± 0.07	4575 ± 70	−0.08 ± 0.11	2.64 ± 0.01	9.61 ± 0.36
4049174	94799	1.46 ± 0.09	4670 ± 70	+0.10 ± 0.11	2.54 ± 0.01	6.72 ± 0.33
7680115	95352	3.34 ± 0.04	5065 ± 55	+0.01 ± 0.10	2.74 ± 0.01	7.40 ± 0.24
8752618	95534	1.27 ± 0.07	4750 ± 60	−0.08 ± 0.11	2.49 ± 0.01	5.98 ± 0.35
9411865	96706	2.51 ± 0.10	5050 ± 55	+0.01 ± 0.11	2.79 ± 0.01	7.91 ± 0.33
10323222	92885	1.42 ± 0.08	4560 ± 70	+0.02 ± 0.12	2.57 ± 0.01	7.62 ± 0.38
10425397	98013	1.17 ± 0.07	4705 ± 60	−0.12 ± 0.10	2.41 ± 0.01	7.32 ± 0.37
11408263	96572	1.69 ± 0.09	4815 ± 55	−0.12 ± 0.10	2.56 ± 0.01	7.13 ± 0.30
11808639	94623	2.19 ± 0.09	5050 ± 60	+0.01 ± 0.10	2.91 ± 0.01	7.43 ± 0.39
11918397	96396	1.82 ± 0.11	4705 ± 60	−0.21 ± 0.10	2.41 ± 0.01	6.01 ± 0.27

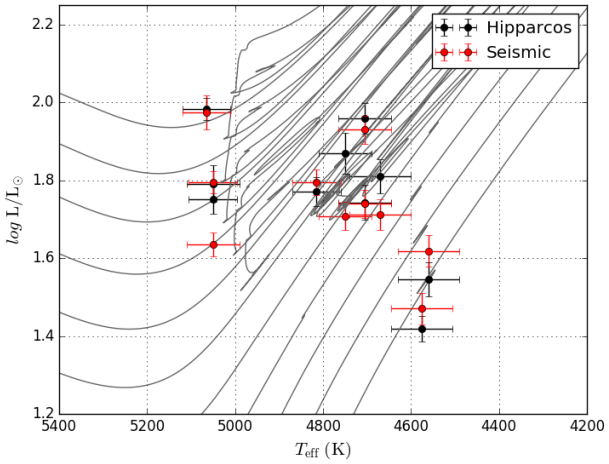

Figure 3.7: HR diagram for the stars in our sample. Red dots are the seismic value of luminosity and black dots are the bolometric luminosities. The range in mass covered by the tracks goes from $1.1M_{\odot}$ to $3.1M_{\odot}$, in steps of $0.2M_{\odot}$.

$$\frac{M}{M_{\odot}} = \left(\frac{\nu_{\rm max}}{\nu_{\rm max,\odot}}\right)^{3} \left(\frac{\Delta\nu}{\Delta\nu_{\odot}}\right)^{-4} \left(\frac{T_{\rm eff}}{T_{\rm eff,\odot}}\right)^{3/2}, \tag{3.1}$$

$$\frac{R}{R_{\odot}} = \left(\frac{\nu_{\rm max}}{\nu_{\rm max,\odot}}\right) \left(\frac{\Delta\nu}{\Delta\nu_{\odot}}\right)^{-2} \left(\frac{T_{\rm eff}}{T_{\rm eff,\odot}}\right)^{1/2}. \tag{3.2}$$

The solar values adopted in this work are $\Delta\nu_{\odot} = 135.1\ \mu Hz$, $\nu_{\rm max\odot} = 3090\ \mu Hz$, $T_{\rm eff} = 5777$ K. This set of equations has been widely used to obtain "direct" estimations of mass and radius for a given set of independent surface temperatures $T_{\rm eff}$. The limitations of the scaling relations are not fully understood yet, but recent tests have show that stellar radii can be accurate to a few percent in dwarfs and sub-giants (e.g. see Huber et al., 2012; Silva Aguirre et al., 2012; White et al., 2013; Coelho et al., 2015), while estimations of Mass can be as good as 10-15% (Miglio et al., 2013b).

In figure 3.8 we show the ratio $\Delta\nu/\Delta\nu_{\odot}$ to $(\rho/\rho_{\odot})^{1/2}$ as a function of effective temperature for models with nearly solar metallicity and a range of masses that goes from 1.1 to 3.0 $M_{\odot}$. The average large separation was computed from model frequencies by using radial modes around $\nu_{\rm max}$. As can be seen on the plot, the ratio deviates from unity. One of the main reasons for this are the discrepancies between model and observed frequencies that arise from imperfect modelling of surface effects (e.g. see Ulrich, 1986; White et al., 2011). This deviation also originate from deviations from simple homology scalings and asymptotic approximations (e.g. see Belkacem 2015). We note that, for the grid-based analysis (section 3.4), we make use of at least one pipeline (PARAM) that account for this discrepancies in the $\Delta\nu$ scaling relation (Rodrigues et. al. 2016, in preparation). From this plot we inferred a correction to our values of $\Delta\nu$ by using period spacing ($\Delta\Pi$, see Table 3.1) as a diagnostic for evolutionary stage. In our sample, the corrections were applied

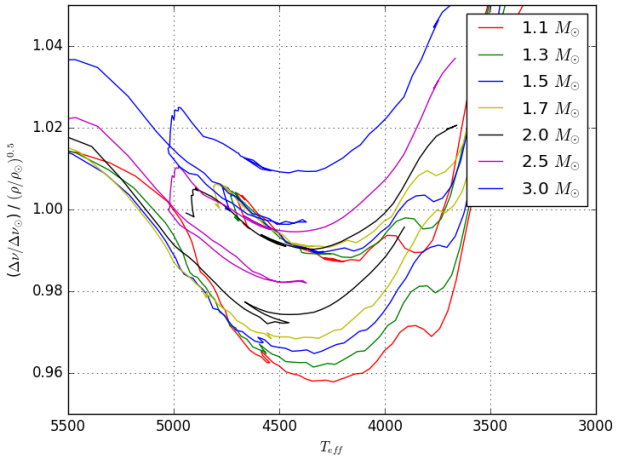

Figure 3.8: Ratio $\Delta\nu/\Delta\nu_\odot$ to $(\rho/\rho_\odot)^{1/2}$ as a function of temperature for models with nearly solar metallicity. $\Delta\nu$ was calculated using model frequencies around $\nu_{\max}$. The effects in low-mass clump stars are almost non-existent, but effects on RGB stars are $\backsim$ 3%. Models were computed using MESA.

for three RGB stars and one slightly more massive clump star, while all other stars have a combination of mass and evolutionary stage that makes a correction to $\Delta\nu$ be negligible, according to figure 3.8.

The values adopted for the correction of $\Delta\nu$ are: an increase of 3.5% for KIC 1720554 ($T_{\rm eff}$ = 4575 K, M $\sim$ 1.2 $M_\odot$) and KIC 10323222 ($T_{\rm eff}$ = 4560 K, M $\sim$ 1.4 $M_\odot$), a decrease of 2% for KIC 7680115 ($T_{\rm eff}$ = 5065 K, M $\sim$ 3.3 $M_\odot$) and and a increase of 2% for KIC 11918397 ($T_{\rm eff}$ = 4705 K, M $\sim$ 1.8 $M_\odot$). One of the grid modelling codes used later (PARAM) will do this step self consistently, and the corrections presented here can be considered as a first iteration.

Since we have parallaxes and magnitudes from *Hipparcos*, we can combine them with spectroscopic temperatures to obtain stellar radii. If the radius is known, we can obtain different estimation of masses by combining particular seismic constraints:

$$\frac{M}{M_\odot} = \left(\frac{\Delta\nu}{\Delta\nu_\odot}\right)^2 \left(\frac{R}{R_\odot}\right)^3, \tag{3.3}$$

$$\frac{M}{M_\odot} = \left(\frac{\nu_{\max}}{\nu_{\max,\odot}}\right) \left(\frac{R}{R_\odot}\right)^2 \left(\frac{T_{\rm eff}}{T_{\rm eff,\odot}}\right)^{1/2}, \tag{3.4}$$

where we used the corrected values of $\Delta\nu$ to obtain Masses from equation 3.3.

In figure 3.9, we compared masses obtained using different combinations of seismic and non-seismic constraints. The typical uncertainties on mass determinations are the following: $\backsim$ 6% when using $\nu_{\max}, \Delta\nu$ and spectroscopic $T_{\rm eff}$ (blue dots), $\backsim$ 8% when using $\Delta\nu$ and the radius obtained from *Hipparcos* parallaxes (green dots) and, finally, $\backsim$

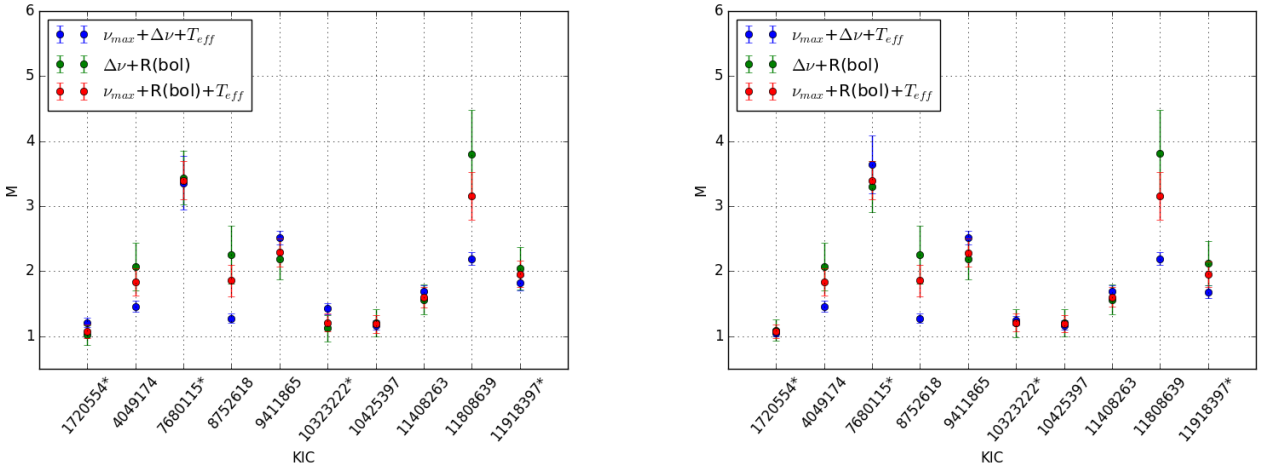

Figure 3.9: Left panel: Masses computed using different combinations of seismic parameters. The blue dots indicate calculations made using $\nu_{\rm max}$, $\Delta\nu$ and the spectroscopic temperatures ($T_{\rm eff}$, see Equation 3.1). Green dots are calculated using $\Delta\nu$ and the radius obtained from *Hipparcos* parallaxes (van Leeuwen, 2009) (Equation 3.3). Red dots are calculations made using $\nu_{\rm max}$, spectroscopic temperatures and the the same radius as before (Equation 3.4). Right panel: same left panel, but without corrections to $\Delta\nu$ applied to four RGB stars, indicated by asterisks in the KIC numbers.

5% when using the combination of $\nu_{\rm max}$, spectroscopic $T_{\rm eff}$ and the radii derived from *Hipparcos* parallaxes (red dots).

We calculated a set of distances using asteroseismic parameters and compared them to the values retrieved from the *Hipparcos* extended catalogue (van Leeuwen, 2009). The bolometric magnitudes can be written as:

$$m_{\rm bol} = M_{\rm bol} + 5\log\left(\frac{d}{10}\right) \tag{3.5}$$

$$M_{\rm bol} = M_{\rm bol,\odot} - 2.5\log\left(\frac{L}{L_\odot}\right) \tag{3.6}$$

where d is the distance, $m_{\rm bol}$ is the apparent bolometric magnitude and $M_{\rm bol}$ is the absolute bolometric magnitude. Equation 3.5 can be rewritten as:

$$\log d = 0.2(m_{\rm bol} - M_{\rm bol}) + 1 \tag{3.7}$$

When inserting equation 3.6 into equation 3.7, we have:

$$\log d = 1 + 0.5\log\left(\frac{L}{L_\odot}\right) + 0.2(m_{\rm bol} - M_{\rm bol,\odot}) \tag{3.8}$$

Equation 3.2 can be inserted in the Stefan-Boltzmann, $\frac{L}{L_\odot} = \left(\frac{R}{R_{odot}}\right)^2\left(\frac{T_{\rm eff}}{T_{\rm eff\odot}}\right)^4$, as:

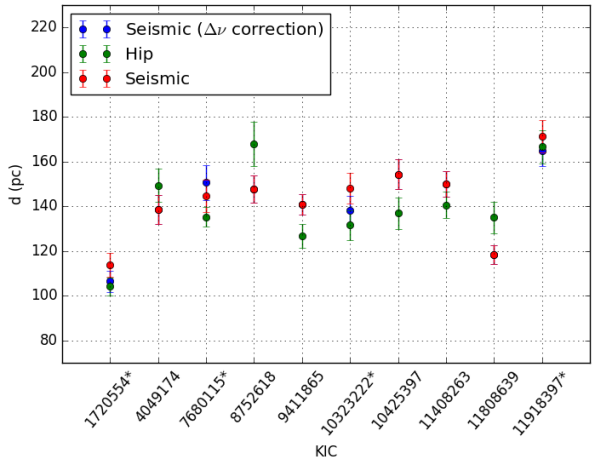

Figure 3.10: Comparison between the distances obtained using two methods. The green dots show the *Hipparcos* distances, while red dots are the distances determined by combining asteroseismic constraints ($\Delta\nu$, $\nu_{\rm max}$) and spectroscopic $T_{\rm eff}$. The blue dots are the four RGB stars with applied corrections on $\Delta\nu$, also indicated by asterisks in the KIC numbers.

$$\log\left(\frac{L}{L_\odot}\right) = 2\log\left(\frac{\nu_{\rm max}}{\nu_{\rm max,\odot}}\right) - 4\log\left(\frac{\Delta\nu}{\Delta\nu_\odot}\right) + 5\log\left(\frac{T_{\rm eff}}{T_{\rm eff,\odot}}\right) \tag{3.9}$$

By inserting equation 3.9 into equation 3.8, we obtain a way to estimated distances by using seismic parameters:

$$\log d = 1 + 2.5\log\frac{T_{\rm eff}}{T_{\rm eff,\odot}} + \log\frac{\nu_{\rm max}}{\nu_{\rm max,\odot}} - 2\log\frac{\Delta\nu}{\Delta\nu_\odot} + 0.2(m_{\rm bol} - M_{\rm bol,\odot}) \tag{3.10}$$

Our results are shown on Figure 3.10.

The relative difference between *Hipparcos* and seismic distances are shown on Fig. 3.11. The weighted average of the relative differences is -0.0094 with a statistical uncertainty of 0.0316. To compute the weighted average, we used the same approach as the one presented in Miglio et al. (2012b) and Chaplin et al. (1998). We also have included the Student t-distribution with a level of confidence of 68% and N-1 degrees of freedom, where N number of points. This was done to take into account the small number of points.

There is a good agreement between Hipparcos distances and their seismic counterparts. However, this may not be a stringent test due to the low number of stars.

We combined the seismic radii and the spectroscopic temperatures to derive a second set of "seismic" luminosities and compare it with the classical bolometric luminosities. The results can be found on the HR Diagram presented at Figure 3.7.

For KIC 10323222, the stellar radius obtained by using the measured angular diameter is 9.54 ± 0.50$R_\odot$, and the stellar mass and surface temperature are 1.13 ± 0.18$M_\odot$ and

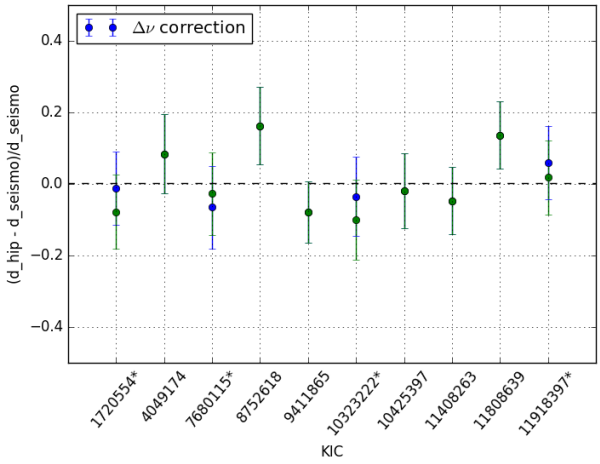

Figure 3.11: Relative differences between *Hipparcos* and seismic distances (green dots) estimated using equation 3.10. Blue dots shows the four RGB stars with corrections applied to $\Delta\nu$, also indicated by asterisks in the KIC numbers. The black dashed line is the weighted average difference of 0.003225.

4668 ± 80 K, respectively (see Huber et al., 2012). The corresponding values we have obtained in this work are: 10.34 ± 0.27$R_{\odot}$, 1.42 ± 0.08$M_{\odot}$ (obtained by using equations 3.2 and 3.1) and $T_{\rm eff}$ = 4560 ± 70 K from spectroscopy.

3.4 Grid based modelling

After deriving seismic and spectroscopic constraints, we decided to run a grid - modelling analysis on all of our red giants. This analysis was made using different grids of models and pipelines:

- The Pisa group used stellar models computed from ZAMS to the RGB tip (no He-burning evolution models are present in the grid). The grid contains models computed without convective core overshooting and accounting for microscopic diffusion, as in Thoul et al. (1994). The initial helium (Y) is linked to initial amount of heavy elements (Z) by adopting the usual linear relationship $Y = Yp + (\frac{\Delta Y}{\Delta Z}) * Z$ with Yp = 0.2485 being the value adopted for primordial helium abundance, and $\frac{\Delta Y}{\Delta Z} = 2$. The choice for solar abundances was taken from Asplund et al. (2009). The models don't account for mass loss in the RGB.

- Non-canonical BaSTI isochrones with no mass loss (described in Silva Aguirre et al. 2013, ApJ), while the statistical pipeline applied is the BAyesian STellar Algorithm (BASTA), described in Silva Aguirre et al. 2015. Results have been computed using the OCT solar values in the scaling relations and the Serenelli.

2016 correction to the $\Delta\nu$ theoretical values.

- A grid comprising models made using MESA Paxton et al. (2011) was used in the PARAM pipeline (da Silva et al. 2006; Miglio et al. 2013; Rodrigues et al. 2014) using Bayesian statistics to obtain global stellar parameters. Each evolutionary track has a pre-computed set of frequencies that PARAM uses to calculate the large separation directly (Rodrigues et. al. 2016, in preparation), avoiding the use of the $\Delta\nu$ scaling relation and the systematic effects associated with it (e.g see White et al., 2013).

The main procedure is to run the pipelines using the following parameters as input: $\nu_{\rm max}$, $\Delta\nu$, $T_{\rm eff}$ and [Fe/H]. In return, the codes were able to provide global stellar parameters such as: masses, radii, surface gravities, ages, and densities (and their associated uncertainties). In some occasions, the asymptotic period spacing, when it could be measured (see Table 3.1), was used to give some insights on the evolutionary status.

We compared the parameters obtained by the models with their respective values obtained using seismology. Results are shown on Figures 3.12. The star KIC 7680115 have an incomplete time series and this is translated as a error in $\nu_{\rm max}$ and $\Delta\nu$ larger than the rest of the sample. This is very clear when $\log g$ is compared to other stars.

On the upper left panel of figure 3.12 are the grid results for stellar radii compared with estimation obtained using stellar parallaxes (black triangle). The results agree well with each other with error bars with dispersions within $\sim$ 10% of the value of seismic radii obtained through scaling relation 3.2. However, three stars (KIC 4049174, KIC 8752618 and KIC 11808639) have radii obtained through parallaxes which are $\sim 2\sigma$ higher than the seismic ones.

As for the stellar masses, there is also a good agreement in general between different grid estimations, but with a higher dispersion of $\sim$ 20% from the seismic mass (see equation 3.1). One of the main reason for the larger deviation from the seismic value of stellar mass is due to the higher powers used with $\nu_{\rm max}$, $\Delta\nu$ and $T_{\rm eff}$ in equation 3.1. This will translate into larger uncertainties when using 3.1 to obtain seismic massed. It is also important to note that the grid results for the four ascending red giant stars have systematically lower values of mass when compared with the seismic values. This may be due to the systematics present when using $\Delta\nu$ to derive global seismic parameters (see figure 3.8).

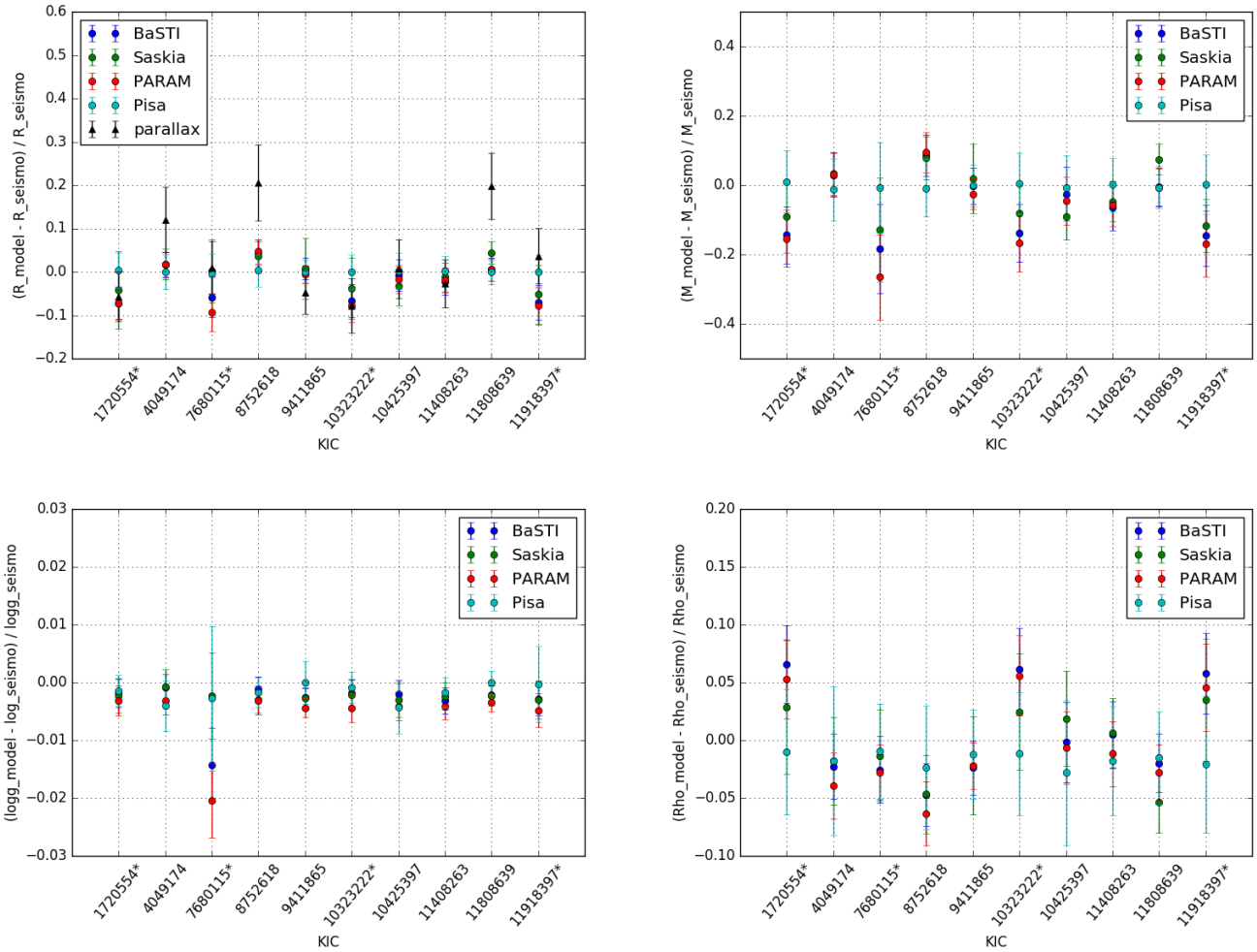

Figure 3.12: Results from all grid pipelines. Upper left: Relative residual values between the radii obtained by different grid-modelling pipelines and the radii obtained by using seismic data and the scaling relations. The seismic value is taken as the "true value". Note that, for the case of stellar radii only, a comparison with the radius obtained using parallaxes are shown as black triangles. Asterisks in the KIC numbers indicates RGB stars. Upper right: same as the upper left panel, but for masses. Lower left: same as the upper left panel, but for surface gravities. Lower right: same as the upper left panel, but for densities.

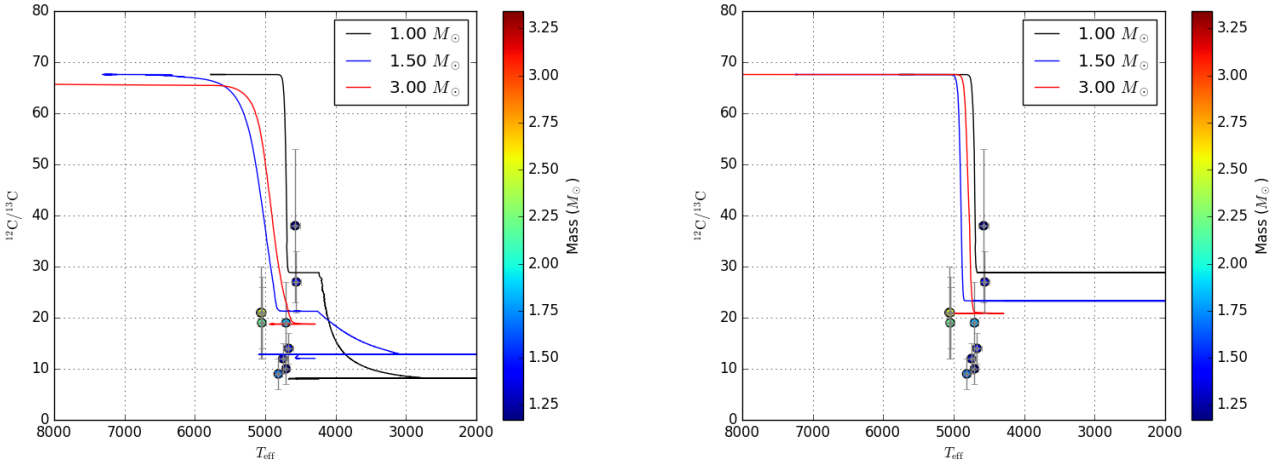

Figure 3.13: The theoretical evolution of carbon isotopic ratio $^{12}C/^{13}C$ at the stellar surface for models with M=1.0, 1.5 and 3.0 $M_\odot$ at solar metallicity, including the effects of thermohaline instability and rotation-induced mixing (left panel) and following the standard prescriptions (right panel). Dots represent our *Kepler* red giant stars.

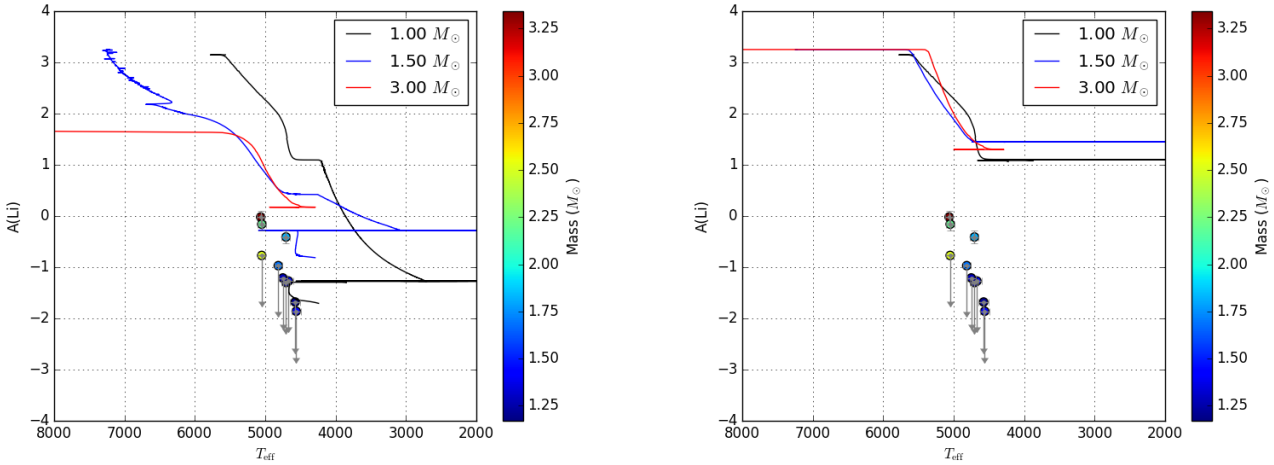

Figure 3.14: The theoretical evolution of Lithium abundances A(Li) at the stellar surface for models with M=1.0, 1.5 and 3.0 $M_\odot$ at solar metallicity, including the effects of thermohaline instability and rotation-induced mixing (left panel) and following the standard prescriptions (right panel). Dots represent our *Kepler* red giant stars. Downward arrows represent stars that only have an upper limit in A(Li).

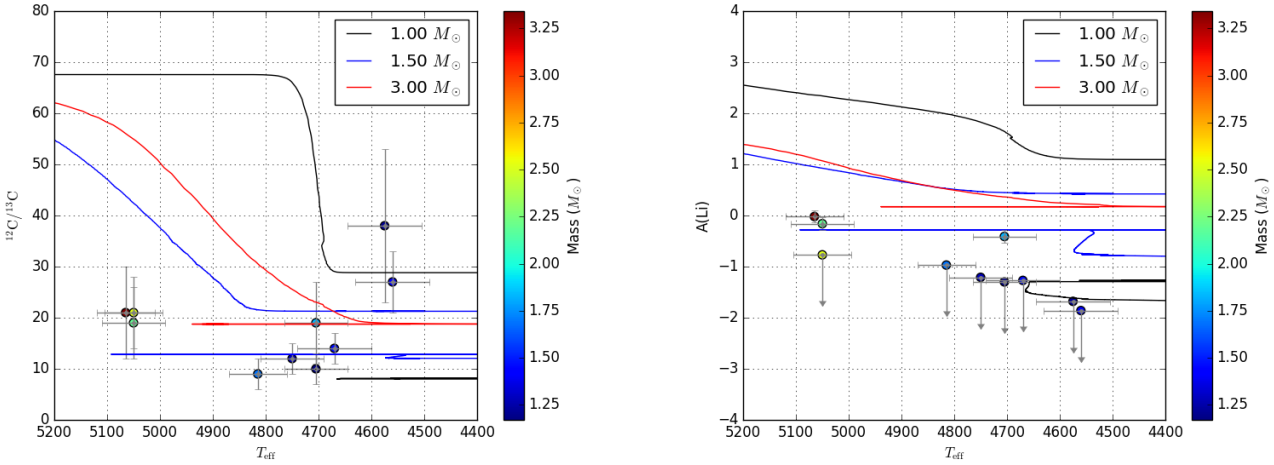

Figure 3.15: This plot is a zoomed version of Figures 3.13 and 3.17, but here we show only theoretical models that including the effects of thermohaline instability and rotation-induced mixing. The left panel shows the carbon isotopic ratio $^{12}C/^{13}C$, while the right panel shows Lithium abundances A(Li). Downward arrows represent stars that only have an upper limit in A(Li).

3.5 Discussion of key chemical elements

3.5.1 Surface Lithium and Carbon isotopic ratio

For the comparison, we consider stellar evolution models computed with the STAREVOL code including the effects of rotation-induced mixing and thermohaline instability all along the stellar evolution (Lagarde et al., 2012). These models reproduced spectroscopic data in open clusters, and field stars (e.g see Charbonnel & Lagarde, 2010). Although its efficiency is still discussed in the literature, thermohaline mixing seems to be the main physical process governing the surface abundances of C, N, and Li for stars more evolved than the bump luminosity on the red giant branch. Thermohaline mixing induces a decrease of ^{3}He at the stellar surface after the RGB-bump. ^{13}C and ^{14}N diffuse outwards, while ^{12}C diffuses inwards (see for more details Charbonnel & Lagarde 2010), implying a decrease of $^{12}C/^{13}C$ and [C/N]. Charbonnel & Lagarde (2010) showed that the efficiency of thermohaline instability decreases when the stellar mass or stellar metallicity increase.

On the other hand, rotation-induced mixing modifies the internal chemical profiles during the main sequence (e.g. Palacios et al., 2003, 2006). Its effects on the surface abundances are revealed only after the first dredge-up at the base of the RGB, and increase when the initial velocity increases. The net result is an depletion in the surface abundance elements such as lithium and carbon.

We can distinguish three regimes according to the initial stellar mass: for low-mass stars ($M \leq 1.8 M_\odot$), thermohaline mixing is the main process that changes the surface

abundances compared to rotation-induced mixing. For intermediate-mass stars (1.8≤ M ≤ 2.2$M_\odot$) both mechanisms play an equivalent role to change surface abundances. And finally, for more massive stars (M>2.2$M_\odot$) thermohaline mixing plays no role because these stars ignite central helium burning before reaching RGB bump. As results, thermohaline mixing does not occur in these stars, only rotation has an impact on surface abundances.

Figure 3.13 show the theoretical evolution of carbon isotopic ratio for three models at $1.0M_\odot$, $1.5M_\odot$ and $3.0M_\odot$, while Figure 3.17 shows the theoretical evolution of Lithium for the same stellar evolution models. They show the evolution from the zero-age main sequence to the early-AGB phase. We compared the theoretical predictions with our observations in all figures.

3.5.2 Low-mass stars

- KIC1720554 (M=1.21$M_\odot$± 0.07) is a low-mass RGB stars according to the period spacing of g-modes (66s). Although the large uncertainty on the surface $^{12}C/^{13}C$ (38± 15), the chemical properties of this stars indicate an early-RGB stars, not enough evolved to undergo thermohaline mixing.

- KIC10323222 (M=1.42$M_\odot$± 0.08) is low-mass stars with an high $^{12}C/^{13}C$ at the surface, which is consistent with early RGB stars. We could not detect period spacing for this star, possibly due to having a low value of ΔΠ, which implies an RGB status. The measured carbon isotopic ratio further solidify this argument.

- KIC4049174 (M=1.46$M_\odot$± 0.09, ΔΠ=319.7s, $^{12}C/^{13}C$=14± 3) ; KIC8752618 (M=1.27$M_\odot$± 0.07, ΔΠ=298.9s, $^{12}C/^{13}C$=12± 3) ; KIC10425397 (M=1.17$M_\odot$± 0.07, ΔΠ=324.5s, $^{12}C/^{13}C$=10± 3) ; KIC11408263 (M=1.69$M_\odot$± 0.09, ΔΠ=289.4s, $^{12}C/^{13}C$=9± 3) are low-mass stars with low carbon isotopic ratio measure at the surface. The period spacing of g-modes indicate clump stars while the low-surface carbon isotopic ratio confirm this evolutionary states by comparison with stellar evolution models including thermohaline mixing (see Fig. 3.15). The bottom panel of Fig 3.13 shows that standard models are not able to reproduce this low value of $^{12}C/^{13}C$.

3.5.3 Intermediate-mass stars

In addition to carbon isotopic ratio, we have an estimate of surface lithium abundance for these two stars. Lithium abundance is defined here as $A(Li) = \log(\frac{X(Li)}{X(H)}\frac{A_H}{A_{Li}}) + 12$, where X(Li) is the lithium mass fraction.

- KIC 11918397 (M=1.82$M_\odot$± 0.11) is an intermediate-mass star with low-metallicity ([Fe/H]=-0.21± 0.10). Although the period spacing of g-modes is not available for

this star, its chemical properties seem to indicate a clump star.

- According to the asymptotic period spacing (226.9s), KIC11808639 (M=2.19$M_{\odot}$± 0.09) is a clump star. The surface chemical properties confirms this evolutionary state, and are explained with stellar models including rotation and thermohaline mixing (Fig. 3.15).

3.5.4 More massive stars

In more massive stars, theoretical models do not show changes in the surface chemical properties during the red giant branch. According to stellar evolution models, red giant and clump stars show the same surface $^{12}C/^{13}C$ and lithium abundances.

- KIC9411865 (M=2.51$M_{\odot}$±0.10) is classified as being on the secondary clump, according to the period spacing. Although the upper limit of lithium abundance does not give additional constraints, this evolutionary state is consistent with its $^{12}C/^{13}C$.

- KIC7680115 (M=3.34$M_{\odot}$± 0.40) is one of the three stars without period spacing, probably due to the limited time series. The chemical properties ($^{12}C/^{13}C$=21± 9, A(Li)=-0.02± 0.12) of this star are in agreement with theoretical models including rotation (Fig 17).

  It is important to point the limitations of predictions made by models that account for rotational mixing. The initial rotation velocity in particular, despite its importance for the models, is an arbitrary parameter that can be adjusted, to some extent, in order to obtain a better agreement with the observed data (See figure 6 in Lagarde et al., 2015, for a detailed discussion).

3.6 Conclusions

We presented our results for the analysis of a group of 10 nearby red giants observed by *Kepler* and with accurate values of parallaxes obtained by *Hipparcos*. We combined seismic and spectroscopic parameters to conduct our analysis. We made tests using the seismic estimations of global parameters and compared results with stellar models. Results show a good agreement between different grid-pipelines.

We also compared estimation of parallaxes obtained using seismic parameters with those measured by *Hipparcos*. We obtained a good agreement between the two, with a weighted difference of 0.003225 ± 0.031026. However, we point that our sample might be too small.

In the context of constrained spectroscopic analysis using seismic $\log g$, and we have ascertained that using excitation balance wields slightly larger values of effective temper-

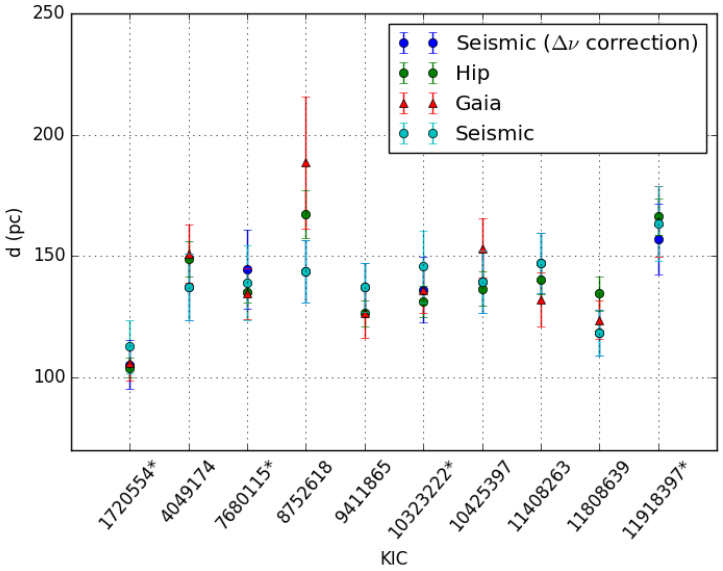

Figure 3.16: Updated version of figure 3.10 with the new parallaxes obtained from the *Gaia* mission. There is a good agreement in general between distances from *Gaia* (red triangles) and *Hipparcos* (green dots), with four notable exceptions: KIC 8752618, KIC 10425397, KIC 11408263 and KIC 11808639. We should note that a systematic error of ±0.3 mas was added to parallaxes uncertainties from Gaia. This systematic error comes from early calibration effects (see Gaia Collaboration et al., 2016a, for more details).

ature for hotter ($T_{\rm eff} \geq 5000$ K) stars. Our results using iron ionization balance wields values of $T_{\rm eff}$ which are in good agreement with estimations of photometric $T_{\rm eff}$ obtained using seismic $\log g$.

We compared the observed surface abundances of lithium and carbon with prediction made by models with and without extra mixing processes. The spectroscopic abundances have a better agreement with stellar models where non-standard mixing processes are included in the calculations.

During the final writing stages this thesis, the data from the *Gaia* Mission had been released to the public. We plot on figure 3.16 the new values of distances and compare them with the previous values from the *Hipparcos* catalogue. We plan to include a detailed comparison with the *Gaia* values of parallaxes before publishing the results of this project. This, however, will require re-calculations of various parameters, such as reddening, for example.

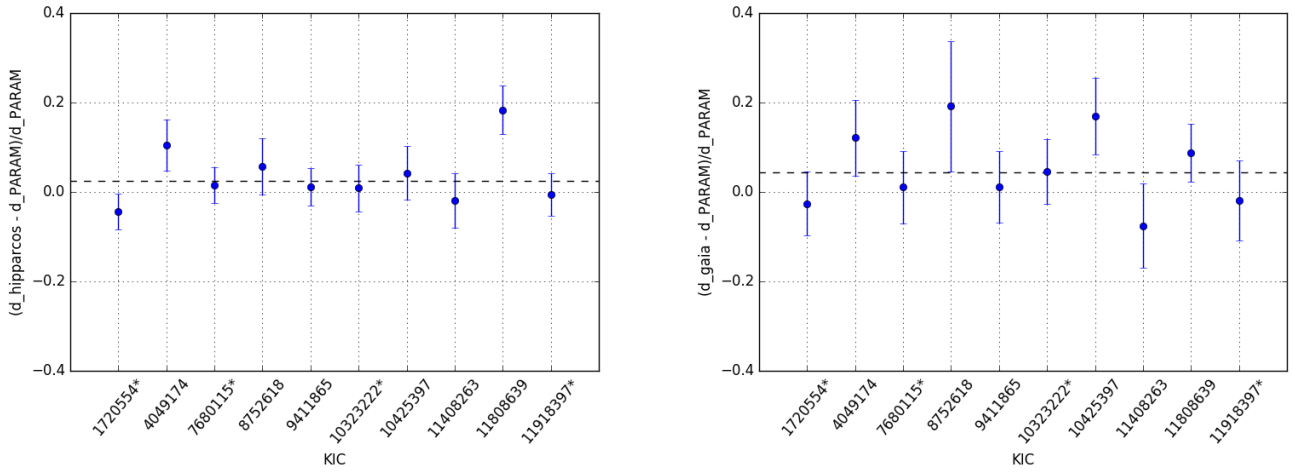

Figure 3.17: Left: residual differences between distances from PARAM and the distances obtained from *Hipparcos* parallaxes. PARAM obtain distances from a grid search (see section 3.4 for more details). The weighted average of the residuals is 0.02571 (black dashed line). Right: same as the left figure, but using parallaxes from *GAIA* instead. The weighted average of the residuals in this case is 0.04394.

Chapter 4

Signatures of Rapid Variation

Regions of sharp structural change in the stellar structure produce a sudden variation in sound speed. The sudden change in the value of sound speed will affect the frequencies of oscillation, producing deviations from the regular frequency separations predicted by the asymptotic theory. Such deviations appear as oscillatory components in the eigenfrequencies with respect to the mode's radial order. This oscillatory pattern, the so-called acoustic glitch, contains valuable information about the regions of where the sharp-structure variation occurs. Glitches can be used to obtain model-independent estimations of the acoustic depth of the boundary between the radiative and convective zone, and zones of Helium ionization near the stellar surface.

In section 4.1, we will cover the minimization algorithms and statistical tools used during the analysis of stellar glitches. In section 4.2 we describe the origin of the oscillatory signal and how to amplify it. In section 4.3 we describe the mathematical expressions used to extract the glitch signature from the stellar frequencies. In section 4.4, we describe the methodology we used to test the validity of our methods applied to both the solar frequencies and a group of artificial stars. In section 4.5 we report our estimations of acoustic location when analysing a group of 13 *Kepler* stars, as well as a comparison with representative stellar models. Concluding remarks can be found in section 4.6.

4.1 Introduction to MCMC

The available information for a certain set of variables of interest is fundamental to conduct statistical inference. If the true values for of those variables are not known, the main procedure is try to reduce this uncertainty. Besides, the amount of uncertainty may have different shapes or scales. From the Bayesian point of view, those different degrees of uncertainty are represented by probabilistic modes for each variable. In this context, it is natural that distinct models may have different degrees of uncertainties.

4.1.1 Bayes theorem

Consider an unknown quantity of interest θ, which usually is a non-observable. The information that we have available for θ, can be resumed, in a probabilistically approach, as $p(\theta)$, and can be improved by observing a random quantity X associated with θ. The distribution $p(x|\theta)$ defines this relation. The main idea is that after observing $X = x$, the amount of information we have on θ will increase and the Bayes theorem allow us to update the information we have for θ and quantity this increase of knowledge as:

$$p(\theta|x) = \frac{p(\theta, x)}{p(x)} = \frac{p(x|\theta)p(\theta)}{p(x)} = \frac{p(x|\theta)p(\theta)}{\int p(\theta, x)d\theta} \tag{4.1}$$

Note that $1/p(x)$, which is independent of θ, work as a normalization factor of $p(\theta|x)$.

For a fixed value of x, the function $L(\theta; x) = p(x|\theta)$ gives the *likelihood* function of each one of the possible values of θ, while $p(\theta)$ is the *prior* distribution of θ. Those two sources of information, priors and likelihood, are combined to produce the *posterior* distribution of θ, $p(\theta|x)$. Hence, the usual form of Bayes theorem is:

$$p(\theta|x) \propto L(\theta; x)p(\theta) \tag{4.2}$$

By omitting the term $p(x)$ in equation 4.1, the equal sign is replaced by a proportionality in equation 4.2. This simplified version of Bayes theorem is useful in problems that require estimations of parameters (such as the work presented in chapter 5), since the denominator is only a normalization factor called evidence, which isn't necessary to calculate for computational methods.

The formal definition of the likelihood is the probability of obtaining a set of N observations, x, given a known model and its set of model parameters, θ.

If we assume that the errors of a particular data set are not correlated, the log-likelihood function of the data x_n given the parameter θ can be written as:

$$\ln p(x_n|\theta) = -\frac{1}{2}\sum_{n=1}^{N}\frac{[x_n - f_\theta]^2}{\sigma_n^2} + A, \tag{4.3}$$

where σ is the error on the data, f_θ is our model function and A doesn't depend on θ and can be discarded. However, if the errors are correlated, equation 4.3 must be generalized to include the covariance between data points. This can be done by rewriting equation 4.3 in a matrix form:

$$\ln p(x_n|\theta) = -\frac{1}{2}\mathbf{r}^T\mathbf{K}^{-1}\mathbf{r} - \frac{1}{2}\ln(\det\mathbf{K}) - \frac{N}{2}\ln(2\pi) \tag{4.4}$$

where:

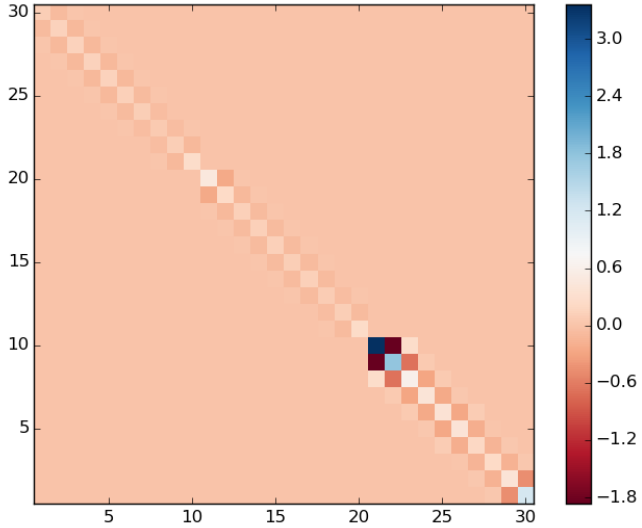

Figure 4.1: Example of a covariance matrix used to calculate the Likelihood function. This matrix in particular is obtained from calculating second differences ($\Delta_2 \nu$) using 36 frequencies with angular degree $l = 0$, 1 and 2.

$$\mathbf{r} = \begin{bmatrix} x_1 - f_{\theta 1} \\ x_1 - f_{\theta 1} \\ \vdots \\ x_N - f_{\theta N} \end{bmatrix}$$

is the residual vector, and $\mathbf{K}$ is the $N \times N$ covariance matrix, where N is the total number of data points (see figure 4.1).

4.1.2 Markov Chain Monte Carlo

The form of the likelihood function can be quite complex, and needs to be combined with the prior information for all the free parameters in a model in order to create a multi-dimensional posterior distribution, which the exact form can be extremely complicated. To ascertain the uncertainty in our models, we need to draw samples from the posterior so that we can have an idea of the shape of the distribution. This can be done using computational methods.

In non-iterating methods, the sample taken from the posterior distribution is done in a single step, and the values are generated in an independent way and it is not interested with the convergence of the algorithm, relying instead on a sufficiently large sample. However, in many cases, it can be very difficult, and sometimes impossible, to find function that is, at the same time, a good approximation of the posterior distribution and easy to be sampled.

The method of the Markov Chain Monte Carlo (MCMC) is a reliable alternative to non-iterating method when dealing with complex distributions. The main idea is still to obtain a sample from the posterior distribution in order to characterize the shape of the distribution. The difference with MCMC lies in using an iterative method based on Markov chains, generating non-independent values.

A Markov chain is a stochastic process $\{X_0, X_1, \dots\}$ such as that the distribution of X_t, given by all the previous values of $X_0, \dots, X_{t-1}$, depends only on X_{t-1}. Mathematically,

$$P(X_t \in A | X_0, \dots, X_{t-1}) = P(X_t \in A | X_{t-1}) \tag{4.5}$$

for any subset A. Therefore, the next step made in a Markov chain only depends on present values, making the chain explore the parameter space without any bias from the old values that would, otherwise, have an effect on the shape of the sampled posterior.

The main procedure done by a MCMC algorithm consists in defining a starting point defined by a model that is considered to be acceptable, and then measure how well the free parameters are constrained. This information is used to define a scale length to slightly perturb each of the free parameters, usually in a random manner, obtained from a random-walk distribution. After that, the posterior probability is computed for this initial state, $p(\theta_{old}|x)$. Then, the initial state is left behind after a random step, and then the posterior probability of this new position, $p(\theta_{new}|x)$ is computed. If $p(\theta_{new}|x)$ is better than $p(\theta_{old}|x)$, the new state is accepted. Otherwise, it might still be accepted based on the ratio of their posterior probabilities used in the Metropolis-Hastings algorithm (see below). Since this ratio is obtained using the same models, the normalization factor, or evidence $p(x)$, doesn't need to be computed. Finally, after the new value is either accepted or rejected, a new random step is generated, and the entire process is repeated again until a chain of states is created. By sampling this chain, we are able to obtain a reasonably good approximation of the posterior distribution.

A popular method used to create a Markov chain is the so called Metropolis-Hastings algorithm (Metropolis et al. 1953, Hastings 1970). This algorithm uses the idea that a certain value is sampled from a distribution and accepted with a given probability. This mechanism of correction ensures the convergence of the chain towards the equilibrium distribution, which in our case is the posterior distribution.

Suppose that a chain is in a state θ, and a new value θ' is generated from a proposed distribution $q(.|\theta)$. Observe that the proposed distribution can depend of the current state of the chain. For example, $q(.|\theta)$ could be a normal distribution centred around θ. The new value of θ' is accepted with probability:

$$\alpha(\theta, \theta') = \min\left(1, \frac{\pi(\theta')q(\theta|\theta')}{\pi(\theta)q(\theta'|\theta)}\right) \tag{4.6}$$

where π is the distribution for interest. An interesting property is that we only need to

know the distribution of π partially, i.e. without a constant, since the probability shown in 4.6 does not change in this case. This is fundamental in Bayesian processes where we do not know the posterior completely.

4.2 Theoretical Background

The main reason for mentioning the frequency combinations presented in chapter 1 (section 1.4) lies in the dependence of the mode frequencies on localized and rapid changes in stellar density and structure. A departure in the periodic spacings of frequencies predicted by the asymptotic relation will appear due to the sharp structure variations in the internal stellar structure. A shift will be present in each eigenfrequency, here called δ_n^{glitch}, where we ignore the dependency in l. This shift is characterized by a periodic function of frequency and will depend mainly on the location and on how abrupt the transition is.

To understand the nature of the signal we can begin by considering the following wave equation (assuming adiabatic approximation, see Brodsky and Vorontsov, 1993):

$$\frac{d^2}{d\tau^2}\zeta + [\omega^2 - V(\tau)]\zeta = 0, \tag{4.7}$$

where here we define τ as the acoustic depth of the star, given by $d\tau = -dr/c$, noting that $\tau = 0$ at $r = R$. The parameter ζ is the eigenfunction of the oscillation and we can try to explain the reason for the existence of the oscillatory signature. Assume that we have an acoustic potential V as a function of τ, and is V heavily dependent on the internal stellar structure with terms that contain the first and second derivatives of the sound speed c. If there is a discontinuity in the first derivative of c, we will create a delta function in the acoustic potential V. Similarly, if we introduce a discontinuity in the second derivative of c, the result will be a step function of the acoustic potential. Assume now that we have two expressions for V that exemplifies both types of singularities, for which we can find exact solutions:

$$V_1(\tau) = \begin{cases} V_b, & \text{for } 0 \geq \tau < \alpha_1\tau \\ V_a, & \text{for } \alpha_1\tau \geq \tau < \tau_t \end{cases}$$

and

$$V_2(\tau) = V_a + A_\delta\delta(\tau - \alpha_2\tau_t), \tag{4.8}$$

where τ_t is the total acoustic depth of the star. If we take equation 4.7 and expand the solutions (Brodsky and Vorontsov, 1993) using the the potentials V_1 and V_2 defined above, keeping first order terms in $\delta\omega = \omega - \omega_0$, which represents the frequency shift, and doing the same for $\delta V^2 = V_a^2 - V_b^2$, which represents variation in structure ,we obtain a periodic approximation for $\delta\omega$ given by:

$$\delta\omega_1 \approx \frac{\delta V^2}{4\tau_t \omega_0^2} \sin[2\Lambda_0(\alpha_1\tau_t)], \tag{4.9}$$

and

$$\delta\omega_2 \approx \frac{A_\delta}{2\tau_t \omega_0} \cos[2\Lambda_0(\alpha_2\tau_t)], \tag{4.10}$$

where,

$$\Lambda_0(\tau) = \int_0^\tau (\omega_0^2 - V_a^2)^{\frac{1}{2}} d\tau. \tag{4.11}$$

The approximations presented above may be simplistic, but offer an idea on how the amplitude of the signal depends on frequency, and they are not much different from the results obtained in a star, for which the acoustic potentials are replaced for more complex functions and can be obtained from models (for more detail, see Monteiro et al., 1994). By doing so, the complete expression for the potential can be written as (see e.g. Vorontsov et al., 1989; Roxburgh, 1994):

$$V^2 = N^2 + \frac{c^2}{4}\left(\frac{2}{r} + \frac{N^2}{g} - \frac{g}{c^2} - \frac{1}{2c^2}\frac{dc^2}{dr}\right)^2 - \frac{c}{2}\frac{d}{dr}\left[c\left(\frac{2}{r} + \frac{N^2}{g} - \frac{g}{c^2} - \frac{1}{2c^2}\frac{dc^2}{dr}\right)\right] - 4\pi G\rho \tag{4.12}$$

At the boundary between the convective envelope and the radiative zone, g, c^2 and ρ are continuous, but the derivatives of the sound speed are discontinuous. The potential can then be simplified as:

$$V(\tau) = V_0(\tau) + A_H H(\tau - \tau_{bcz}) + A_\delta \frac{1}{c}\delta(\tau - \tau_{bcz}) \tag{4.13}$$

where $V_0(\tau)$ is a smooth function of τ, τ_{bcz} is the acoustic depth of the base of the convective zone and H is the Heaviside function. The equation above has terms that are similar to the potentials defined in equation 4.8 in such way that the base of the convection zone will induce a periodic signal on frequencies that is a combination of equations 4.9 and 4.10.

The same analysis can be applied to the second Helium ionization zone near the surface of the star. In this case, there will be an induced effect on the first adiabatic index Γ_1. The potential can then be written as (Marchenkov et al., 1991):

$$V^2 \sim \frac{g}{16c^2}\left[(1+\Gamma_1)(3-\Gamma_1) + 2(1+\Gamma_1)\frac{d\Gamma_1}{d\ln\rho} - (\frac{d\Gamma_1}{d\ln\rho})^2 + 4\Gamma_1\frac{d^2\Gamma_1}{d(\ln\rho)^2},\right] \tag{4.14}$$

however, we can't consider discontinuities in the derivatives of Γ_1 here. Instead of an abrupt jump, we end up with a depression in the first adiabatic index (see figure 4.2).

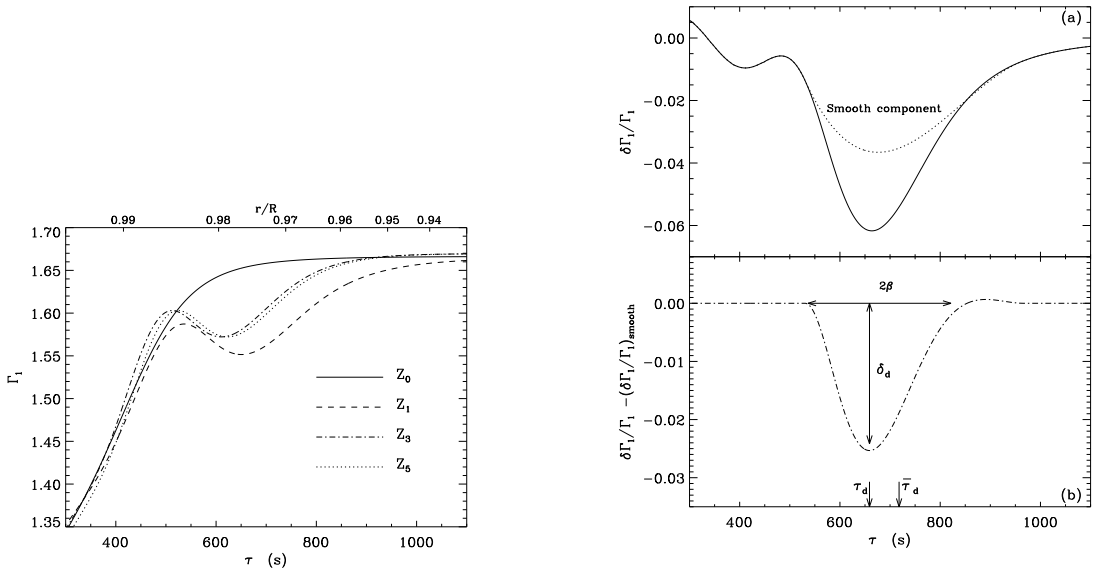

Figure 4.2: Left: The first adiabatic index Γ_1 for different solar models. In model Z_0, the second ionization of Helium has been suppressed while the other three models have different equations of state. Right: a) The differences in Γ_1 between two models with and without the second ionization of Helium (Z_0 and Z_1 respectively) plotted as a function of acoustic depth τ. b) The change in Γ_1 relative to a smooth reference structure. The parameters that define the signal present in the frequencies are represented schematically. Figure from Monteiro & Thompson (2005).

To model the signature induced by the second Helium ionization zone, we follow the same approach used in Monteiro & Thompson (2005) and assume that the depression in Γ_1 has a width β in acoustic depth and at a height δ_d. When compared with a model with Helium ionization, the frequencies will assume a periodic component of the form:

$$\delta\omega \approx A(\omega)\exp(-c_2/\omega)\cos(2\omega\tau^*_{HIZ} + \phi), \tag{4.15}$$

where τ_{HIZ} is the acoustic depth of the helium ionization zone (expressed as τ_d in figure 4.2) and c_2 is a parameter related to the thickness of the HeII ionization zone. The exponential factor models the bump on Γ_1 with a Gaussian function (see figure 4.2). $A(\omega)$ give a measurement of the amplitude of the glitch signal. This amplitude depends on the amount of Helium present in the ionization zone, and can be used to determine the helium abundance (Basu et al., 2004; Monteiro & Thompson, 2005; Verma, 2014). It should be noted that no trivial relation exists between the true location of τ_{HIZ} and the measured signal τ^*_{HIZ}, due to near-surface effects affecting our estimations. However, Monteiro & Thompson (2005) showed that a difference of 140 seconds between the two is to be expected in the Sun.

4.2.1 Methods to Amplify the Signal

The periodic component is very small but the corresponding signature can be amplified by using second differences (defined in Eq. 1.44). This is present in the work done by Houdek and Gough (2007) that we shall briefly follow here. Consider a simple oscillatory signal such as:

$$\delta\nu_n^{glitch} = A_n \cos x_n \tag{4.16}$$

where x_n and A_n are dependent on frequency. If we use Taylor expansion on $x_{n\pm1}$ and $A_{n\pm1}$, we obtain:

$$x_{n\pm1} \simeq x_n \pm \frac{\mathrm{d}\nu_\mathrm{n}}{\mathrm{dn}}\frac{\mathrm{dx_n}}{\mathrm{d}\nu_\mathrm{n}} \simeq \Delta\nu\frac{\mathrm{dx_n}}{\mathrm{d}\nu_\mathrm{n}} \equiv x_n + a \tag{4.17}$$

$$A_{n\pm1} \simeq \left(1 \pm \frac{\nu}{A_n}\frac{\mathrm{dA_n}}{\mathrm{d}\nu_\mathrm{n}} + \frac{{\nu_0}^2}{2A_n}\frac{\mathrm{d^2A_n}}{\mathrm{d}{\nu_\mathrm{n}}^2}\right)A_n \equiv (1 \pm b + c)A_n \tag{4.18}$$

where Eq. 1.28 was used to obtain the derivatives of ν_n at a fixed value of l and keeping only the leading term. By using Eq. 1.44 and writing the frequencies as a sum of a smooth component ν_s and the shift $\delta\nu_n^{glitch}$, we then have:

$$\Delta_2\nu_{n,l} = \Delta_2\nu_s + FA_n\cos(x_n - \delta), \tag{4.19}$$

where

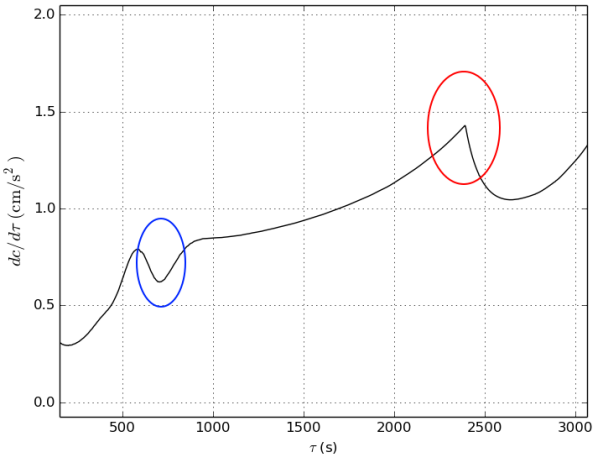

Figure 4.3: $\frac{dc}{d\tau}$ as a function of acoustic depth τ for a typical sun-like, main-sequence star. The red circle mark the location of the base of the convective zone, and the blue circle mark the location of the second helium ionization zone.

$$F = 2\left\{[1 - (1 + c)\cos a]^2 + b^2 \sin^2 a\right\}, \tag{4.20}$$

and $\delta = \delta(a, b, c)$. In the case of the Sun and the glitch associated with the helium ionization zone located near the surface, Houdek and Gough (2007) find that $a \simeq 1.4$, $b \simeq -0.33$ and $c \simeq 0.04$ and the oscillatory signature of the glitch is amplified by the second differences by a factor of $F \simeq 1.7$. In the case of the glitch associated with the base of the convective zone, they found that $a \simeq 4$, $b \simeq -0.10$ and $c \simeq 0.01$, with $F \simeq 3.4$.

4.3 Complete expressions

An extensive work has been done using the glitch signals in solar frequencies to locate the base of the convective envelope and to constrain the amount of overshooting below the boundary between the convective envelope and the radiative zone (e.g. see Vorontsov, 1988; Gough et al., 1993; Monteiro et al., 1994; Basu et al., 1994; Roxburgh, 1994; Basu, 1997; Christensen-Dalsgaard & Thompson, 2011). Also, it is possible to use the signal created by the helium ionization zone to obtain an estimation of helium abundances in the envelope (e.g. see Christensen-Dalsgaard et al., 1991; Basu et al., 1994; Monteiro et al., 1994; Basu & Antia, 1995; Monteiro & Thompson, 2005; Christensen-Dalsgaard & Thompson, 2011).

It has been proposed that the same procedure may be used for distant stars to obtain estimations of location of the base of the convective envelope or the second helium ionization zone (Mazumdar et al., 2001; Roxburgh, 2003; Ballot et al., 2004; Basu et al., 2004; Houdek, 2004; Mazumdar, 2005; Houdek and Gough, 2007). This was achieved later by

using frequencies obtained by *CoRoT* and *Kepler* (e.g see Miglio et al., 2010; Mazumdar et al., 2012).

To fit *Kepler* stars, we use a more complete expression relating the second differences to the periodic signature of the glitch. We ignore dependencies in the spherical degree l, since we are working with only low degree modes. We shall write all expressions in terms of the cyclic frequency $\nu = \omega/2\pi$. The frequency combinations used here to amplify the signal of the glitch are the second differences ($\Delta_2\nu$, equation 1.44) and the frequency ratios (r_{01} and r_{10}, equations 1.42 and 1.42).

By using the second differences, we can estimate $\tau_{\rm BCZ}$ and $\tau_{\rm HIZ}$ simultaneously by fitting a suitable function to the oscillatory signals (Mazumdar et al. 2014):

$$\Delta_2\nu = a_0 + \frac{b_2}{\nu^2}\sin(4\pi\nu\tau_{\rm BCZ} + 2\phi_{\rm BCZ}) + c_0\nu\exp^{-c_2\nu^2}\sin(4\pi\nu\tau_{\rm HIZ} + 2\phi_{\rm HIZ}) \tag{4.21}$$

where a_0 is represent the smooth term, b_2 and c_0 are the amplitude of each signal, c_2 is associated to β and, finally, $\phi_{\rm BCZ}$ and $\phi_{\rm HIZ}$ are the phase constants associated with the oscillatory signature of the base of the convective zone and Helium ionization zone, respectively. We have a total of eight free parameters: $a_0, b_2, c_0, c_2, \tau_{\rm BCZ}, \phi_{\rm BCZ}\tau_{\rm HIZ}$ and $\phi_{\rm HIZ}$. For some of the stars, we used a different expression for the smooth term a_0, where instead of a simple linear function we used a parabolic expression: $a_0 + a_1\nu + a_2\nu^2$. This was necessary for stars with a large range of frequencies available, like the Sun and some bright *Kepler* stars, and is justifiable by the sensitivity of fitted values of τ to small perturbation on the input frequencies. We don't use this parabolic function for all stars because it interferes with the HIZ component when the range of frequencies is more limited, making robust estimations of $\tau_{\rm HIZ}$ more difficult. When using second differences we assume, for most stars, that the smoothing term is simplified to a constant shift.

Equation 4.21 is a simpler version of the equation presented in Houdek and Gough (2007), however it keeps the most important elements and has a reasonable amount of free parameters. It worth noting that Basu et al. (2004) have shown the results are not significantly affected by the exact expressions of signal amplitude.

By using second differences, we can indeed obtain signatures from both HIZ and BCZ. However, the estimation of acoustic depth are biased by near-surface effects (see Christensen-Dalsgaard & Thompson, 1995). Such bias can be removed by using the acoustic radius of the signature T instead. The acoustic radius is defined as the time that a sound wave takes to travel from core to surface ($T = 0$ at $R = 0$). It is possible to directly measure acoustic radii by using frequency ratios r_{01} and r_{10}, defined in equations 1.42 and 1.43, respectively (see Roxburgh, 2003). We use the notation r_{010} to denote the set $\{r_{01}, r_{10}\}$.

$$r_{010} = \{r_{01}(n), r_{10}(n), r_{01}(n+1), r_{10}(n+1), r_{01}(n+2), ...\} \tag{4.22}$$

As we mentioned in Chapter 1, the near-surface effects in the outer layers of the star are cancelled when taking the frequency ratios (Roxburgh, 2005). As a consequence, information on the stellar core can be retrieved in the global trend of these variables (e.g. Silva Aguirre et al., 2011b; Cunha & Brandão, 2011). At the same time, the signature of internal glitches produced by the BCZ can be obtained by using these ratios. For the case of the Sun, Roxburgh (2009) obtained the acoustic radii of the BCZ (T_{BCZ}) by using a Fourier transform on the residuals left after removing the global trend. However, it is essential to note that information on the glitches near the surface (namely the signal from HIZ) are suppressed when taking frequency ratios, leaving only the signal of the BCZ.

We followed an approach similar the one presented in Mazumdar et al. (2014): we define the variable $y = \nu^* r_{010}$, where $\nu^* = \frac{\nu}{\nu_r}$ and ν_r is a reference frequency. We do the fit of y to the frequency ratios using the following equation:

$$f(\nu) = \sum_{k=0}^{m} \frac{c_k}{(\nu + \nu_r)^k} + A \sin(4\pi T_{\rm BCZ}\nu + \phi) \tag{4.23}$$

We end up with $m + 3$ free parameters: $\{c_k\}$, A, $T_{\rm BCZ}$ and ϕ. We choose $m = 2$ and $\nu^* = 0.8\nu_{max}$, same as done in Roxburgh (2009).

We used a Markov Chain Monte Carlo (MCMC) algorithm to obtain estimations of $\tau_{\rm BCZ}$ and $\tau_{\rm HIZ}$ using equation 4.21 with second differences and $T_{\rm BCZ}$ when using equation 4.23 applied to the frequency ratios. For both methods, the MCMC algorithm used parallel tempering with a tempering level equal to one. To check if MCMC has converged, we check if there is consistency in the results of the first and second half of the chain. MCMC was run for 10^6 iterations, using uniform distributions for the priors of all free parameters.

For equation 4.21, the prior for the smoothing term a_0 was restricted to $[0, \max(\Delta_2\nu)]$. For b_2, c_0 and c_2, we used very broad priors spanning two orders of magnitude around the initial guess of the parameters. The phase angles $\phi_{\rm BCZ}$ and $\phi_{\rm HIZ}$ had a uniform prior over the interval $[-2\pi, 2\pi]$. The prior for the acoustic depth $\tau_{\rm BCZ}$ is restricted by the interval $[0.3\tau_0, 0.7\tau_0]$, where τ_0 is the total acoustic depth. This interval in acoustic depth is where we expect to find the the base of the convective envelope in a main sequence star (see figure 4.9). Similarly, the prior for $\tau_{\rm HIZ}$ is defined by the interval $[0.05\tau_0, 0.3\tau_0]$, since we expect to find the helium ionization zone near the surface of the star.

When using equation 4.23 to fit the frequency ratios, the prior for the amplitude A is defined as between 0 and $\max(y)$ while the phase angle ϕ is once again defined over $[-2\pi, 2\pi]$. Priors for ck were defined by using a simple mean least square fitting without using the oscillatory component (see figure 4.4). Once the least square fit is done, we use the associated uncertainties σ_k to define the priors for ck in the range $[ck - 3\sigma_k, ck + 3\sigma_k]$. The acoustic radius $T_{\rm BCZ}$ had priors over $[0.3T_0, 0.7T_0]$, where T_0 is the total acoustic radius.

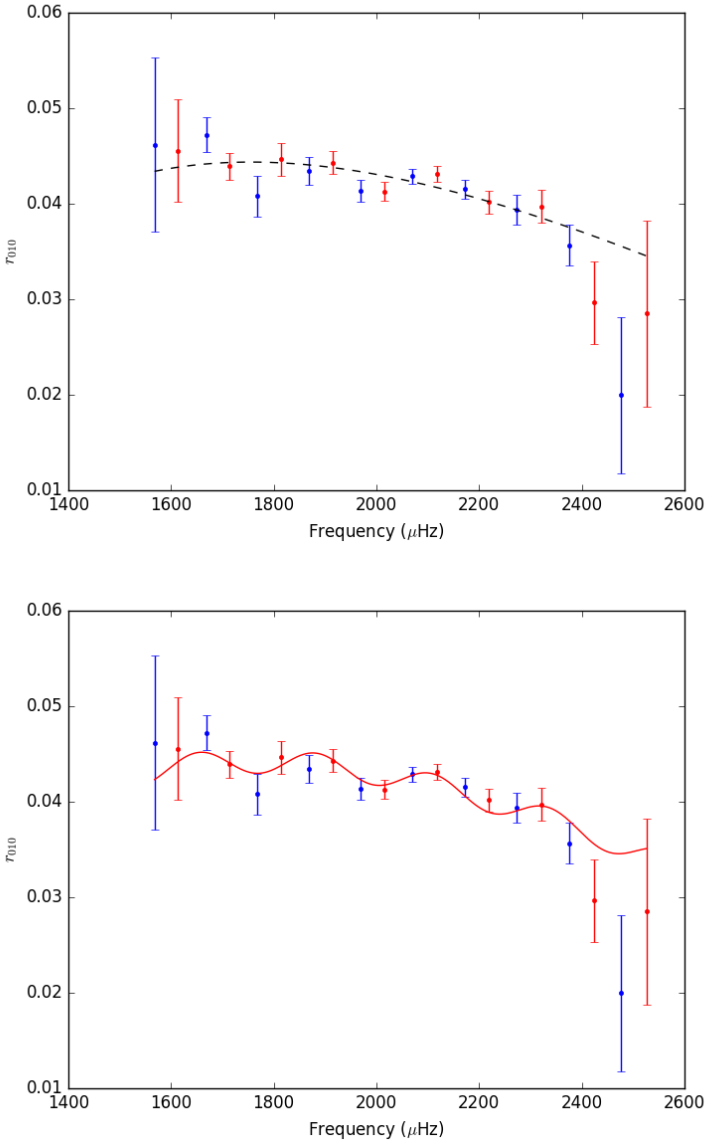

Figure 4.4: Upper panel: Fit for the *ck* values with k = 2 for the frequency ratios of KIC 11295426 without using the oscilatory component of equation 4.23. Lower panel: Fit using the full expression shown in equation 4.23.

4.4 Code Validation

We tested our code by using solar frequencies and artificial stellar data. This is important before applying the code to *Kepler* stars.

4.4.1 Solar frequencies

We use low-degree solar frequencies, obtained from the BoSON network presented in Broomhall et al.(2009) and compare with results of previous works. The data used here correspond to a set of 79 modes with l = 0,1,2 and 3 and with a mean uncertainty of 0.032 μHz. Our results when using second differences are presented in figures 4.5 and 4.6. Our estimation of the acoustic depth of the convective zone and the second helium ionization zone are $\tau_{\rm BCZ} = 2276 \pm 3.46s$ and $\tau_{\rm HIZ} = 635 \pm 0.60s$, respectively.

Houdek and Gough (2007) made a more complete fit using 197 modes with $5 < l < 20$, using a more elaborated expression to fit the signature to data from GOLF and BiSON, obtaining a estimation of $\tau_{\rm BCZ} = 2337s$ and $\tau_{\rm HIZ} = 649s$. Verma (2014) used a fit to the second difference using BiSON frequencies of low degree modes (l = 0,1,2 and 3). The values obtained are $\tau_{\rm BCZ} = 2323 \pm 4s$ and $\tau_{\rm HIZ} = 707 \pm 1s$ (see Table 1 in Verma, 2014).

We also used a limited number of solar frequencies with increased error bars, in order to simulate the data obtained in stars observed by *Kepler* (see figure 4.7). Our results for the acoustic locations of the glitches are: $\tau_{\rm BCZ} = 2335 \pm 230s$ and $\tau_{\rm HIZ} = 758 \pm 38s$ when using second differences and $T_{\rm BCZ} = 1477 \pm 194$ when using frequency ratios. In figure 4.10, we compare this analysis of restricted solar frequencies with the predictions of acoustic locations retrieved from the solar model presented in Christensen-Dalsgaard et al. (1996). This solar model in particular used strong seismic constraints during calibration.

The results presented above can be considered to be a successful validation of our code. Our estimations based on second differences are close to values mentioned in the literature, and a perfect agreement is not to be expected since different frequency sets, different fitting equations and different methods were used.

As a final test, we show how the use of diffusion on solar models might affect the location of the base of the convective zone. The solar models used for this comparison were computed with the CLÉS code (Scuflaire et al., 2008). To ascertain the value of $T_{\rm BCZ}$ in the models, we used the derivative of the sound speed $dc/d\tau$. Results can be found in table 4.1.

4.4.2 Artificial stars

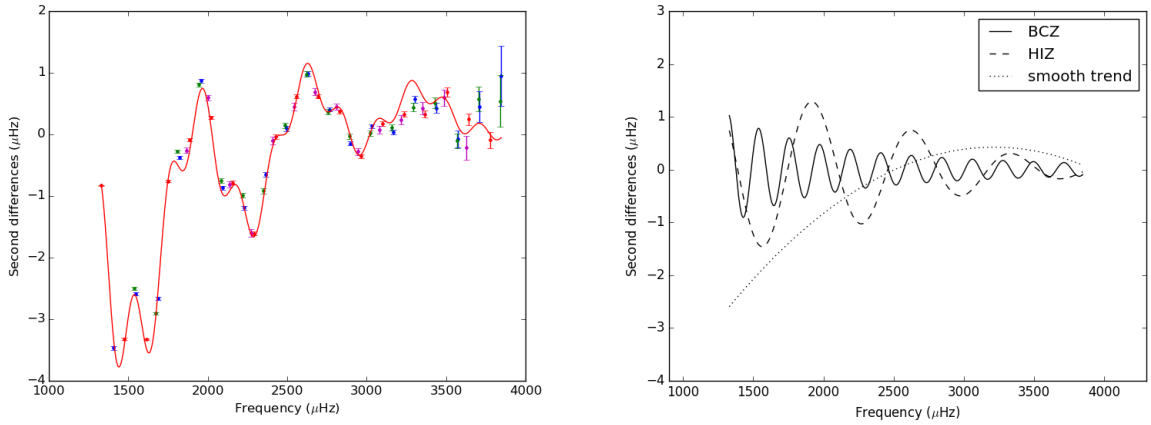

Figure 4.5: Left: Fit to the solar frequencies using second differences. Blue dots represent $l = 0$ modes, red dots represent $l = 1$, green dots represent $l = 2$ and magenta represents $l = 3$. This color convention is going to be adopted for the rest of the chapter. The solid red line show the best fit obtained by MCMC. Right: Individual components from the base of the convective zone (BCZ - solid line), the second helium ionization zone (HIZ - dashed line), and the smoothing trend. For solar frequencies, we did not use a constant term for the smooth component due to the large range in frequencies (≈ 3000 μHz). A second degree polynomial is used instead and it does not interfere with the HIZ component.

We conducted further tests on a set of 10 solar-type stellar models used in a hares-and-rounds exercise presented in Reese (2016). Our objective, as in the solar case, is to ascertain the effectiveness of our MCMC fitting algorithm, this time applied to models that mimic the observational properties and frequencies of stars observed by *Kepler*. In terms of global "observed" properties, the models have a range of 5735 to 6586 K in effective temperature, 0.73 to 4.36 $L_\odot$ in luminosity, and 0.78 to 1.33 $M_\odot$ in mass (see Table 4.2). This covers the part of the HR diagram where solar-like oscillations are detected in main sequence and sub-giant stars.

In this exercise, we acted as one of the 'hounds' designed to obtain estimations of the acoustic location of the base of the convective zone and the second helium ionization zone of the artificial stars (or 'hares'). As such, we initially received only their 'observational' properties, which, in our case, translates as the models frequencies with additional perturbations that try to replicate realistic noise levels observed by *Kepler*. After obtaining our estimations, we latter received the 'exact' frequencies together with structure files containing the exact location of BCZ and HIZ.

Our results can be found in Appendix A and Table 4.3. We should point that, in most stars, the phase angle of the oscillatory term related to the base of the convective envelope, $\phi_{\rm BCZ}$, gives a posterior distribution that is not very informative, often returning the prior

Table 4.1. Comparison of acoustic radius of the base of the convective envelope (T_{BCZ}) in solar models with and without diffusion and with different chemical mixtures: GN93 from Grevesse & Noels (1993) and AGS05 from Asplund et al. (2005)

Model ID	Mixture type	Diffusion	T_{BCZ} (s)
O1	GN93	Yes	1439
M1	AGS05	Yes	1469
D0	GN93	No	1485

Table 4.2. Fundamental properties of the artificial stars. T_{eff} is the effective temperature, L is the luminosity, M is the mass, R the radius and t is the stellar age.

ID	T_{eff} (K)	L ($L_\odot$)	M ($M_\odot$)	R ($R_\odot$)	t (Gyrs)
Aardvark	5735	0.89	1.00	0.815	3.058
Blofeld	5921	2.04	1.22	1.359	2.595
Coco	5914	0.73	0.78	0.815	9.616
Diva	5932	2.04	1.22	1.353	4.622
Elvis	5822	1.22	1.00	1.087	6.841
Felix	6256	4.07	1.33	1.719	2.921
George	6406	4.36	1.33	1.697	2.944
Henry	6400	1.95	1.10	1.138	2.055
Izzy	6390	1.95	1.10	1.141	2.113
Jam	6586	3.65	1.33	1.468	1.681

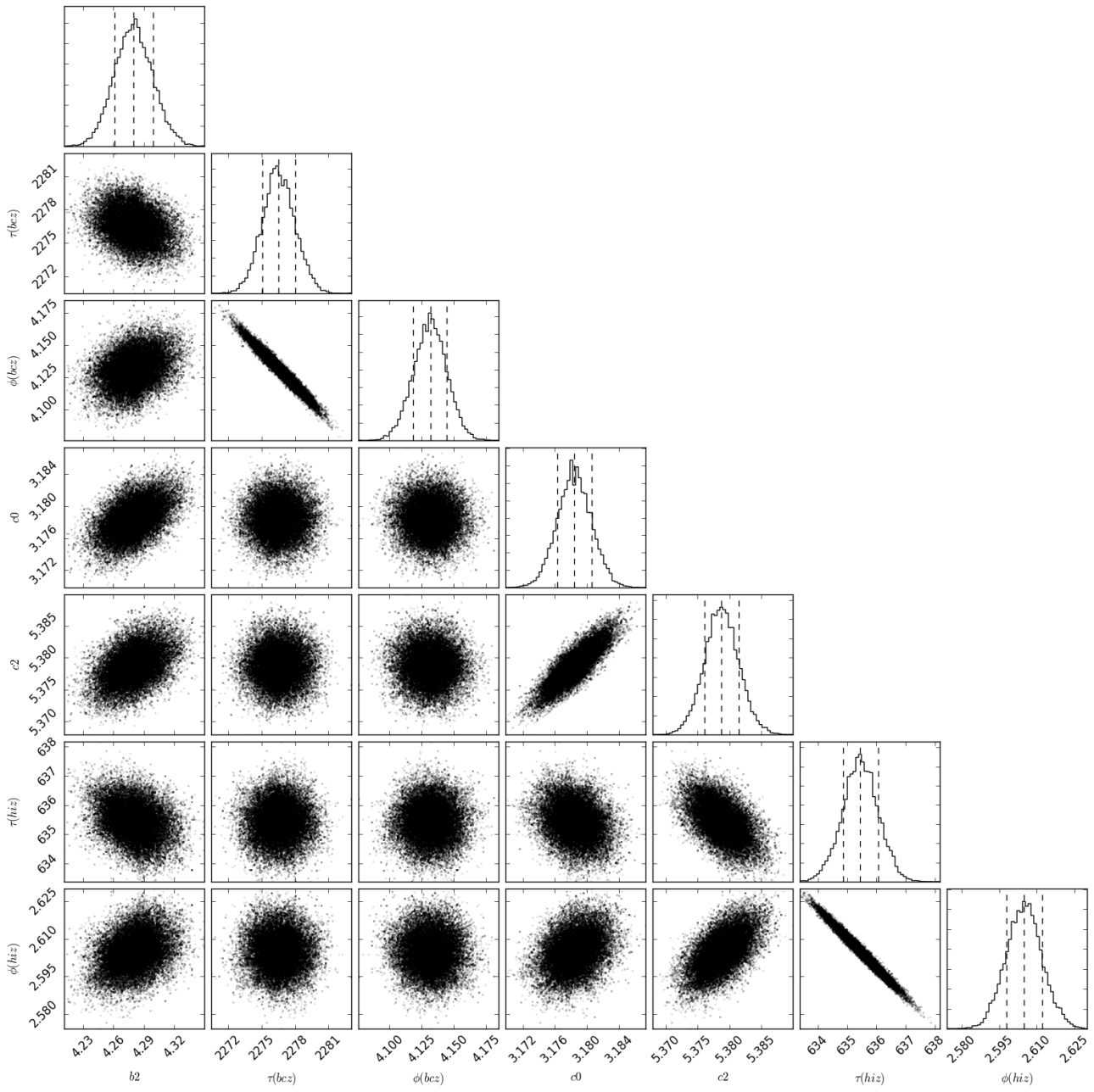

Figure 4.6: PDFs and fit for the second differences for the solar frequencies.

information (characterized by a flat distribution). We don't consider this to be a major issue since $\phi_{\rm BCZ}$ don't have a great impact on estimations of $\tau_{\rm BCZ}$ or $T_{\rm BCZ}$. Additionally, results presented in this thesis may differ from the ones published in Reese (2016) due to several improvements made on our MCMC algorithm since then.

In Appendix A, we compare our estimations of acoustic locations with the true values of the models. Our results agree well between both methods, except for a few cases. Particularly, the stars 'Diva', 'Felix', 'George' and 'Jam' proved to be problematic. This, however, is pointed in Reese (2016), where it is mentioned that those three stars were challenging for the other 'hounds' as well, most probably due to their higher mass and

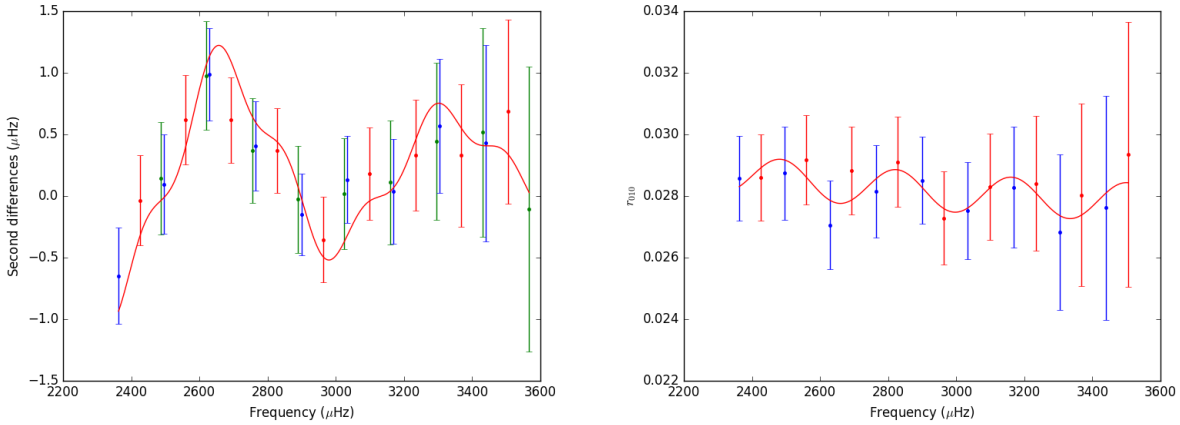

Figure 4.7: Fit to the solar frequencies using a low number of frequencies with increased error bars. The color code used here are the same as presented in previous figures. Left panel: fit using second differences. Right panel: fit using frequency ratios.

temperature. Hotter stars have shorter mode lifetimes and larger error bars on their frequencies, and this has a major impact during the glitch analysis. Additionally, for those cases, the acoustic location of base of the convective zone obtained through the two different methods (fitting to $\Delta_2\nu$ and r_{010}) are not in good agreement between each other, and don't agree well with the 'true' model values. The bad estimation of the acoustic location of base of the convective zone in those stars may be due to the periodic component related to the Helium ionization zone being much larger that the component of the signal related to the base of the convective zone (see Appendix A). In this conditions, the low amplitude of the signal of the base of the convective zone may difficult estimations of the related acoustic location. Finally, we had access to the unperturbed frequencies and realised a new analysis using the same number of frequencies, obtaining results much closer to the model values.

Therefore, when analysing *Kepler* stars, we will consider a certain result for the acoustic location of the base of the convective zone to be robust when there is a good agreement between estimations obtained with both methods, and without an over-dominance of the helium component.

4.5 Results for *Kepler* stars

For a first test using observed *Kepler* frequencies, we used the stars present in the paper of Mazumdar et al. (2014) and used the same modes in order to compare our estimations of acoustic locations with the values present on the paper. We consider this to be a fundamental step since the equations used in this work to fit the glitch signature to the second differences and frequency ratios are the same equations used in Mazumdar et al. (2014).

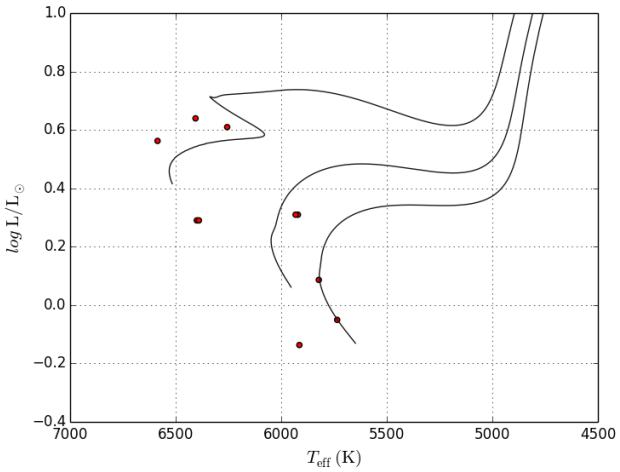

Figure 4.8: HR diagram with the artificial stars used to test our code (see table 4.2). The tracks used correspond to 1.0, 1.1 and 1.3 solar masses with solar metallicity.

Table 4.3. Comparison of acoustic radius of the base of the convective envelope ($T_{\rm BCZ}$) and the second helium ionization zone ($T_{\rm HIZ}$) by two independent methods for the artificial stars.

ID	T_0 (s)	$T_{\rm BCZ}$ (s)		$T_{\rm HeIIZ}$ (s)
		$\Delta_2\nu^1$	r_{010}	$\Delta_2\nu^1$
Aardvark	3342	1297 ± 129	1472 ± 250	2728 ± 24
Blofeld	5133	2614 ± 73	2876 ± 64	4385 ± 37
Coco	3107	1282 ± 124	1316 ± 327	2574 ± 75
Diva	5000	2493 ± 129	2879 ± 272	4195 ± 37
Elvis	4226	1793 ± 122	1737 ± 241	3516 ± 23
Felix	7142	3322 ± 184	3373 ± 275	5996 ± 69
George	7267	3138 ± 192	2791 ± 327	6560 ± 62
Henry	4251	2219 ± 163	1372 ± 292	3674 ± 57
Izzy	4363	1993 ± 113	2176 ± 326	3651 ± 56
Jam	5787	1357 ± 206	3257 ± 370	5063 ± 96

[1]When using second differences ($\Delta_2\nu$), we actually estimate the acoustic *depth*, $\tau_{\rm BCZ}$ ($\tau_{\rm HIZ}$), which has been converted to the corresponding acoustic radius, $T_{\rm BCZ}$ ($T_{\rm HIZ}$) using the T_0 value derived from the average large separation.

Table 4.4. Comparison of acoustic radius of the base of the convective envelope ($T_{\rm BCZ}$) and the second helium ionization zone ($T_{\rm HIZ}$) by two independent methods for stars observed by *Kepler*.

KIC ID	T_0 (s)	$T^1_{\rm BCZ}$ (s)		$T^1_{\rm HeIIZ}$ (s)	$T^2_{\rm BCZ}$ (s)		$T^2_{\rm HeIIZ}$ (s)
		$\Delta_2\nu$	r_{010}	$\Delta_2\nu$	$\Delta_2\nu$	r_{010}	$\Delta_2\nu$
6603624	4549	1455 ± 139	1275 ± 298	3648 ± 36	1315^{+133}_{-438}	1262^{+171}_{-171}	3652^{+36}_{-37}
6933899	6963	2865 ± 86	2964 ± 105	5653 ± 48	2848^{+74}_{-65}	2949^{+107}_{-107}	5648^{+54}_{-45}
8006161	3353	1167 ± 44	1085 ± 45	2832 ± 70	1167^{+35}_{-39}	1184^{+30}_{-30}	2845^{+80}_{-101}
10963065	4882	2030 ± 61	2079 ± 86	4030 ± 25	2028^{+47}_{-42}	2030^{+112}_{-112}	4031^{+24}_{-28}
11244118	7012	2196 ± 138	2141 ± 95	5513 ± 38	2168^{+246}_{-133}	2161^{+125}_{-125}	5506^{+41}_{-33}
16CygA[3]	4828	1716 ± 48	1695 ± 139	3921 ± 9	1749^{+34}_{-34}	...	3909^{+9}_{-9}
16CygB[3]	4273	1556 ± 92	1903 ± 217	3381 ± 12	1721^{+147}_{-147}	...	3453^{+17}_{-17}

[1]This work.

[2]Literature values from Mazumdar et al. (2014)

[3]Results for 16 CygA and 16CygB were compared with the estimations presented in Verma (2014).

Results are shown in Table 4.4 and agree remarkably well. We also consider important to conduct tests on two of the brightest stars in the *Kepler* field, 16 CygA and 16CygB, which are not presented in the work done by Mazumdar et al. (2014). We used instead the work of Verma (2014), from which we used the same frequencies to run tests for 16 CygA and 16CygB. However, Verma (2014) did not use frequency ratios r_{010}.

After comparing our results with previous works, we conducted a glitch analysis on a group of 13 planet-hosting stars observed by *Kepler*, where we used both $\Delta_2\nu$ and r_{010} to estimate the acoustic locations of the glitches. All relevant results and plots are presented in Appendix A and Table 4.6.

To ascertain if our results are consistent with estimations obtained by stellar models, we used 12 models obtained with the Yale Stellar Evolution Code (YREC - Demarque et al. 2008), which is described by Silva Aguirre et al. (2013). Those models don't include the effects of diffusion. For KIC 3632418, we could not compute a model that had initial helium abundance larger than the primordial helium abundance. The procedure used to model the stars was to fit the observed frequency ratios as described in Silva Aguirre et al. (2015). These models reasonably reproduce the observed average seismic and spectroscopic properties of the stars. On figure 4.10, we compare the fractional acoustic radii of the base of the convective zone and the second helium ionization zone obtained from the

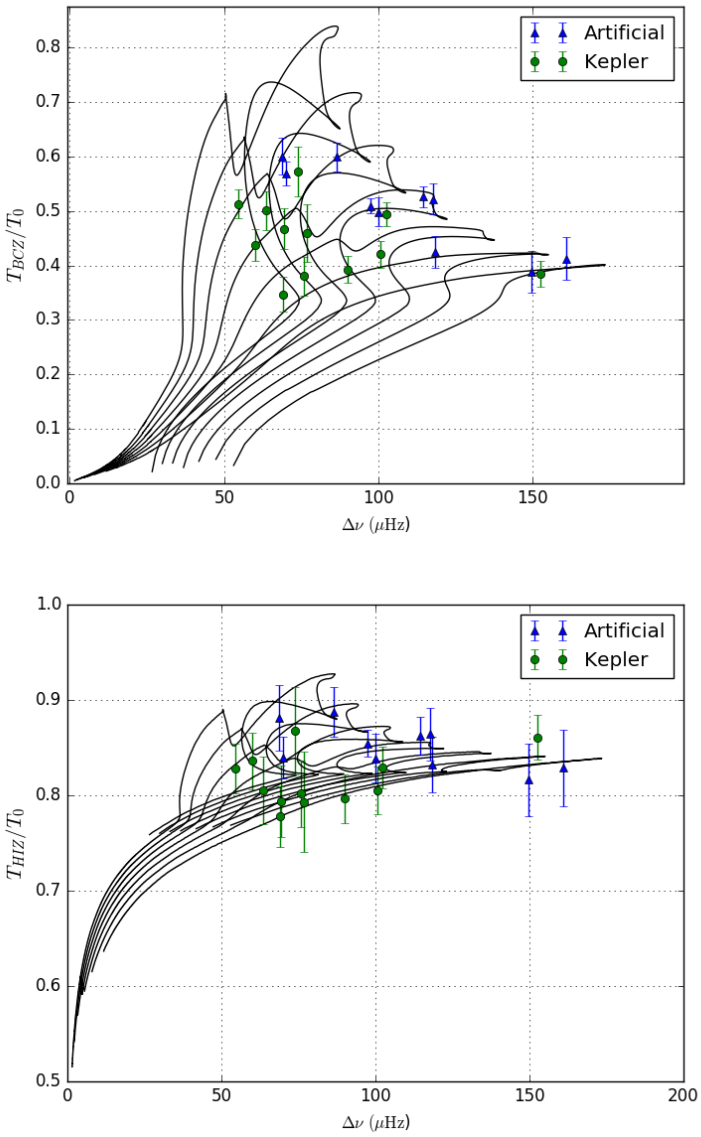

Figure 4.9: Upper panel: fractional acoustic radii of the BCZ versus the large separation $\Delta\nu$. Coloured symbols represent estimations of $T_{\rm BCZ}$ obtained using second differences. Blue triangles correspond to results for the artificial stars, and green circles are results for *Kepler* stars. The solid black lines are models computed using the CLÉS evolutionary code (Montabán et al. 2008) with near solar metallicity and masses that range from $1.0M_{\odot}$ to $1.6M_{\odot}$ in steps of 0.1. Lower panel: same as the upper plot, but for the acoustic location of the helium ionization zone.

Table 4.5. Fundamental properties of the models obtained with YREC that best represents the observed *Kepler* stars.

ID	$T_{\rm eff}$ (K)	L ($L_\odot$)	M ($M_\odot$)	R ($R_\odot$)	t (Gyrs)
5094751	5993	2.09	1.08	1.34	6.62
6521045	5920	2.56	1.13	1.52	6.21
8077137	6110	3.48	1.19	1.66	4.83
8554498	5778	3.00	1.17	1.73	6.74
9414417	6276	4.89	1.28	1.87	3.42
9592705	6195	6.27	1.63	2.17	1.72
9955598	5432	0.60	0.88	0.88	7.28
10666592	6323	5.75	1.54	2.00	1.63
10963065	6158	1.93	1.06	1.22	5.02
11295426	5775	1.57	1.11	1.26	6.85
11401755	5954	3.02	1.07	1.63	7.19
11807274	6210	3.30	1.21	1.57	4.26

models with our model-independent estimations, obtained directly from the observed *Kepler* frequencies. The reason for basing our calculations in terms of acoustic radii instead of acoustic depth lies in the way that calculations are done. In a model, the acoustic radius of a glitch is computed from the center to the surface, eliminating the problematic effects of near surface layers that lie above the location of the glitch. Meanwhile, the acoustic depth will include the sound speed profile of the complex near-surface layers, since it is calculated from surface to core. Therefore, the acoustic radius is, in principle, a more robust quantity. We convert our estimations of acoustic depth $\tau_{\rm BCZ}$ (and $\tau_{\rm HIZ}$) using the relation $T_{\rm BCZ} = T_0 - \tau_{\rm BCZ}$ (or $T_{\rm HIZ} = T_0 - \tau_{\rm HIZ}$). T_0 can be obtained from the observed average large separation by the approximation $T_0 \approx (2\Delta\nu)^{-1}$. Additionally, on Appendix A, we made direct comparisons of acoustic radii using the derivative of the sound speed, $dc/d\tau$, for each star. The main properties of the YREC models can be found in Table 4.5.

We find, for most cases, a good agreement between the estimations of acoustic location of the base of the convective zone obtained using the two different methods, with the two values falling in the quoted 1σ error bars.

For the second helium ionization zone, our estimations of $T_{\rm HIZ}$ are, on average, smaller than the model values by $\sim$ 200s. This effect occur for the majority of the stars and might

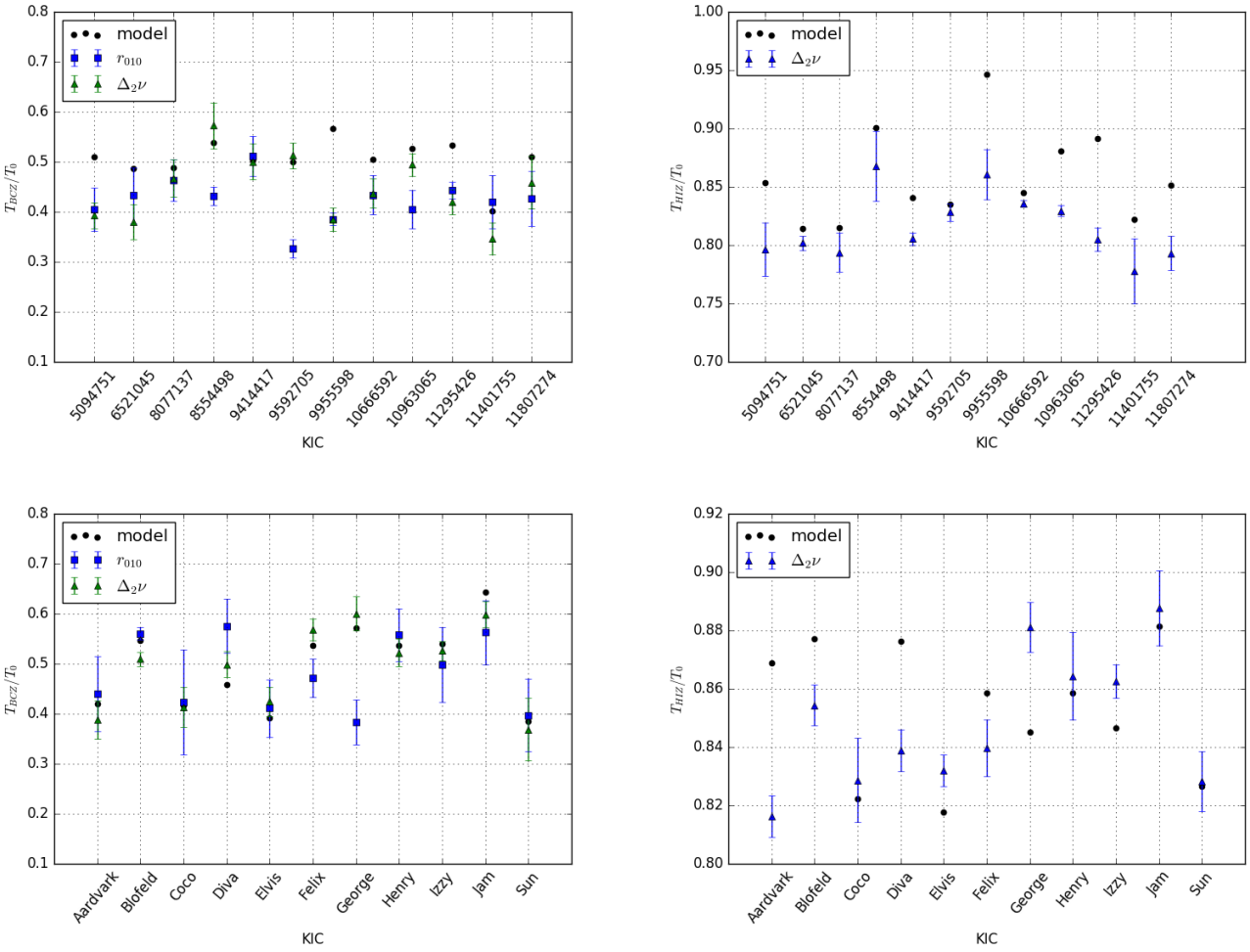

Figure 4.10: Upper left panel: Acoustic radius of the base of the convective zone ($T_{\rm BCZ}$) divided by the total acoustic radii (T_0). Such values were obtained from the oscillatory signal in the *Kepler* frequencies of 12 stars by using frequency ratios r_{010} (blue squares) and second differences $\Delta_2\nu$ (green triangles). Black dots represents the results from YREC models. Upper right panel: Same as left, this time showing results for the second helium ionization zone. Lower panels: same as the upper plots, but showing results for the artificial stars together with results obtained with a limited set of solar frequencies, or 'sun as a star' (see text). The black dots are the acoustic locations of the exact models for the artificial stars, and model S for the Sun (Christensen-Dalsgaard et al., 1996).

Table 4.6. Comparison of acoustic radius of the base of the convective envelope ($T_{\rm BCZ}$) and the second helium ionization zone ($T_{\rm HIZ}$) by two independent methods for stars observed by *Kepler*

KIC ID	T_0 (s)	$T_{\rm BCZ}$ (s)		$T_{\rm HeIIZ}$ (s)
		$\Delta_2\nu^1$	r_{010}	$\Delta_2\nu^1$
3632418	7765	2179 ± 140	2244 ± 241	4421 ± 127
5094751	5551	2182 ± 159	2242 ± 241	4418 ± 130
6521045	6597	2509 ± 231	2855 ± 369	5289 ± 39
8077137	7205	3376 ± 273	3337 ± 300	5718 ± 120
8554498	6775	3879 ± 311	2924 ± 124	5881 ± 203
9414417	7852	3931 ± 270	4016 ± 310	6325 ± 42
9592705	9183	4707 ± 241	3000 ± 174	7606 ± 70
9955598	3279	1265 ± 76	1264 ± 39	2819 ± 70
10666592	8337	3558 ± 249	3618 ± 325	6969 ± 24
10963065	4883	2413 ± 107	1926 ± 174	4050 ± 22
11295426	4963	2085 ± 124	2200 ± 81	3995 ± 50
11401755	7465	2513 ± 231	3046 ± 383	5645 ± 203
11807274	6486	2907 ± 342	2774 ± 361	5158 ± 97

[1]When using second differences ($\Delta_2\nu$), we actually estimate the acoustic *depth*, $\tau_{\rm BCZ}$ ($\tau_{\rm HIZ}$), which has been converted to the corresponding acoustic radius, $T_{\rm BCZ}$ ($T_{\rm HIZ}$), using the T_0 value derived from the average large separation.

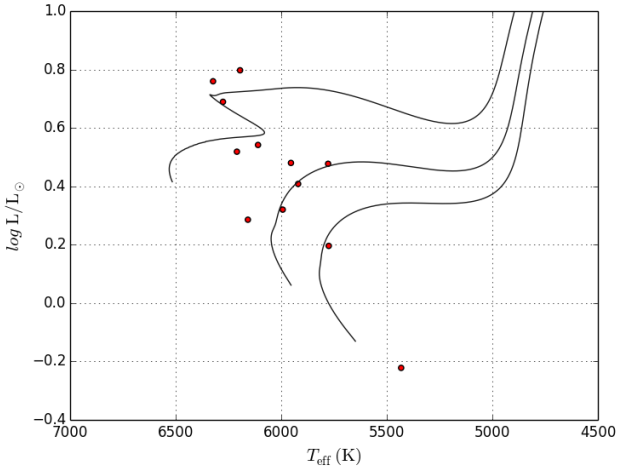

Figure 4.11: HR diagram with the YREC model that best represents the observed *Kepler* stars (see table 4.5). The tracks used correspond to 1.0, 1.1 and 1.3 solar masses with solar metallicity.

be explained by the fact that the helium ionization zone covers a certain range in stellar radius, being difficult to pinpoint a exact location, while the base of the convective zone is defined as a specific layer within the star. Additionally, this might be due to MCMC returning the local maxima in the first adiabatic index Γ_1 instead of the local minima, as discussed in Broomhall et al. (2014). To test this, we defined the acoustic location of the second Helium ionization zone as the local maxima in Γ_1 and in the derivative of the sound speed, $dc/d\tau$. When this change is adopted, the difference between the MCMC results and the model values is reduced to $\sim$ 150s (see figure 4.10). Also, the MCMC estimation for $\tau_{\rm HIZ}$ using solar frequencies agrees almost perfectly with Model S, a solar model created using observed seismic values as additional hard constraints during calibration (see Christensen-Dalsgaard et al., 1996, for more details).

Here we discuss results of 9 specific stars.

- KIC 9414417 and KIC 8077137: they are both low mass stars ($M_{model} = 1.28 M_\odot$ and $M_{model} = 1.19 M_\odot$, respectively) in the main sequence. Our estimations of $\tau_{\rm BCZ}$ and $T_{\rm BCZ}$ agree remarkably well and are very close to the model values. $\tau_{\rm HIZ}$ is also close to model values.

- KIC 8554498, KIC 9592705 and KIC 10963065: estimations for $\tau_{\rm BCZ}$ and $T_{\rm BCZ}$ do not agree well. The $T_{\rm BCZ}$ obtained by using frequency ratios produce a peak in the posterior distribution, but at a point where it is unlikely to correspond to the location of base of the convective zone. For KIC 8554498, $\tau_{\rm BCZ}$, obtained using second differences, has values close to the models. However, KIC 9592705 and KIC 10963065 has values of $\tau_{\rm HIZ}$ that are roughly $\sim$ 200s off the value obtained by models.

- KIC 5094751, KIC 9955598, KIC 10666592 and KIC 11295426: our estimations of $\tau_{\rm BCZ}$ and $T_{\rm BCZ}$ are systematically lower when compared with model results. However, we consider our estimations of BCZ to be robust since there is an excellent agreement between both methods.

The remaining three stars have estimations of BCZ that agree between the two different methods and the model values within 1σ error bar.

4.6 Conclusion

We conducted tests in the frequencies of 13 stars observed by the *Kepler* space telescope. We focus our attention on the oscillatory signals that arises in the frequencies due to variations of the sound speed in the stellar interior. Such signals can be used to locate the acoustic glitches related to the base of the convective zone and the second helium ionization zone. We used two independent methods to extract the signals from the second differences and from the frequency ratios. We have found remarkable agreement between estimation of acoustic location of BCZ made with the two methods, except for discrepancies found in three cases. We used theoretical evolutionary models to compare our values of the acoustic radii of the glitches extracted from the observed frequencies. For the majority of the stars, estimations of the location of the glitch are close to model values within the quoted 1σ errorbars.

The results presented here help to confirm the validity of the method. However, the use of the glitch analysis is more powerful when combined with stellar models to place an additional observable parameter to be fitted in calibrations. Furthermore, results obtained here form the basis for further work: determining the location of the base of the convective zone will help to constrain the modelling of convection (e.g. Christensen-Dalsgaard et al., 2011), and the amplitude of the oscillatory signal associated with the helium ionization zone can be used to estimate of the amount of helium in the stellar envelope (e.g. Miglio et al., 2013a; Basu et al., 2004; Monteiro & Thompson, 2005; Houdek and Gough, 2007).

Chapter 5

Conclusions and prospects

In this thesis we report a variety of tests where asteroseismology was used to obtain direct and indirect estimations of key stellar parameters. We have used indirect seismic inferences of global stellar parameters in the form of scaling relations and seismic distances. We have also obtained direct, model-independent measurements of regions of structural stratification retrieved from observed *Kepler* frequencies. Comparing our results with stellar models yields a reasonably good agreement in general. However, in a few cases, reveals their limitations in some aspects. Bellow we give a brief review of the projects presented in this thesis, together with plans for continuing the work.

We conducted a detailed test on the scaling relation used for the parameter $\nu_{\rm max}$, defined as the frequency of maximum amplitude in a power spectrum. The classic scaling relation assumes that $\nu_{\rm max}$ scales with surface gravity and effective temperature according to $gT_{\rm eff}^{-1/2}$. We have explored the origins of this relation in the form of the acoustic cut-off frequency ν_{ac} and the thermal frequency τ^{-1}. We used the Mach number defined in the super-adiabatic layers of stellar models to derive an approximation for $\nu_{\rm max}$, and compared it to the values obtained from the classic scaling relation. We have tested how well the detected oscillations in a large sample of solar-type stars observed by the *Kepler* Mission adhere to classic scaling relation relation by comparing the observed $\nu_{\rm max}$ of the stars with independent estimates of the combination $g\,T_{\rm eff}^{-1/2}$. Our results rule out departures from the classic $\nu_{\rm max}$ scaling at the level of $\simeq 1.5$ percent over the full $\simeq 1560$ K range in $T_{\rm eff}$ that we tested. There is some uncertainty over the absolute calibration of the scaling, but any variation with $T_{\rm eff}$ is evidently small, with limits similar to those above.

In the future we plan to extend this analysis using a grid of red-giant stars, and see how the classic scaling relation behaves on both the ascending RGB stage and in the core helium-burning phase.

We presented our results for the analysis of a group of 10 nearby red giants observed by *Kepler* and with accurate values of parallaxes obtained by *Hipparcos*. We combined seismic and spectroscopic parameters to conduct our analysis. We made tests using the

seismic estimations of global parameters and compared results with stellar models. Results show a good agreement between different grid-based pipelines. We also compared estimation of parallaxes obtained using seismic parameters with the observed *Hipparcos* values. We obtained a good agreement between both, however we point that our sample might be too small. In the context of constrained spectroscopic analysis using seismic $\log g$, and we have ascertained that using excitation balance wields slightly larger values of effective temperature for hotter ($T_{\rm eff} \geq 5000$) stars. Our results using iron ionization balance wields values of $T_{\rm eff}$ which are in good agreement with estimations of photometric $T_{\rm eff}$ obtained using seismic $\log g$. We compared the observed surface abundances of lithium and carbon with prediction made by models with and without extra mixing processes. The spectroscopic abundances have a better agreement with stellar models where significant mixing episodes are included in the calculations.

Our results are almost ready to be published, with a draft already circulating between our collaborators. We plan to further update our values of parallaxes using the data from the *Gaia* survey, which has been released during the final writing stages of this thesis. We plan to compare *Hipparcos* parallaxes with the values obtained from *Gaia*, and also to see how well the seismic inferences will agree with both values.

We also conducted tests in the frequencies of 13 stars observed by the *Kepler* space telescope. We focus our attention on the oscillatory signals that arises in the frequencies due to variations of the sound speed in the stellar interior. Such signals can be used to locate the acoustic glitches related to the base of the convective zone and the second helium ionization zone. We used two independent methods to extract the signals from the second differences and from the frequency ratios. We have found remarkable agreement between estimation of acoustic location of BCZ made with the two methods, expect for discrepancies found in three cases. We used theoretical evolutionary models to compare our values of the acoustic radii of the glitches extracted from the observed frequencies. For the majority of the stars, estimations of the location of the glitch are close to model values within the quoted 1σ errorbars. The results presented here help to confirm the validity of the method. However, the use of the glitch analysis is more powerful when combined with stellar models to place an additional observable parameter to be fitted in calibrations. Furthermore, determining the location of the base of the convective zone will help to constrain the modelling of convection (e.g. Christensen-Dalsgaard et al., 2011), and the amplitude of the oscillatory signal associated with the helium ionization zone can be used to estimate of the amount of helium in the stellar envelope (e.g. Miglio et al., 2013a; Basu et al., 2004; Monteiro & Thompson, 2005; Houdek and Gough, 2007).

The results presented in this thesis for the acoustic glitches in *Kepler* stars shall be condensed into a paper to be published. We also plan to extend our tests with stellar models, with particular attention to the acoustic location of the helium ionization zone. One of our main focus should be placed on the definition of the helium ionization zone in

the first adiabatic index Γ_1. Estimating this acoustic location in particular has proven to be problematic, with estimation obtained from the frequencies pointing to the local maxima of the $\Gamma 1$ profile instead of the local minima. We also need to further test how different physics in models will affect the acoustic locations of the glitches, especially the acoustic location of the base of the convective zone.

Appendix A

Fit Results from MCMC analysis

A.1 Results for Artificial Stars.

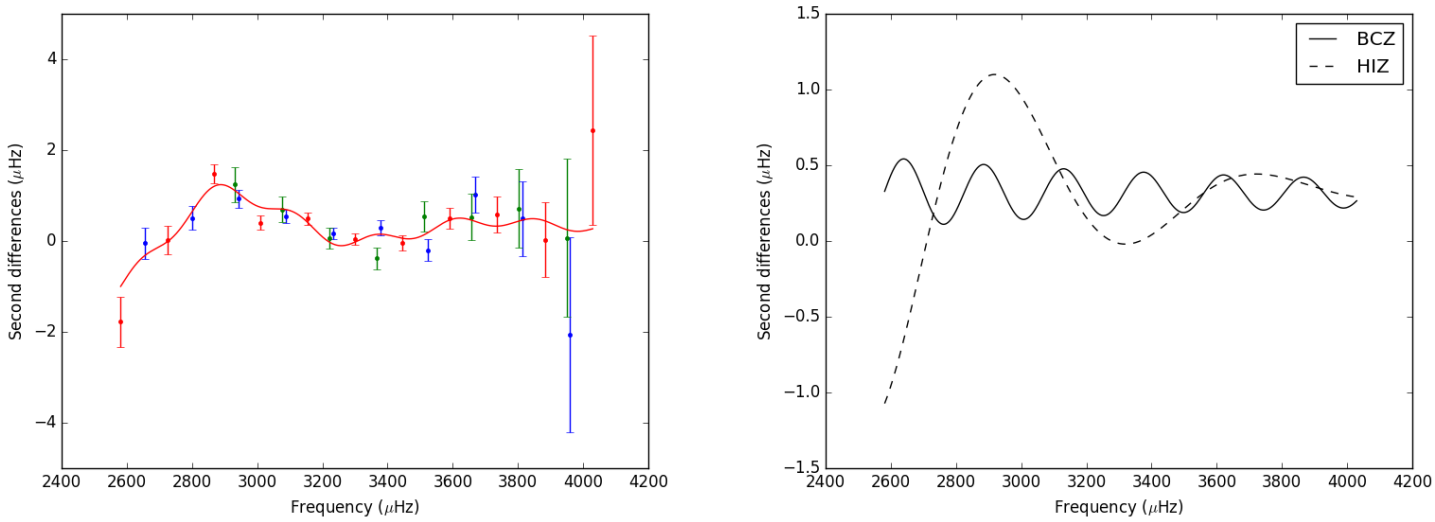

Figure A.1: Left panel: Second differences $\Delta_2\nu$ of the artificial star 'Aardvark'. The solid red line indicates the model containing the final fitted results. Right panel: individual components from the base of the convective zone (BCZ - solid line) and the second helium ionization zone (HIZ - dashed line).

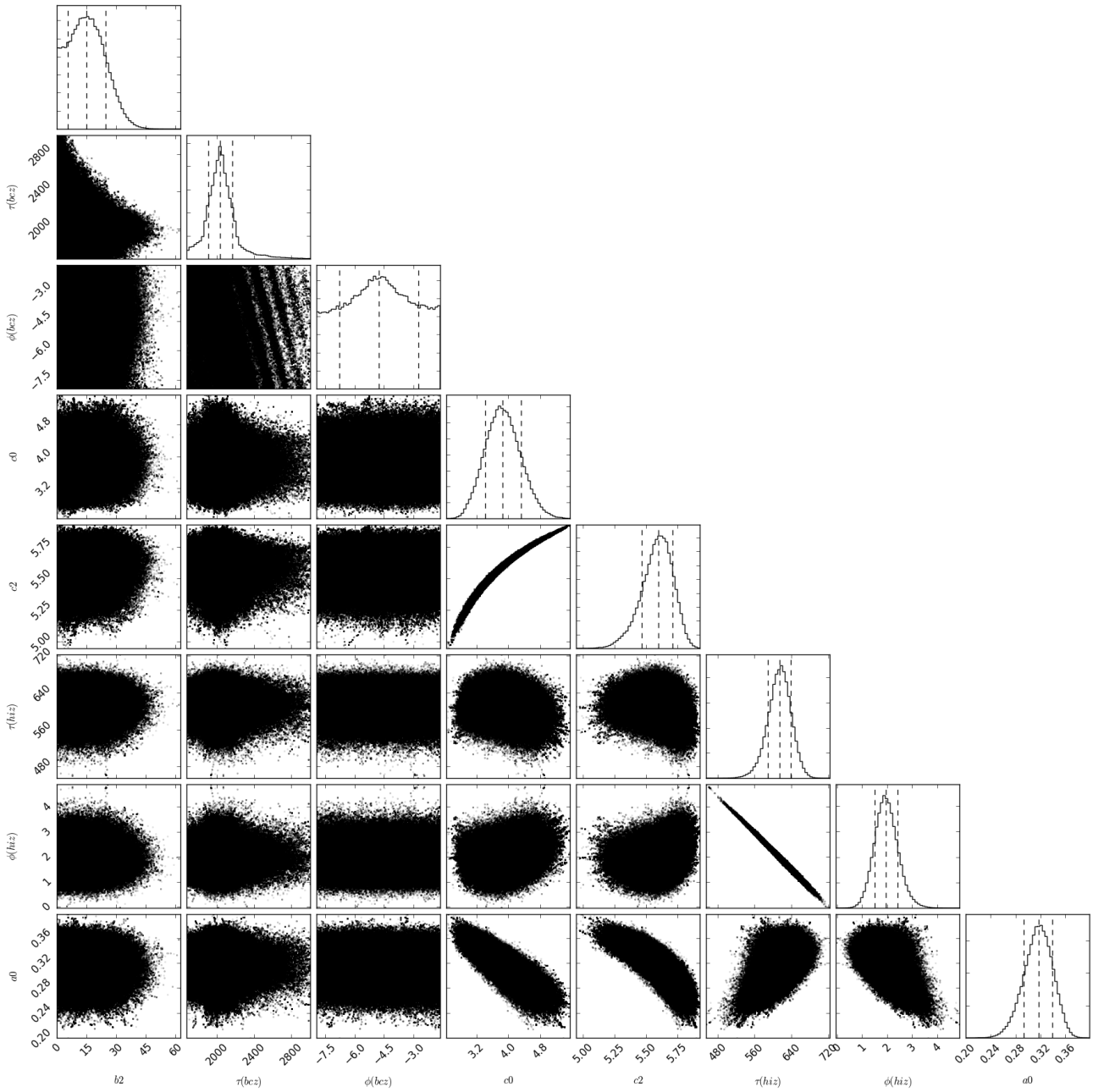

Figure A.2: Posterior distributions of all the free parameters. The vertical dashed lines indicates the 68%-level confidence interval. The distribution for the amplitude of the BCZ signal (far left column) is truncated at zero. The phase angle of the oscillatory term related to the base of the convective envelope, ϕ_{BCZ} (third column from left to right), gives a posterior distribution that is not very informative, often returning the prior information, characterized by a flat (or nearly flat) distribution.

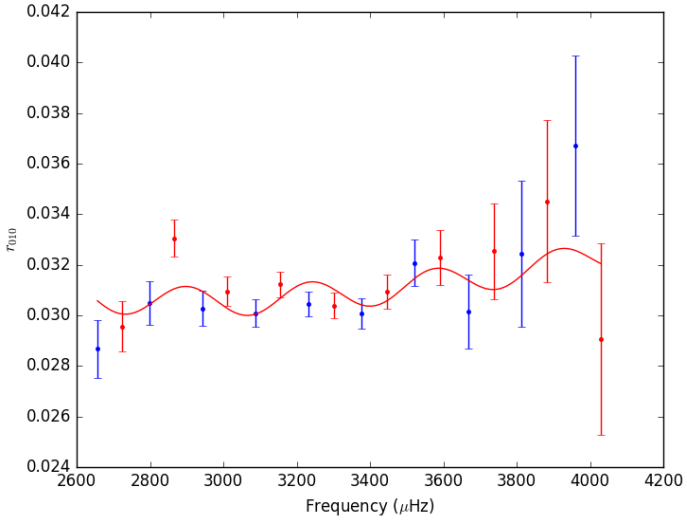

Figure A.3: Fit for the frequency ratios r_{010} for the artificial star 'Aardvark'. The solid red line indicates the model containing the final fitted results.

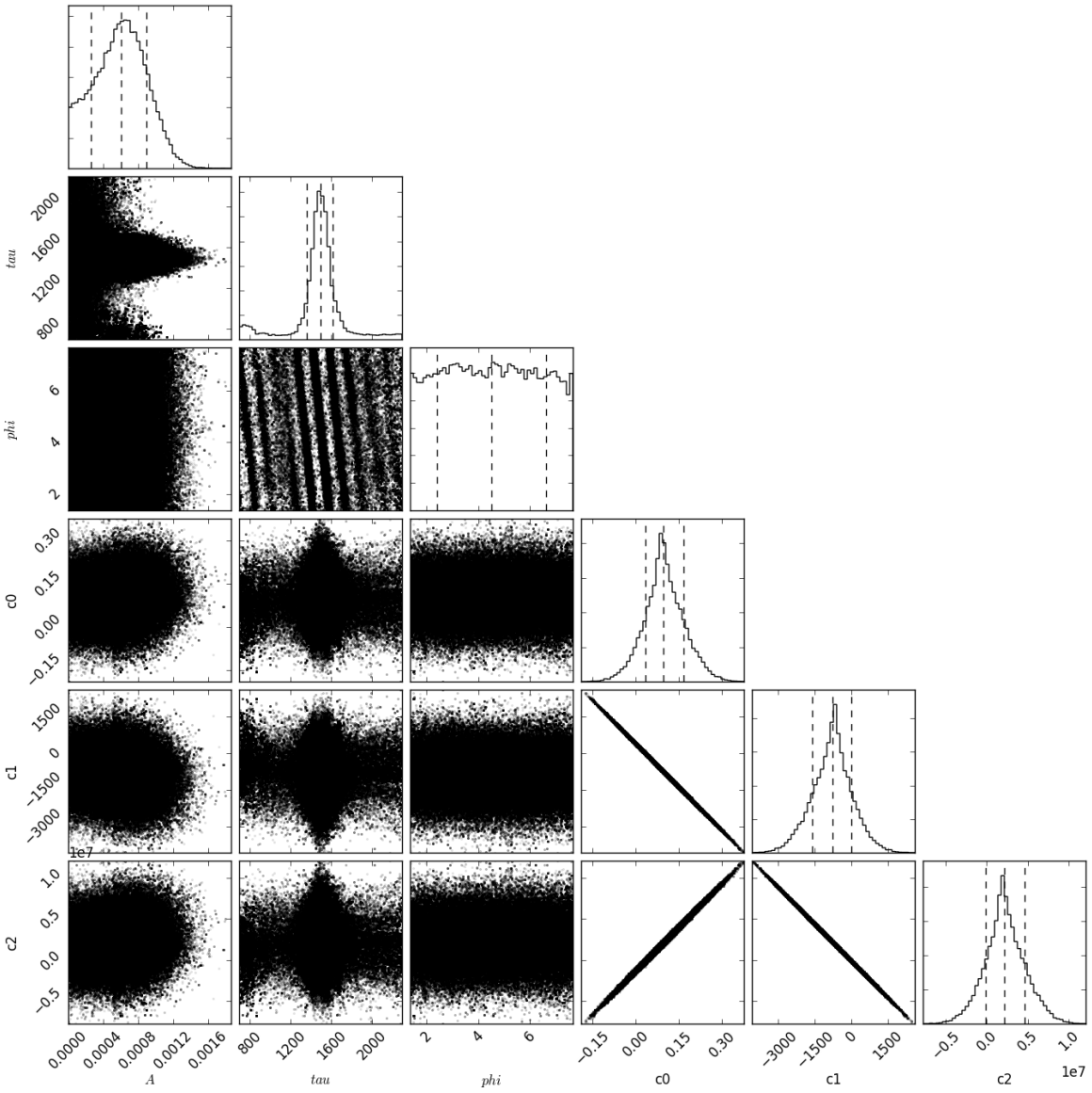

Figure A.4: Similar to A.2, but here we show the posterior distribution when using frequency ratios r_{010} for the artificial star 'Aardvark'.

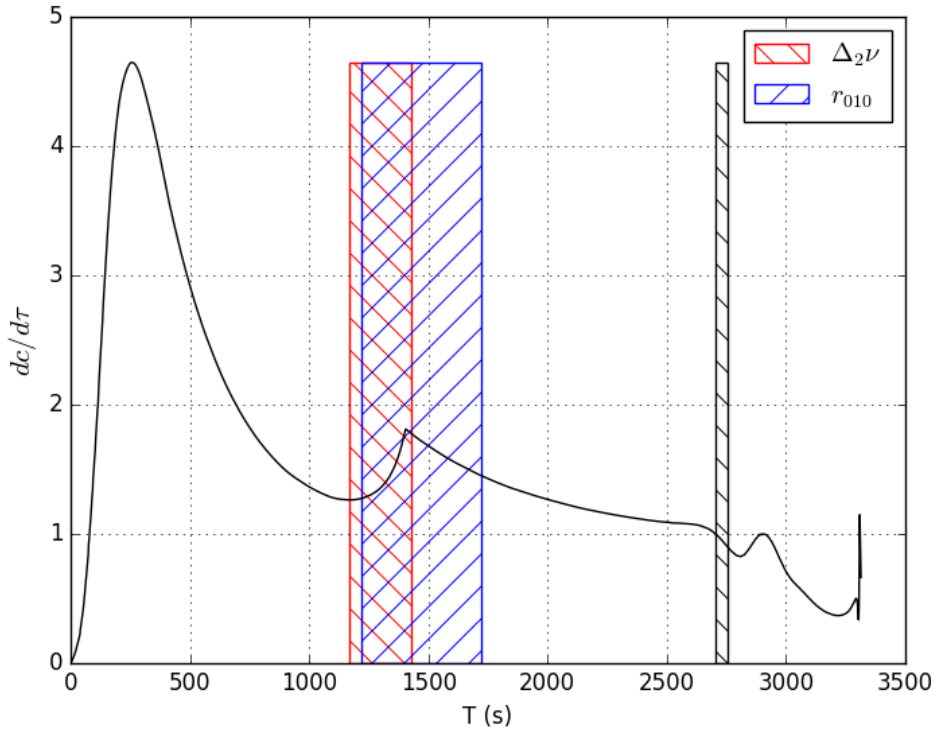

Figure A.5: $\frac{dc}{d\tau}$ versus acoustic radius for the artificial star 'Aardvark'. The coloured dashed rectangles represent our estimation of $T_{\rm BCZ}$ and $T_{\rm HIZ}$ using MCMC. The width of the rectangles represent the errorbars. The colour code is: black = $T_{\rm HIZ}$, red = $T_{\rm BCZ}$ obtained using $\Delta_2\nu$ and blue = $T_{\rm BCZ}$ obtained using frequency ratios r_{010}.

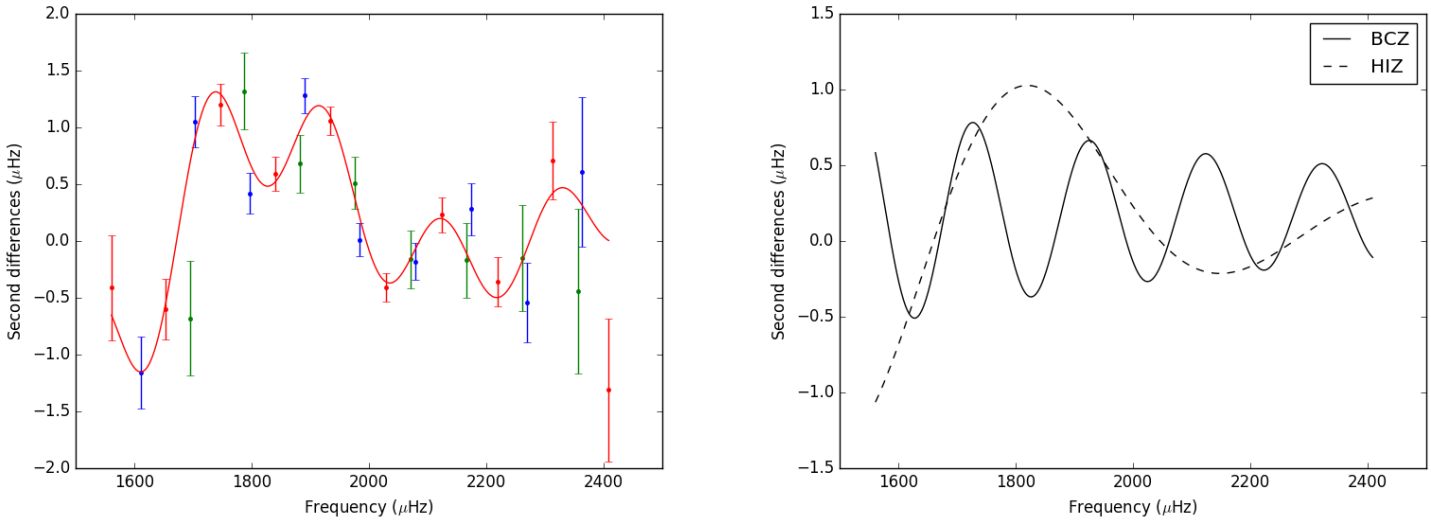

Figure A.6: Same as figure A.1, but for the artificial star 'Blofeld'.

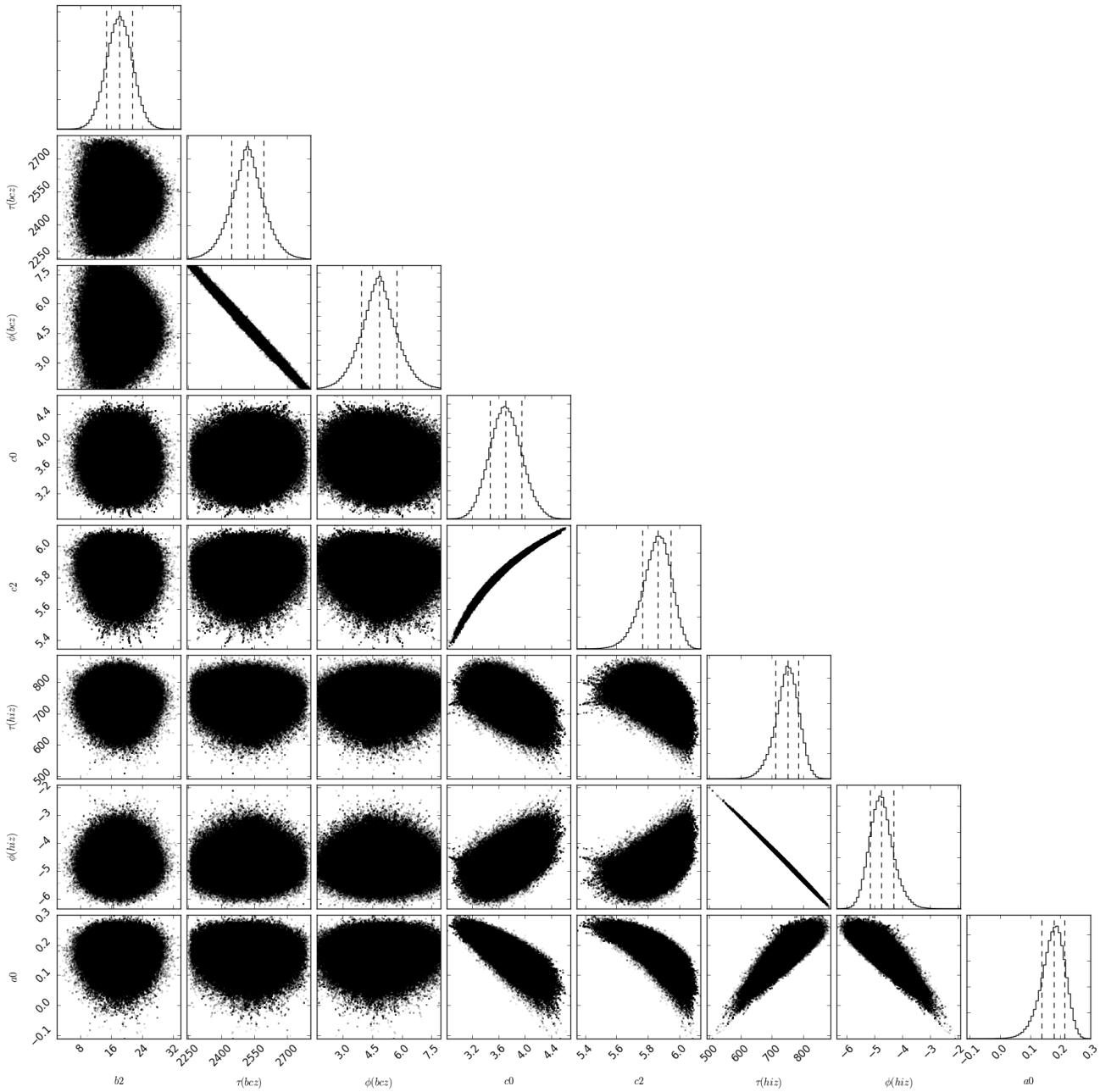

Figure A.7: Same as figure A.2, but for the artificial star ‘Blofeld’.

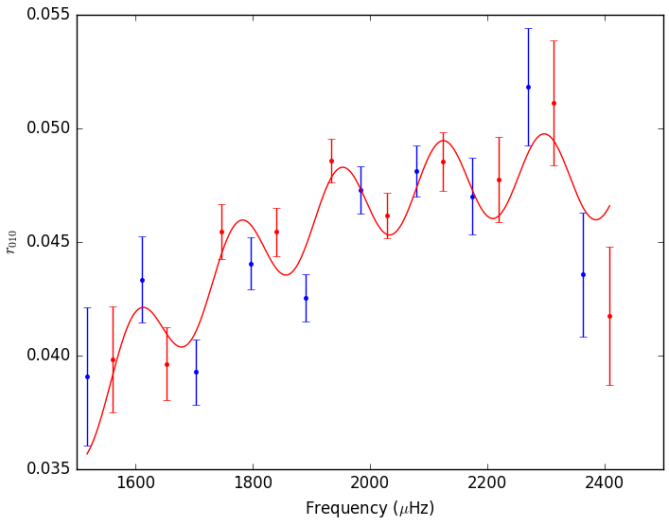

Figure A.8: Same as figure A.3, but for the artificial star ‘Blofeld’.

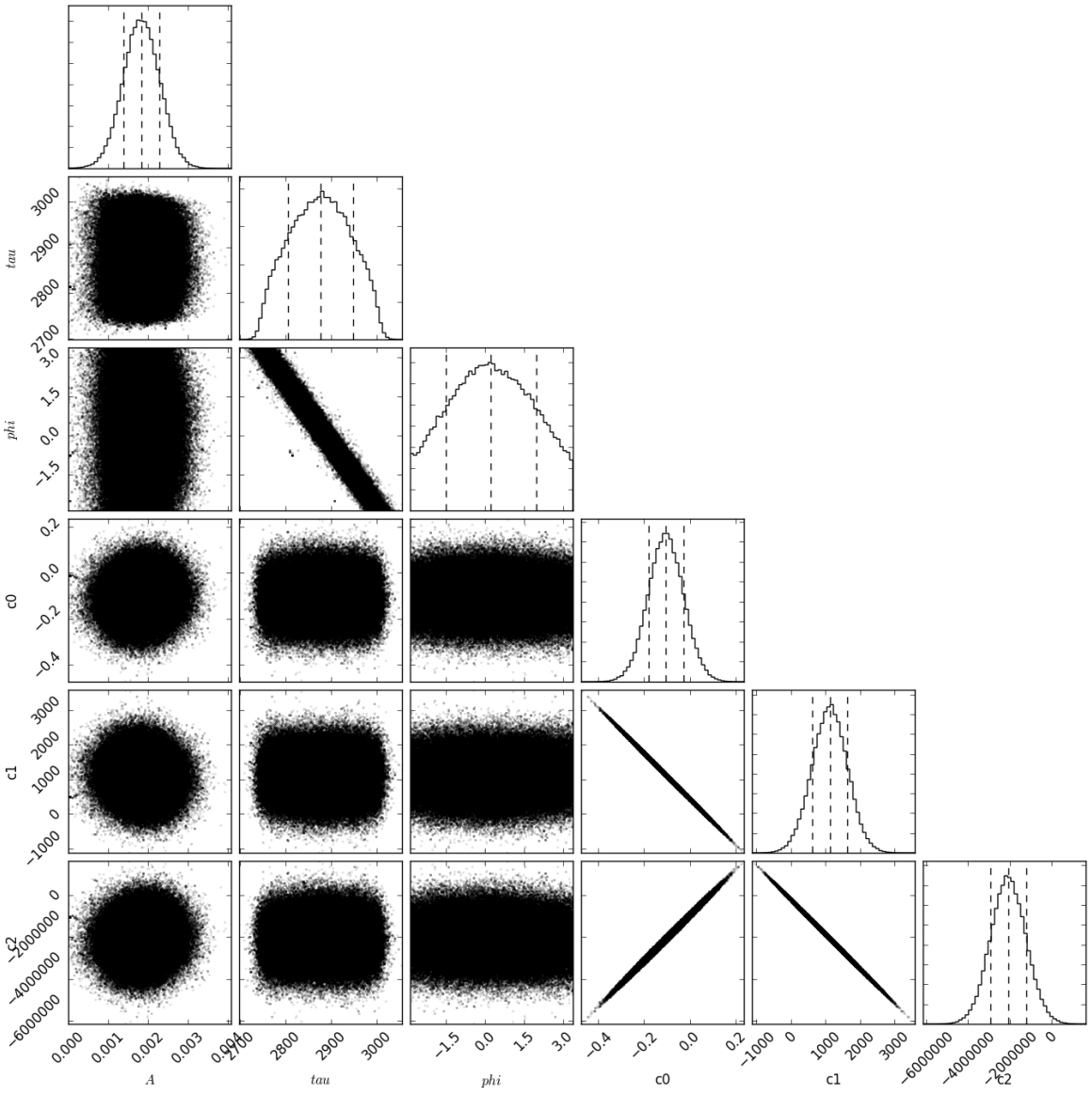

Figure A.9: Same as figure A.4, but for the artificial star ‘Blofeld’.

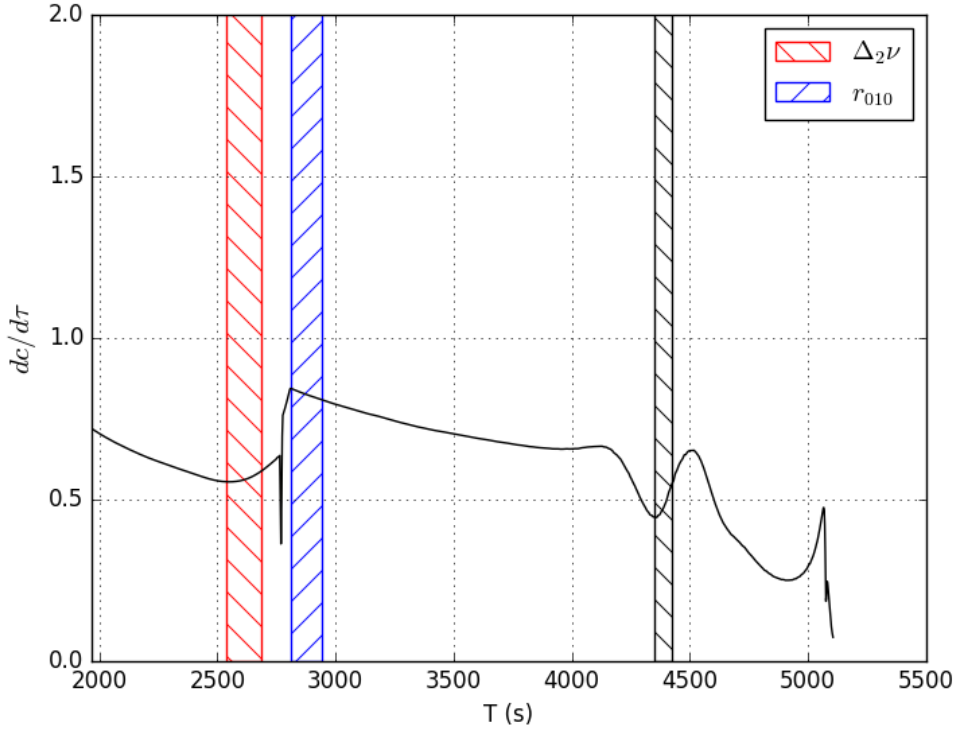

Figure A.10: Same as figure A.5, but for the artificial star ‘Blofeld’.

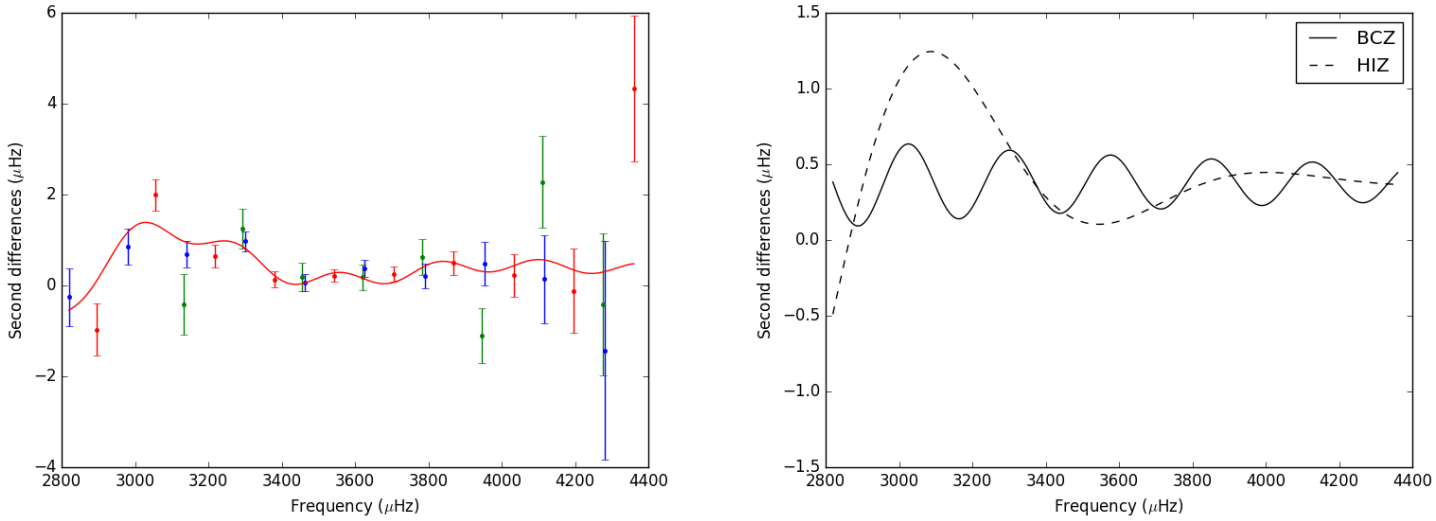

Figure A.11: Same as figure A.1, but for the artificial star ‘Coco’.

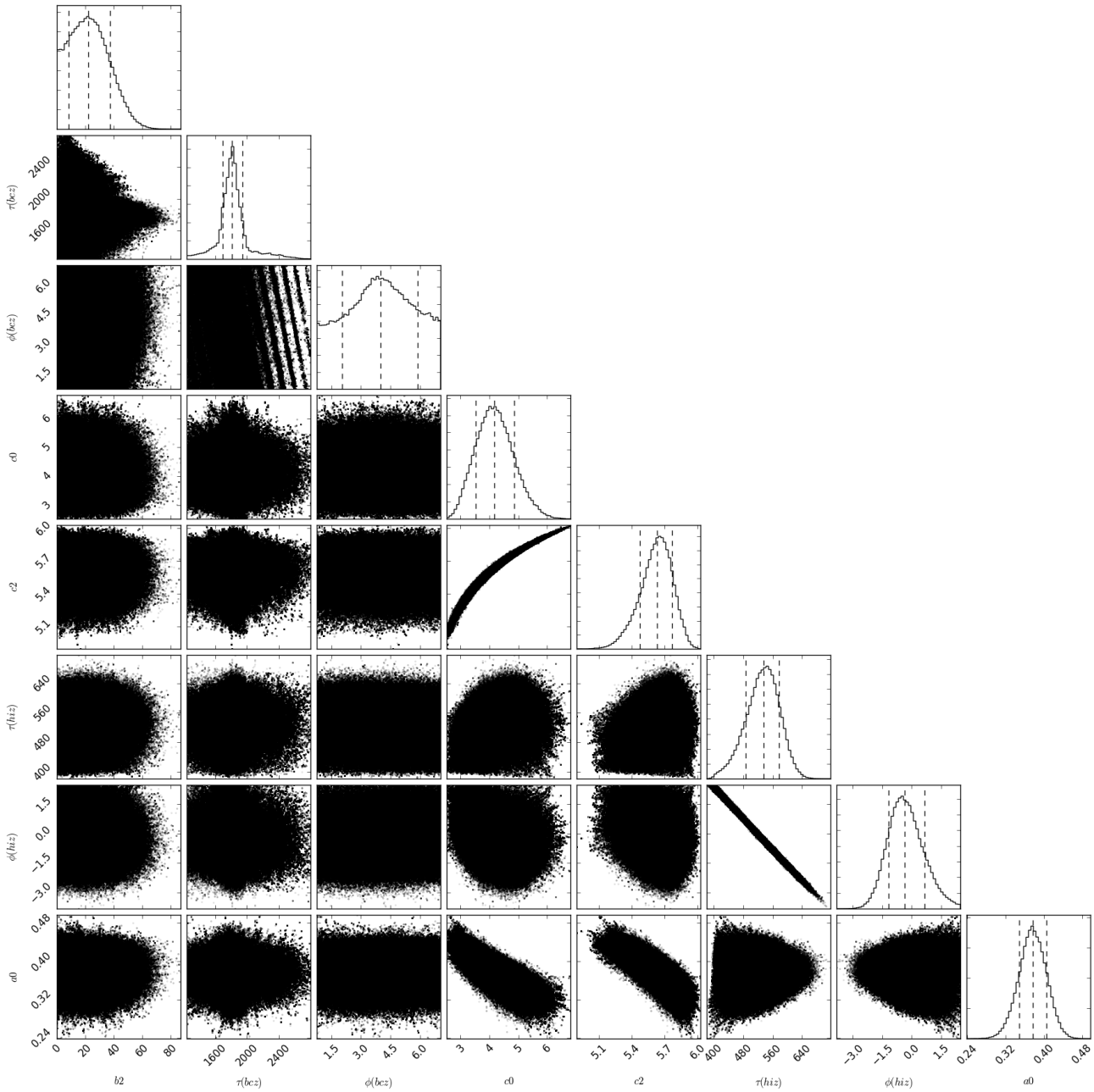

Figure A.12: Same as figure A.2, but for the artificial star ‘Coco’.

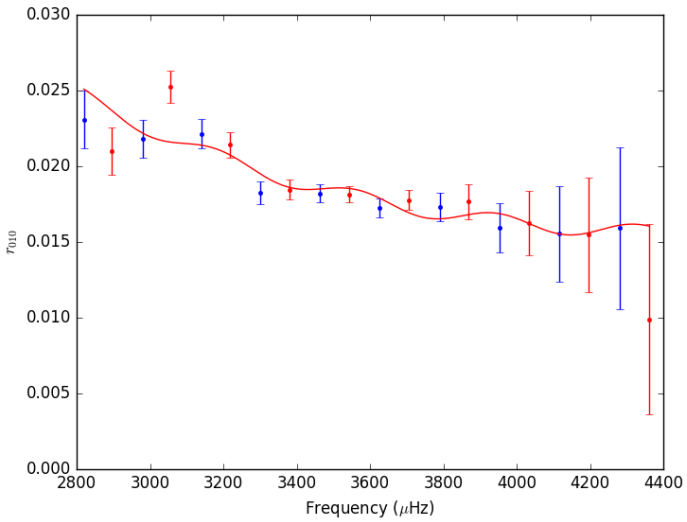

Figure A.13: Same as figure A.3, but for the artificial star ‘Coco’.

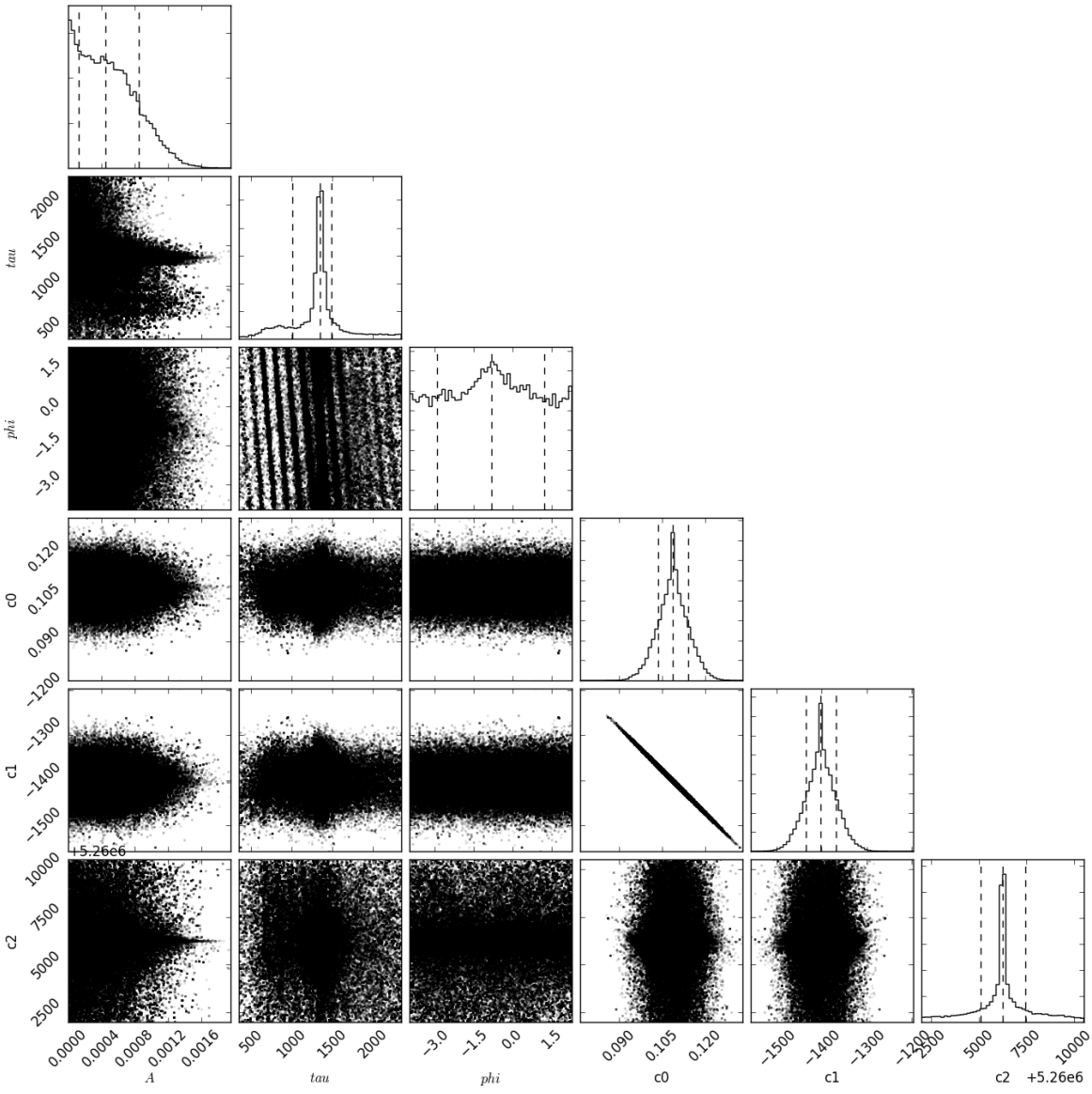

Figure A.14: Same as figure A.4, but for the artificial star ‘Coco’.

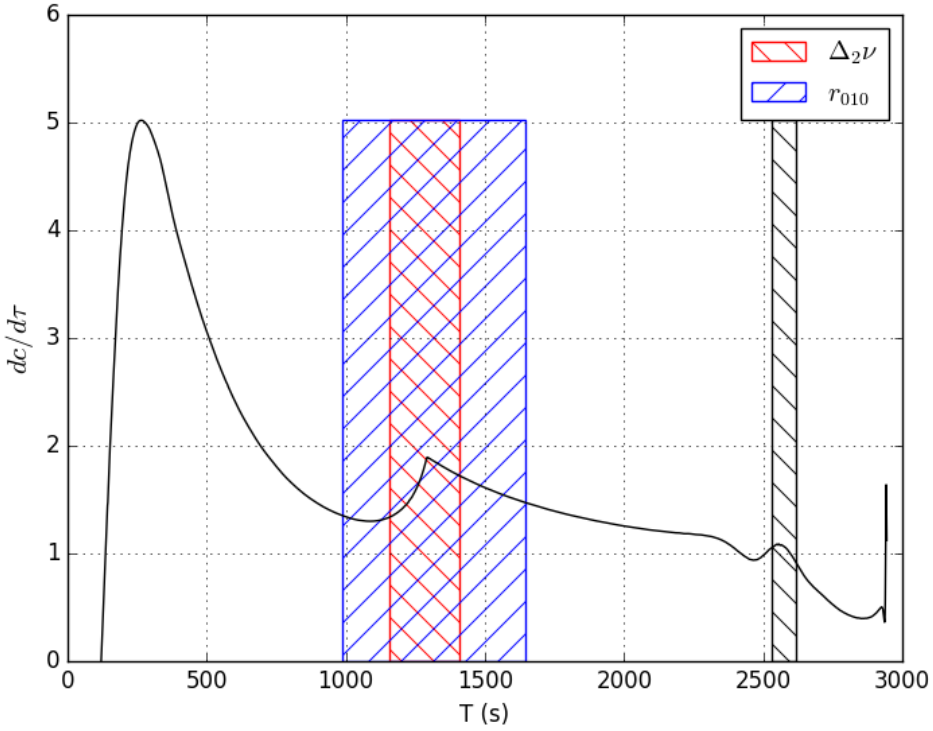

Figure A.15: Same as figure A.5, but for the artificial star ‘Coco’.

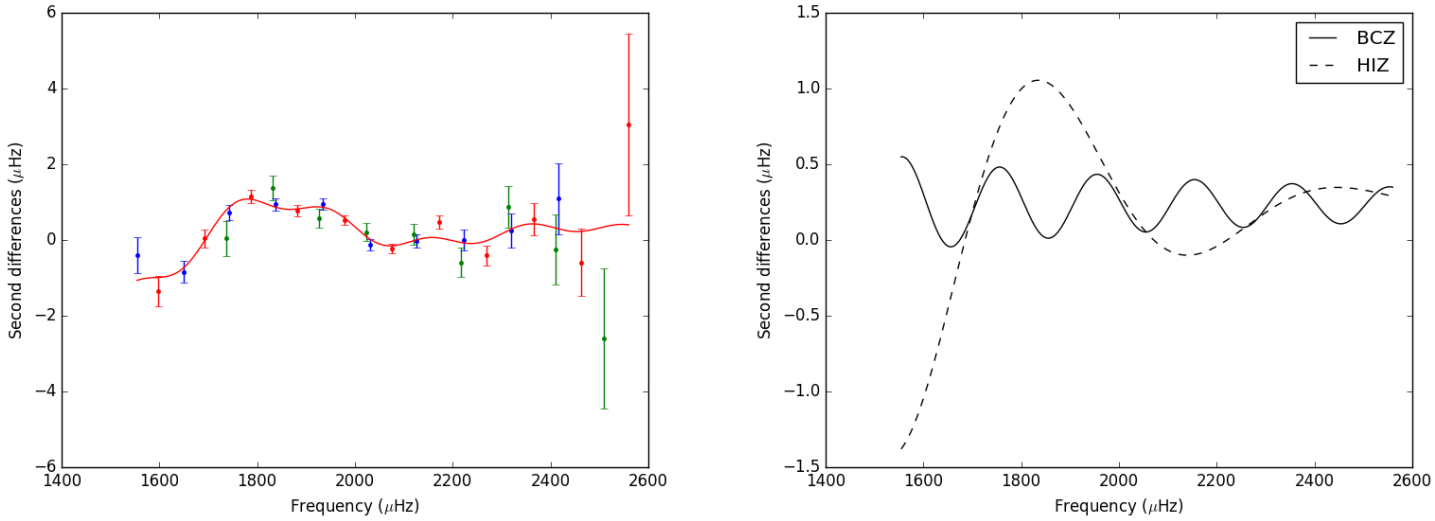

Figure A.16: Same as figure A.1, but for the artificial star ‘Diva’.

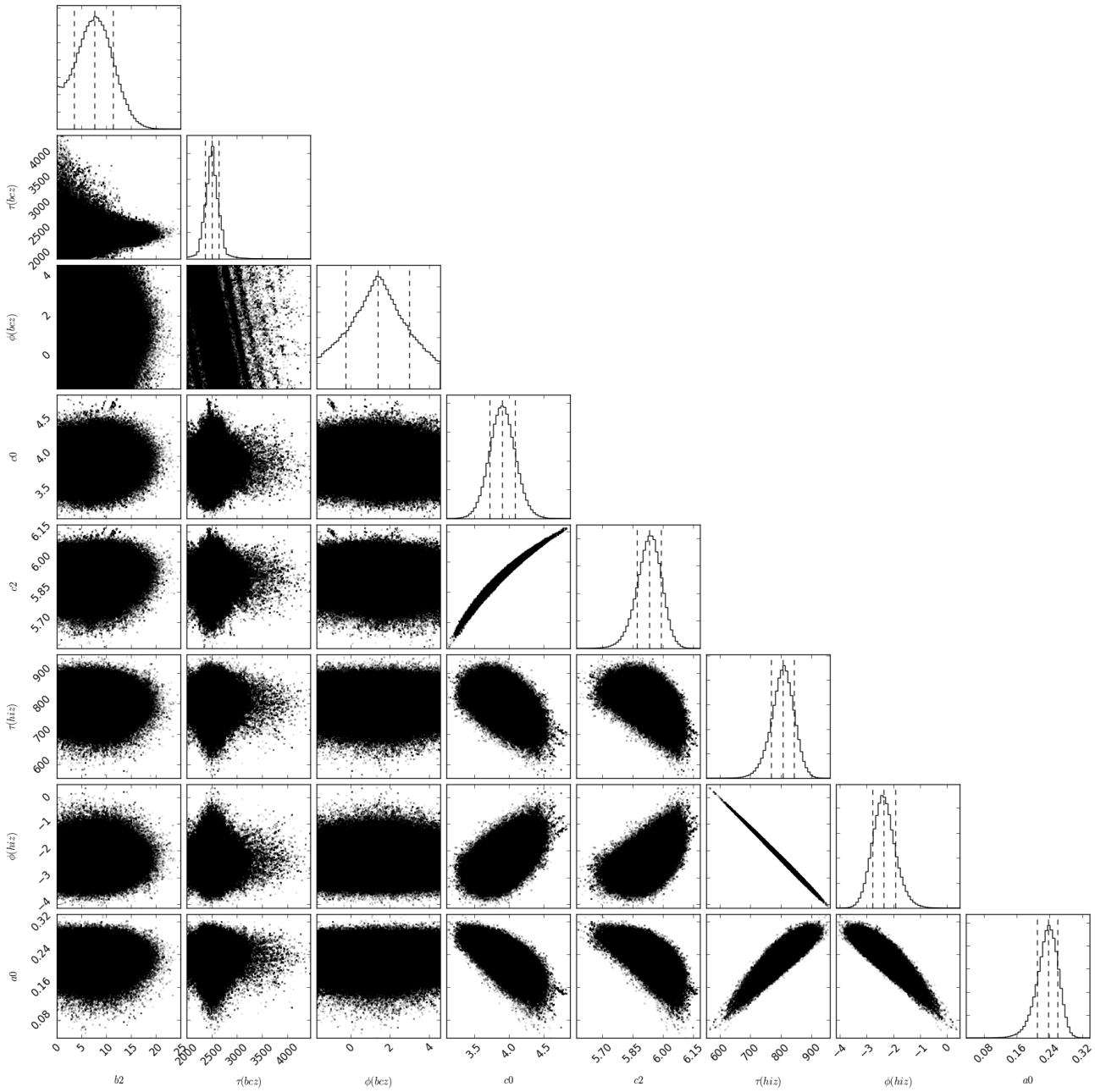

Figure A.17: Same as figure A.2, but for the artificial star ‘Diva’.

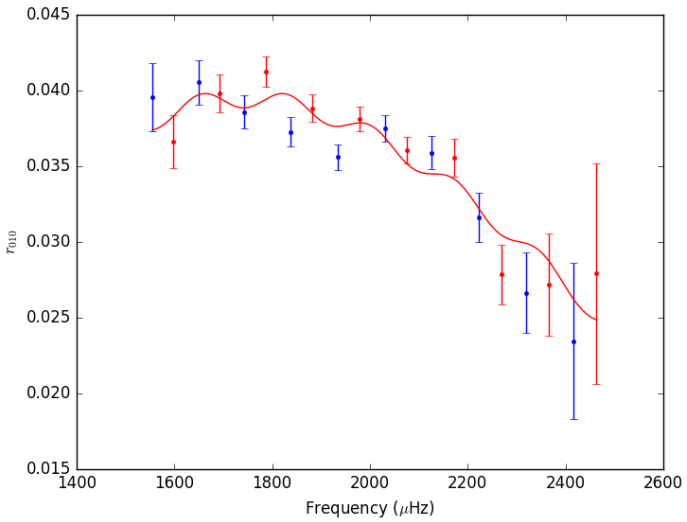

Figure A.18: Same as figure A.3, but for the artificial star ‘Diva’.

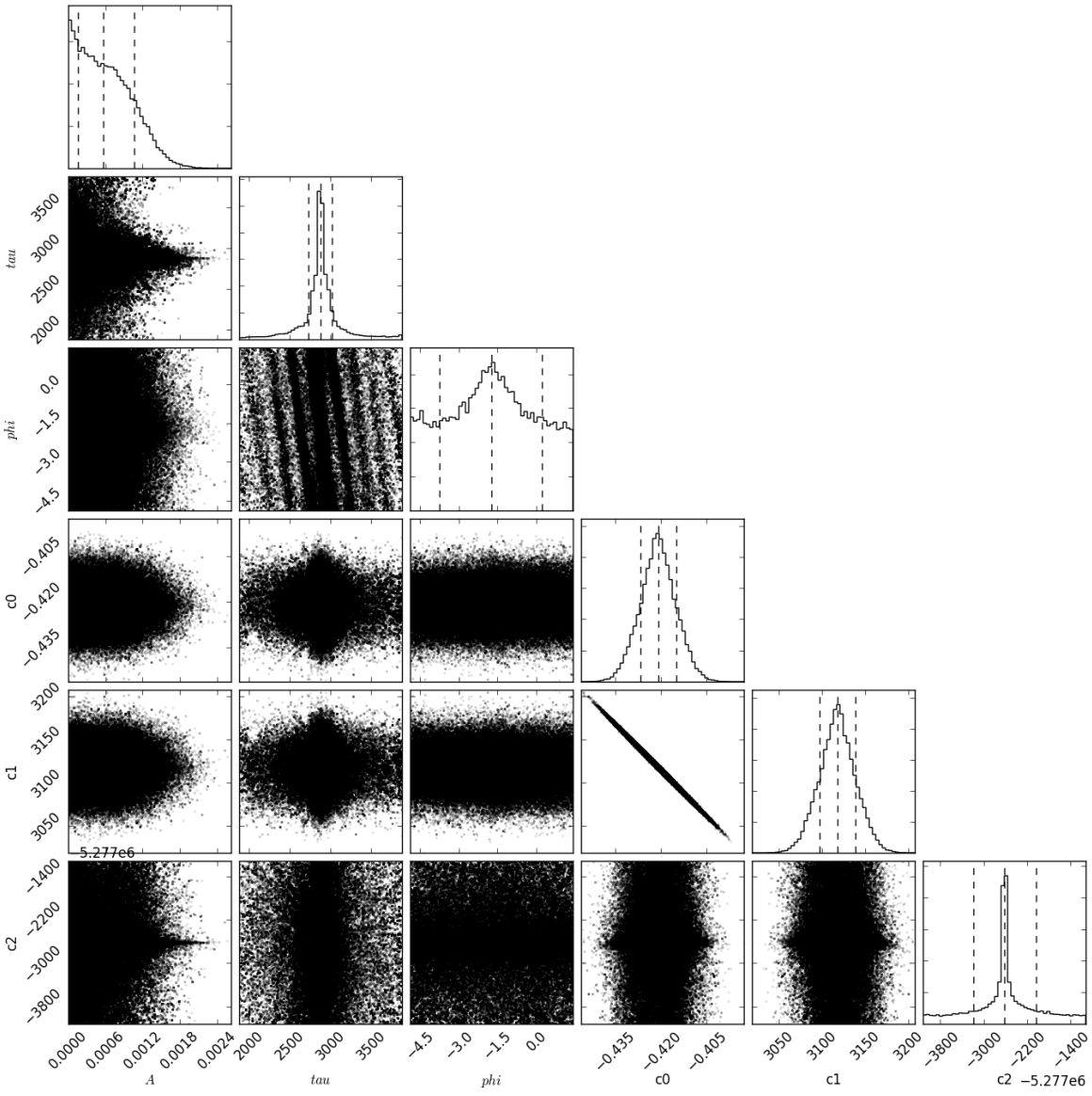

Figure A.19: Same as figure A.4, but for the artificial star ‘Diva’.

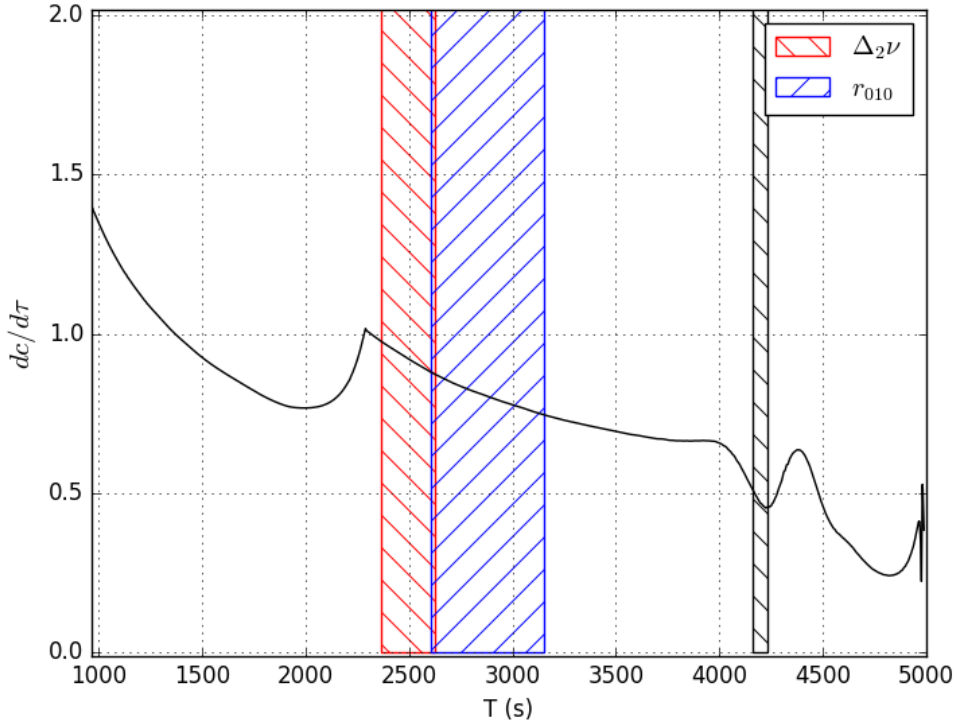

Figure A.20: Same as figure A.5, but for the artificial star ‘Diva’.

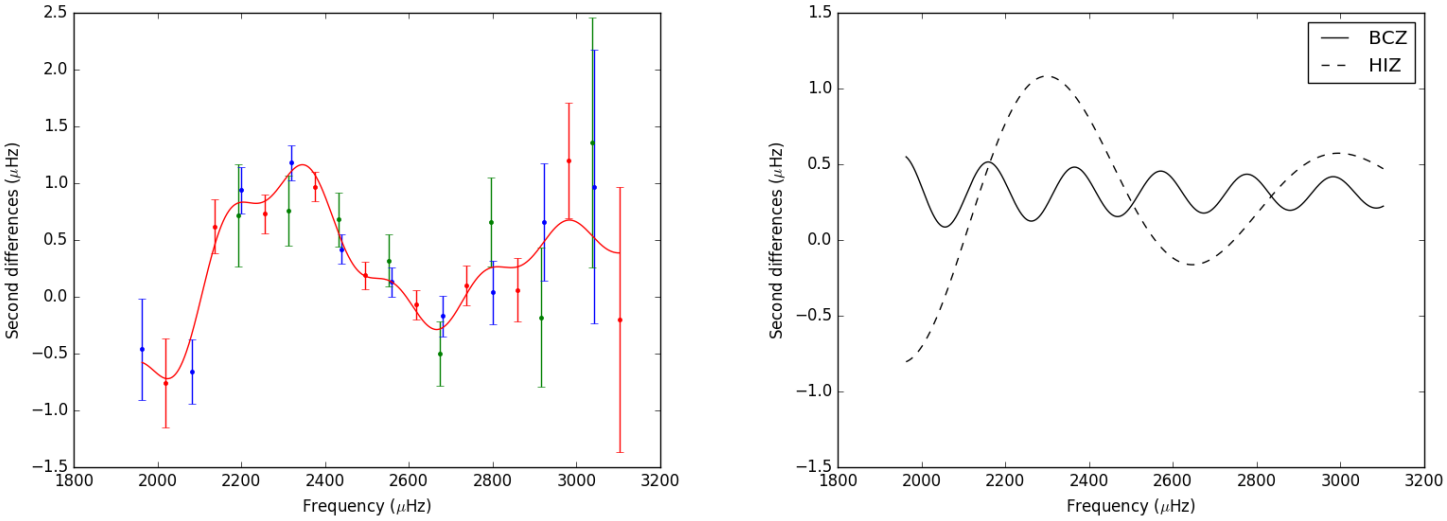

Figure A.21: Same as figure A.1, but for the artificial star ‘Elvis’.

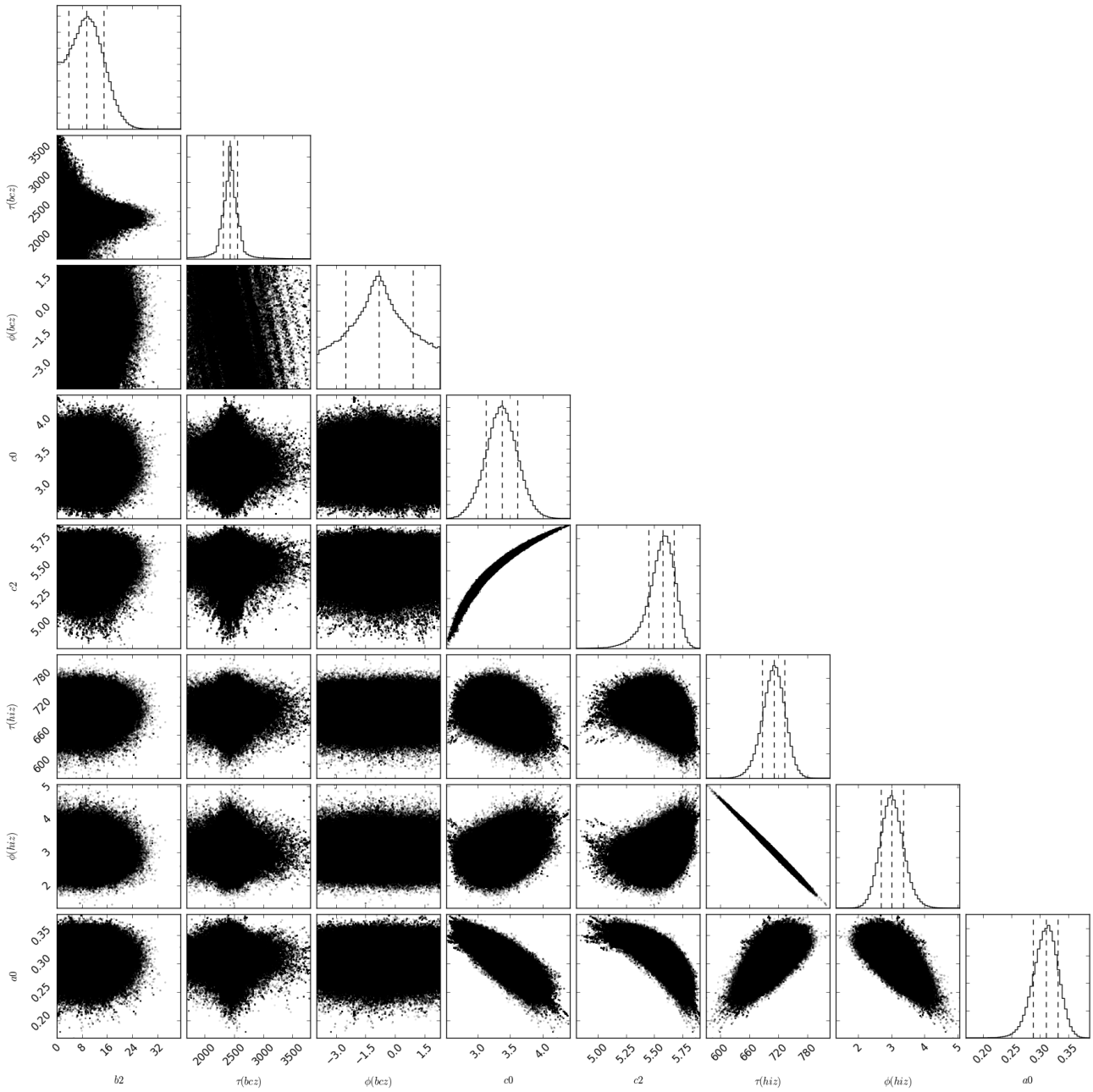

Figure A.22: Same as figure A.2, but for the artificial star ‘Elvis’.

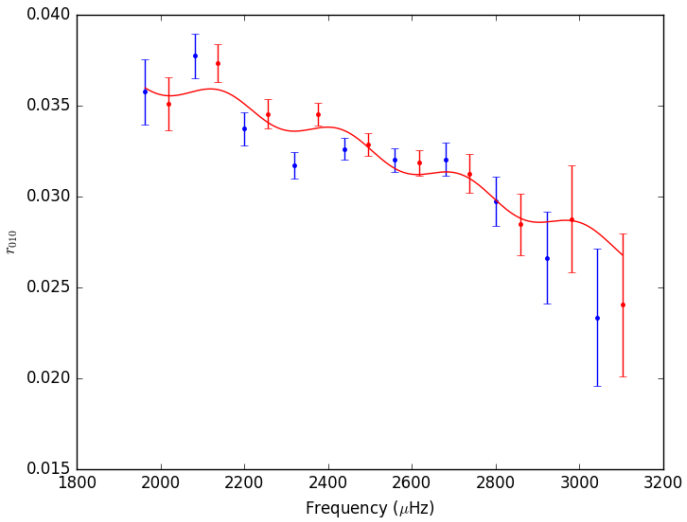

Figure A.23: Same as figure A.3, but for the artificial star ‘Elvis’.

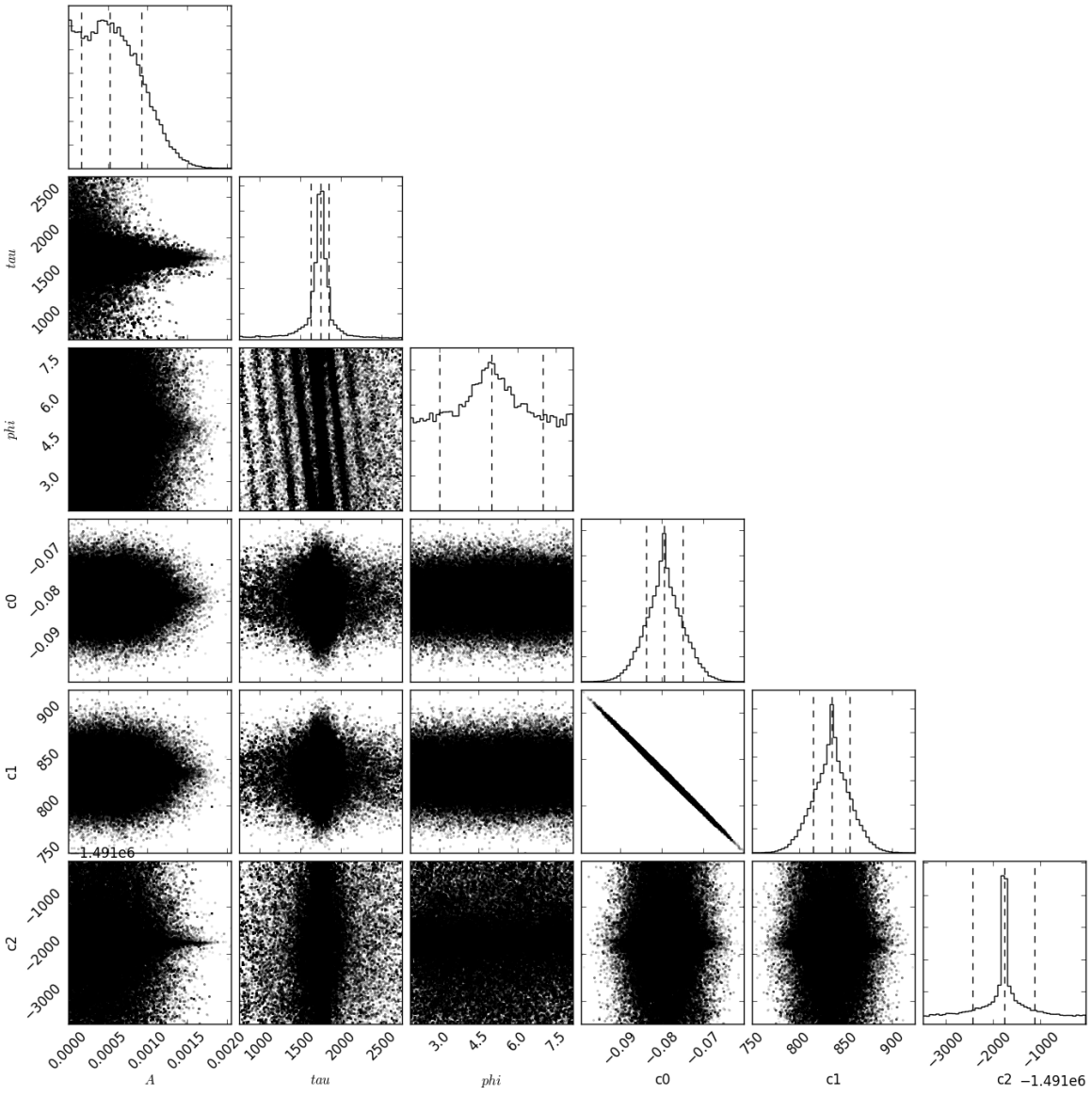

Figure A.24: Same as figure A.4, but for the artificial star ‘Elvis’.

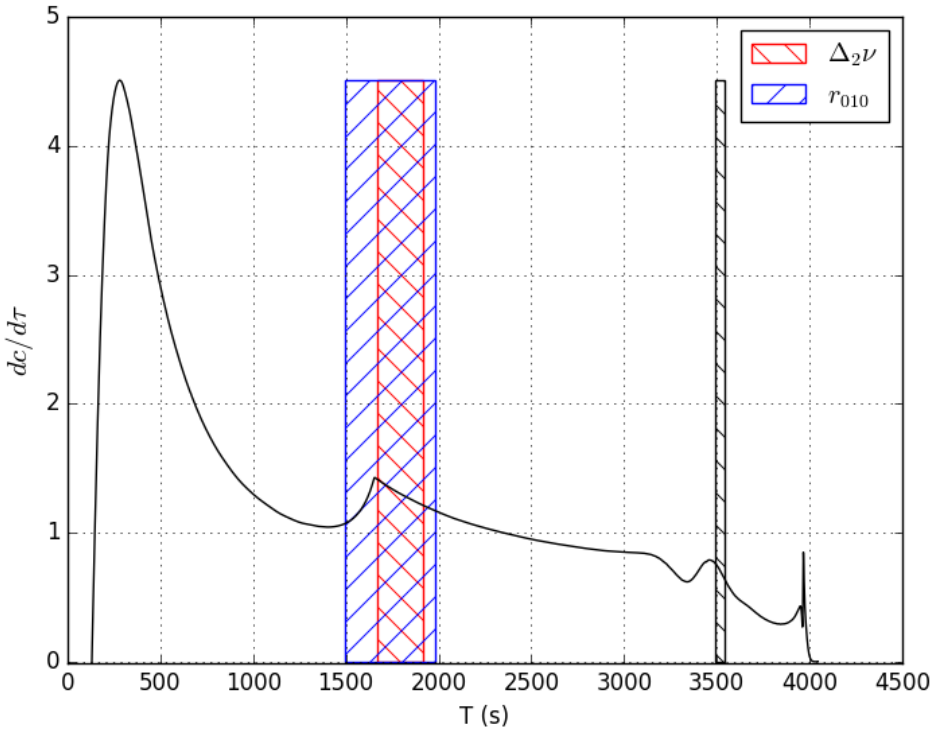

Figure A.25: Same as figure A.5, but for the artificial star ‘Elvis’.

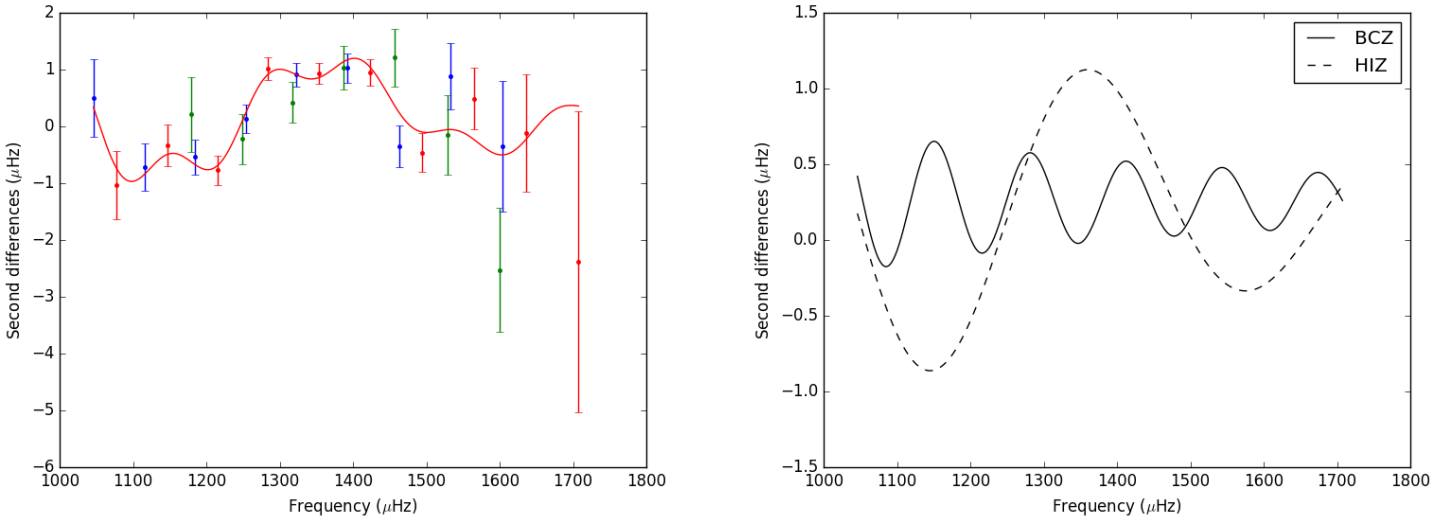

Figure A.26: Same as figure A.1, but for the artificial star ‘Felix’.

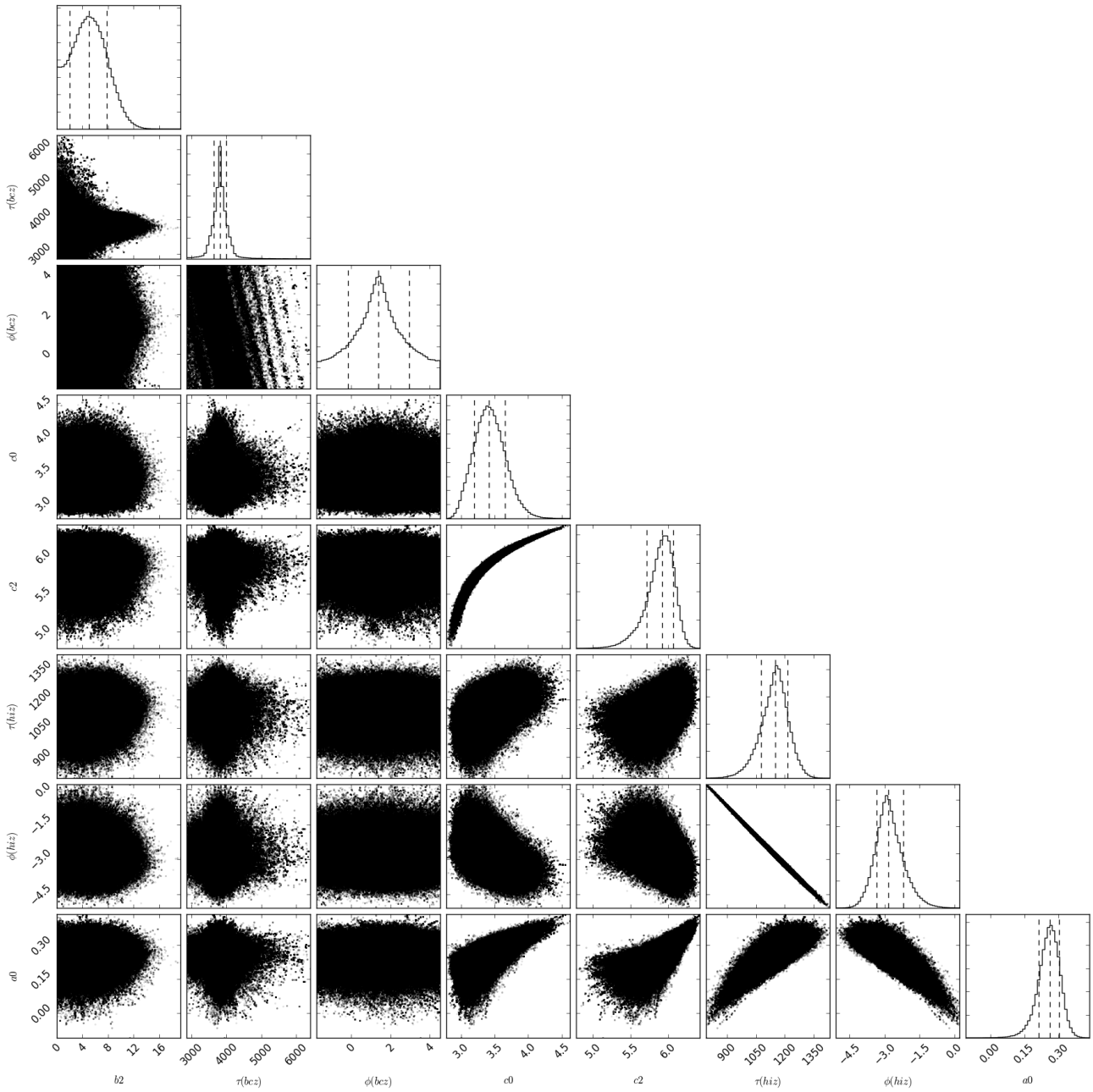

Figure A.27: Same as figure A.2, but for the artificial star ‘Felix’.

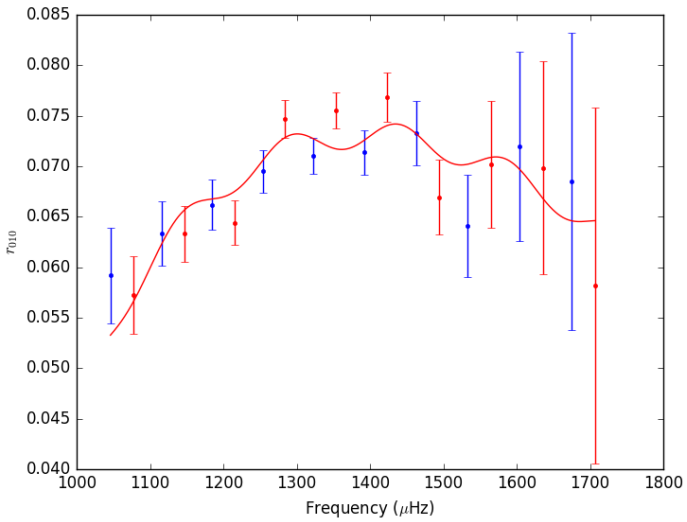

Figure A.28: Same as figure A.3, but for the artificial star ‘Felix’.

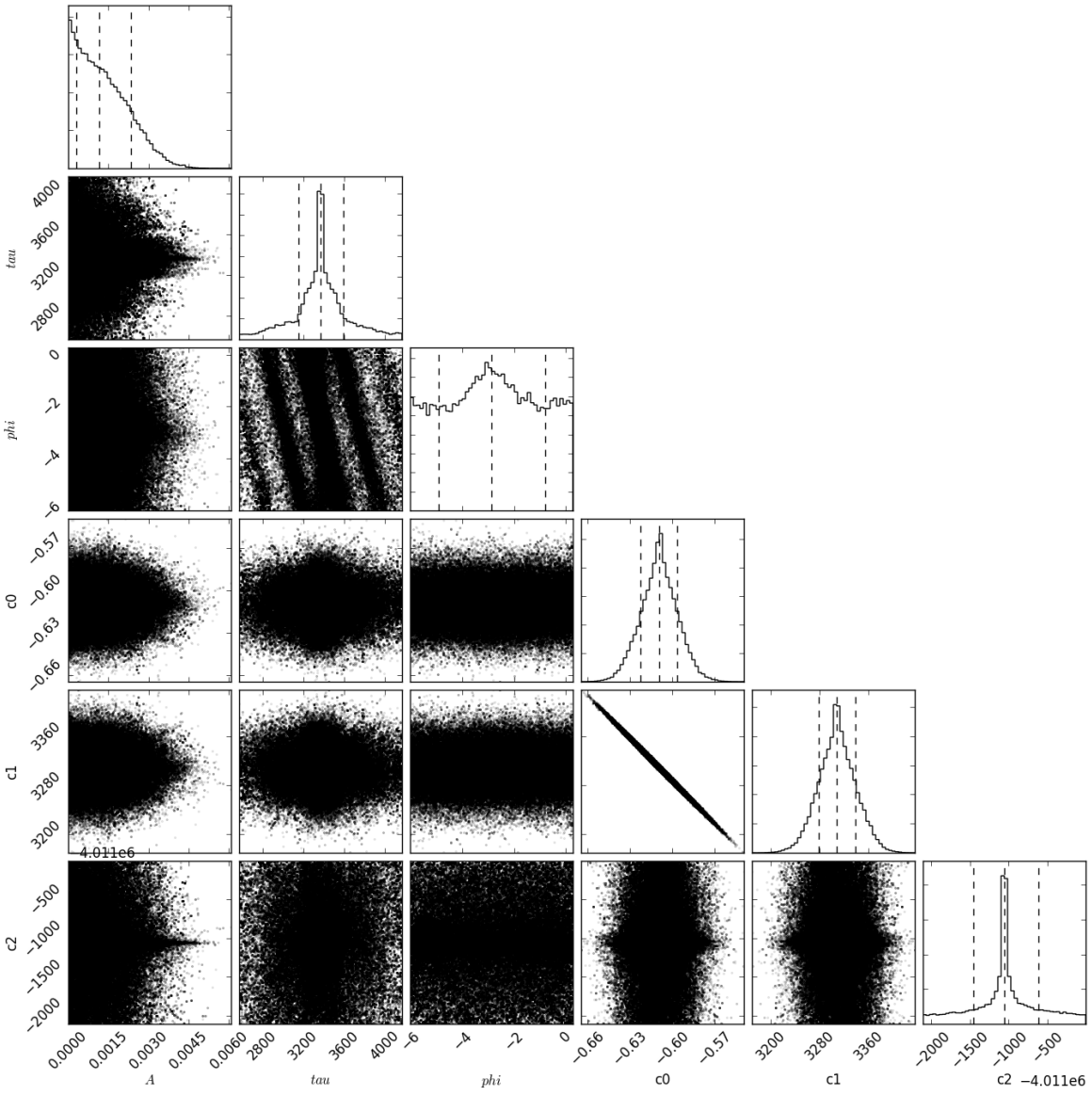

Figure A.29: Same as figure A.4, but for the artificial star ‘Felix’.

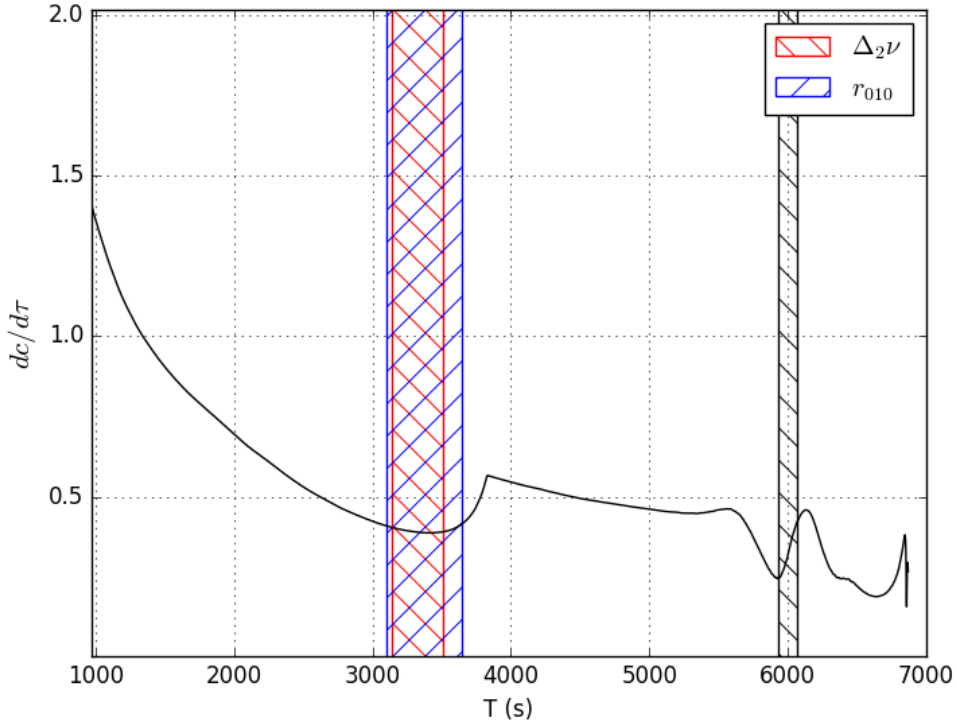

Figure A.30: Same as figure A.5, but for the artificial star ‘Felix’.

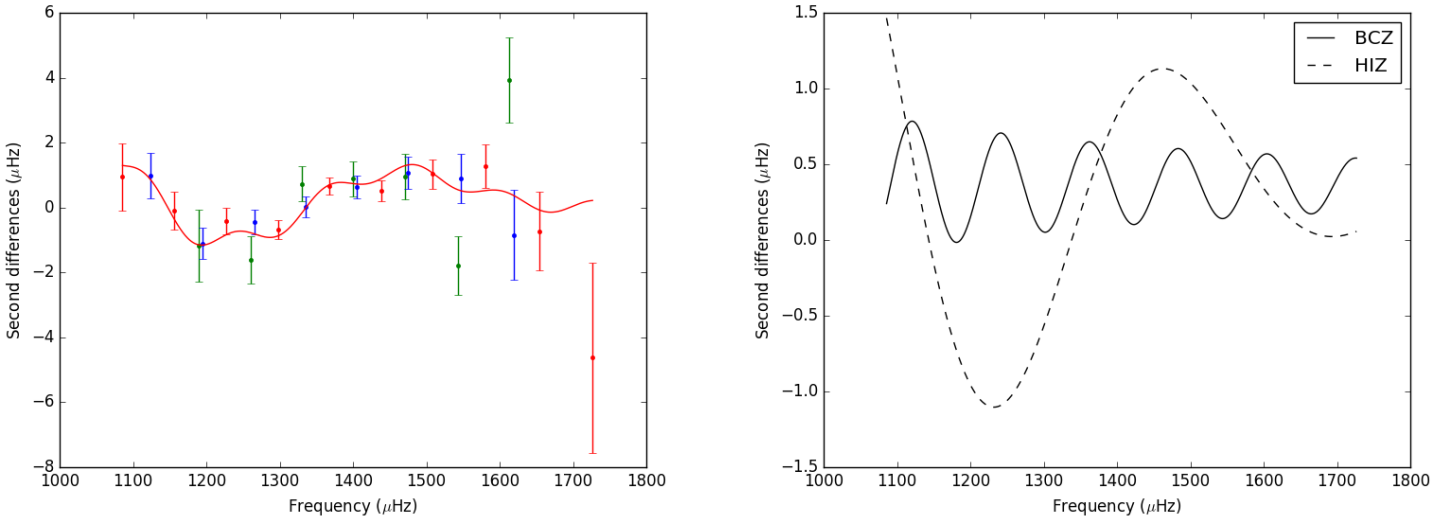

Figure A.31: Same as figure A.1, but for the artificial star ‘George’.

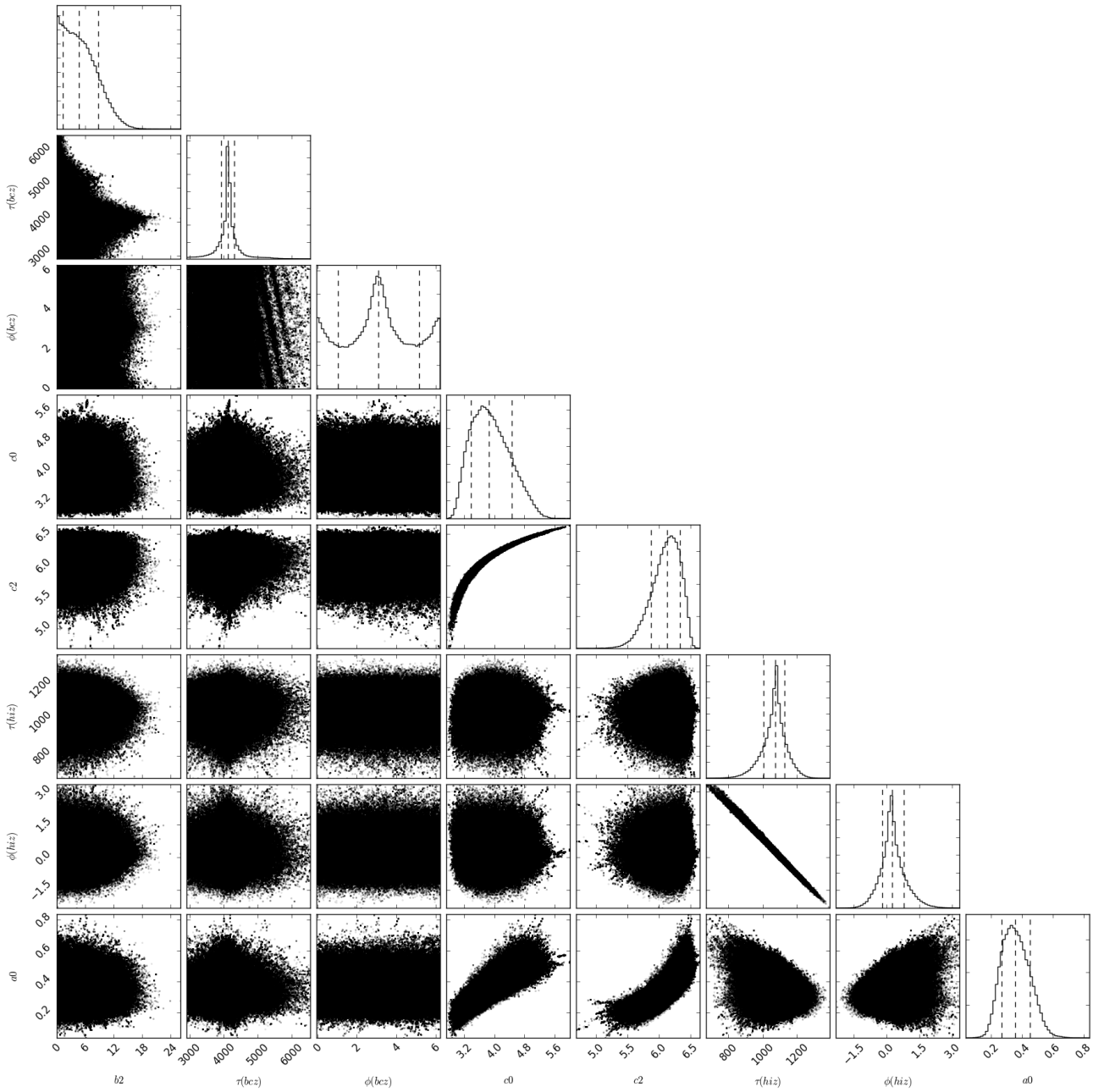

Figure A.32: Same as figure A.2, but for the artificial star ‘George’.

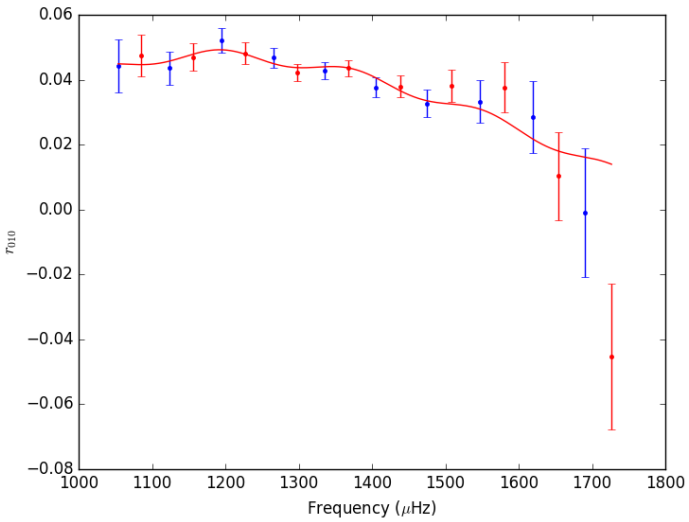

Figure A.33: Same as figure A.3, but for the artificial star ‘George’.

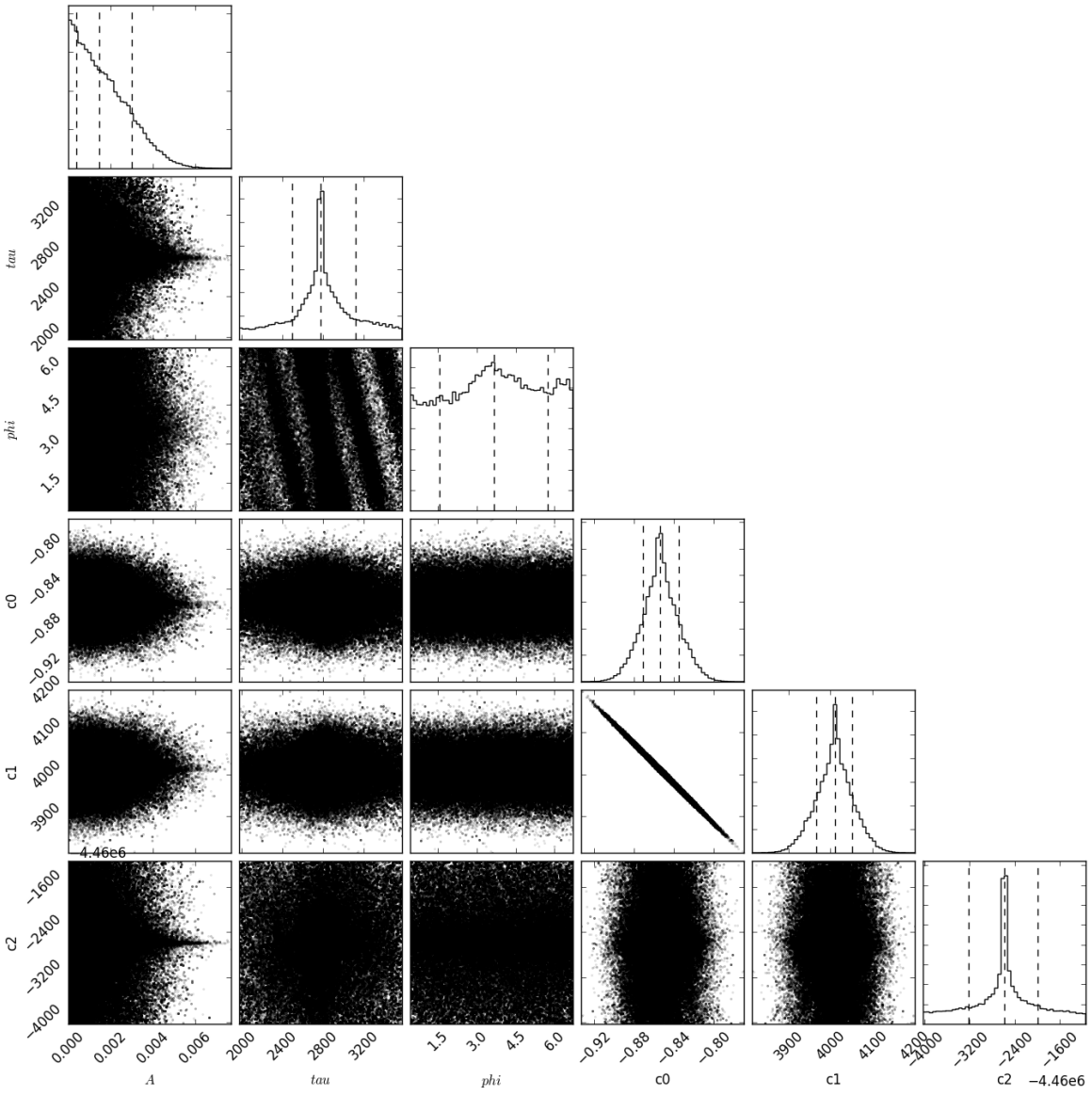

Figure A.34: Same as figure A.4, but for the artificial star ‘George’.

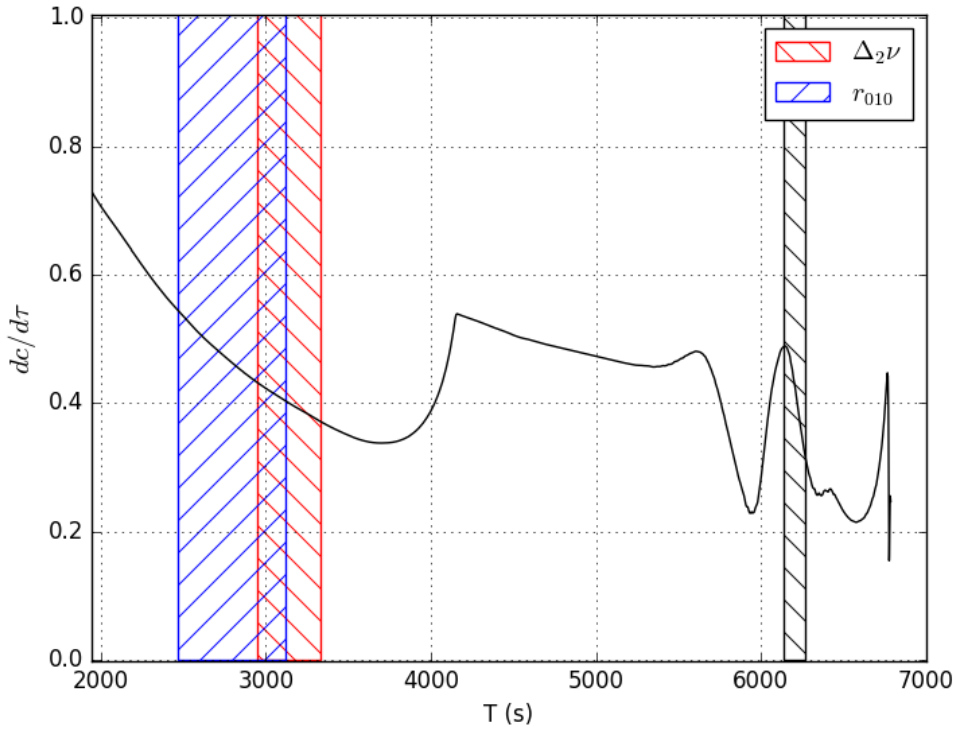

Figure A.35: Same as figure A.5, but for the artificial star ‘George’.

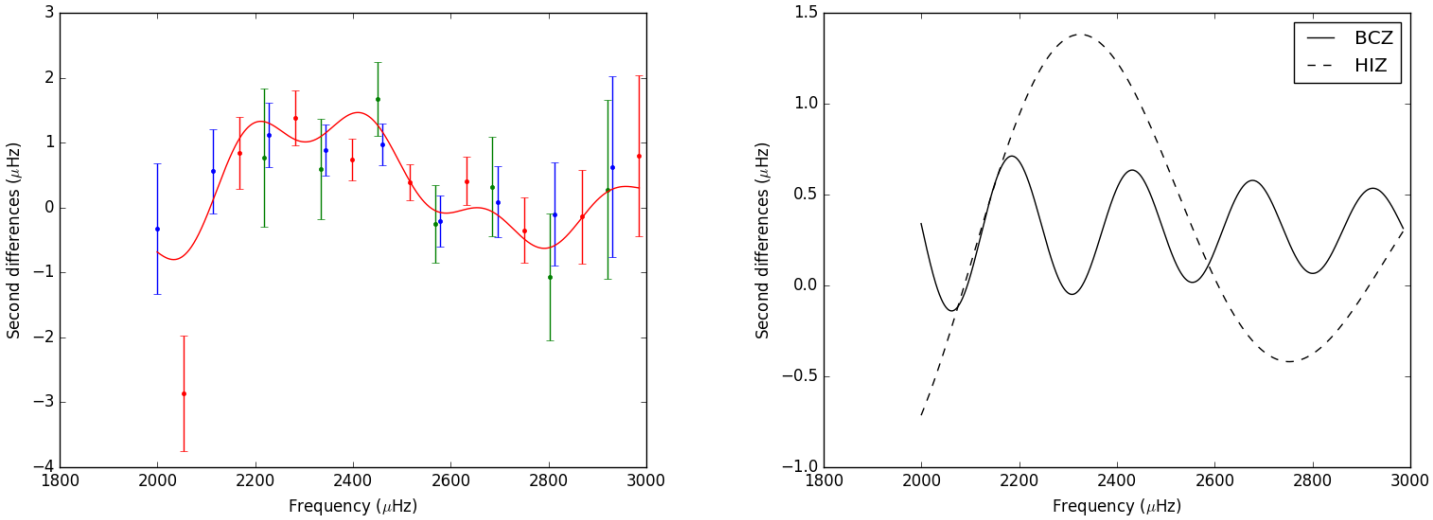

Figure A.36: Same as figure A.1, but for the artificial star ‘Henry’.

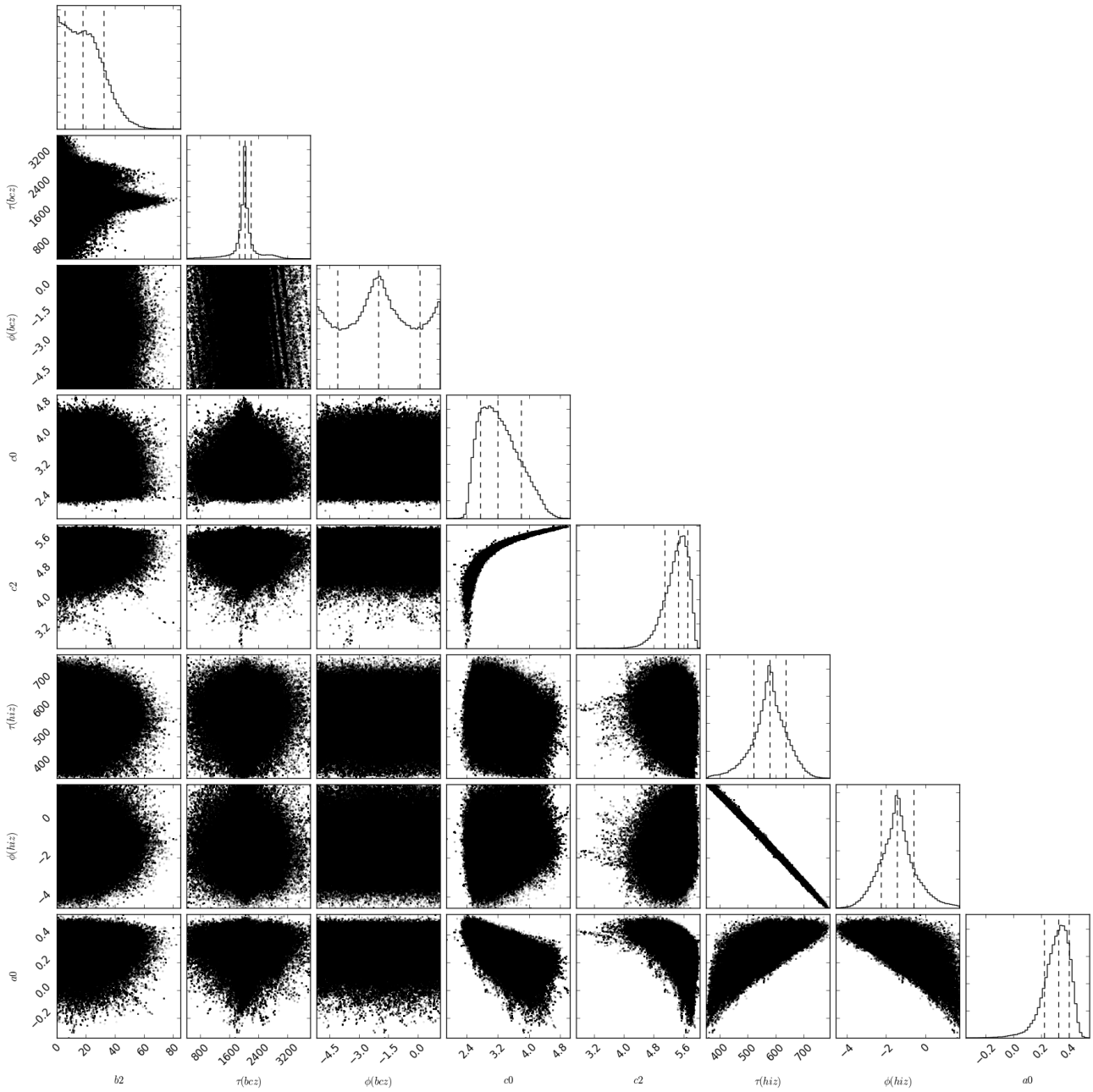

Figure A.37: Same as figure A.2, but for the artificial star ‘Henry’.

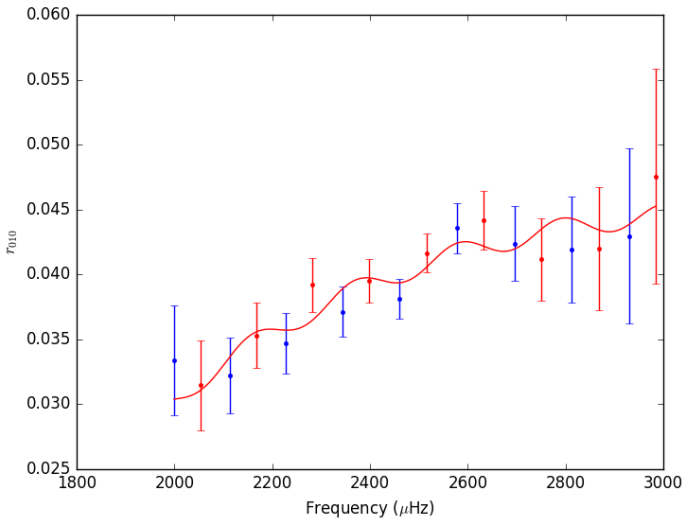

Figure A.38: Same as figure A.3, but for the artificial star ‘Henry’.

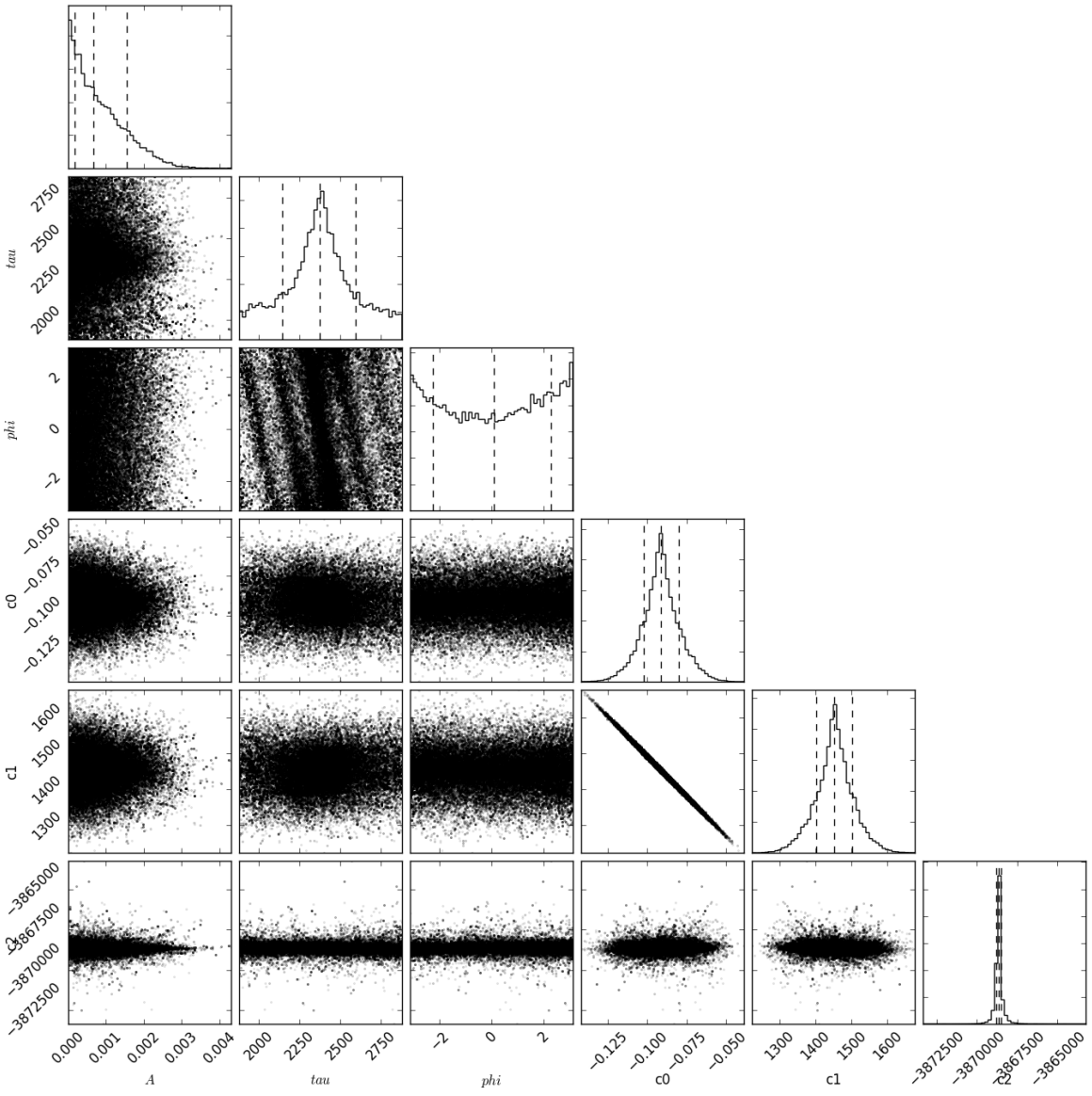

Figure A.39: Same as figure A.4, but for the artificial star ‘Henry’.

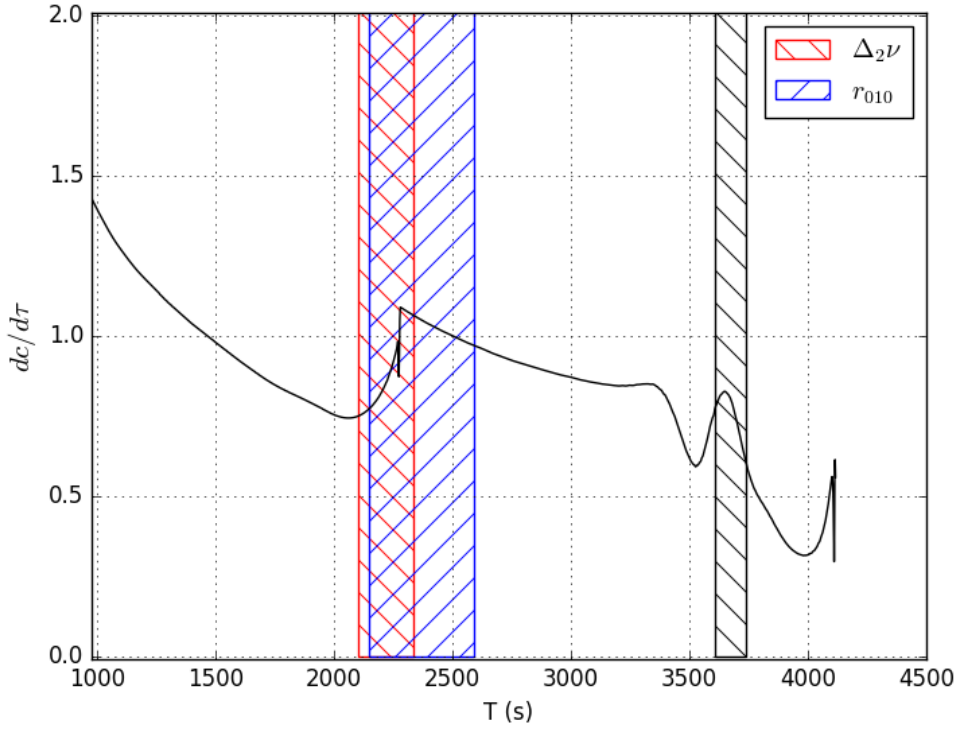

Figure A.40: Same as figure A.5, but for the artificial star ‘Henry’.

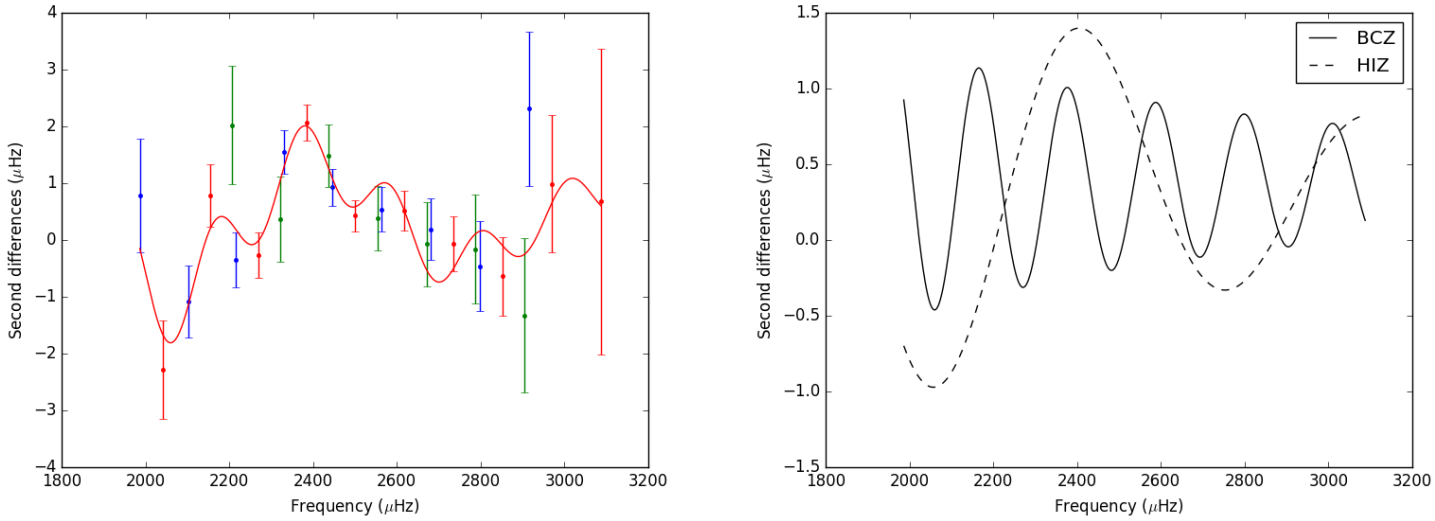

Figure A.41: Same as figure A.1, but for the artificial star ‘Izzy’.

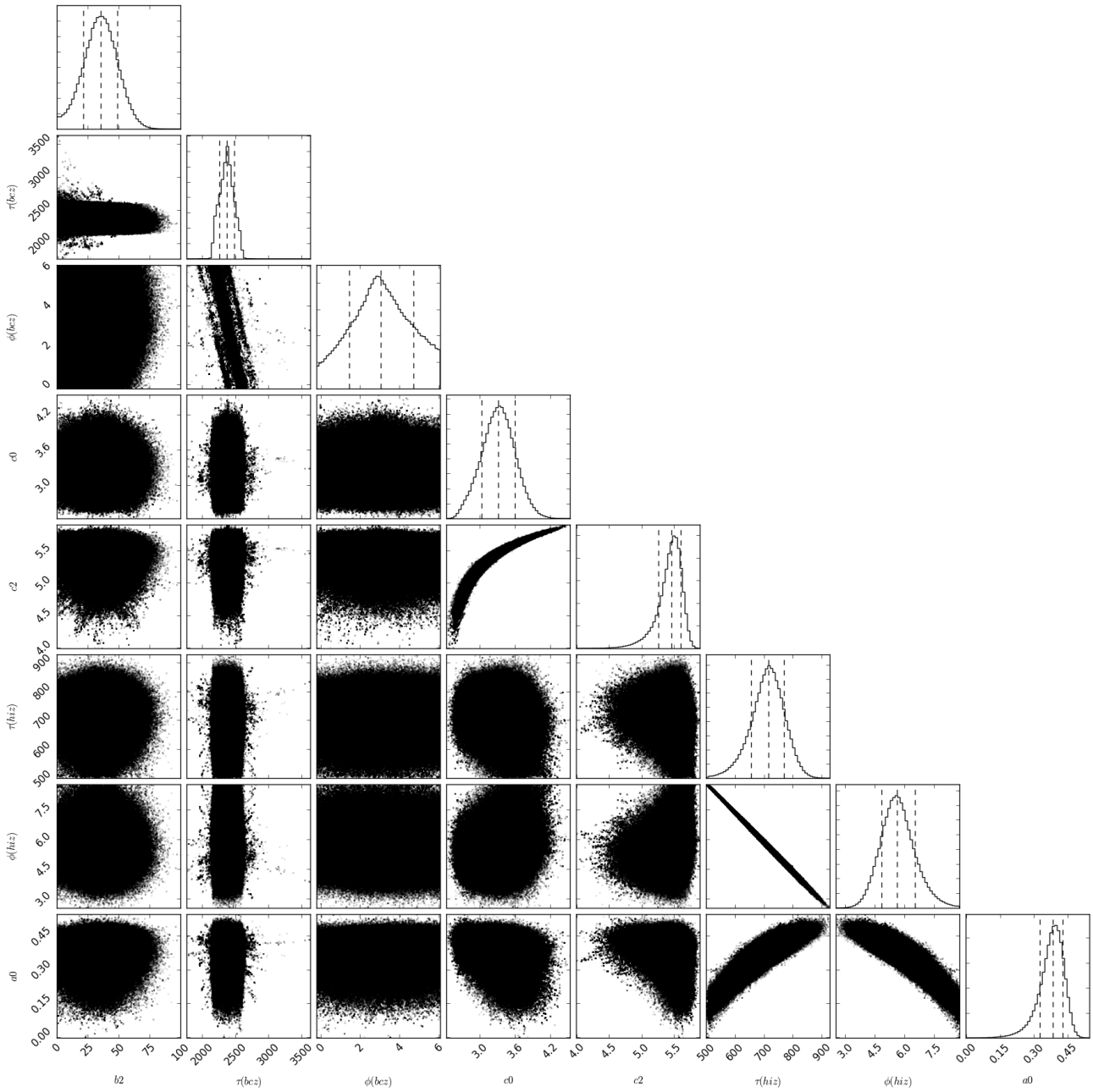

Figure A.42: Same as figure A.2, but for the artificial star ‘Izzy’.

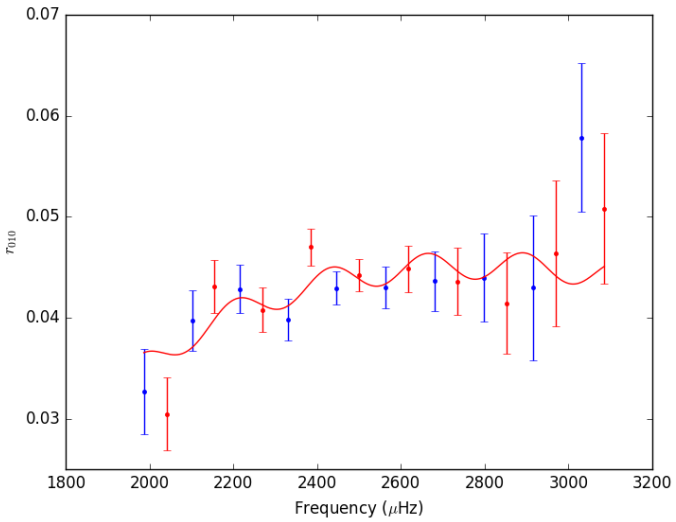

Figure A.43: Same as figure A.3, but for the artificial star ‘Izzy’.

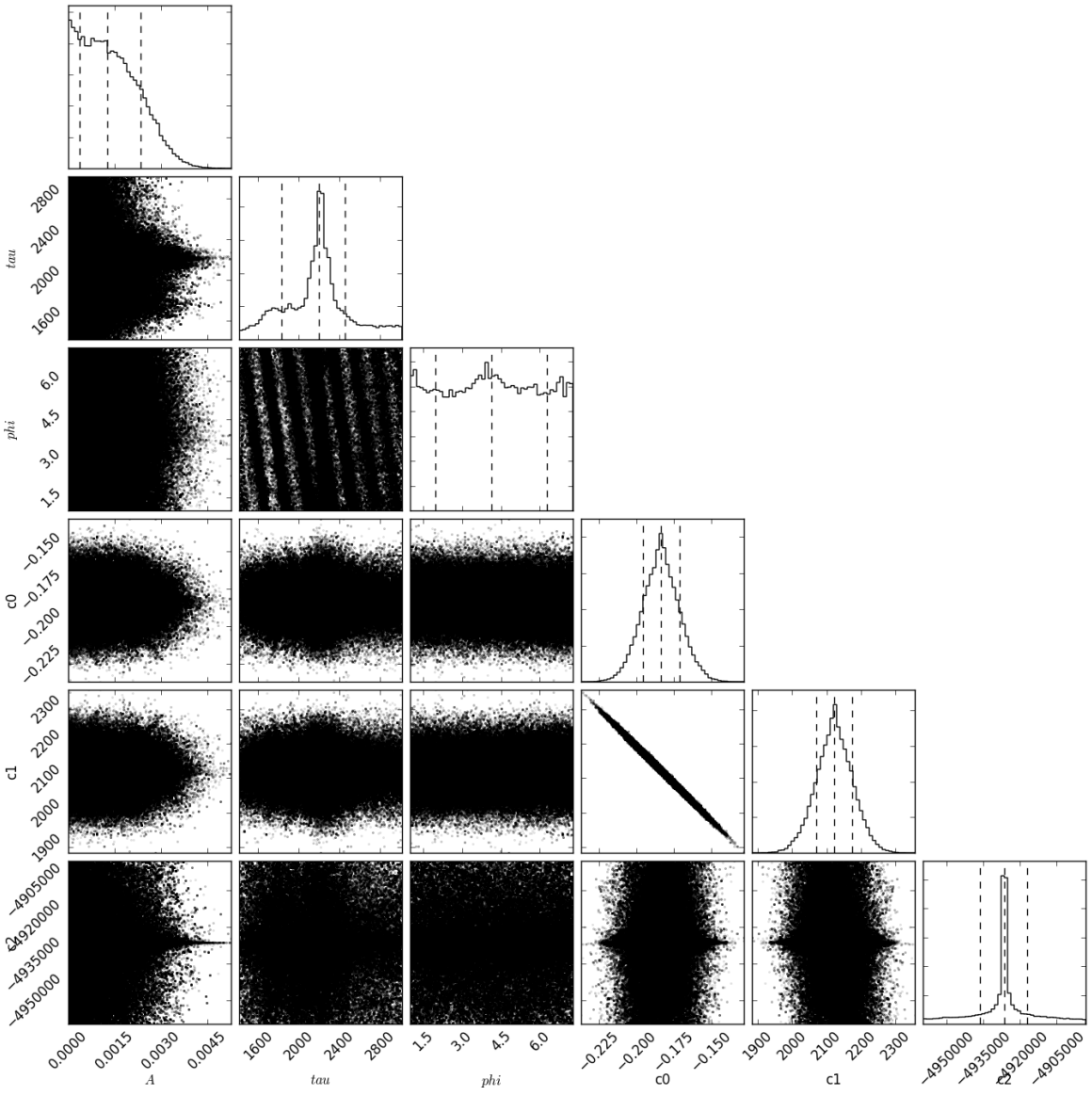

Figure A.44: Same as figure A.4, but for the artificial star ‘Izzy’.

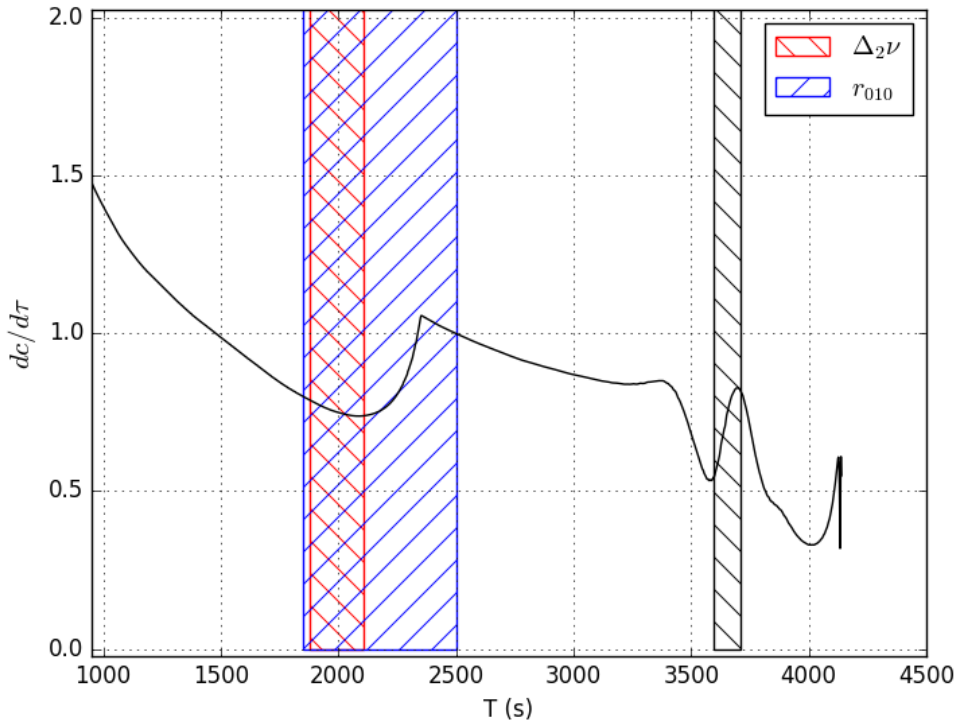

Figure A.45: Same as figure A.5, but for the artificial star ‘Izzy’.

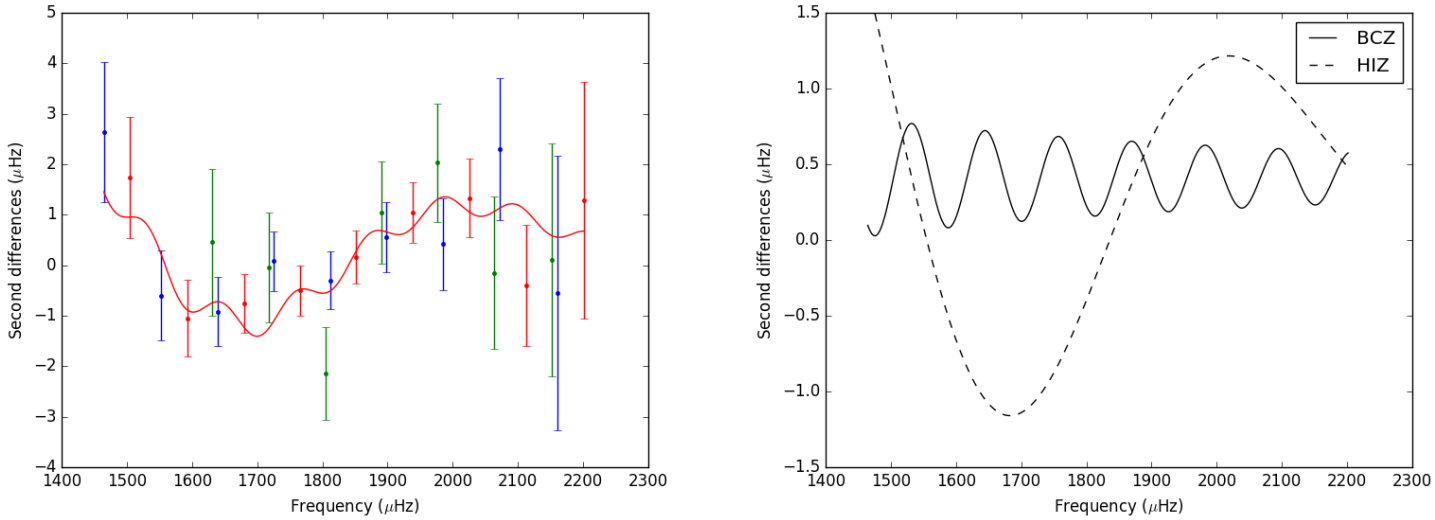

Figure A.46: Same as figure A.1, but for the artificial star ‘Jam’.

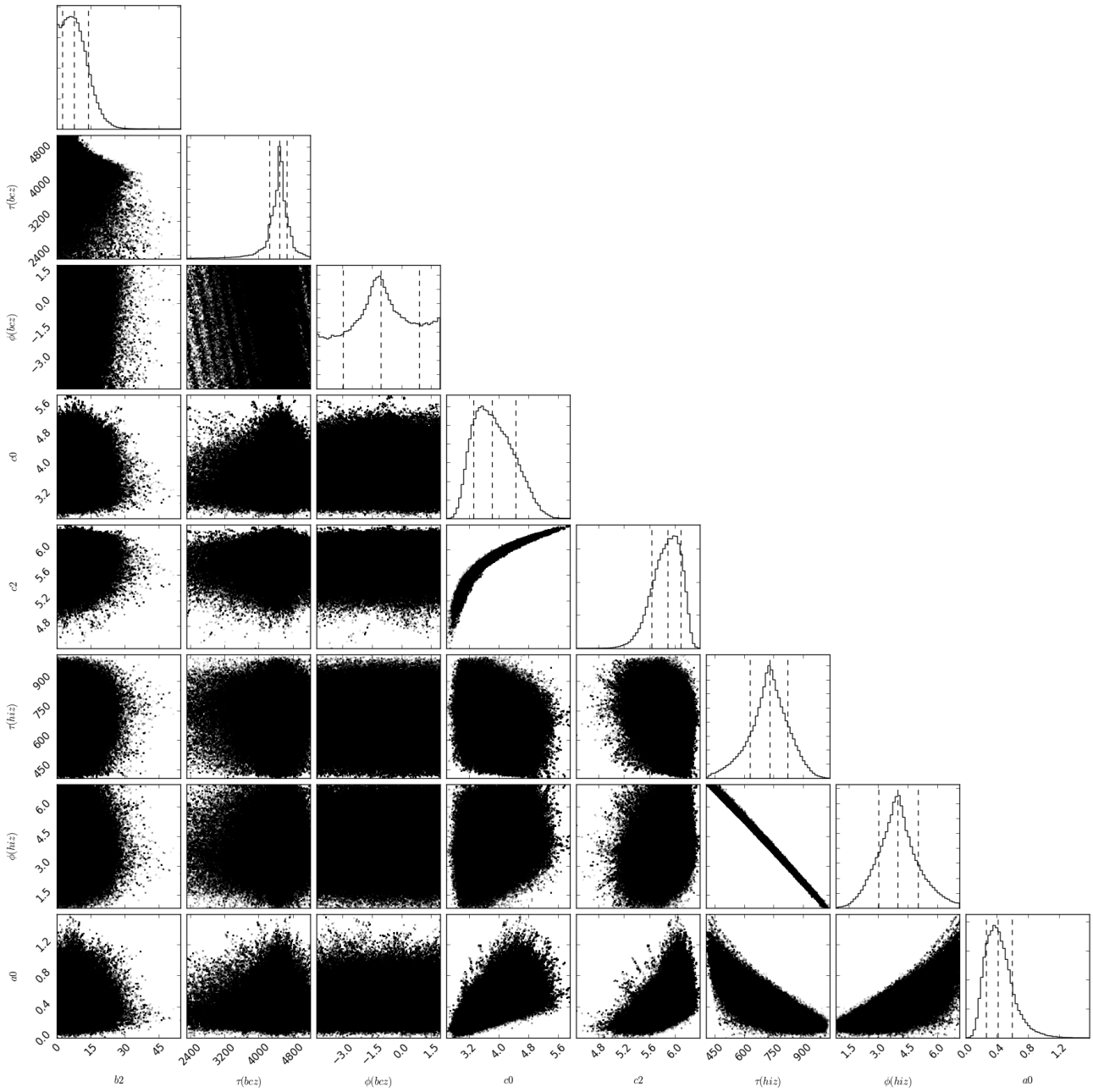

Figure A.47: Same as figure A.2, but for the artificial star ‘Jam’.

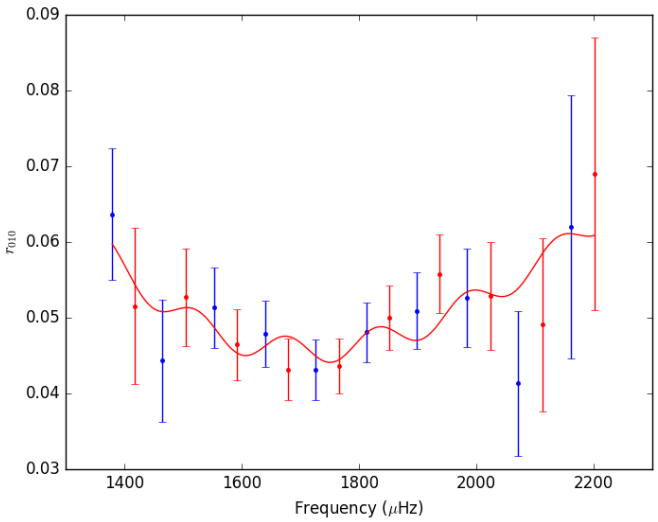

Figure A.48: Same as figure A.3, but for the artificial star ‘Jam’.

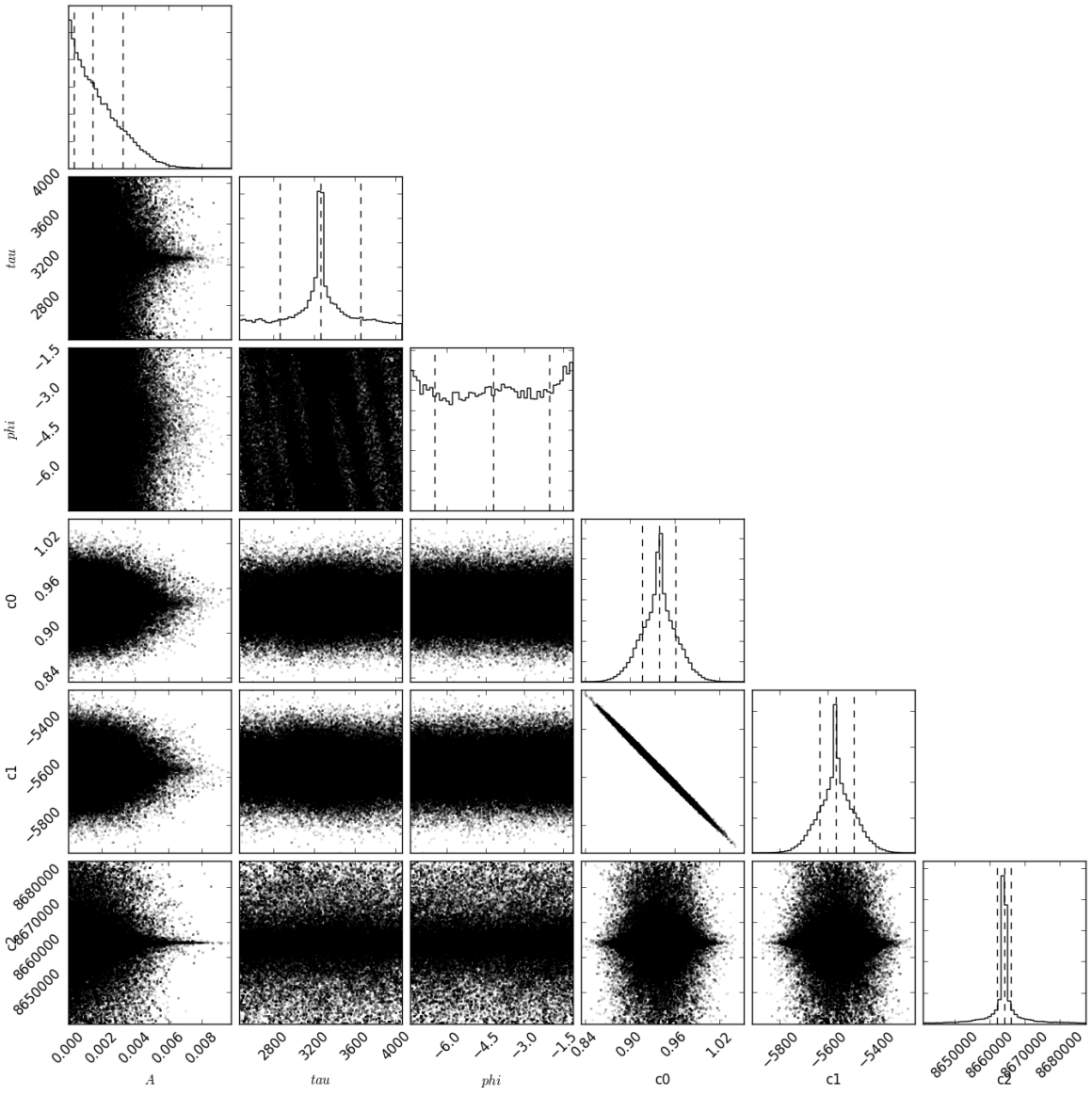

Figure A.49: Same as figure A.4, but for the artificial star ‘Jam’.

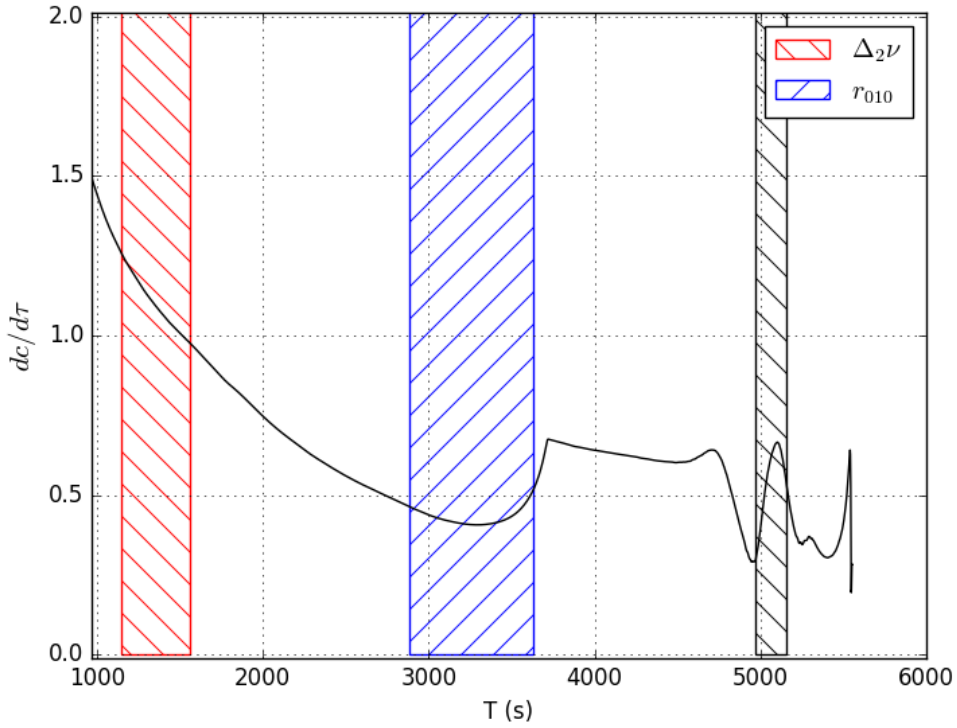

Figure A.50: Same as figure A.5, but for the artificial star ‘Jam’.

A.2 Results for *Kepler* Stars.

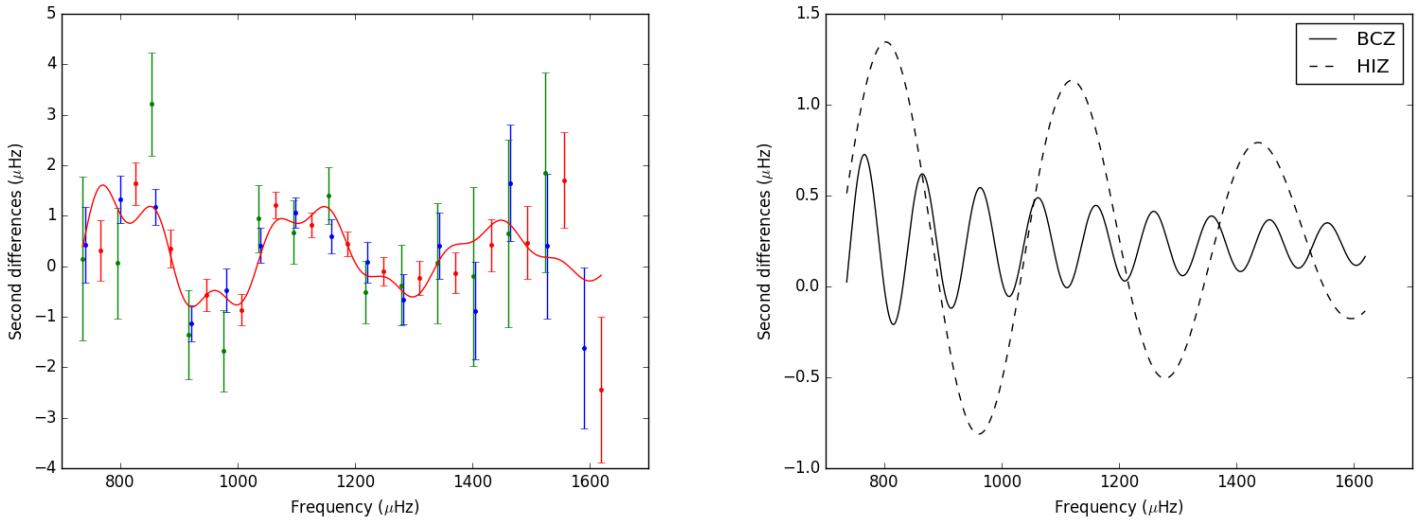

Figure A.51: Left panel: Second differences $\Delta_2\nu$ of the star KIC 3632418. The solid red line indicates the model containing the final fitted results. Right panel: individual components from the base of the convective zone (BCZ - solid line) and the second helium ionization zone (HIZ - dashed line).

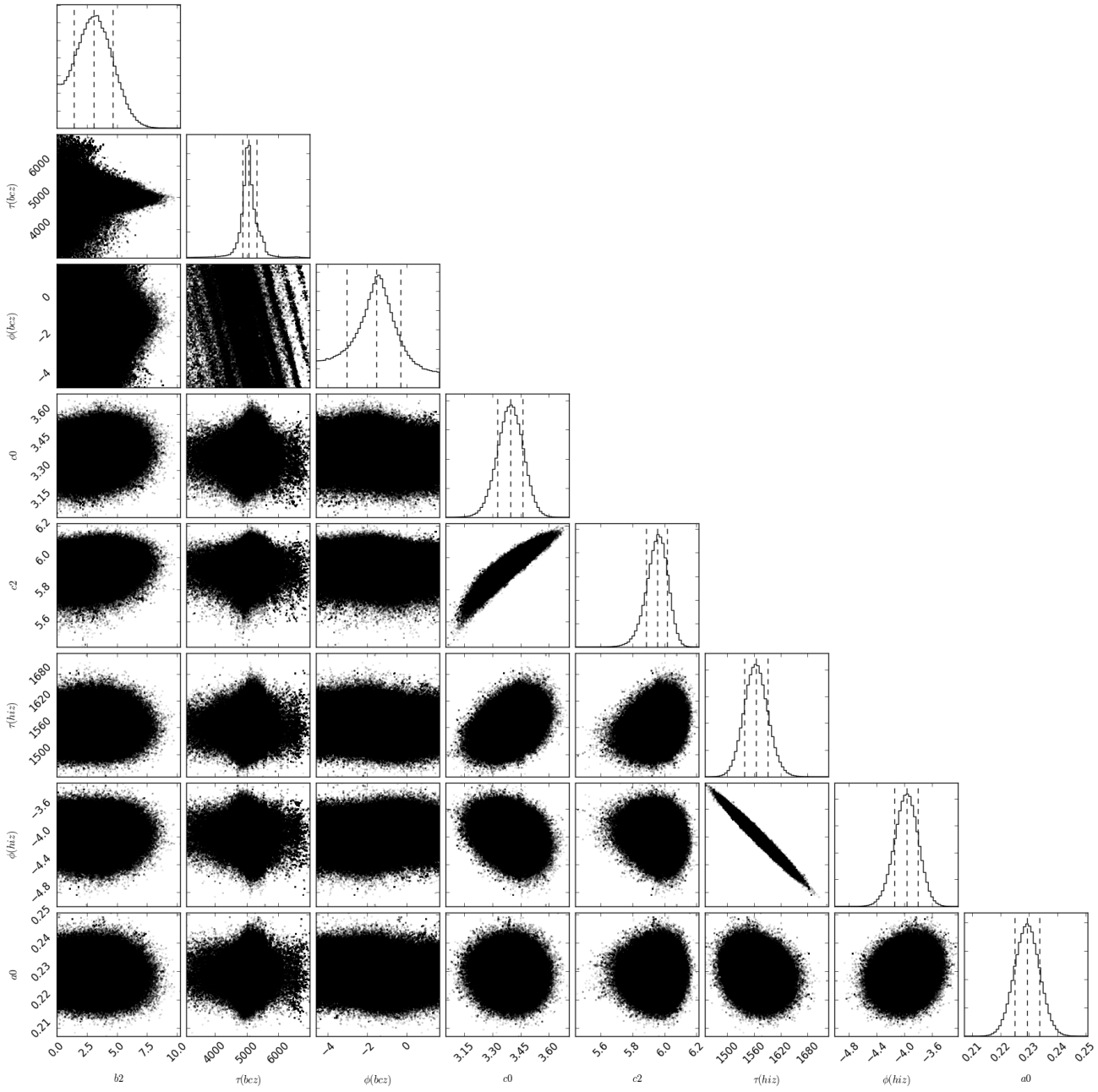

Figure A.52: Posterior distributions of all the free parameters of the fit for the star KIC 3632418. The vertical dashed lines indicates the 68%-level confidence interval.

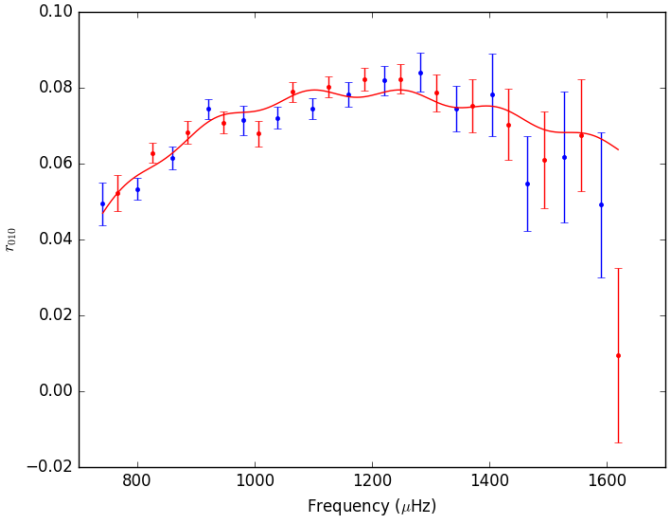

Figure A.53: Fit for the frequency ratios r_{010} for the star KIC 3632418. The solid red line indicates the model containing the final fitted results.

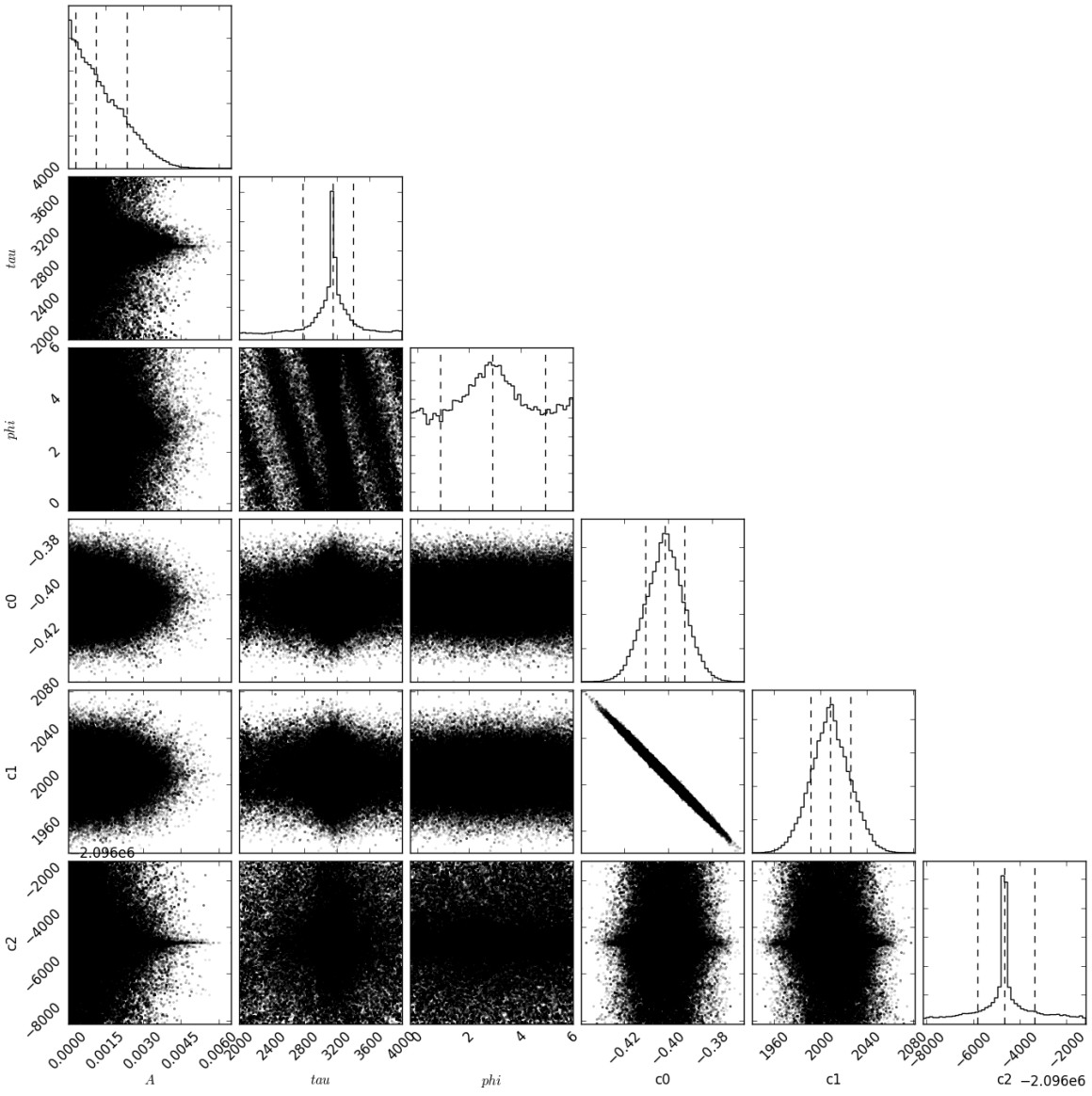

Figure A.54: Similar to A.52, but here we show the posterior distribution when using frequency ratios r_{010} for the star KIC 3632418.

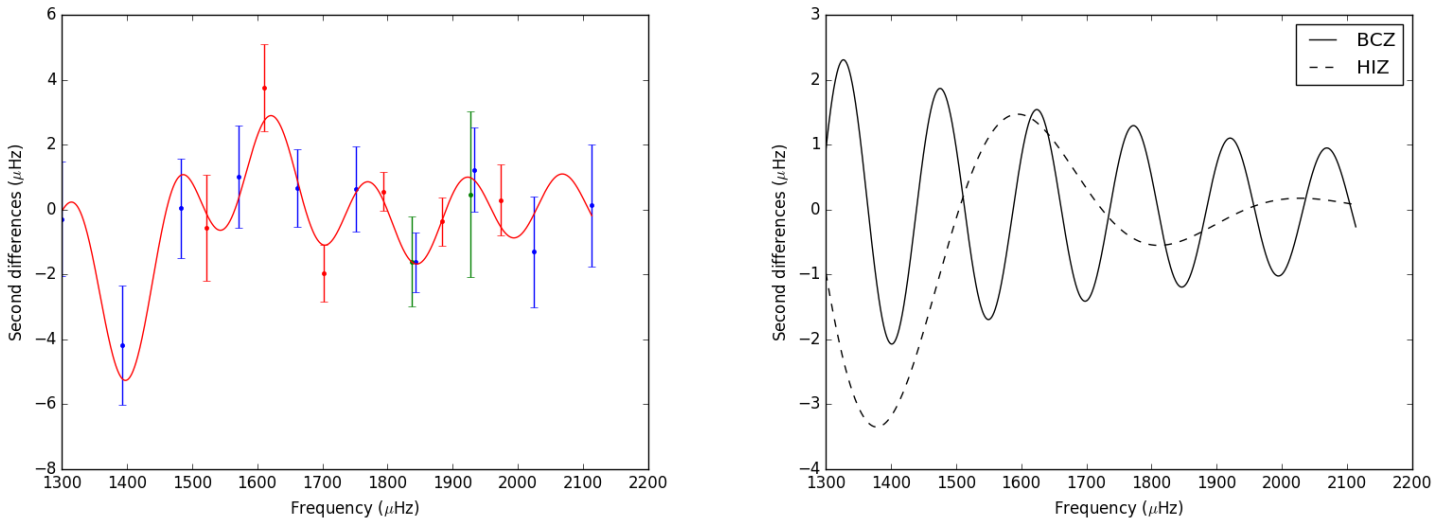

Figure A.55: Same as figure A.51, but for the star KIC 5094751.

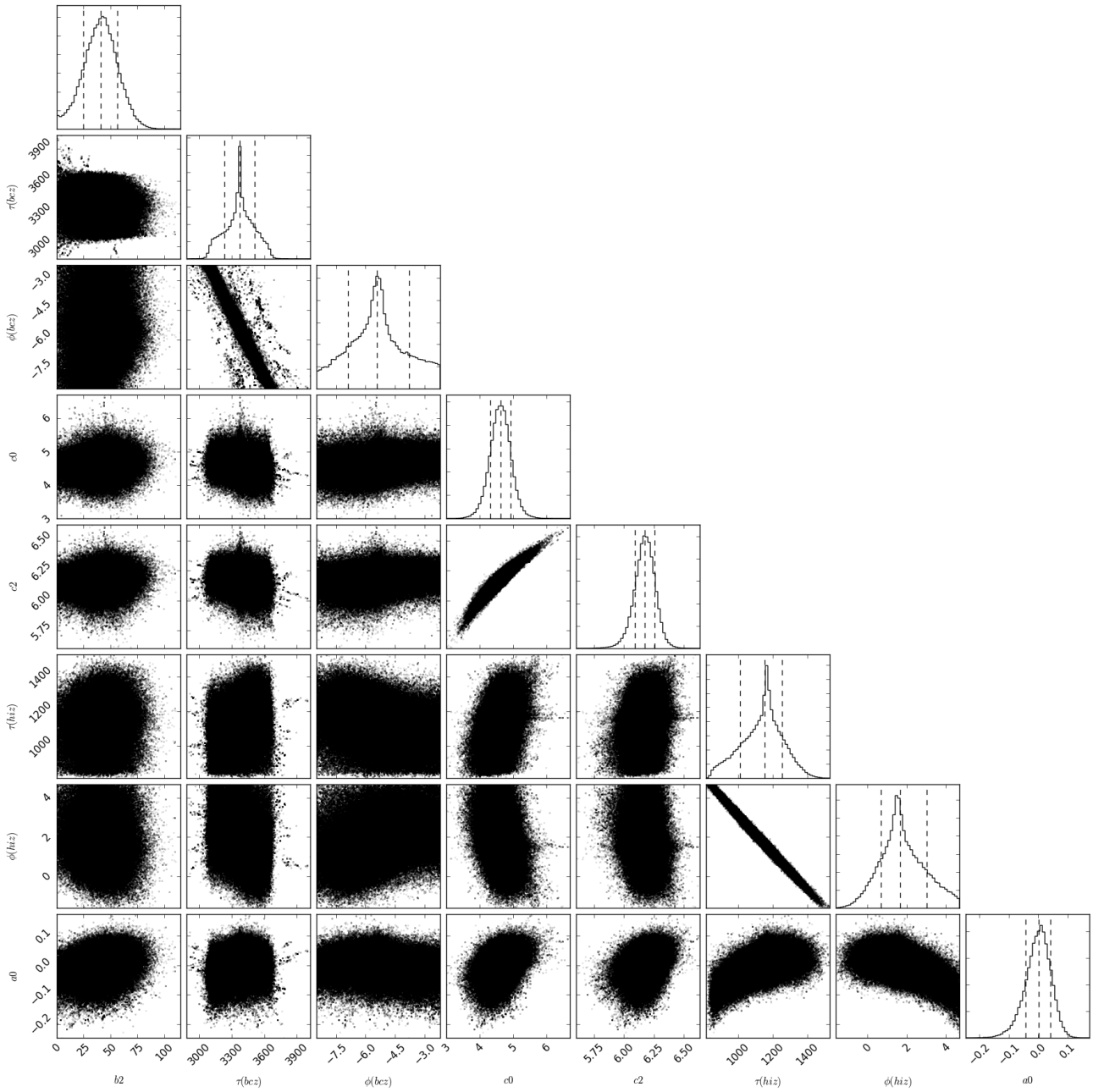

Figure A.56: Same as figure A.52, but for the star KIC 5094751.

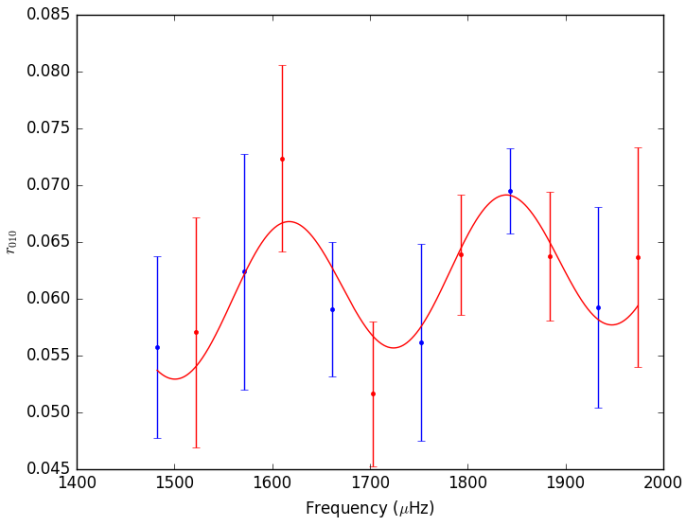

Figure A.57: Same as figure A.53, but for the star KIC 5094751.

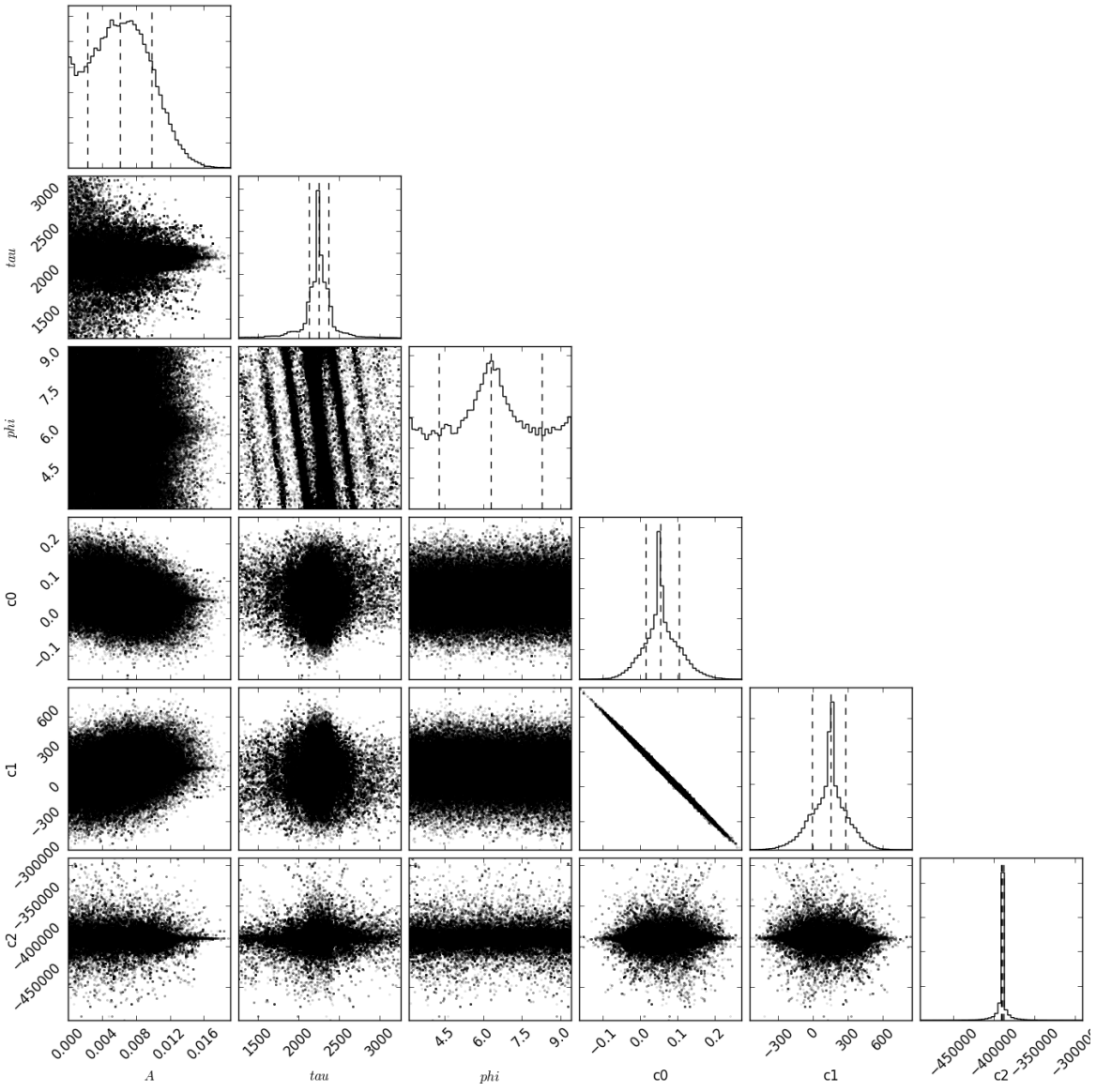

Figure A.58: Same as figure A.54, but for the star KIC 5094751.

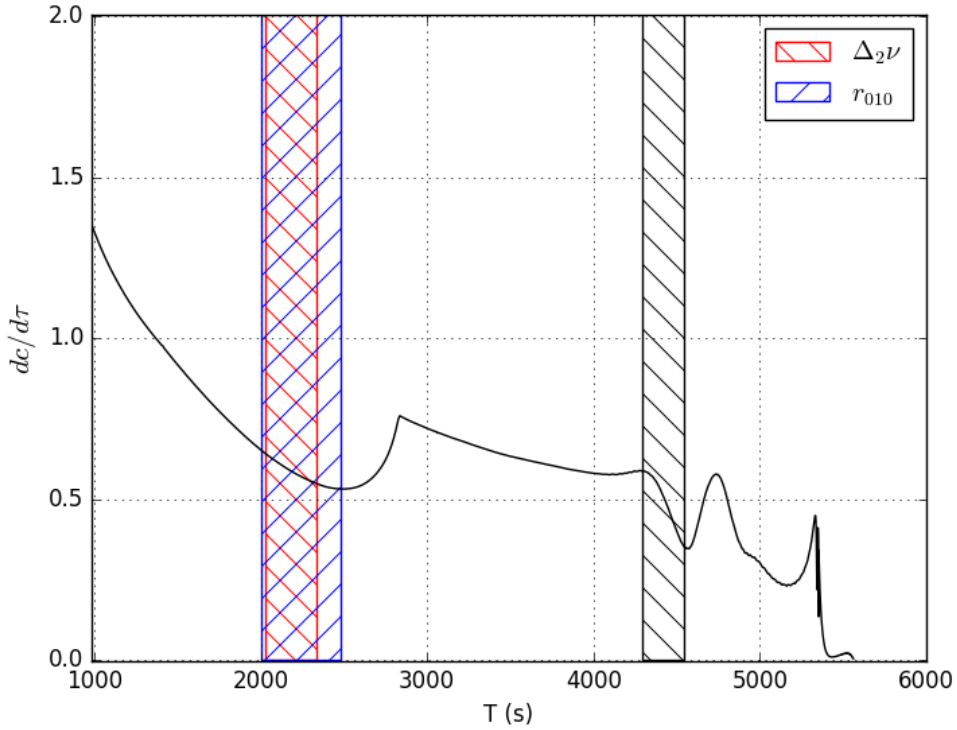

Figure A.59: $\frac{dc}{d\tau}$ versus acoustic radius for the star KIC 5094751. The solid black line are obtained directly from the YREC model. The coloured dashed rectangles represent our estimation of $T_{\rm BCZ}$ and $T_{\rm HIZ}$ using our MCMC algorithm applied to observed *Kepler* frequencies. The width of the rectangles represent the errorbars. The colour code is: black = $T_{\rm HIZ}$, red = $T_{\rm BCZ}$ obtained using $\Delta_2\nu$ and blue = $T_{\rm BCZ}$ obtained using frequency ratios r_{010}

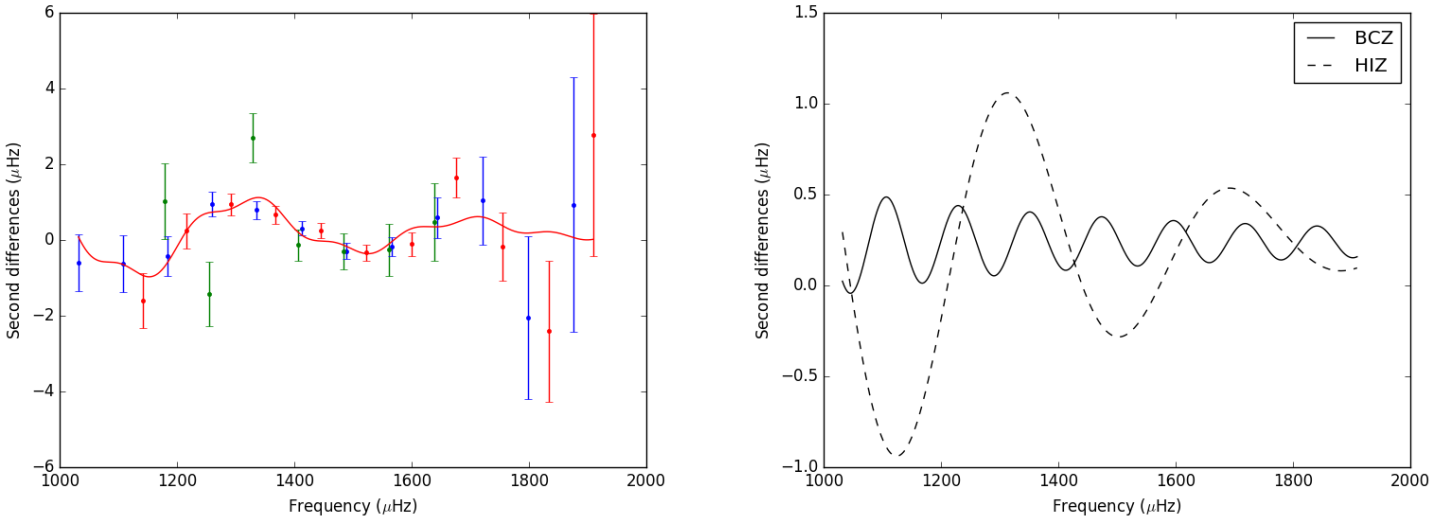

Figure A.60: Same as figure A.51, but for the star KIC 6521045.

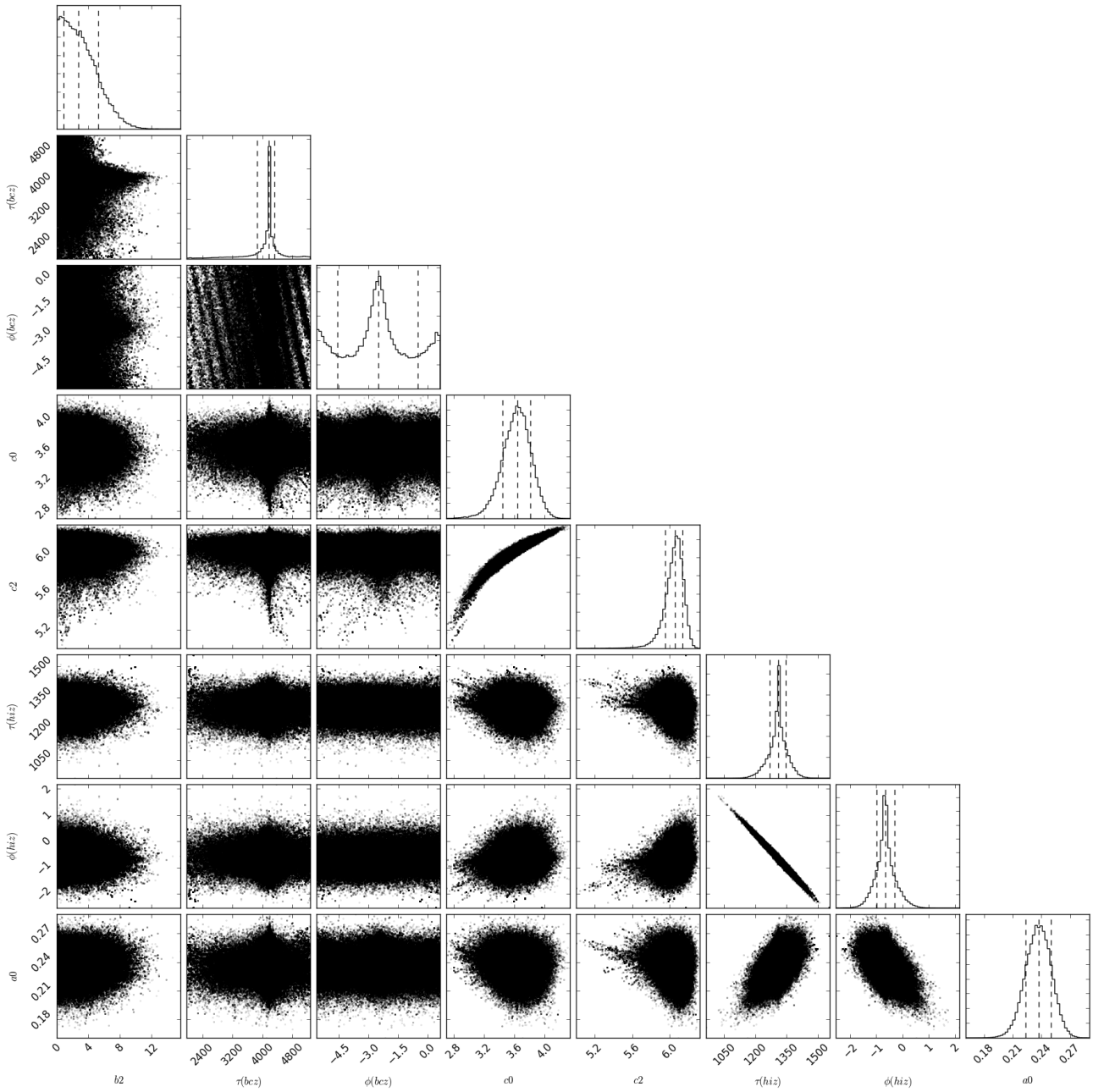

Figure A.61: Same as figure A.52, but for the star KIC 6521045.

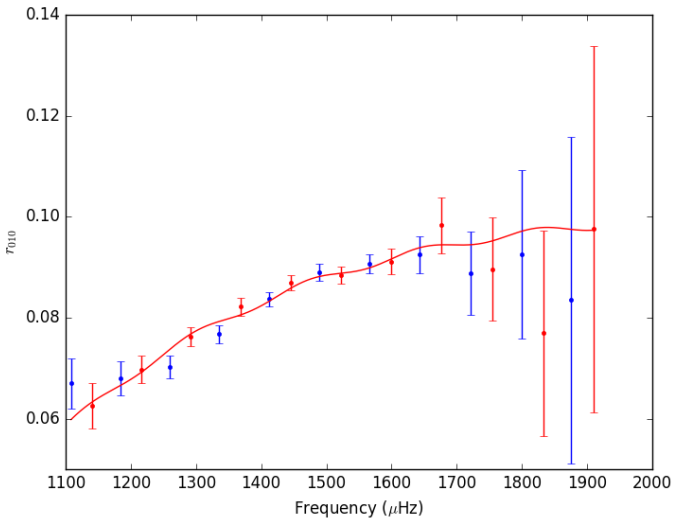

Figure A.62: Same as figure A.53, but for the star KIC 6521045.

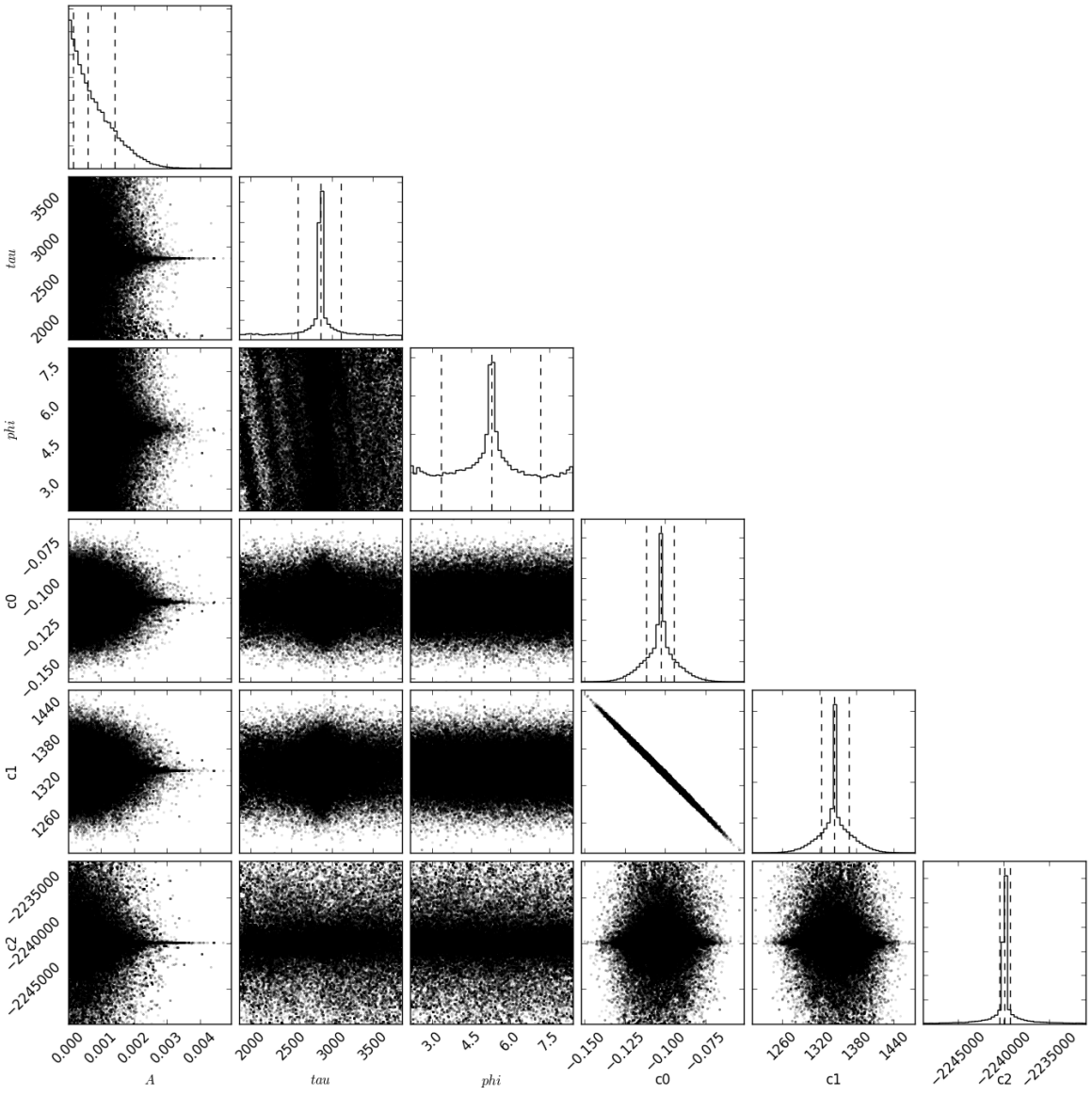

Figure A.63: Same as figure A.54, but for the star KIC 6521045.

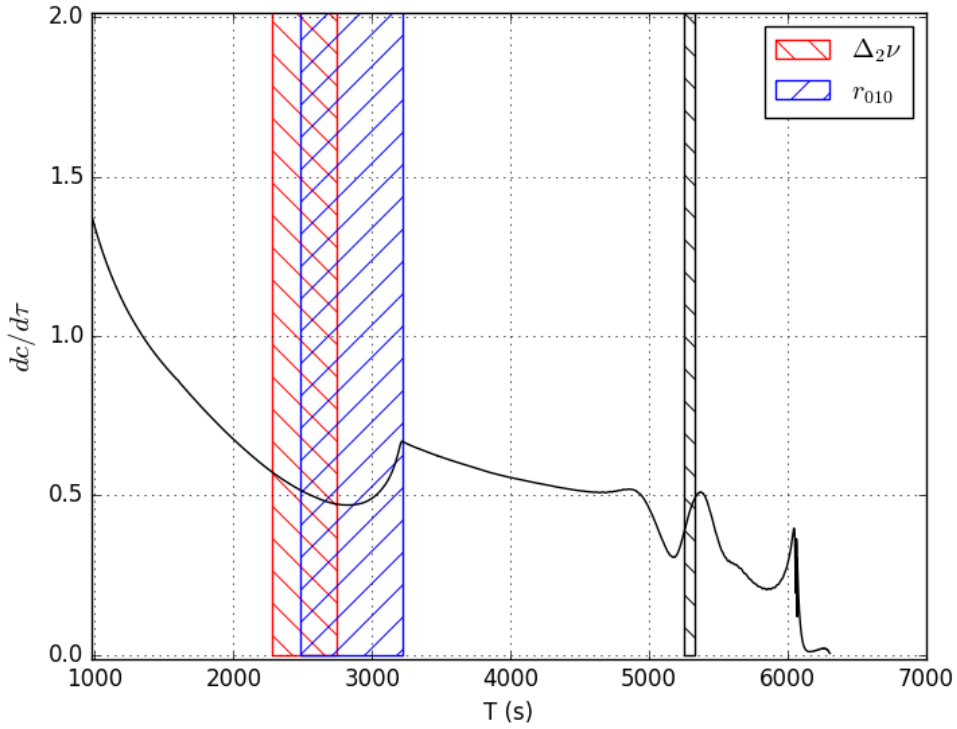

Figure A.64: Same as figure A.59, but for the star KIC 6521045.

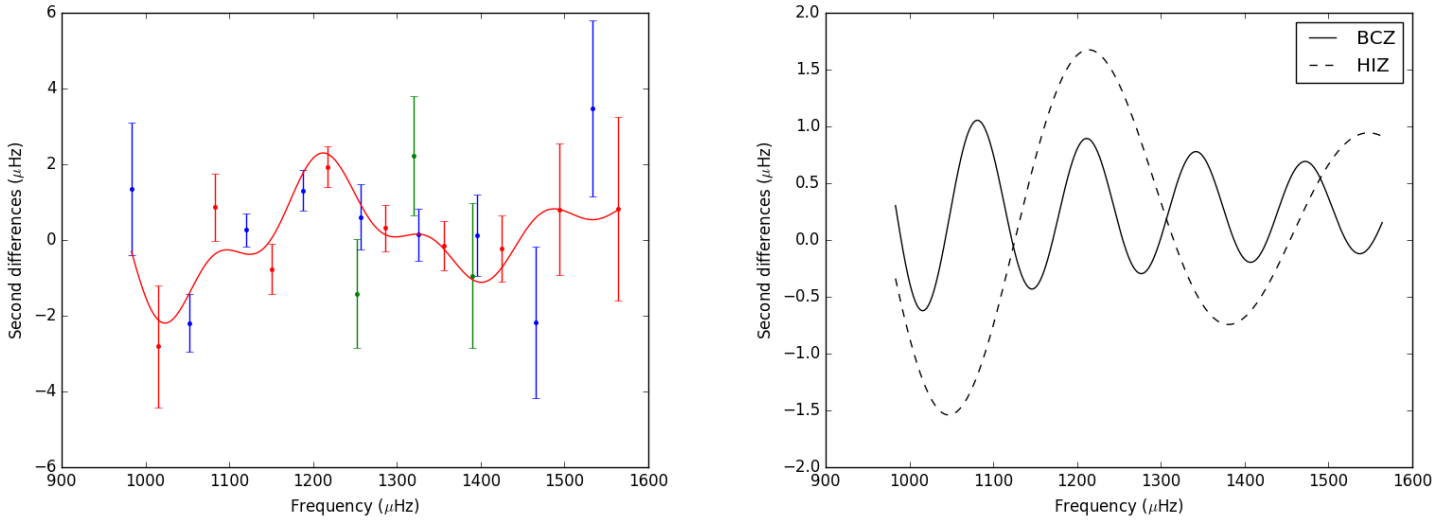

Figure A.65: Same as figure A.51, but for the star KIC 8077137.

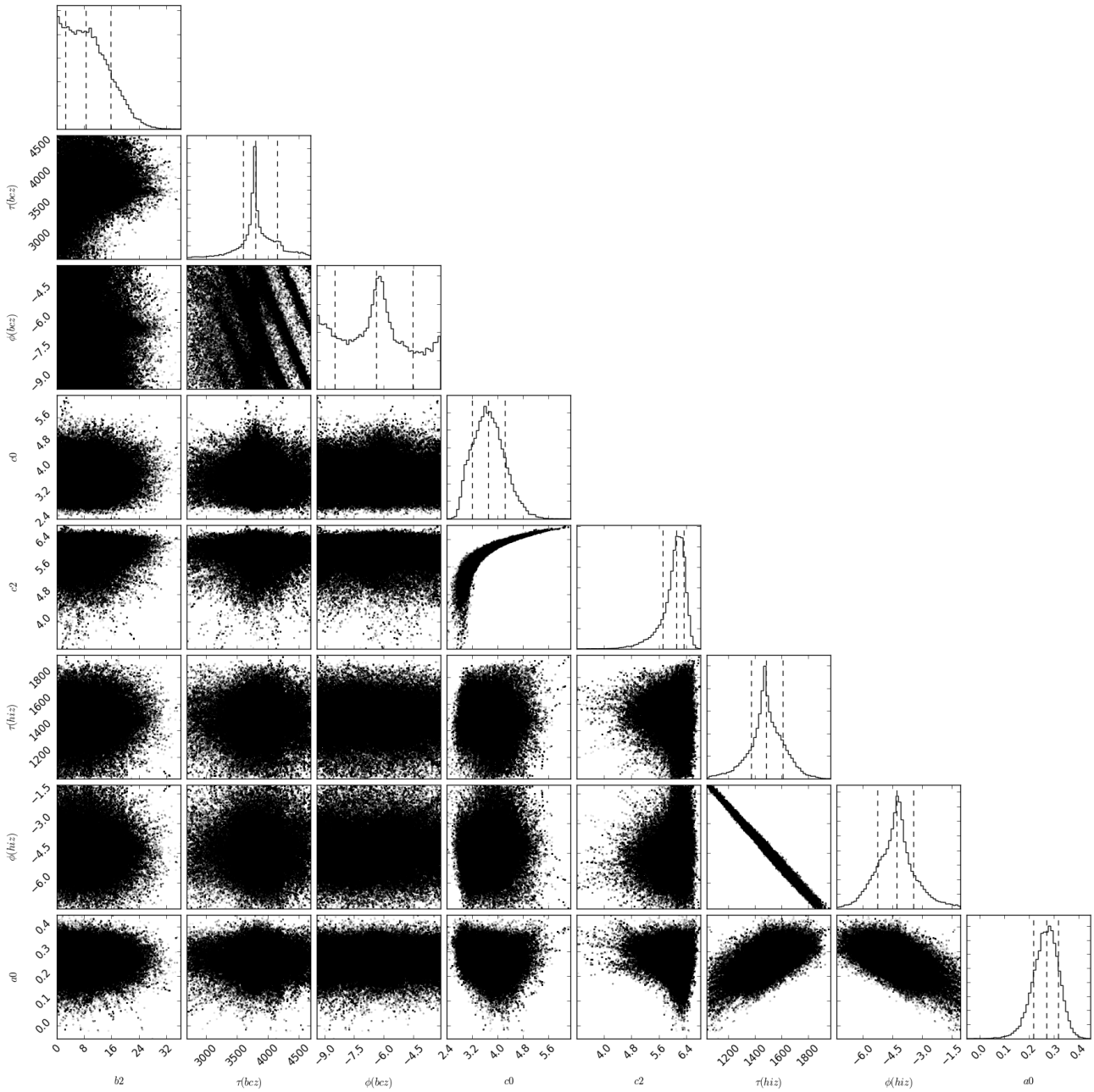

Figure A.66: Same as figure A.52, but for the star KIC 8077137.

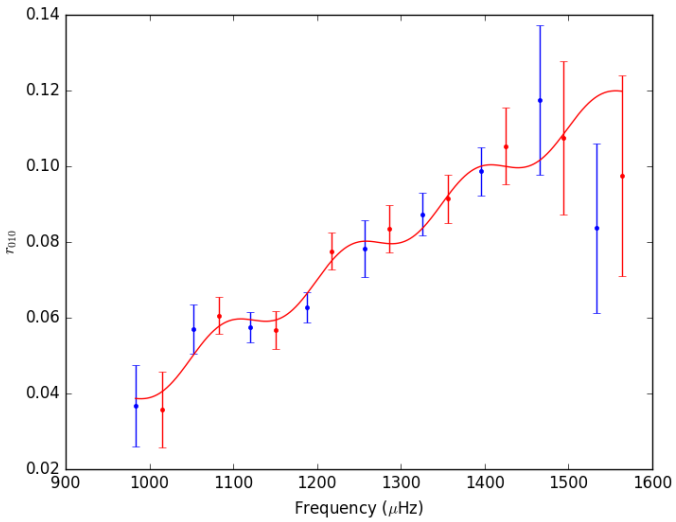

Figure A.67: Same as figure A.53, but for the star KIC 8077137.

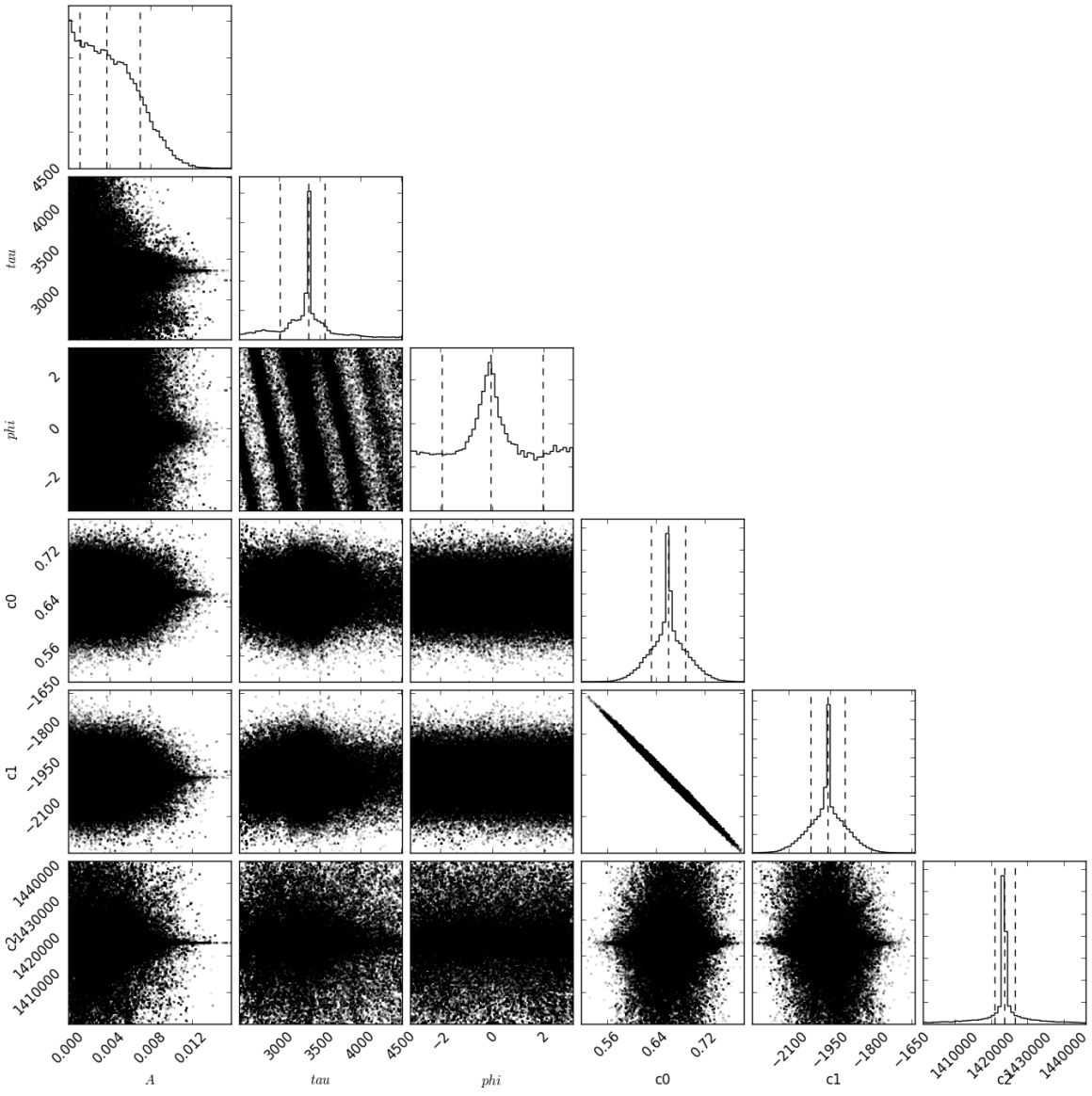

Figure A.68: Same as figure A.54, but for the star KIC 8077137.

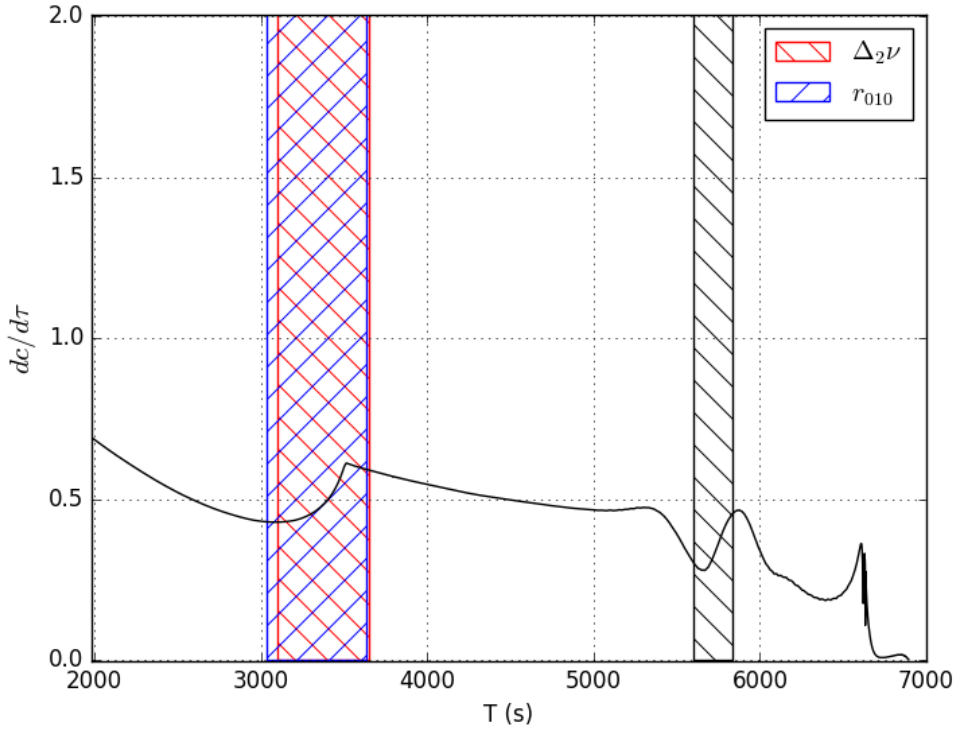

Figure A.69: Same as figure A.59, but for the star KIC 8077137.

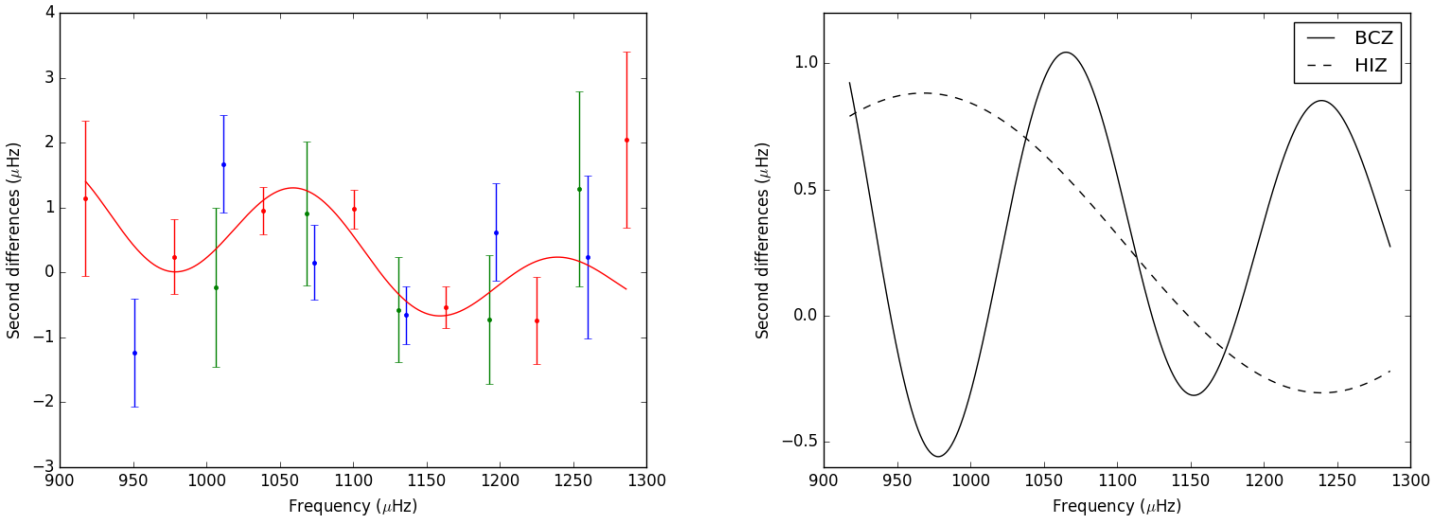

Figure A.70: Same as figure A.51, but for the star KIC 8554498.

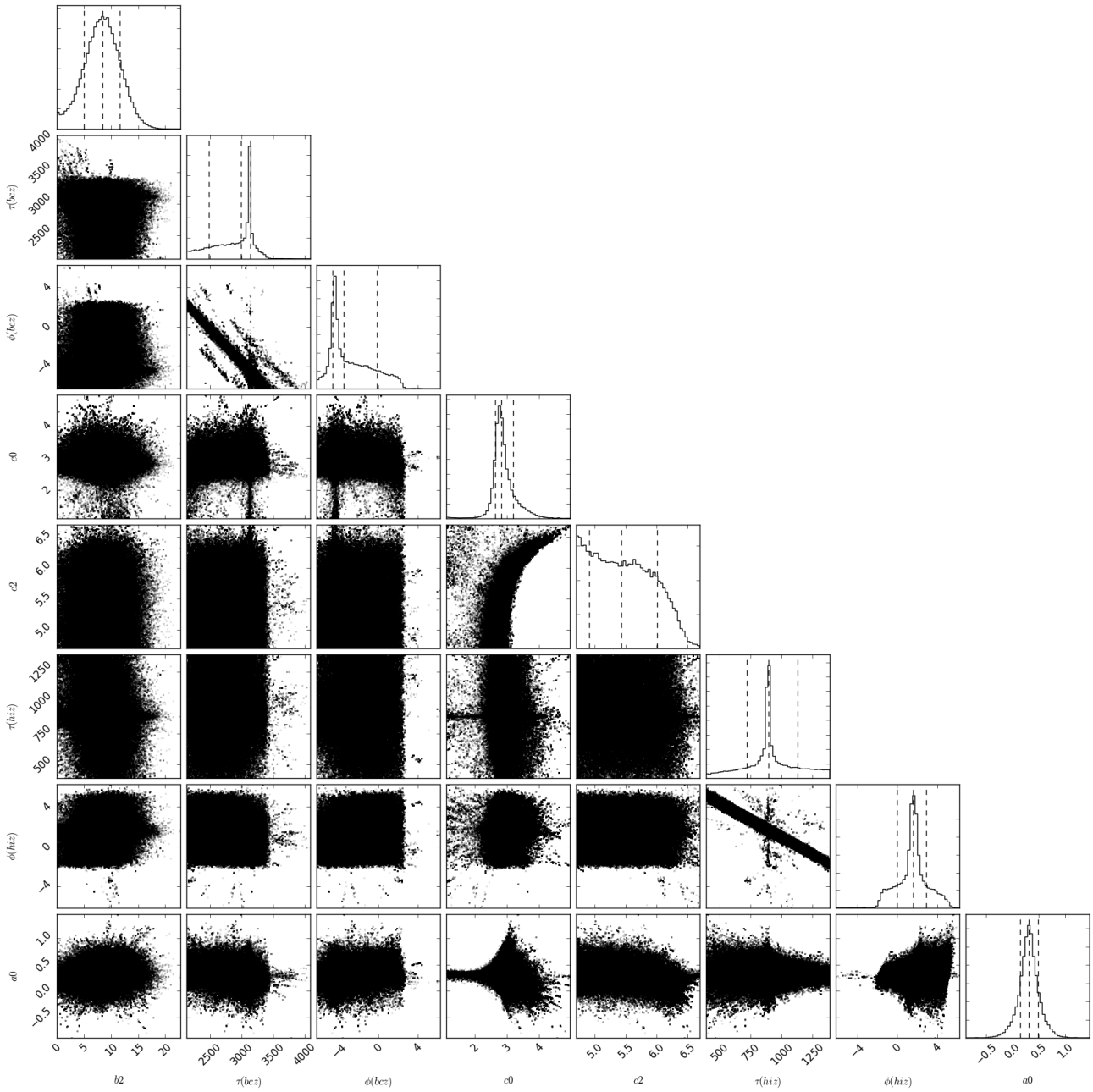

Figure A.71: Same as figure A.52, but for the star KIC 8554498.

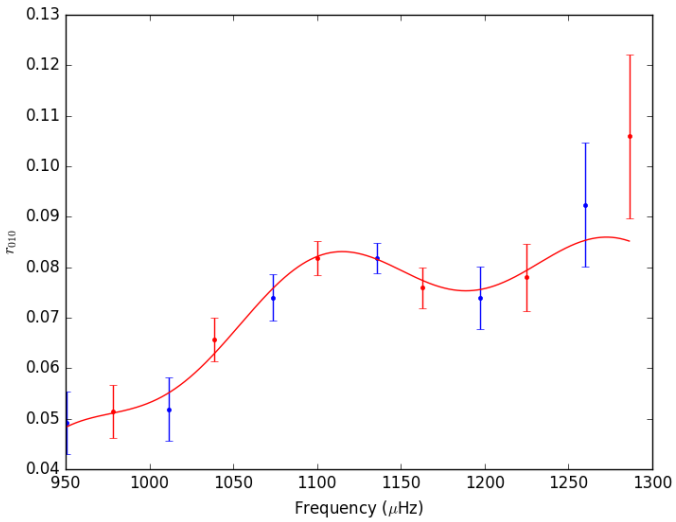

Figure A.72: Same as figure A.53, but for the star KIC 8554498.

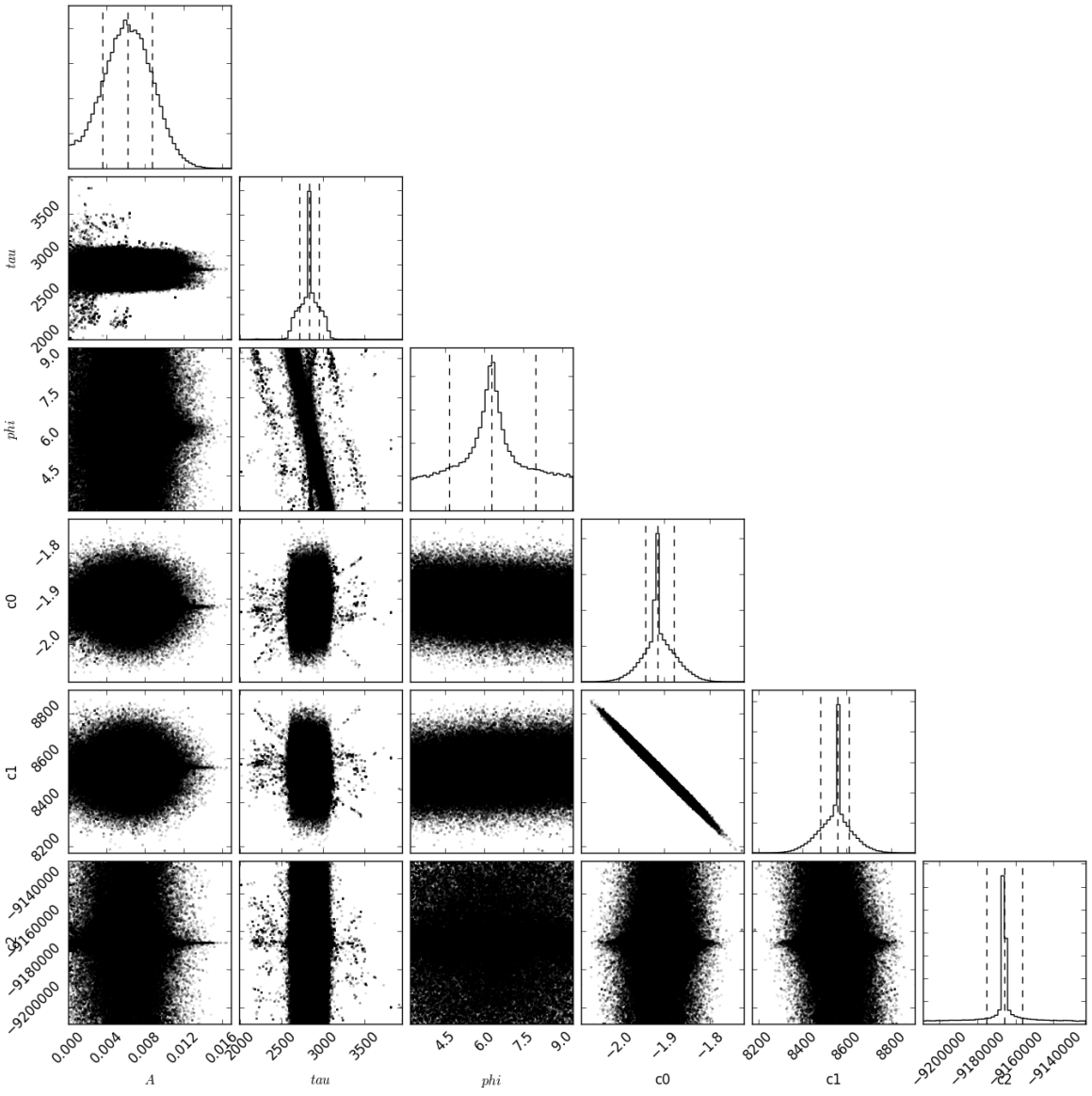

Figure A.73: Same as figure A.54, but for the star KIC 8554498.

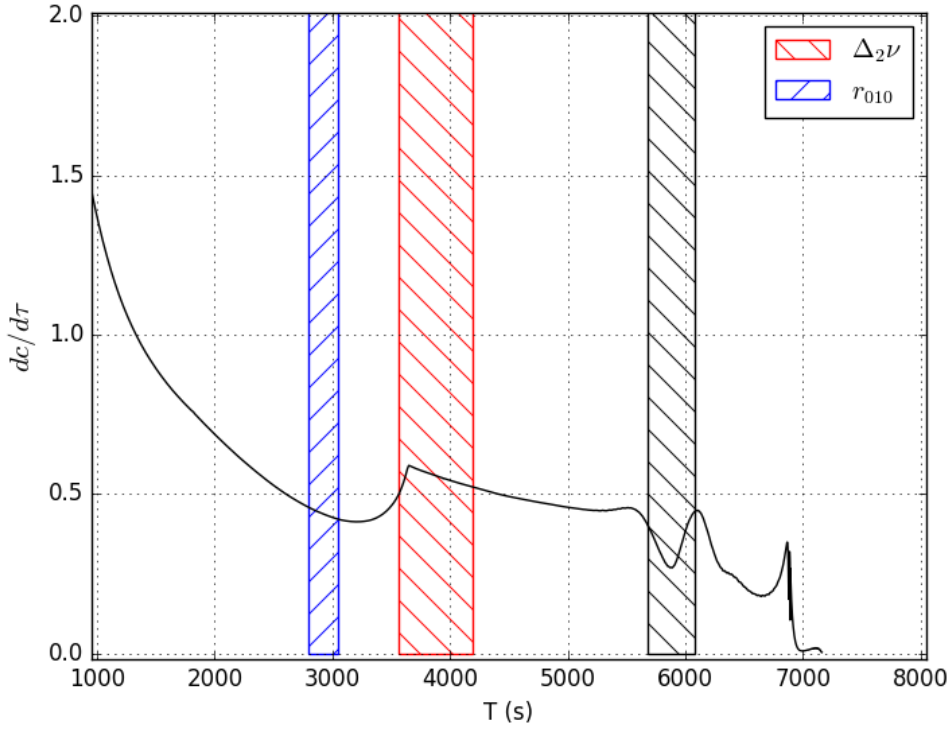

Figure A.74: Same as figure A.59, but for the star KIC 8554498.

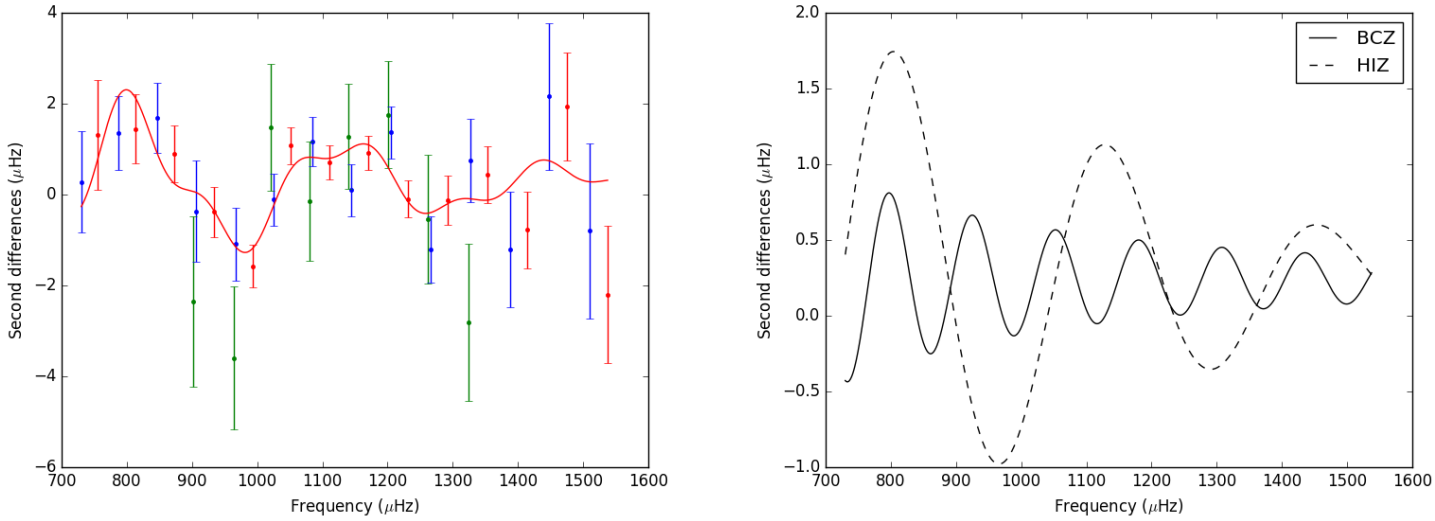

Figure A.75: Same as figure A.51, but for the star KIC 9414417.

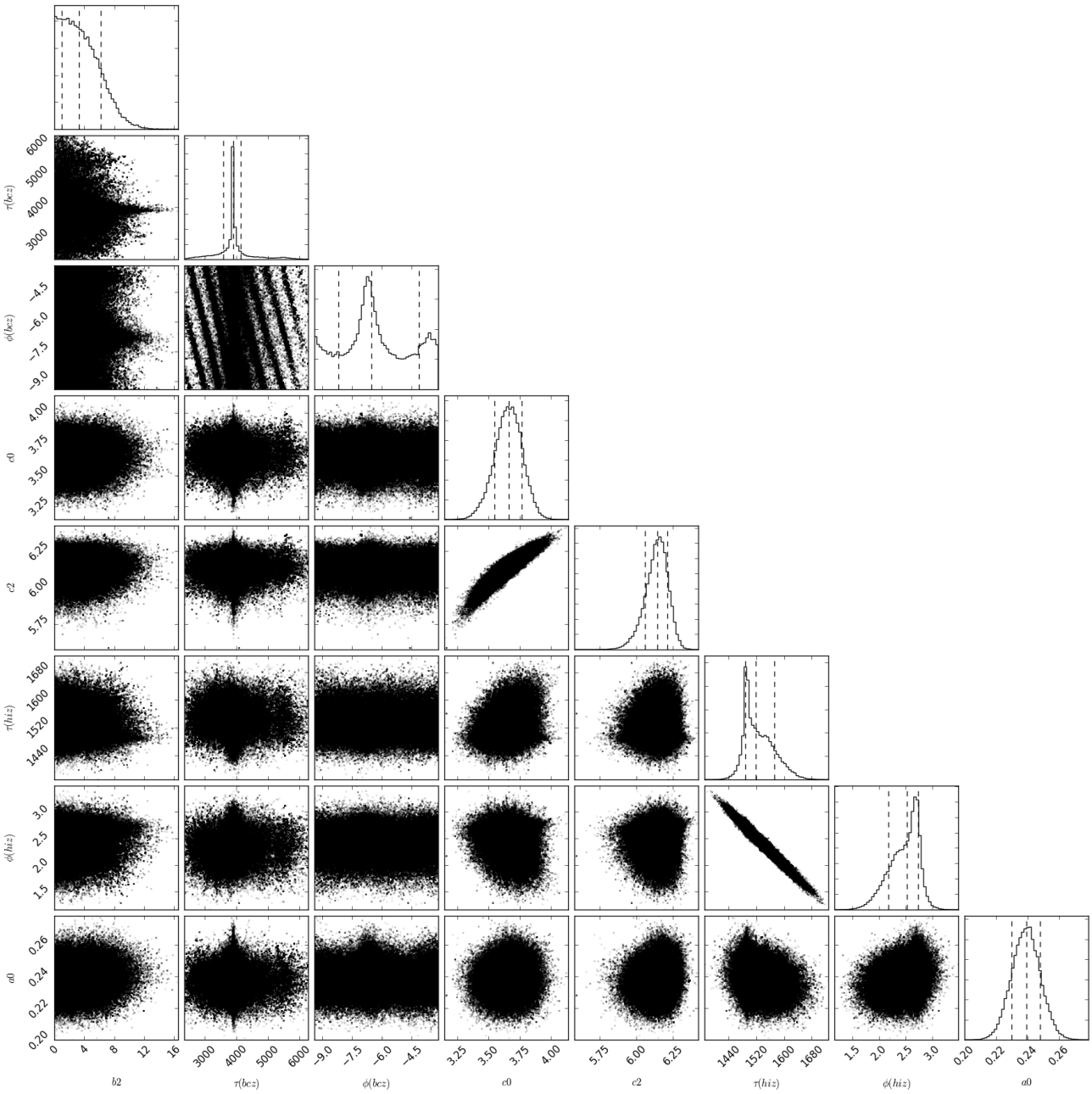

Figure A.76: Same as figure A.52, but for the star KIC 9414417.

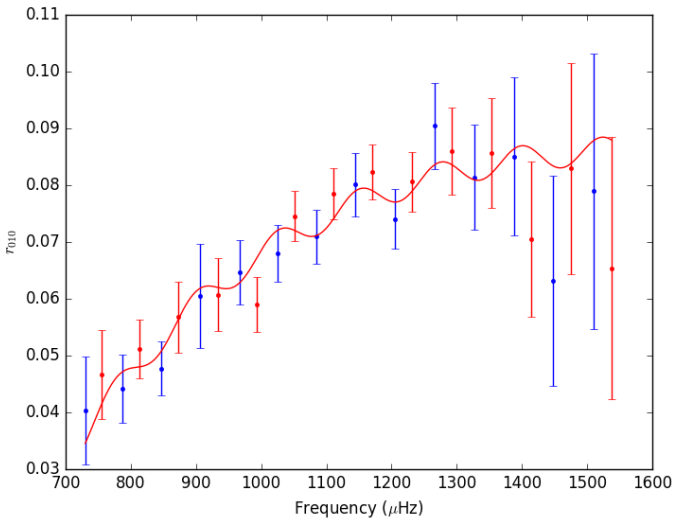

Figure A.77: Same as figure A.53, but for the star KIC 9414417.

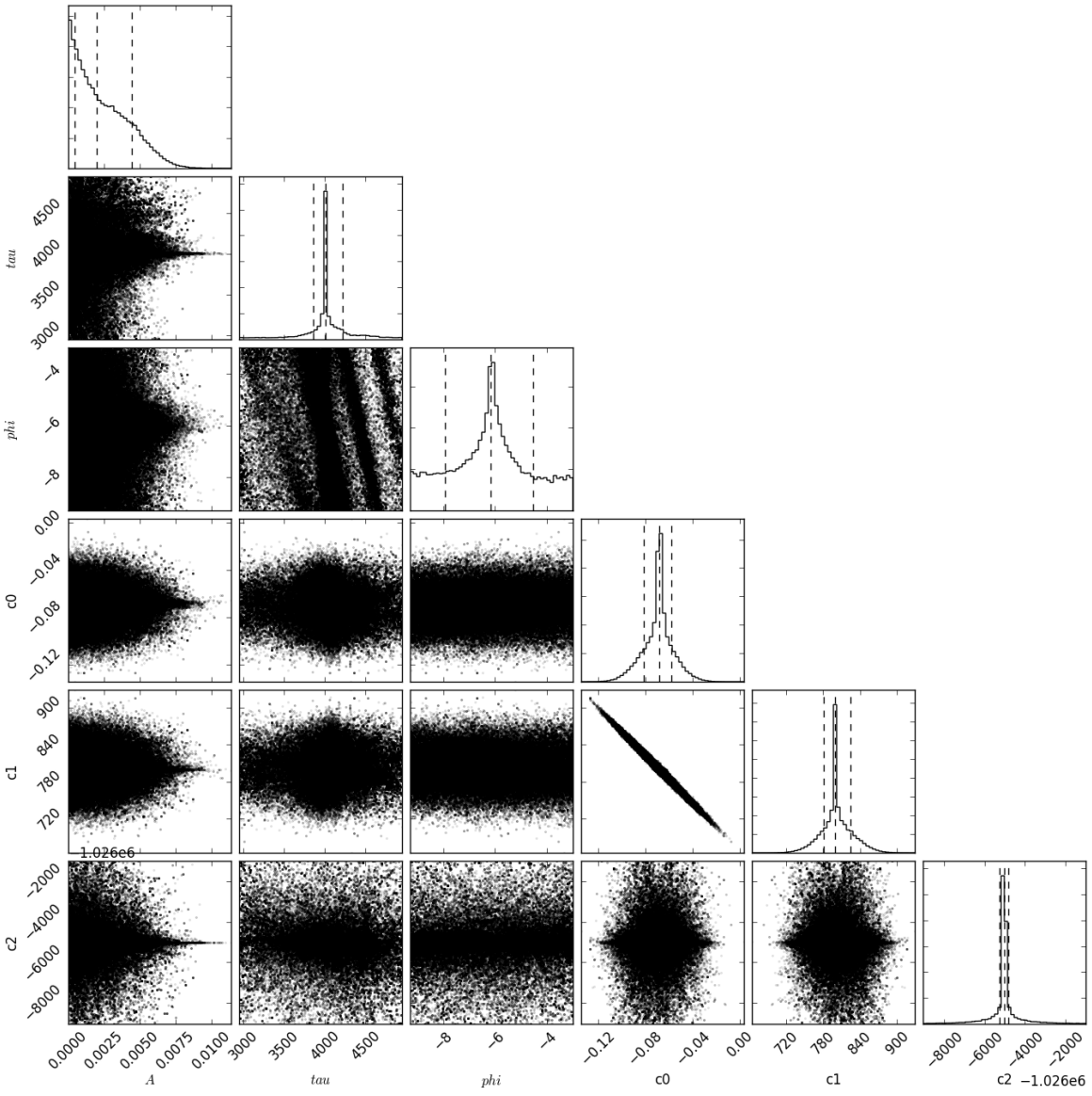

Figure A.78: Same as figure A.54, but for the star KIC 9414417.

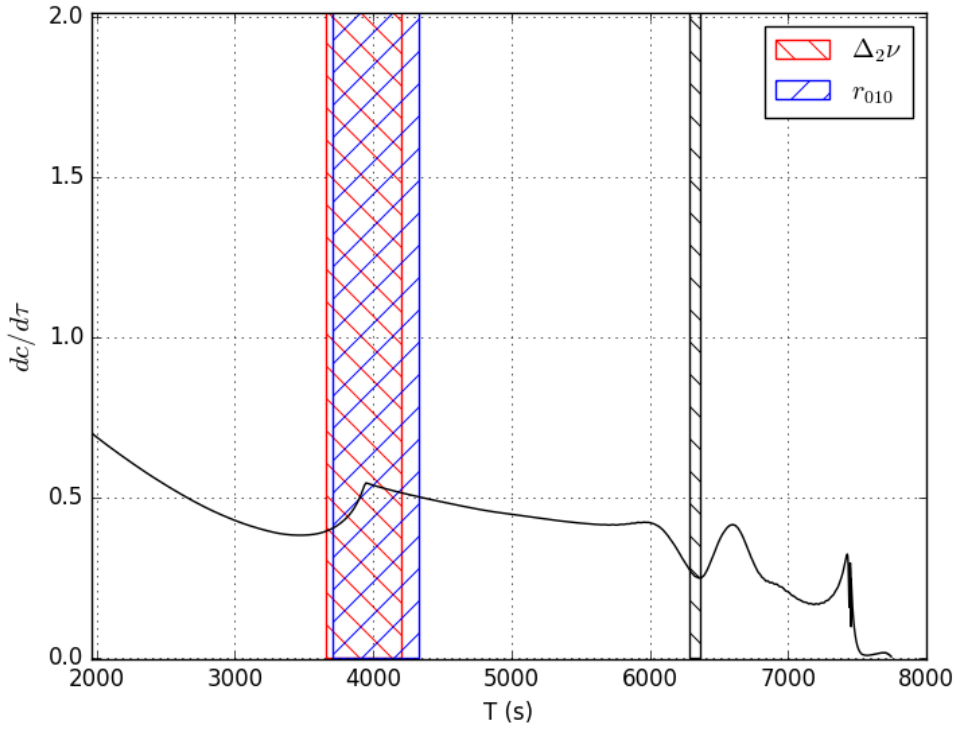

Figure A.79: Same as figure A.59, but for the star KIC 9414417.

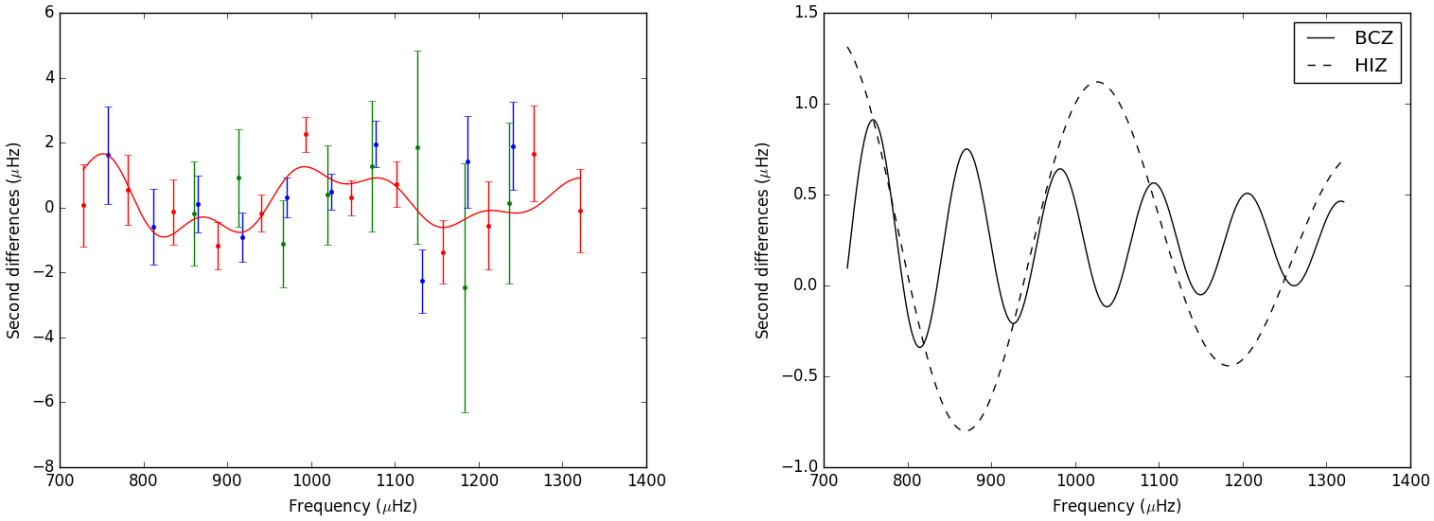

Figure A.80: Same as figure A.51, but for the star KIC 9592705.

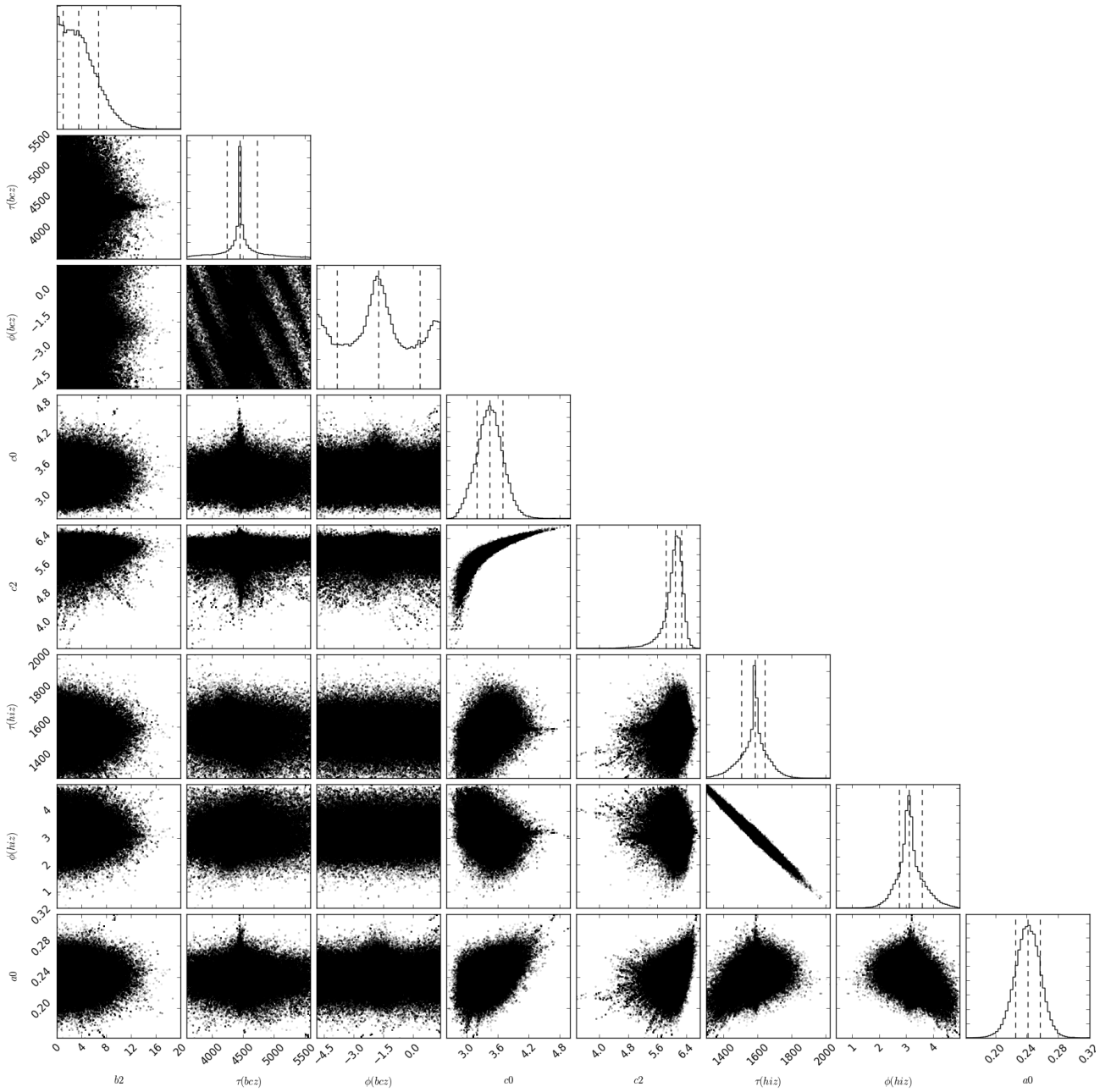

Figure A.81: Same as figure A.52, but for the star KIC 9592705.

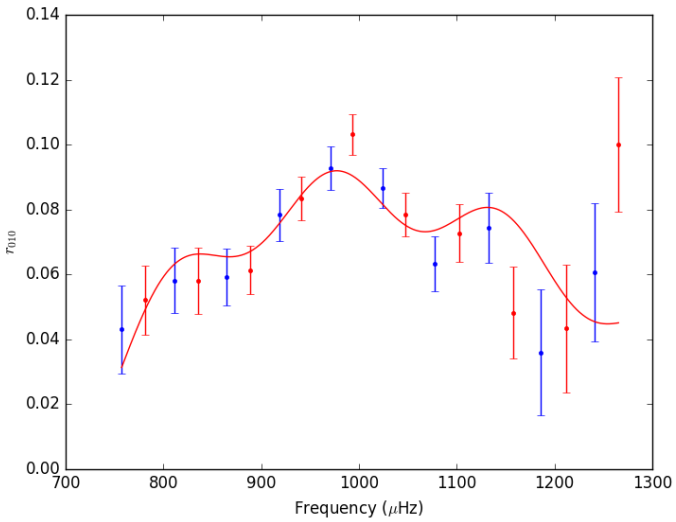

Figure A.82: Same as figure A.53, but for the star KIC 9592705.

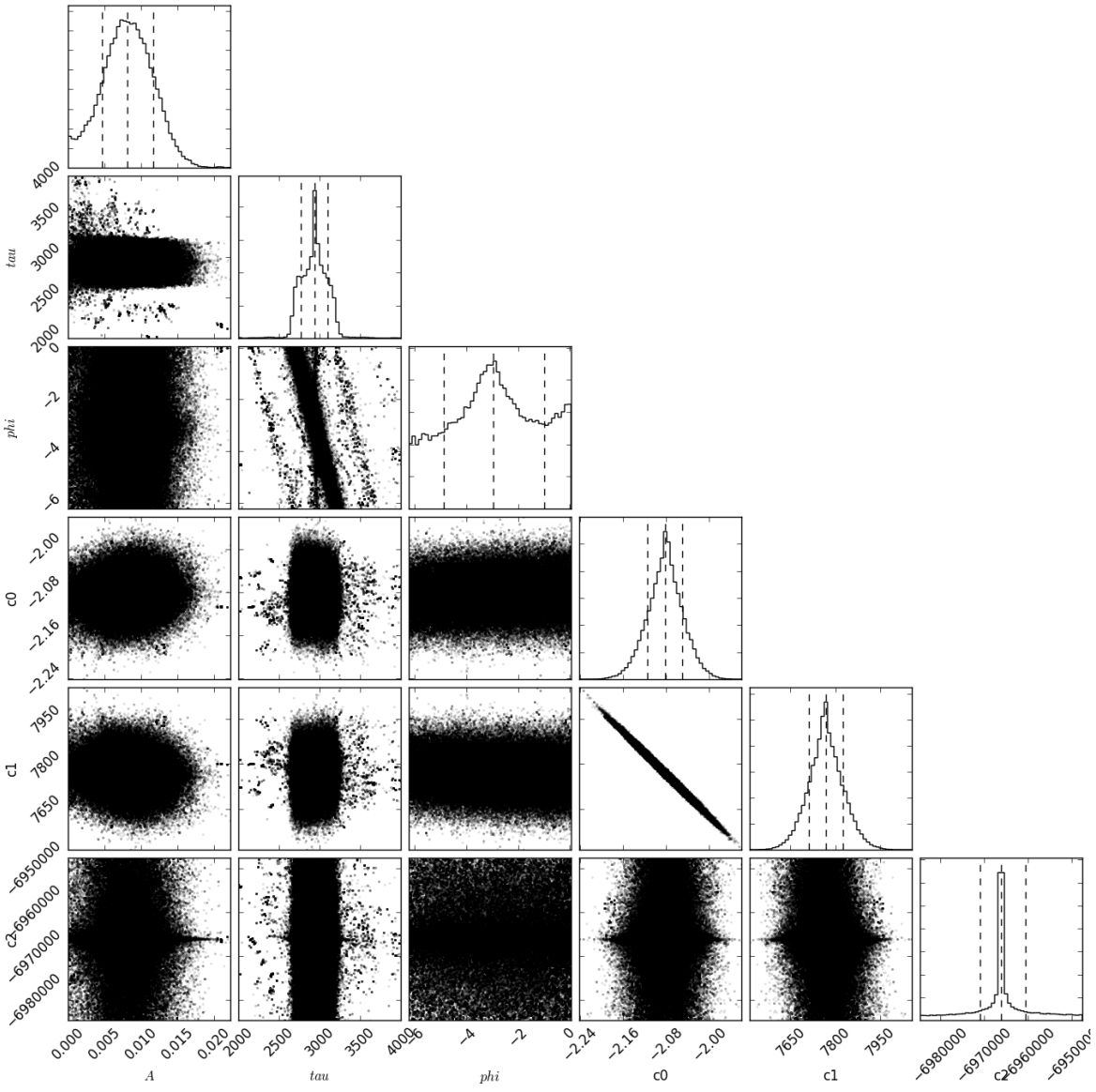

Figure A.83: Same as figure A.54, but for the star KIC 9592705.

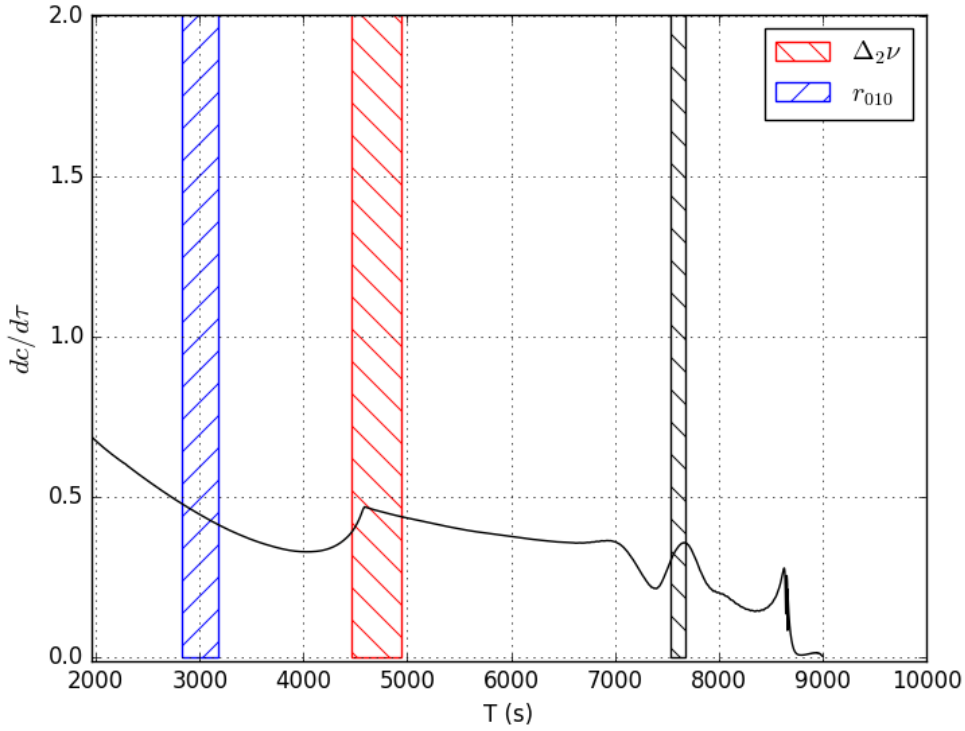

Figure A.84: Same as figure A.59, but for the star KIC 9592705.

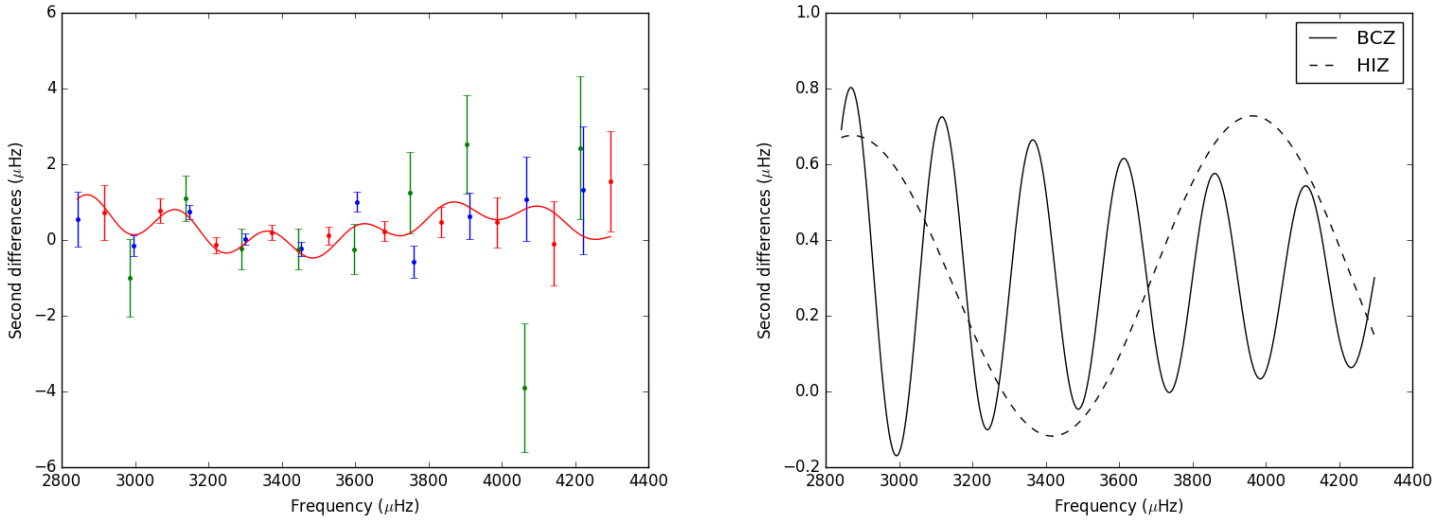

Figure A.85: Same as figure A.51, but for the star KIC 9955598.

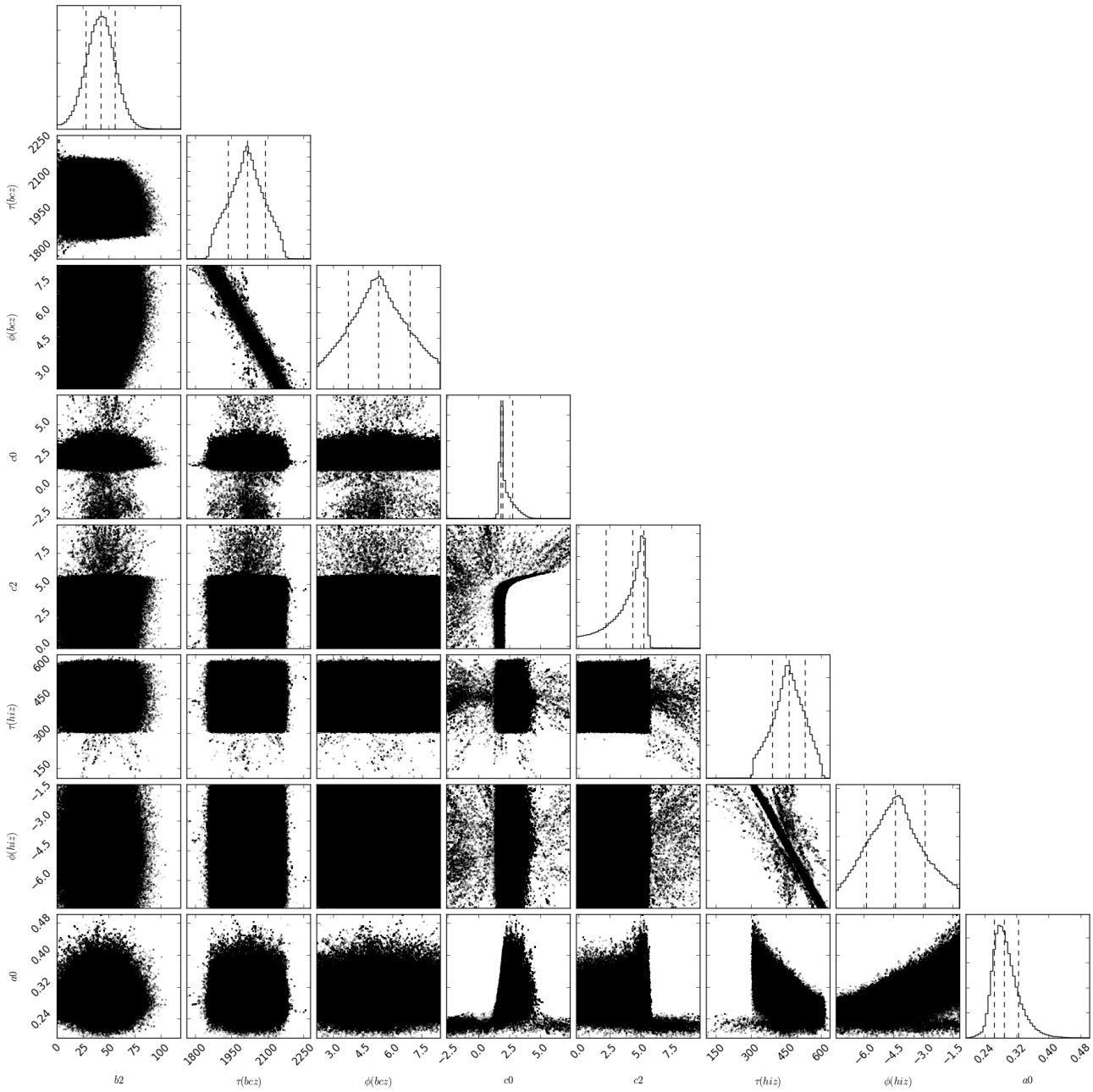

Figure A.86: Same as figure A.52, but for the star KIC 9955598.

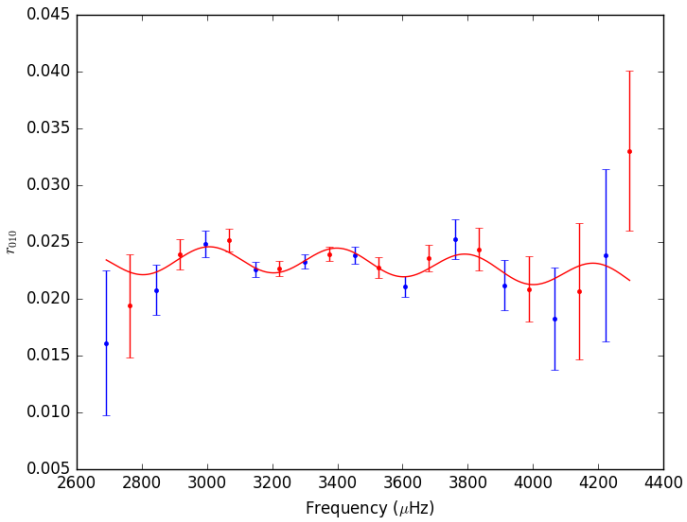

Figure A.87: Same as figure A.53, but for the star KIC 9955598.

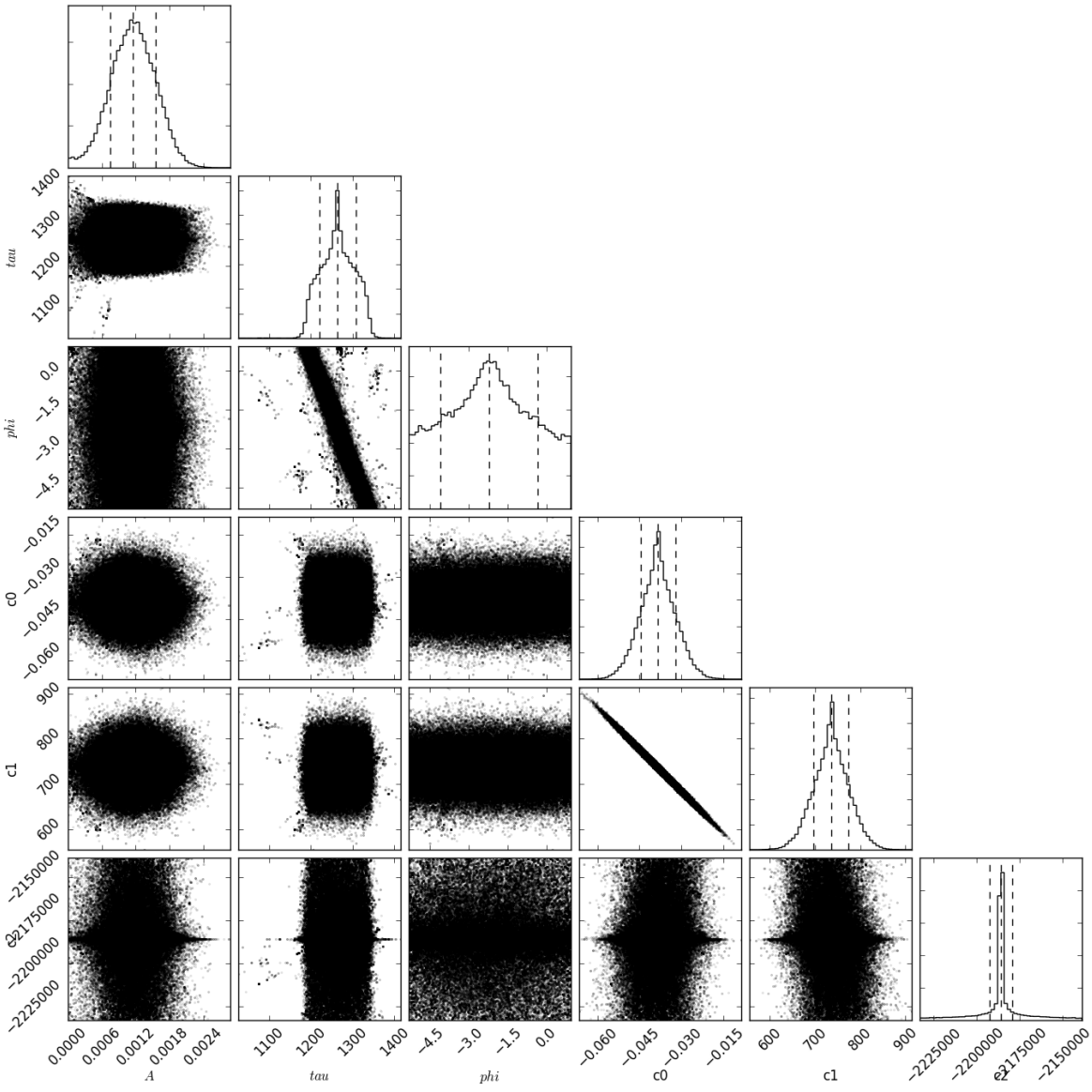

Figure A.88: Same as figure A.54, but for the star KIC 9955598.

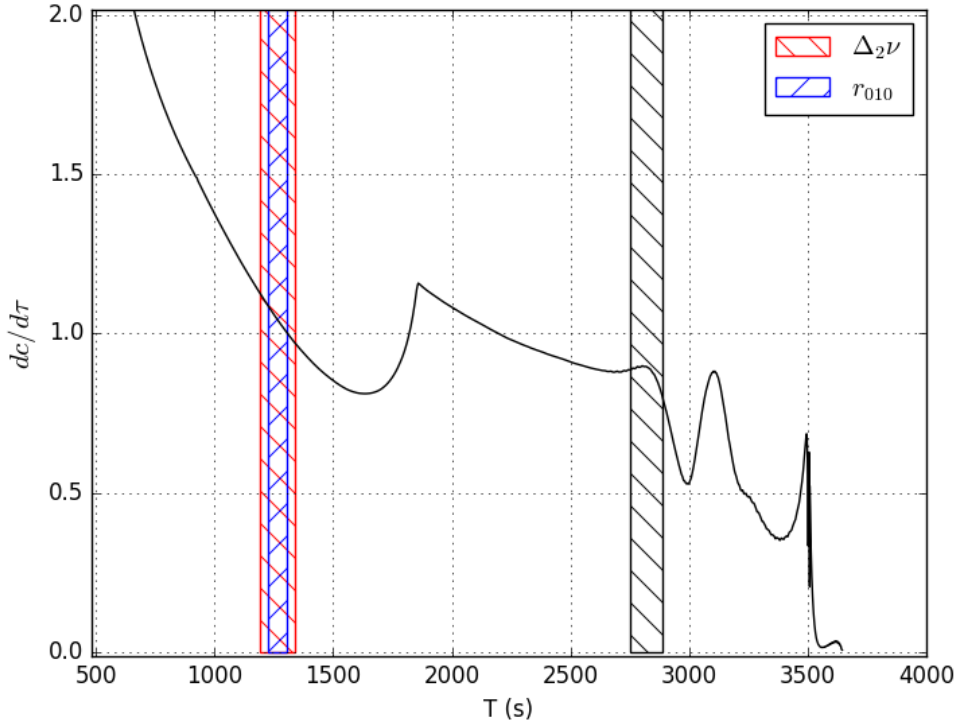

Figure A.89: Same as figure A.59, but for the star KIC 9955598.

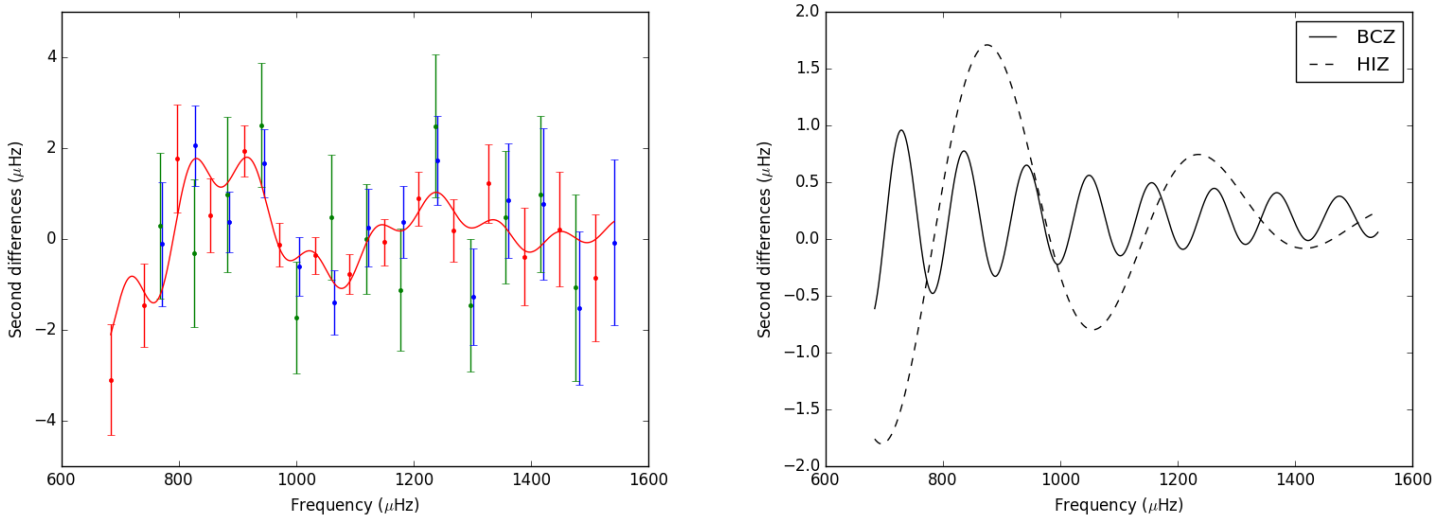

Figure A.90: Same as figure A.51, but for the star KIC 10666592.

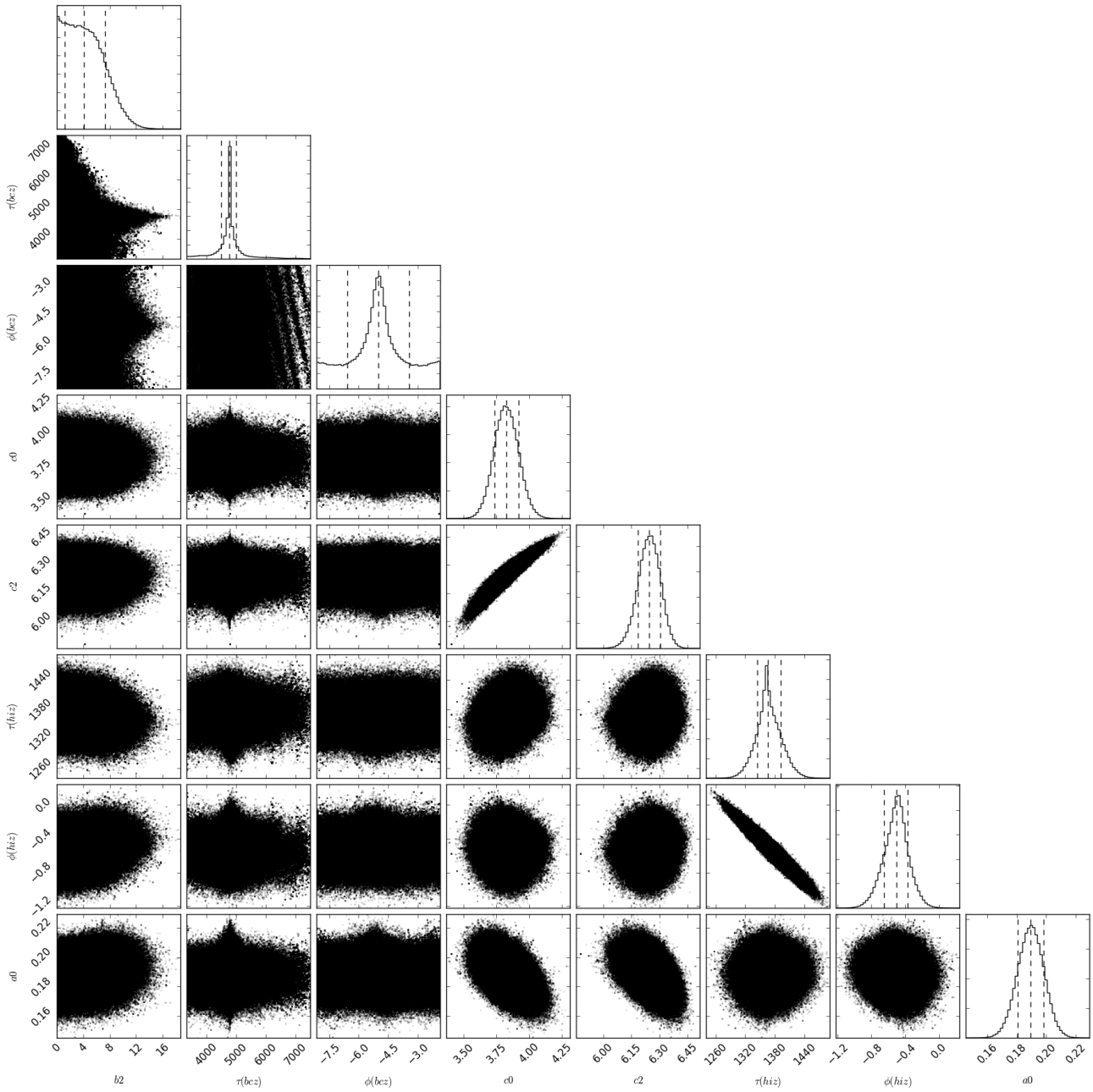

Figure A.91: Same as figure A.52, but for the star KIC 10666592.

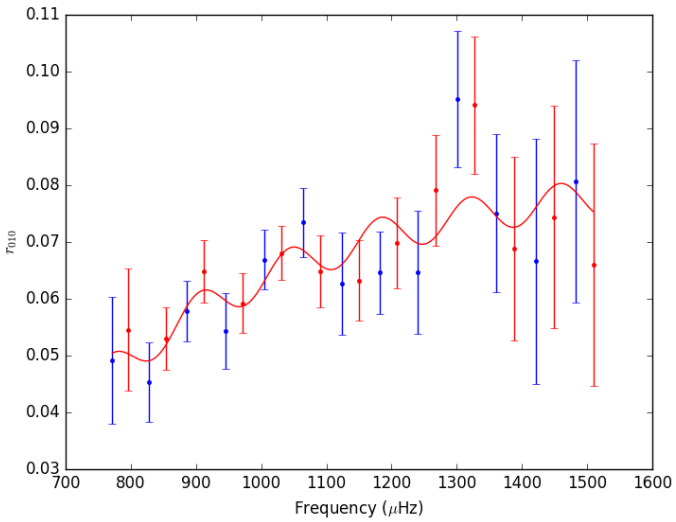

Figure A.92: Same as figure A.53, but for the star KIC 10666592.

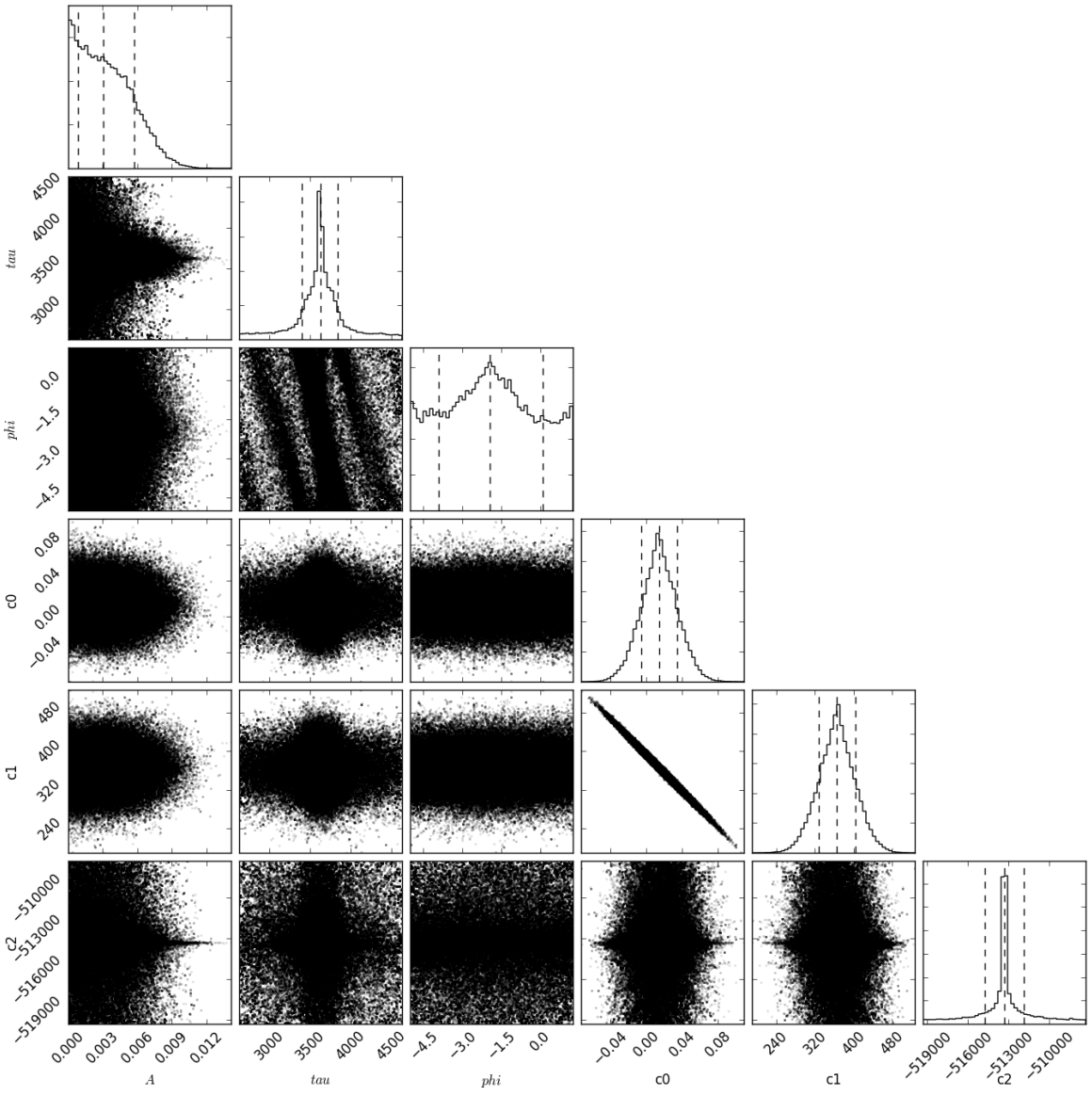

Figure A.93: Same as figure A.54, but for the star KIC 10666592.

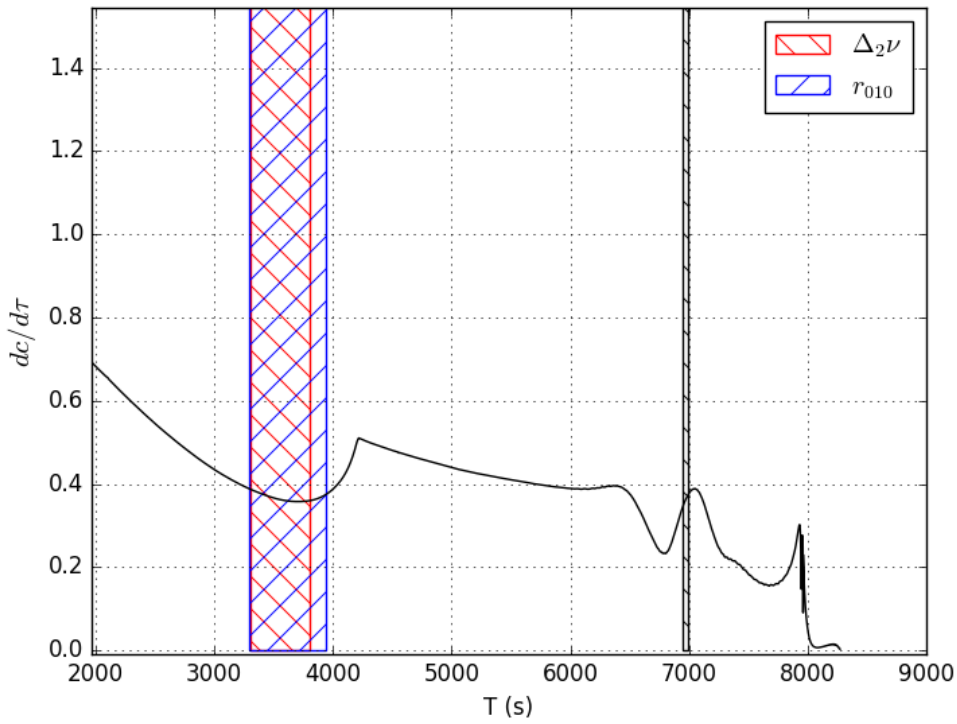

Figure A.94: Same as figure A.59, but for the star KIC 10666592.

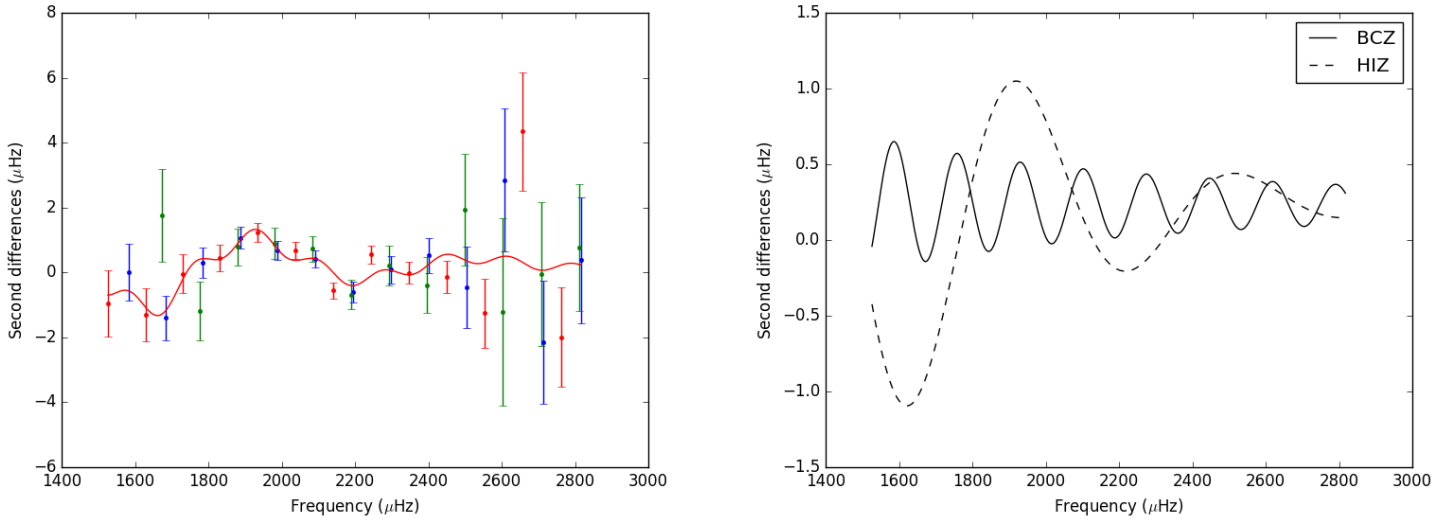

Figure A.95: Same as figure A.51, but for the star KIC 10963065.

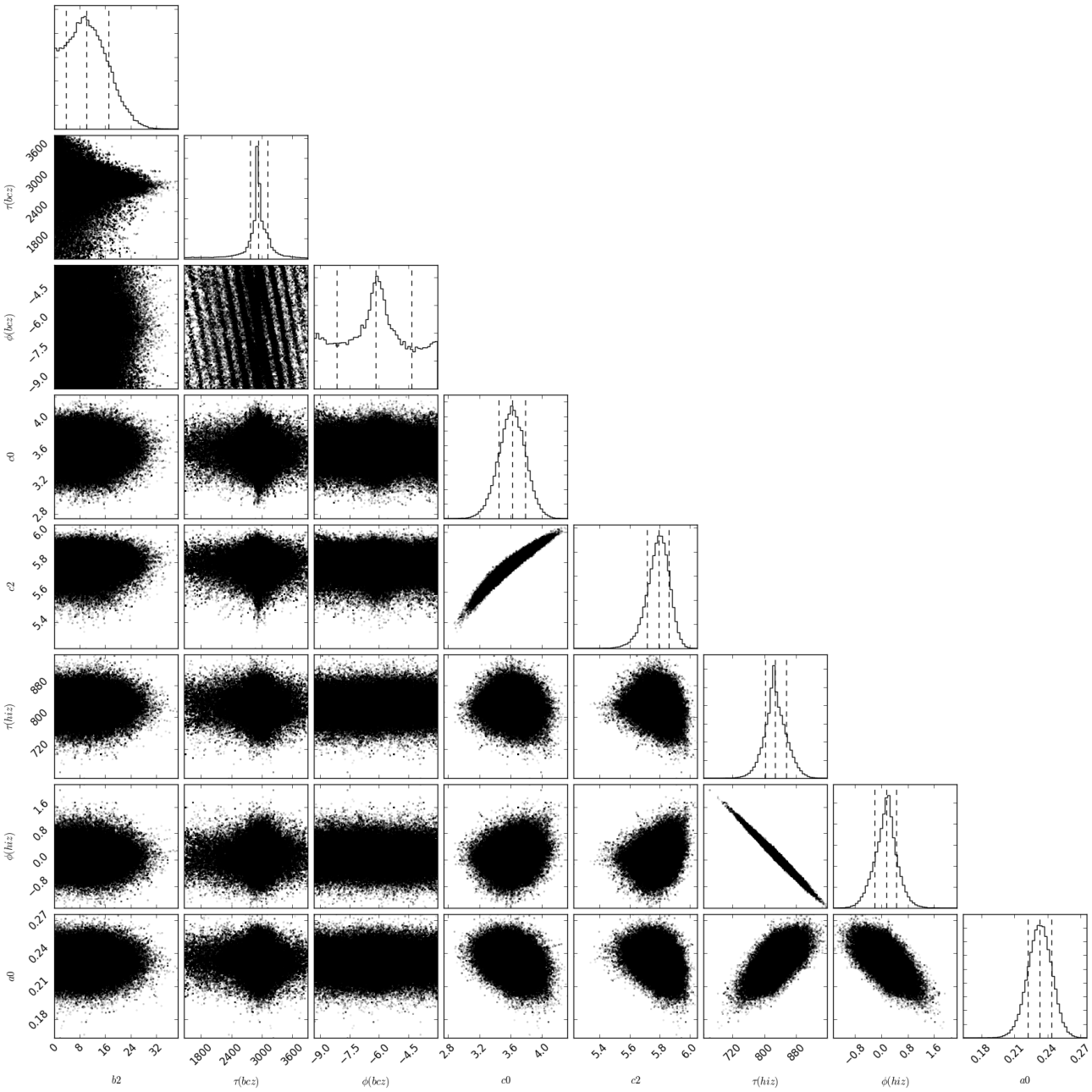

Figure A.96: Same as figure A.52, but for the star KIC 10963065.

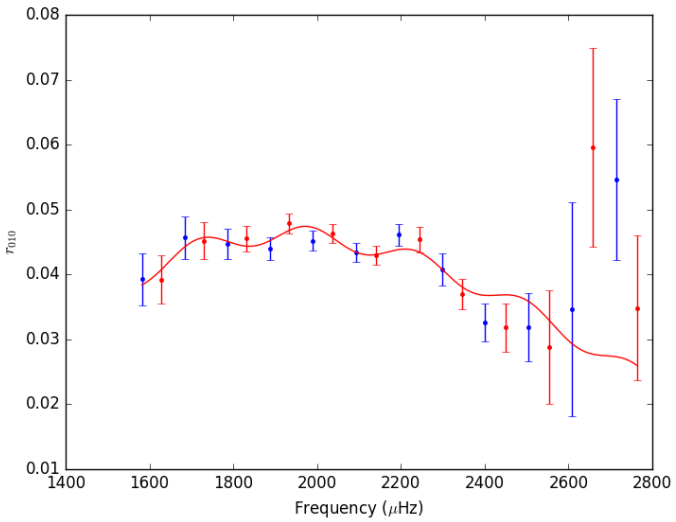

Figure A.97: Same as figure A.53, but for the star KIC 10963065.

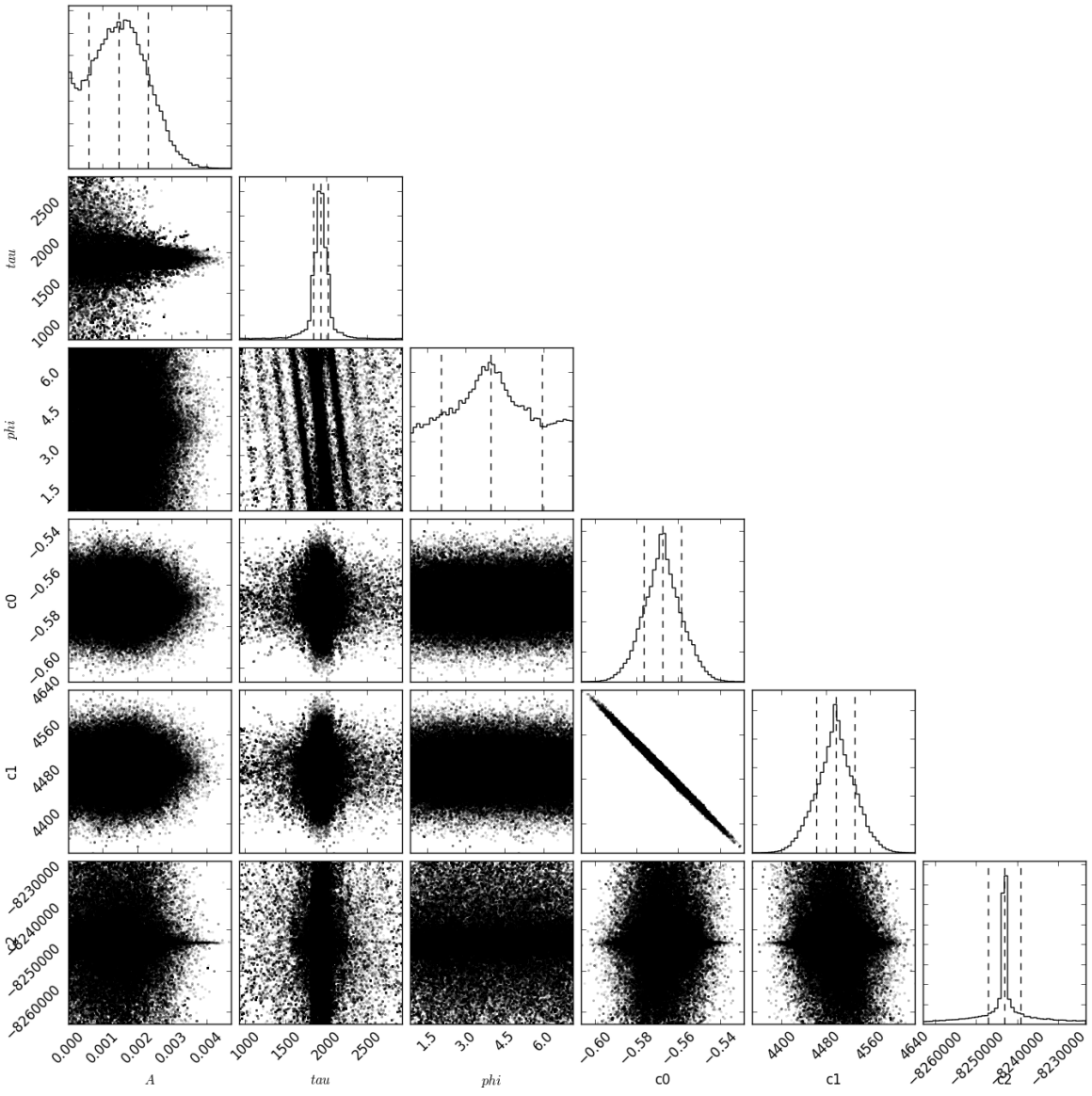

Figure A.98: Same as figure A.54, but for the star KIC 10963065.

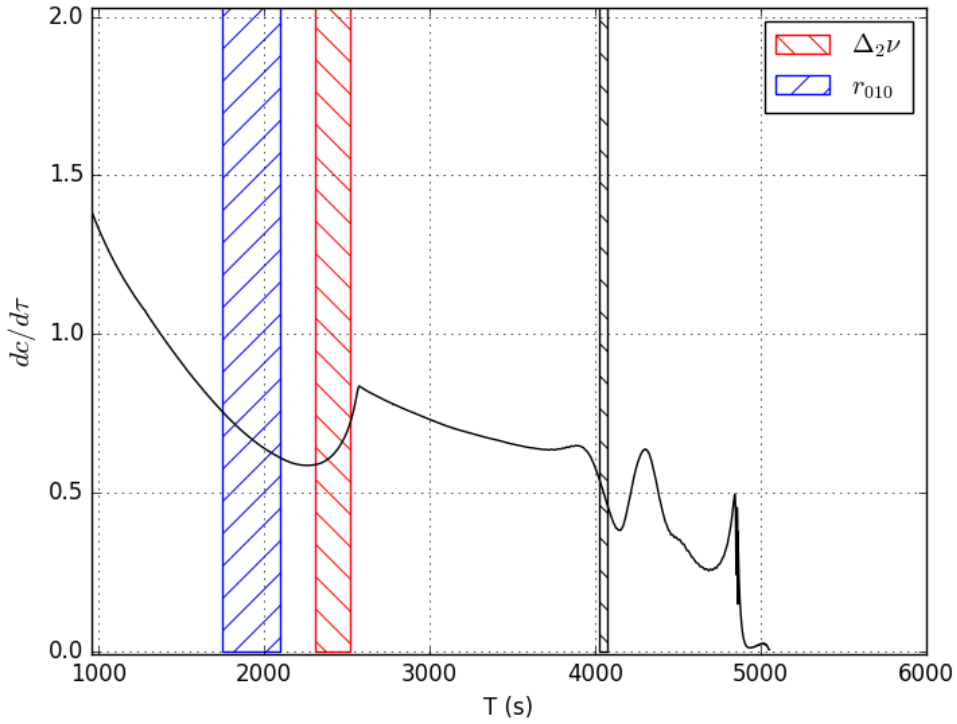

Figure A.99: Same as figure A.59, but for the star KIC 10963065.

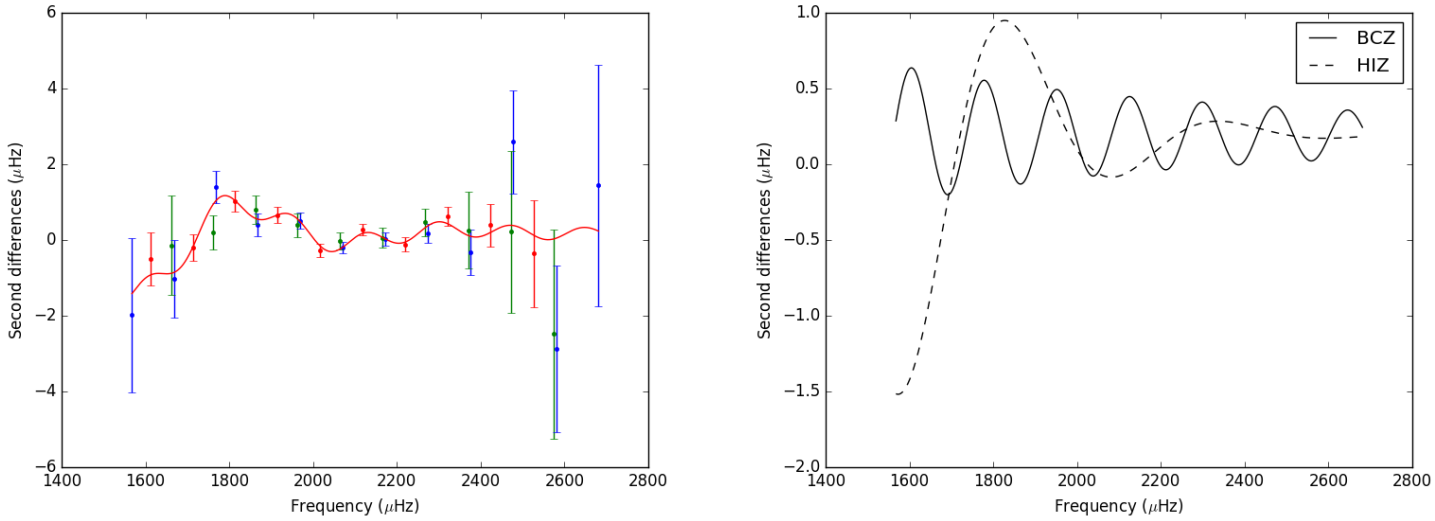

Figure A.100: Same as figure A.51, but for the star KIC 11295426.

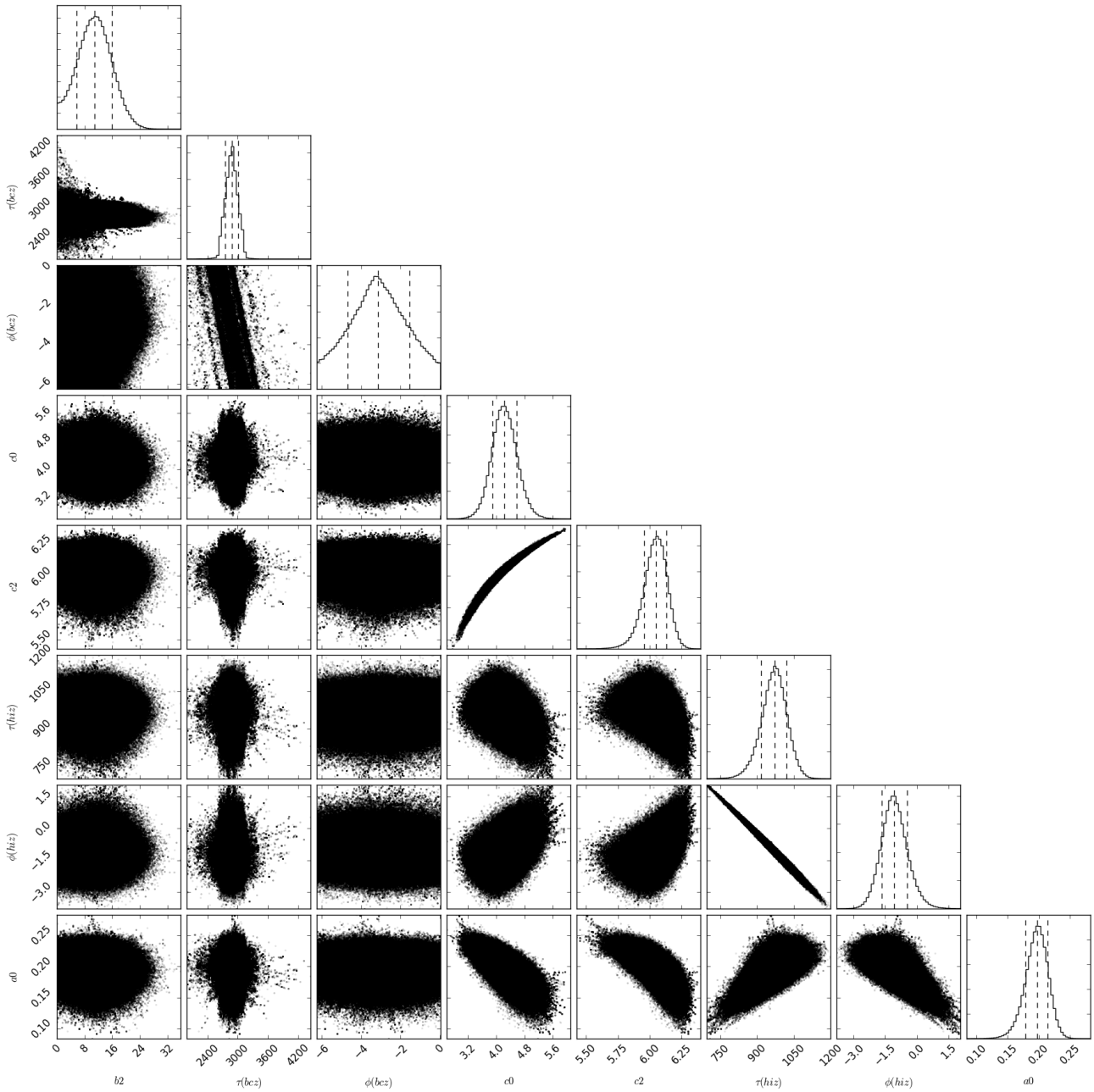

Figure A.101: Same as figure A.52, but for the star KIC 11295426.

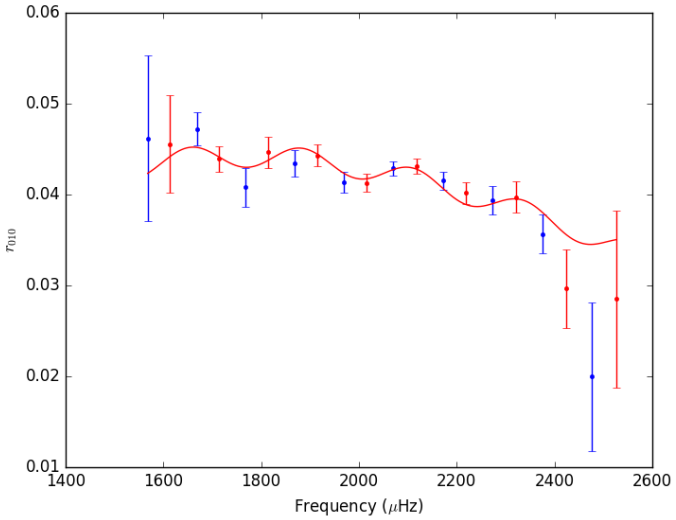

Figure A.102: Same as figure A.53, but for the star KIC 11295426.

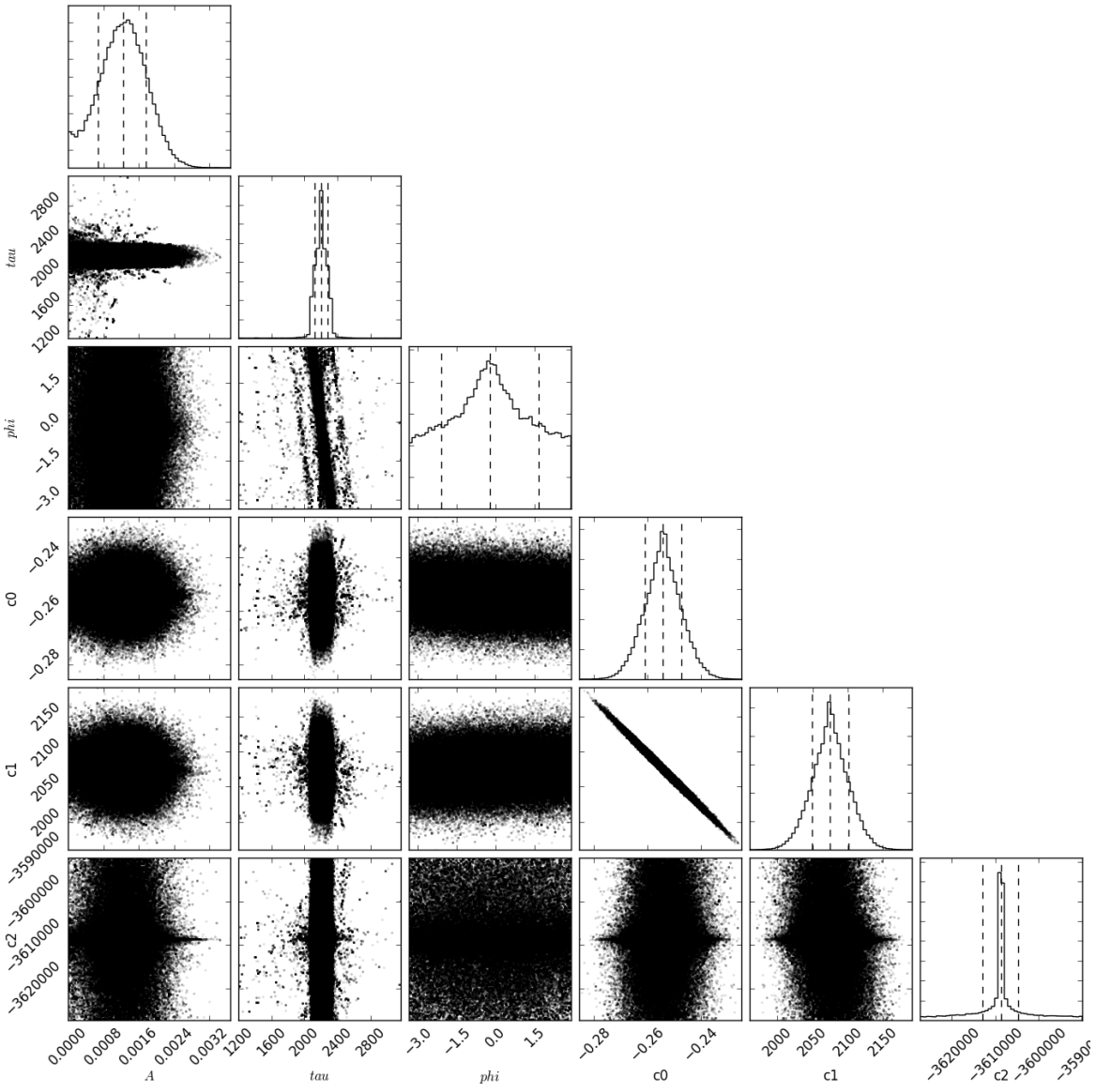

Figure A.103: Same as figure A.54, but for the star KIC 11295426.

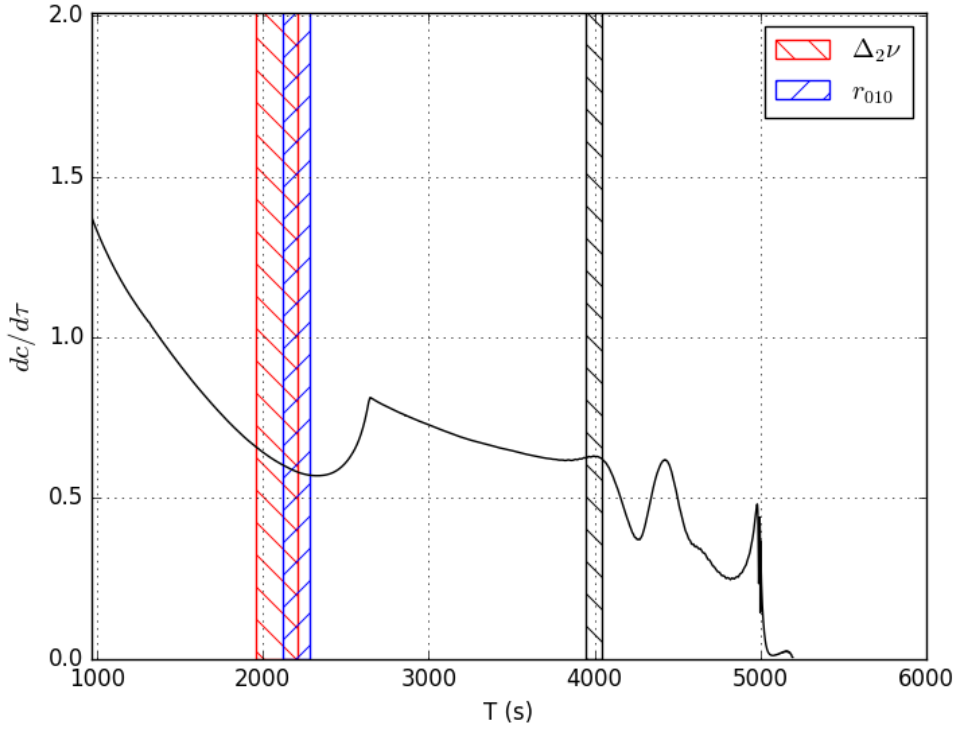

Figure A.104: Same as figure A.59, but for the star KIC 11295426.

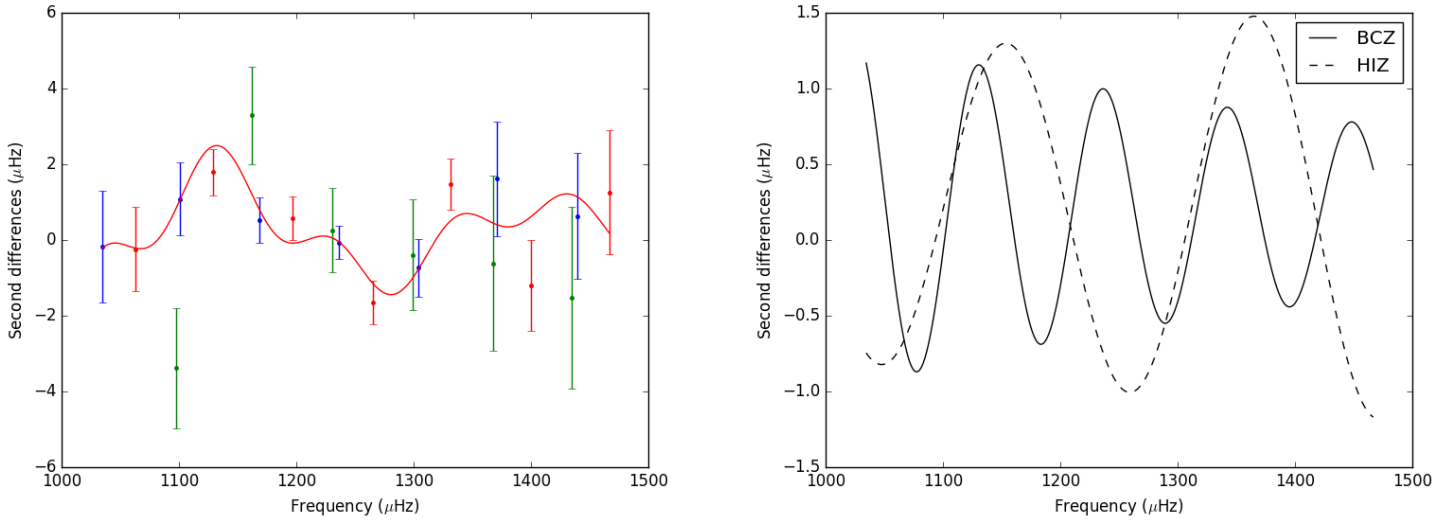

Figure A.105: Same as figure A.51, but for the star KIC 11401755.

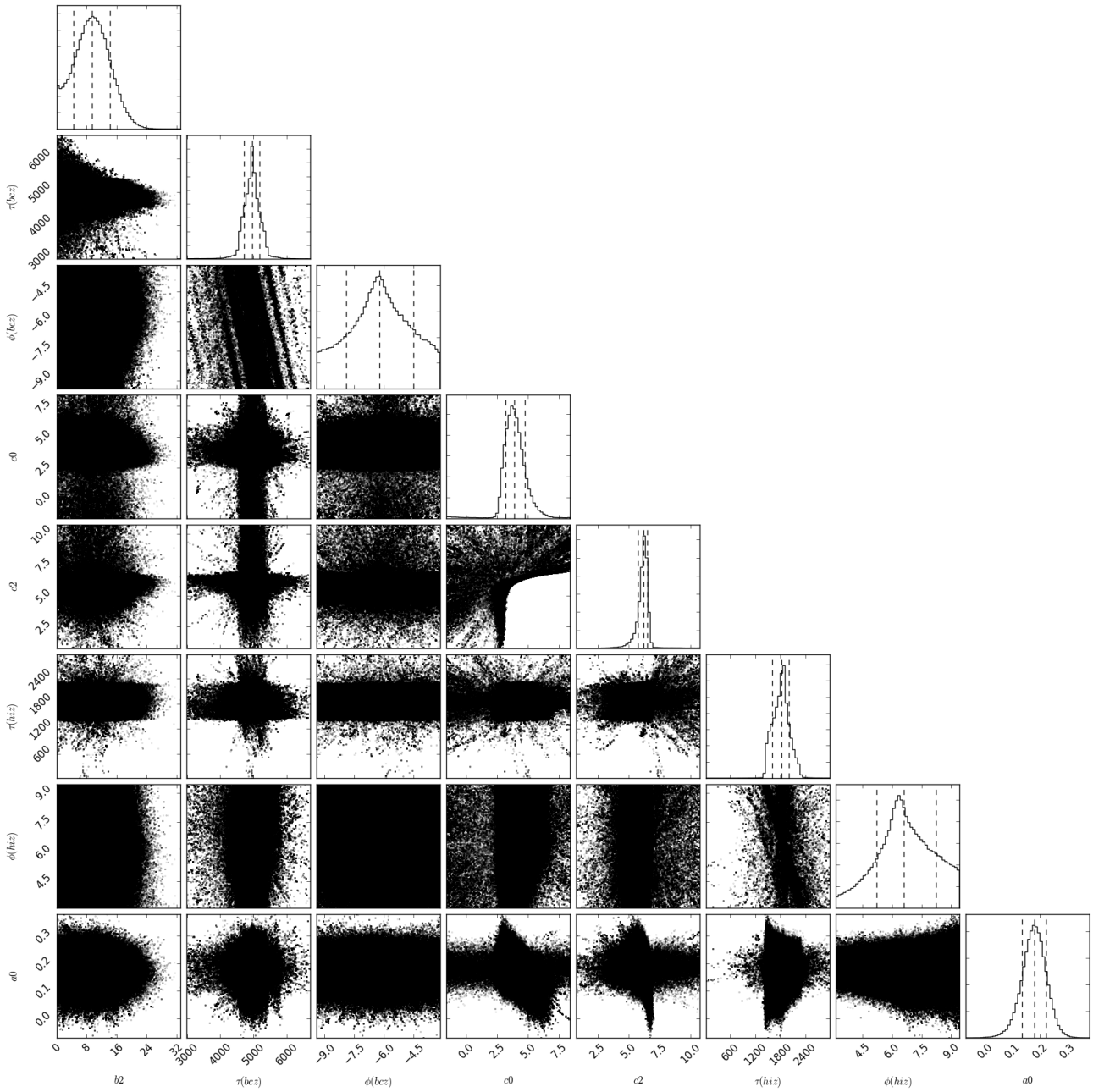

Figure A.106: Same as figure A.52, but for the star KIC 11401755.

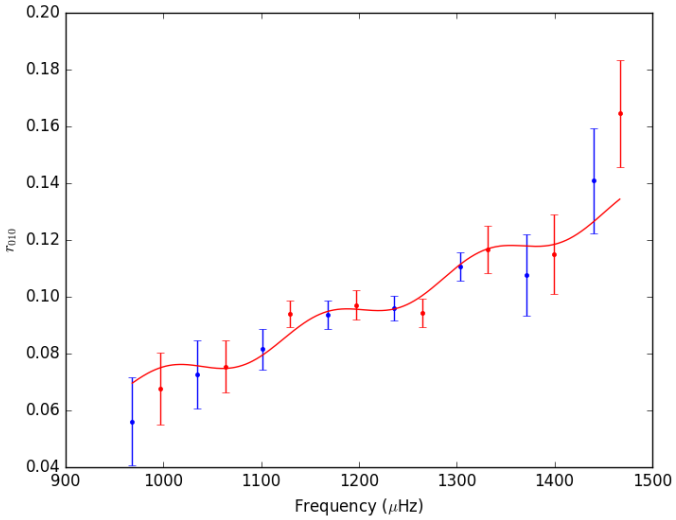

Figure A.107: Same as figure A.53, but for the star KIC 11401755.

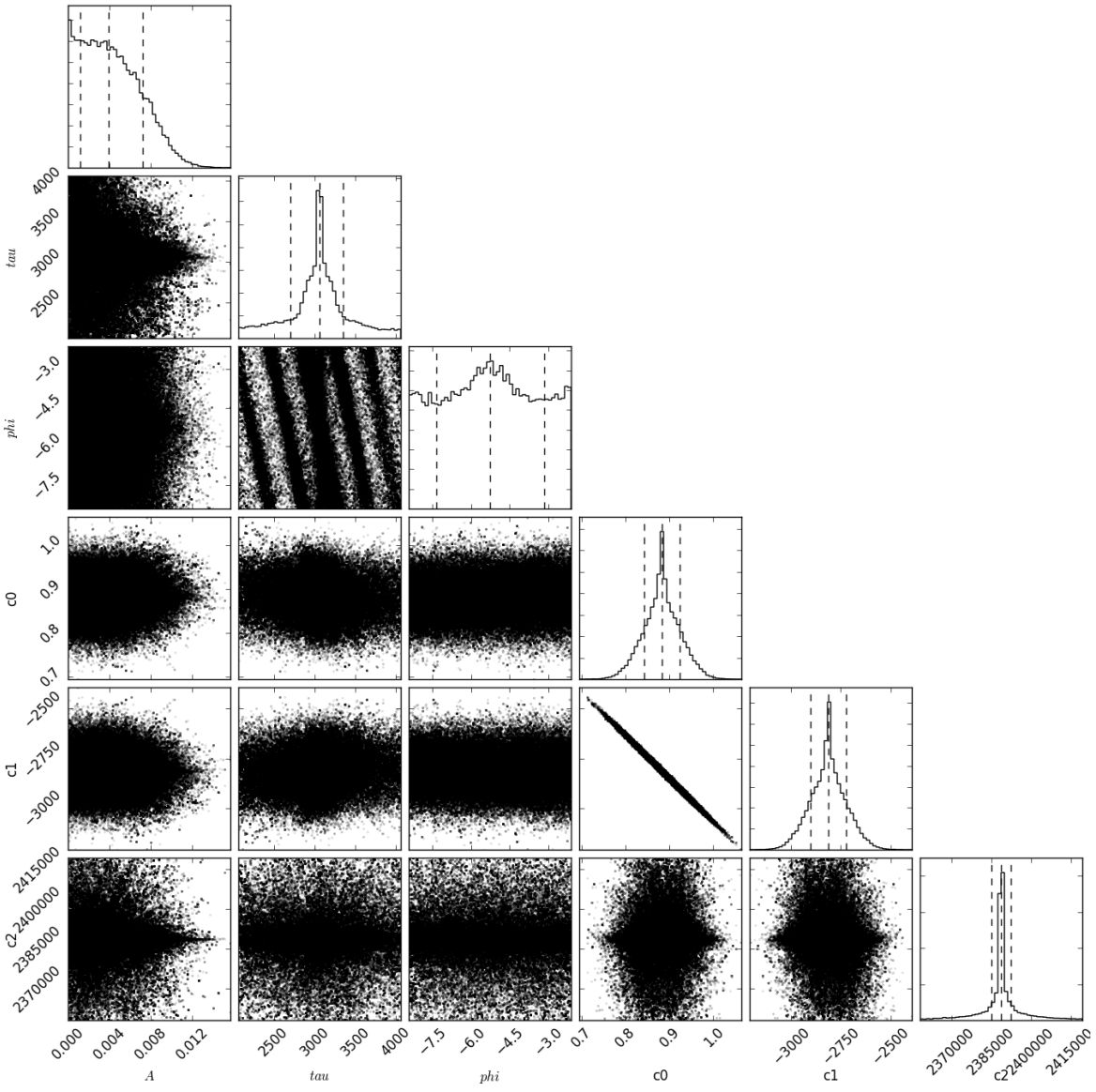

Figure A.108: Same as figure A.54, but for the star KIC 11401755.

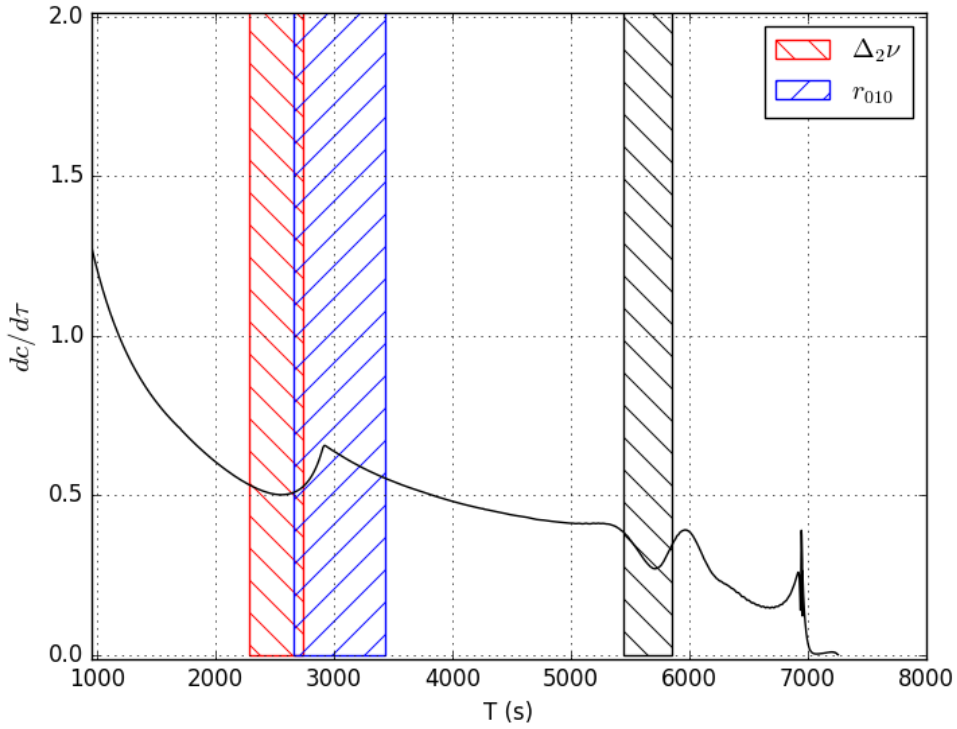

Figure A.109: Same as figure A.59, but for the star KIC 11401755.

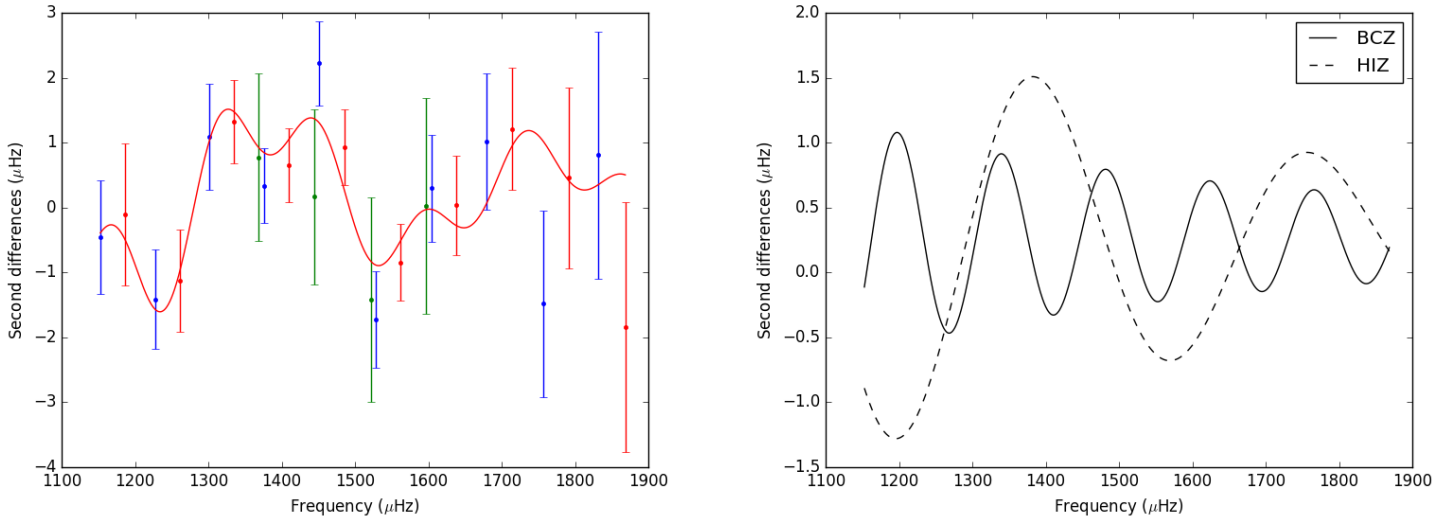

Figure A.110: Same as figure A.51, but for the star KIC 11807274.

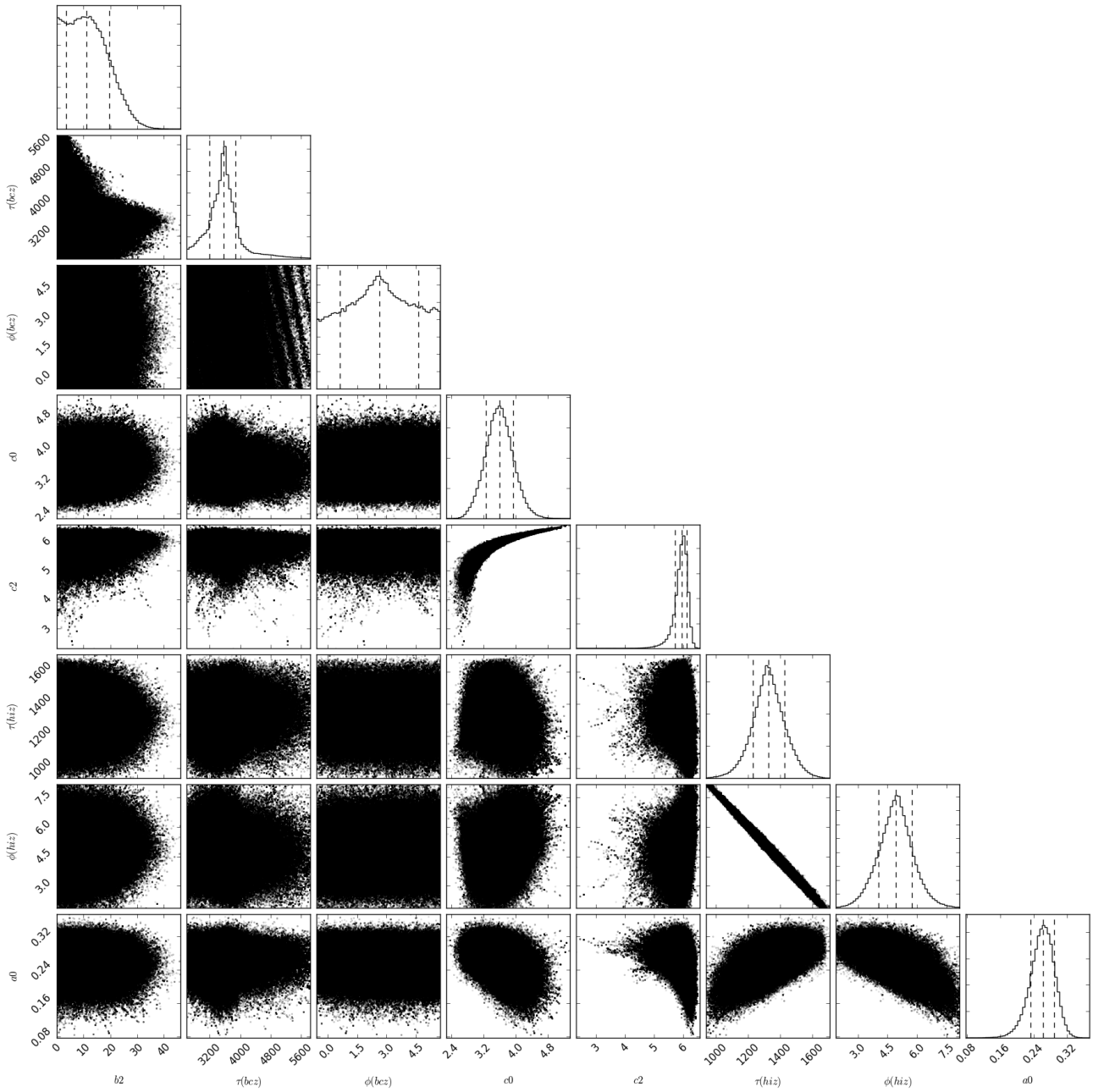

Figure A.111: Same as figure A.52, but for the star KIC 11807274.

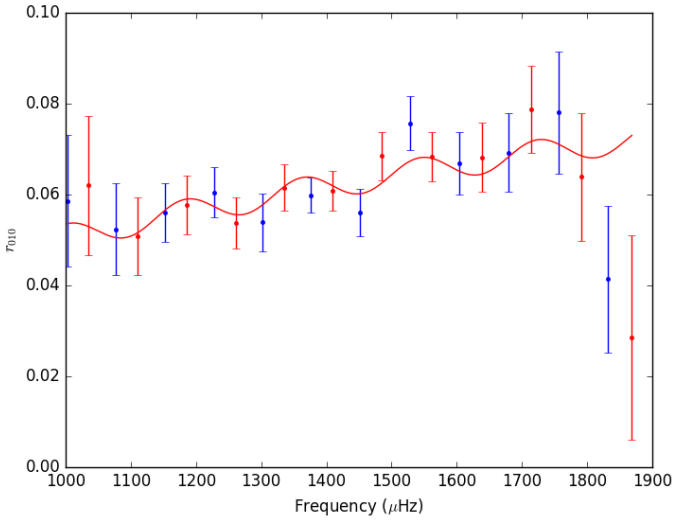

Figure A.112: Same as figure A.53, but for the star KIC 11807274.

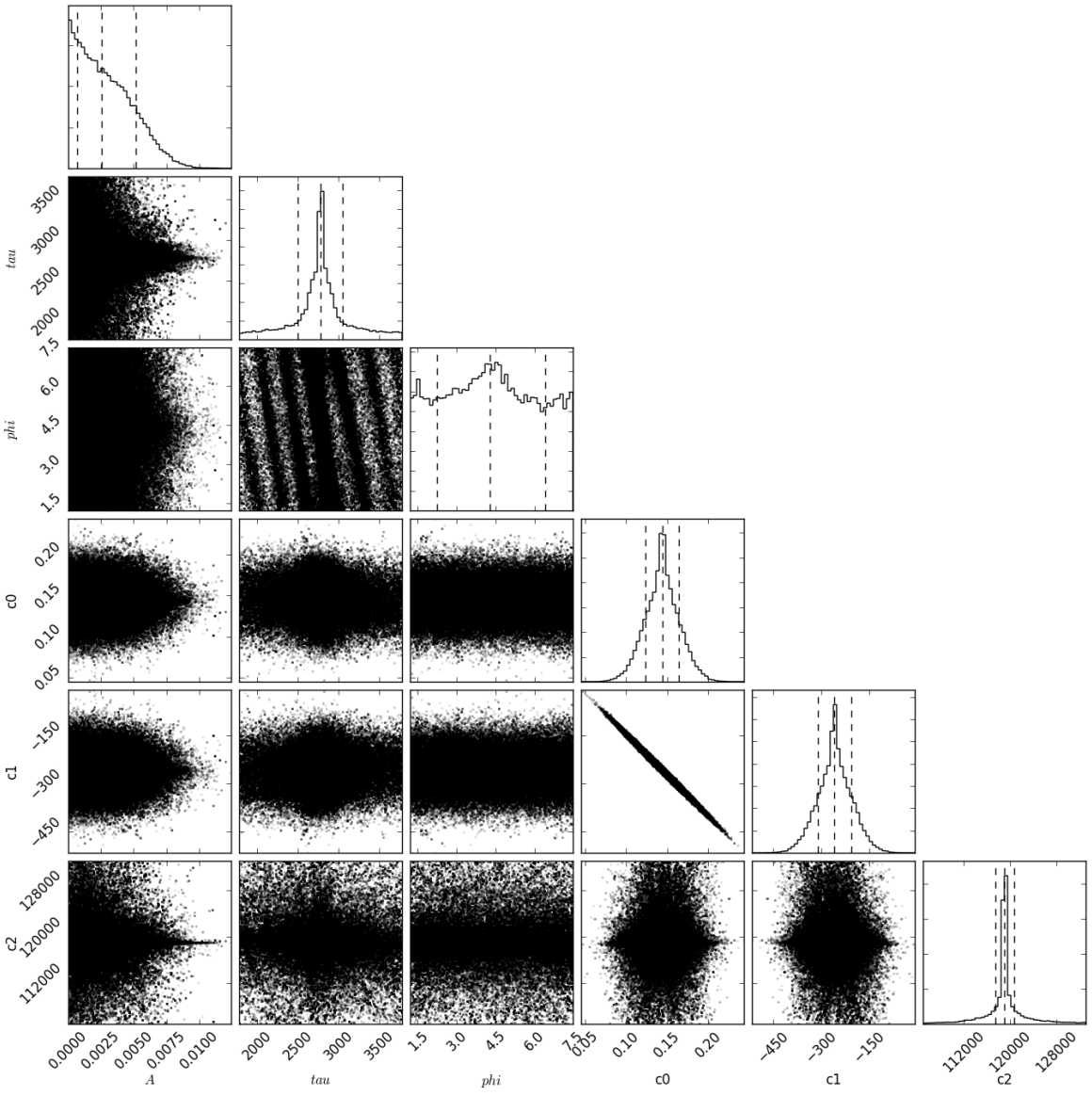

Figure A.113: Same as figure A.54, but for the star KIC 11807274.

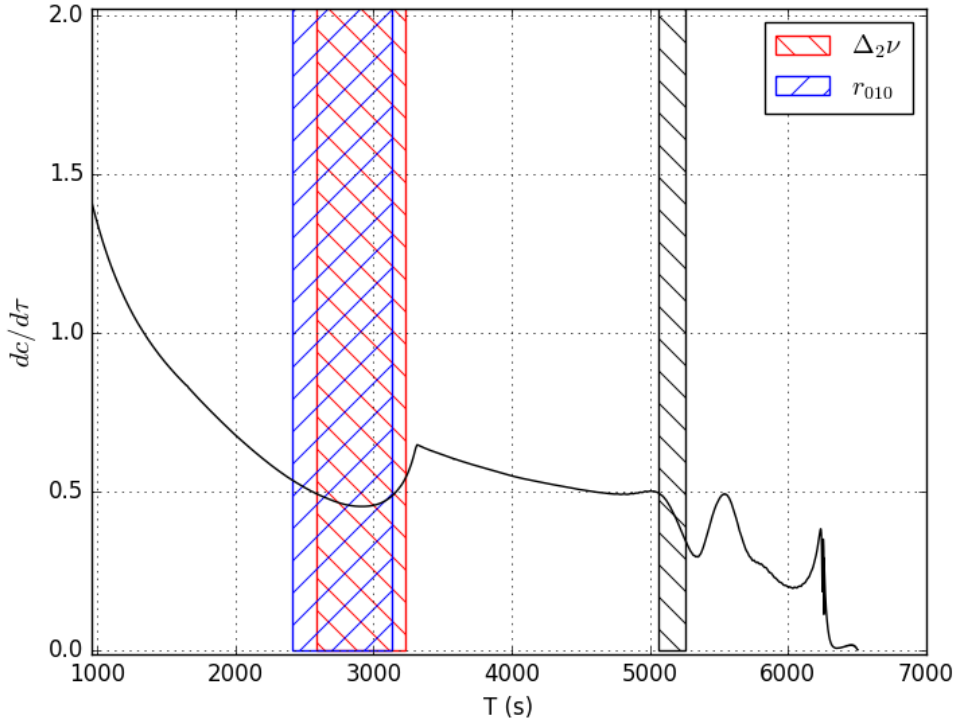

Figure A.114: Same as figure A.59, but for the star KIC 11807274.

Appendix B

Effects of different dust maps

Estimations of bolometric radii and luminosities will be affected significantly the choice of dust map used to calculate reddening and extinctions. We used two models of dust maps from Drimmel et. al. (2003) and Green et al. (2015). They are both three-dimensional models of the distribution of dust in the Milk Way galaxy, with the difference that the maps from Green et al. (2015) were created using up-to-date data from Pan-STARRS 1 and 2MASS photometry.

From the dust maps we obtained estimations of reddening $E(B-V)$ by using the galactic coordinates and distances for each star. Values for stellar extinctions are calculated using the relation $A_V = 3.2E(B-V)$

Figure B.1, B.2 and B.3 show the effects of the different dust maps. We have choosen to pick the models from Green et al. (2015), since the residual between *Hipparcos* distance and seismic distance show the best results (figure B.2)

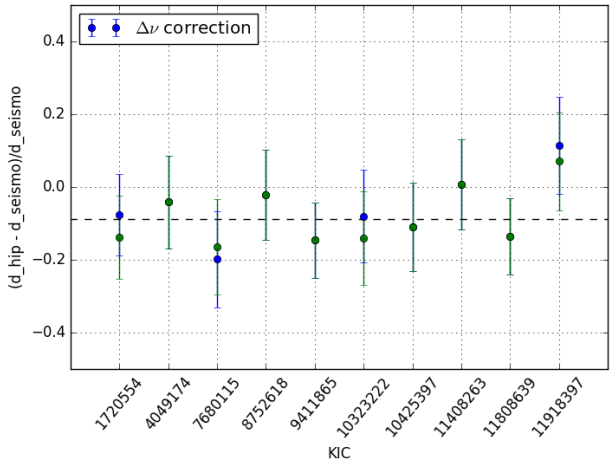

Figure B.1: Relative differences between *Hipparcos* and seismic distances (green dots) estimated using equation 3.10. Blue dots shows the four RGB stars with corrections applied to $\Delta\nu$, also indicated by asterisks in the KIC numbers. The black dashed line is the weighted average of the differences. Effects of reddening and extinction where not taken into account.

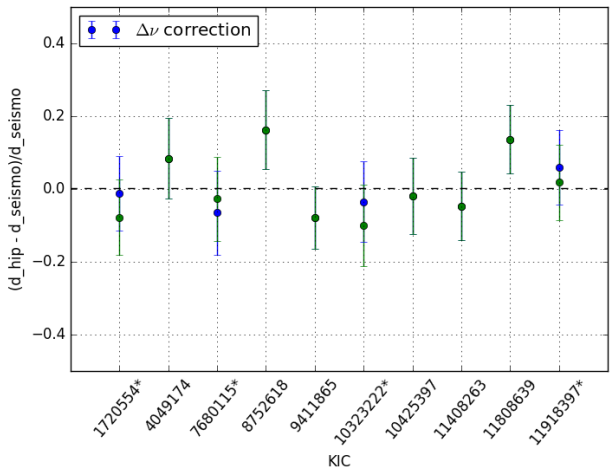

Figure B.2: Same as figure B.1, but here the inferred seismic distances account for the effects of extinction calculated by using the dust map from Green et al. (2015).

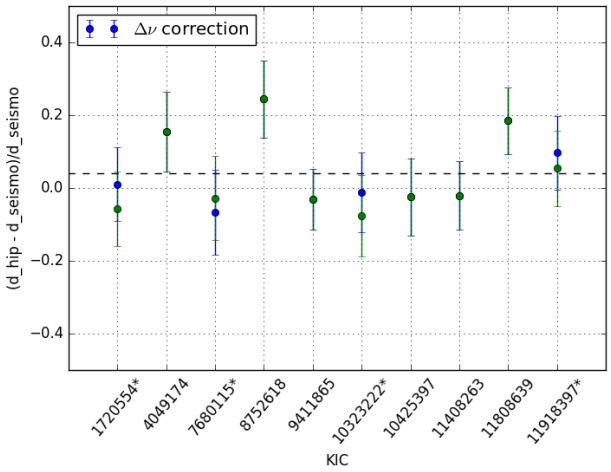

Figure B.3: Same as figure B.1, but here the inferred seismic distances account for the effects of extinction calculated by using the dust map from Drimmel et. al. (2003).

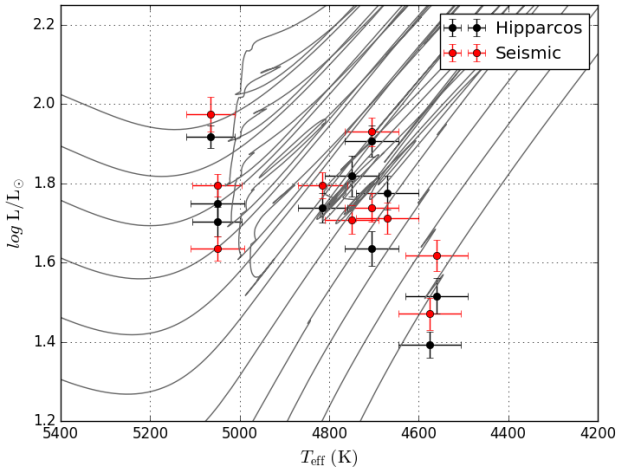

Figure B.4: HR diagram using spectroscopic temperatures and two different sets of luminosities. Bolometric luminosities are obtained by using *Hipparcos* distances. Seismic luminosities are obtained from combining seismic radii and spectroscopic temperatures. Effects of reddening and extinction where not taken into account.

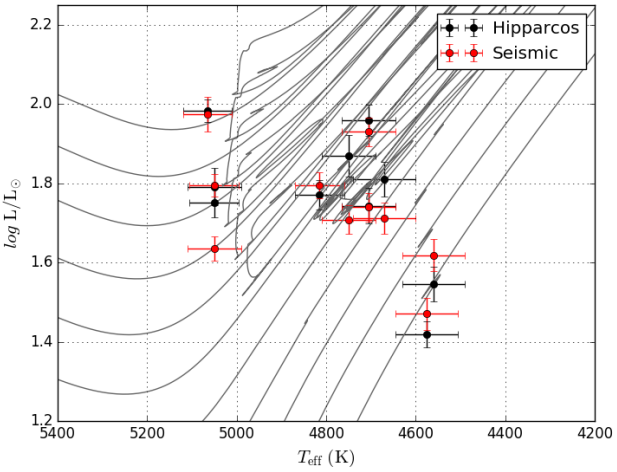

Figure B.5: Same as figure B.4, but here the bolometric luminosities account for the effects of extinction calculated by using the dust map from Green et al. (2015).

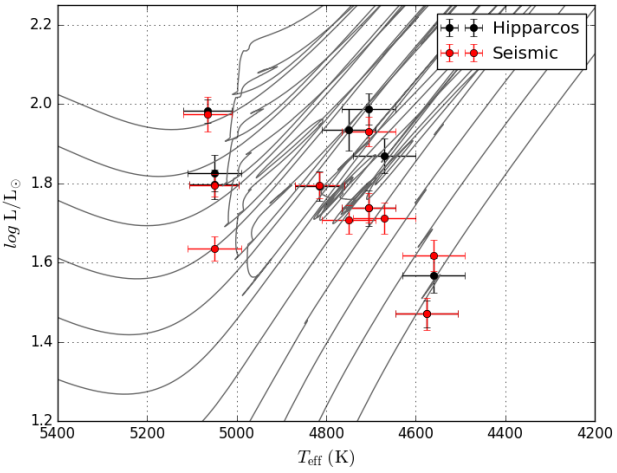

Figure B.6: Same as figure B.4, but here the bolometric luminosities account for the effects of extinction calculated by using the dust map from Drimmel et. al. (2003).

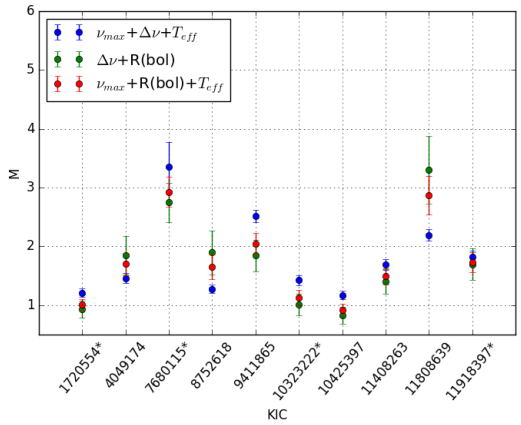

Figure B.7: Masses computed using different combinations of seismic parameters. The blue dots indicate masses obtained by using $\nu_{\rm max}$, $\Delta\nu$ and the spectroscopic temperatures ($T_{\rm eff}$, see Equation 3.1). Green dots are calculated using $\Delta\nu$ and the Radius obtained from *Hipparcos* parallaxes (van Leeuwen, 2009) (Equation 3.3). Red dots are calculations made using $\nu_{\rm max}$, spectroscopic temperatures and the the same Radius as before (Equation 3.4). Effects of reddening and extinction where not taken into account.

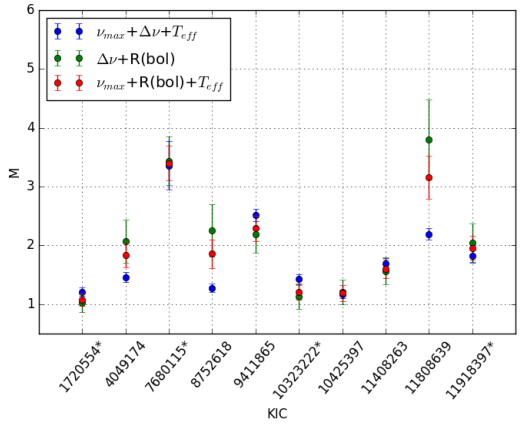

Figure B.8: Same as figure B.7, but here the bolometric radius are affected by corrections on luminosities when accounting for the effects of extinction calculated by using the dust map from Green et al. (2015).

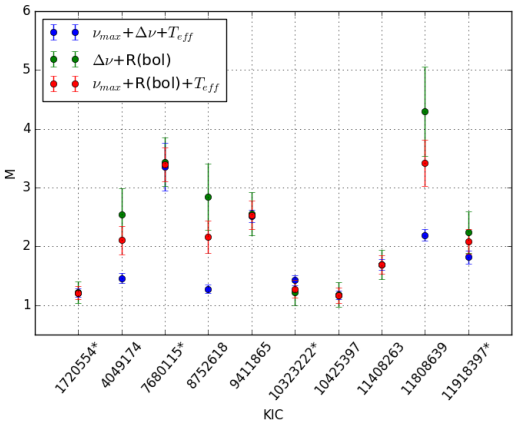

Figure B.9: Same as figure B.7, but here the bolometric radius are affected by corrections on luminosities when accounting for the effects of extinction calculated by using the dust map from Drimmel et. al. (2003).

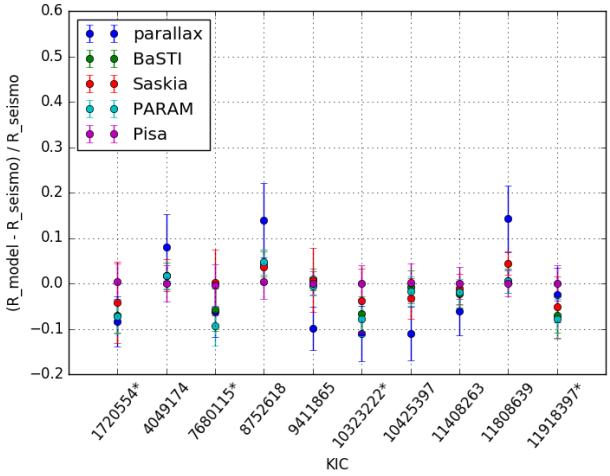

Figure B.10: Comparison between different estimations of setllar radius calculated by grid models taking the seismic radii as the true value. Blue dots are the Radii obtained by using *Hipparcos* parallaxes. Effects of reddening and extinction where not taken into account.

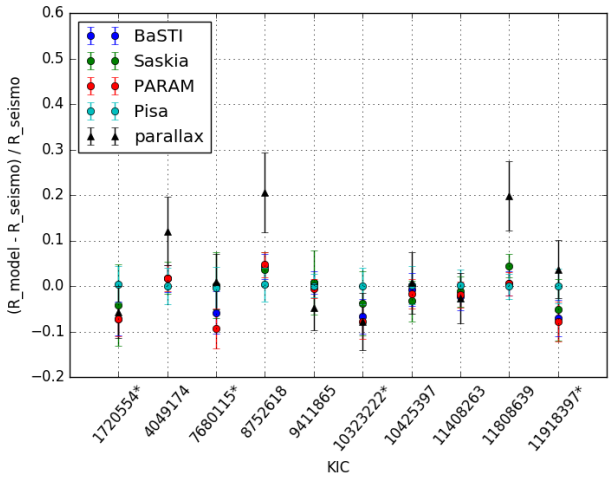

Figure B.11: Same as figure B.10, but here the bolometric radius are affected by corrections on luminosities when accounting for the effects of extinction calculated by using the dust map from Green et al. (2015).

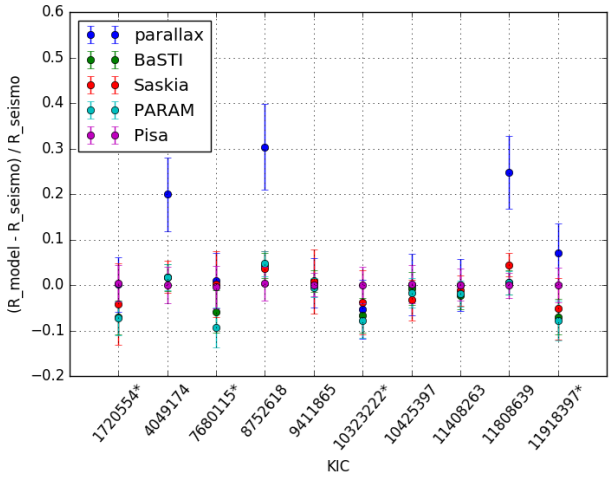

Figure B.12: Same as figure B.10, but here the bolometric radius are affected by corrections on luminosities when accounting for the effects of extinction calculated by using the dust map from Drimmel et. al. (2003).

Appendix C

Publication Record

Articles published in peer-review journals

A test of the asteroseismic $\nu_{\rm max}$ scaling relation for solar-like oscillations in main-sequence and subgiant stars. **Coelho, H. R.**; Chaplin, W. J.; Basu, S.; Serenelli, A.; Miglio, A. and Reese, D. R., Monthly Notices of the Royal Astronomical Society, Volume 451, Issue 3, p.3011-3020

Asteroseismology of Solar-Type Stars with K2: Detection of Oscillations in C1 Data. Chaplin, W. J.; Lund, M. N.; Handberg, R.; Basu, S.; Buchhave, L. A.; Campante, T. L.; Davies, G. R.; Huber, D.; Latham, D. W.; Latham, C. A.; Serenelli, A.; Antia, H. M.; Appourchaux, T.; Ball, W. H.; Benomar, O.; Casagrande, L.; Christensen-Dalsgaard, J.; **Coelho, H. R.**; Creevey, O. L.; Elsworth, Y.; García, R. A.; Gaulme, P.; Hekker, S.; Kallinger, T.; Karoff, C.; Kawaler, S. D.; Kjeldsen, H.; Lundkvist, M. S.; Marcadon, F.; Mathur, S.; Miglio, A.; Mosser, B.; Régulo, C.; Roxburgh, I. W.; Silva Aguirre, V.; Stello, D.; Verma, K.; White, T. R.; Bedding, T. R.; Barclay, T.; Buzasi, D. L.; Dehuevels, S.; Gizon, L.; Houdek, G.; Howell, S. B.; Salabert, D. and Soderblom, D. R., Publications of the Astronomical Society of Pacific, Volume 127, Issue 956, pp. 1038-1044 (2015)

SpaceInn hare-and-hounds exercise: Estimation of stellar properties using space-based asteroseismic data. Reese, D. R.; Chaplin, W. J.; Davies, G. R.; Miglio, A.; Antia, H. M.; Ball, W. H.; Basu, S.; Buldgen, G.; Christensen-Dalsgaard, J.; **Coelho, H. R.**; Hekker, S.; Houdek, G.; Lebreton, Y.; Mazumdar, A.; Metcalfe, T. S.; Silva Aguirre, V.; Stello, D.; Verma, K., Astronomy & Astrophysics, Volume 592, id.A14, 27 pp.

Articles published in conference proceedings.

Testing the $\nu_{\rm max}$ scaling relation **Coelho, H. R.**; Chaplin, W. J.; Basu, S.; Serenelli, A.; Miglio, A. and Reese, D. R., The Space Photometry Revolution - CoRoT Symposium 3, Kepler KASC-7 Joint Meeting, Toulouse, France, Edited by R.A. García; J. Ballot; EPJ Web of Conferences, Volume 101, id.06017

Bibliography

Aerts, C.; Christensen-Dalsgaard, J.; and Kurtz, D. W. 2010: 'Asteroseismology', Springer: Dodrecht

Alonso, A.; Arribas, S. and Martínez-Roger, C. 1999, A&AS, 140, 261

Appourchaux, T.; et al. 2012; A&A; 537A; 134A

Asplund, M.; Grevesse, N.; Sauval, A. J. 2005; ASPC; 336; 25A

Aurière, M. 2003; EAS Publications Series, Vol. 9, EAS Publications Series, ed. J. Arnaud & N. Meunier, 105

Ballot, J.; Turck-Chièze, S.; García, R. A. 2004, A&A, 423, 1051B

Balmforth, N. J.; Gough, D. O. 1990; ApJ; 362; 256B

Balmforth, N. J. 1992; MNRAS; 255; 632B

Basu, Sarbani; Antia, H. M.; Narasimha, D. 1994, MNRAS, 267, 209B

Basu, S.; Antia, H. M. 1995, JApAS, 16, 392B

Basu, Sarbani 1997, MNRAS, 288, 572B

Basu, S.; Mazumdar, A.; Antia, H. M.; Demarque, P. 2004, ESASP, 559, 313B

Basu; S.; Chaplin; W. J.; Elsworth; Y. 2010; ApJ; 710; 1596

Basu; S.; Verner; G. A.; Chaplin; W. J.; Elsworth; Y. 2012; ApJ; 746; 76

Bedding, Timothy R.; Kjeldsen, Hans 2003; PASA; 20; 203B

Bedding, T. R. 2011: 'Solar-like Oscillations: An Observational Perspective', *arXiv*: 1107.1723.

Bedding, T; Mosser, B.; Huber, D. et al. 2011, Nature, 471, 608B

Belkacem, K; Goupil, M. J.; Dupret, M. A. et al. 2013; ASP Conference Proceedings, 479, 61B

Belkacem, K.; Dupret, M. A.; Baudin, F.; Appourchaux, T.; Marques, J. P.; Samadi, R. 2012; A&A; 540L; 7B

Belkacem, K.; Samadi, R.; Mosser, B.; Goupil, M. J.; Ludwig, H. G. 2011; A&A; 530; 142

Borucki, W. J. et al. 2010, Sci, 327, 977

Bossini, D.; Miglio, A.; Salaris, M.; et al. 2015, MNRAS, 453, 2290B

Bressan; A. Marigo; P.; Girardi; L.; Salasnich; B.; Dal Cero; C.; Rubele; S.; Nanni; A. 2012; MNRAS; 427; 127

Brodsky, M.; Vorontsov, S. V. 1993, ApJ, 409, 455B

Broomhall, A. M.; et al. 2014; MNRAS; 440; 1828

Brown T. M.; Gilliland R. L.; Noyes R. W.; Ramsey L. W. 1991, ApJ, 368, 599

Bruntt; H.; Bedding; T. R.; Quirion; P. O.; et al. 2010; MNRAS; 405; 1907

Bruntt; H.; Basu; S.; Smalley; B.; et al. 2012; MNRAS; 423; 122

Bryson, S. T. et al. 2010, ApJ, 713, 97

Carigi; L.; Peimbert; M. 2008; RMXAA; 44; 341

Casagrande; L.; Ramírez; I.; Meléendez; J.; et al. 2010; A&A; 512; 54

Casagrande; L.; Silva Aguirre; V.; Stello; D.; et al. 2013; ApJ; 787; 110

Casagrande, L. & VandenBerg, D. A. 2014, MNRAS, 444, 392-419

Chaplin, W. J. et al. 1998, MNRAS, 308, 1077C

Chaplin, W. J.; Houdek, G.; Appourchaux, T.; Elsworth, Y.; New, R.; Toutain, T. 2008; A&A; 485; 813C

Chaplin, W. J. and Miglio, A. 2013; ARA&A; 51, 353.

Chaplin; W. J.; Basu; S.; Huber; D.; et al. 2014; ApJS; 210; 1

Charbonel, C; in Montmerle, T, Kahane, C. 2006, Stars and Nuclei, EDP Sciences, Paris, p.125

Charbonel, C. 1995, ApJ, 453, L41

Charbonel, C.; Lagarde, N. 2010, A&A, 522, A10

Chiosi; C.; Matteucci; F. M. 1982; A&A; 105; 140

Christensen-Dalsgaard, J.; Gough, D. O.; Thompson, M. J. 1991, ApJ, 378, 413C

Christensen-Dalsgaard; J. 1993; Proc. GONG 1992; Seismic Investigation of the Sun and Stars (ASP Conf. Ser. 42); ed. T. M. Brown (San Francisco; CA: ASP); p. 347

Christensen-Dalsgaard, Jorgen; Monteiro, Mario J. P. F. G.; Thompson, Michael J. 1995, MNRAS, 276, 283C

Christensen-Dalsgaard, J. 1993, Proc. GONG 1992, Seismic Investigation of the Sun and Stars (ASP Conf. Ser. 42), ed. T. M. Brown (San Francisco, CA: ASP), p. 347

Christensen-Dalsgaard, J., et al. 1996, Science, 272, 1286

Christensen-Dalsgaard; J. 2002; Rev.Mod.Phys.74; 1073-1129

Christensen-Dalsgaard; J.; Thompson; M. J. 2011; Proceedings IAU Symposium No. 271

Christensen-Dalsgaard; J. 2011: 'Asteroseismology of red giants'; *arXiv*: 1106.5946.

Christensen-Dalsgaard, J.; Monteiro, M. J. P. F. G.; Rempel, M.; Thompson, M. J. 2011; MNRAS; 414; 1158C

Claverie; A.; Isaak; G. R.; McLeod; C. P.; van der Raay; H. B.; Cortes; T. R. 1979; Nature; 282; 591C

Coelho; H. R.; et al. 2015; MNRAS; 451; 3011

Cox, J. P.; Giuli, R. T. 1968; 'Principles of stellar structure'; New York: Gordon and Breach

Cox, J. P. 1974; RPPh; 37; 563C

Cox, J. P. 1980; SSRv; 27; 389C

Cunha; M. S.; Aerts; C.; Christensen-Dalsgaard; J.; Baglin; A.; et al. 2007; A&A Review; 14; 217C.

Cunha; M. S.; Brandão; I. M. 2011; A&A; 529A; 10C.

Cyburt; R. H.; Fields; B. D.; Olive; K. A. 2003; Phys. Lett. B.; 567; 227

da Silva L.; et al. 2006; A&A; 458; 609

Demarque; P.; Woo; J.-H.; Kim; Y.-C.; Yi; S. K 2004; ApJS; 155; 667

Denissenkov; P. A. 2010; ApJ; 723; 563

Dotter; A.; et al 2008; ApJS; 178; 89

Drimmel; R.; Cabrera-Lavers; A.; Lopes-Corredoira; M. 2003; A&A; 409; 205

Eddington; A. S. 1926; 'The Internal Constitution of the Stars'; Cambridge University Press; Cambridge.

Gai; N.; Basu; S.; Chaplin; W. J.; Elsworth; Y. 2011; ApJ; 730; 63

Gaia Collaboration et al. 2016, A&A, 595, id.A2

Gilroy; K. K.; Brown; J. A. 1991; ApJ; 371; 578

Girardi; L. 1999; MNRAS; 308; 818G.

Gough, D. O.; Sekii, T. 1993; ASPC; 42; 177G

Green, G. M. et al. 2015; ApJ; 810; 25

Grevesse; N.; Noels; A. 1993; PhST; 47; 133

Grigahcène, A.; Dupret, M.-A.; Gabriel, M.; Garrido, R.; Scuflaire, R 2005; A&A; 434; 1055G

Grosjean, M. et al. 2014; A&A; 572; 11

Houdek, G.; Balmforth, N. J.; Christensen-Dalsgaard, J.; Gough, D. O. 1999; A&A; 351; 582H.

Houdek, G. 2004; AIPC; 731; 193H

Houdek, G. 2006; Proceedings of SOHO 18/GONG 2006/HELAS I; Beyond the spherical Sun (ESA SP-624); 28.

Houdek, G. and Gough, D. O. 2006; MNRAS; 375; 861.

Huber, D.; et al. 2012; ApJ; 760; 32

Kippenhahn; R. and Weigert; A. 1994: *Stellar Structure and Evolution*; Springer-Verlag; Berlin.

Kjeldsen, H.; Bedding, T. R. 1995; A&A; 293; 87

Lagarde, N.; Charbonnel, C.; Decressi, T.; Hagelberg, J.; 2011; A&A; 536; A28

Lagarde, N.; Decressin, T.; Charbonnel, C.; Eggenberger, P.; et. al. 2012; A&A; 543; 108

Lagarde, N.; Miglio, A.; Eggenberger, P.; Morel, T.; et. al. 2015; A&A; 580; A141

Leighton; Robert B.; Noyes; Robert W.; Simon; George W. 1962; ApJ; 135; 474L.

Marchenkov, K. I.; Vorontsov, S. V. 1991; SoPh; 133; 149M

Mazumdar, A.; Antia, H. M. 2001; A&A; 377; 192M

Mazumdar, A. 2005; A&A; 441; 1079M

Mazumdar, A. et al. 2012; AN; 333; 1040M

Mazumdar, A. et al. 2014; ApJ; 782; 18M

Miglio, A. et al. 2010; A&A; 520L; 6M

Miglio; A. 2012; in: Red Giants as Probes of the Structure and Evolution of the Milky Way. Berlin: Springer; Miglio; A.; Montalbán J.; Noels; A.; eds.; p. 11

Miglio, A. et al. 2012; MNRAS; 419; 2077M

Miglio, A. et al. 2013; MNRAS; 429; 423-428

Miglio, A.; Chiappini, C.; Morel, T. 2013; European Physical Journal Web of Conferences; Vol. 43; 3004

Mikolaitis, S.; Tautvaisiene, G.; Gratton, R.; Bragaglia, A.; Carretta, E. 2012; A&A; 541; 137

Monteiro, M. J. P. F. G.; Christensen-Dalsgaard, J.; Thompson, M. J. 1994; A&A; 283; 247M

Monteiro, Mário J. P. F. G.; Thompson, Michael J. 2005; MNRAS; 361; 1187M

Morel, T.; Miglio, A.; Lagarde, N.; et al. 2014; A&A; 564; A119

Mosser, B. et al. 2010; A&A; 517A; 22M

Mosser, B. et al. 2012; A&A; 540; 143

Mosser, B.; Benomar, O.; Belkacem, K. 2014; A&A; 572; L5

Palacios, A.; Talon, S.; Charbonnel, C.; Forestini, M. 2006; A&A; 399; 603

Palacios, A.; Charbonnel, C.; Talon, S.; Siess, L. 2006; A&A; 453; 261

Paxton, B.; Bildsten, L.; Dotter, A.; Herwig, F.; Lesaffre, P.; Timmes, F. 2011; ApJS; 192; 3P.

Pietrinferni; A.; Cassisi; S.; Salaris; M.; & Castelli; F. 2004; ApJ; 612; 168

Pinsonneault; M. H.; An; D.; Molenda-Żakowicz; J.; et al. 2012; ApJS; 199; 30

Pinsonneault; M. H.; Elsworth; Y.; Epstein; C.; et al. 2014; ApJS; 215; 19

Reese, D. R.; Marques, J. P.; Goupil, M. J.; Thompson, M. J.; Deheuvels, S. 2012; A&A; 539; 63

Reese, D. R.; et al. 2016; A&A; 592A; 14R

Rodrigues; T. S.; Girardi; L.; Miglio; A.; et al. 2014; MNRAS; 445; 2758

Roxburgh, I. W.; Vorontsov, S. V. 1994; MNRAS; 268; 880R

Roxburgh, I. W.; Vorontsov, S. V. 2003; A&A; 411; 215R

Roxburgh, I. W. 2005; A&A; 434; 665R

Roxburgh, I. W. 2009; A&A; 493; 185R

Sandquist; E. L.; Mathieu; R. D.; Brogaard; K.; et al. 2013; ApJ; 762; 58

Scuflaire, R.; Théado, S.; Montalbán, J.; Miglio, A.; Bourge, P.-O.; Godart, M.; Thoul, A.; Noels, A. 2008; Ap&SS; 316; 83

Serenelli; A. M.; Bergemann; M.; Ruchti; G.; Casagrande; L. 2013; MNRAS; 429; 3645

Shapley; H. 1914; ApJ; 40; 448.

Skrutskie; M. F.; Cutri; R. M.; Stiening; R.; et al. 2006; AJ; 131; 1163

Stello, D.; et al. 2013; ApJ; 765; 41

Silva Aguirre; V.; Chaplin; W. J.; Ballot; J.; et al. 2011; ApJL; 740; L2

Silva Aguirre, V.; Ballot, J.; Serenelli, A. M.; Weiss, A. 2011; A&A; 529A; 63S

Silva Aguirre, V. et al. 2012; ApJ; 757; 99

Silva Aguirre, V.; Basu, S.; Brandão, I. M.; et al. 2013; ApJ; 769; 141

Silva Aguirre, V.; Davies, G. R.; Basu, S.; et al. 2015; MNRAS; 452; 2127S

Tassoul, M. 1980; ApJS; 43; 469

Tautvaisiene, G.; Barisevicius, G.; Chorniy, Y.; Puzeras, E. 2013; MNRAS; 430; 621

Thygesen, A. O.; Frandsen, S.; Bruntt, H.; et al. 2012; A&A; 543; A160

Torres, G.; Andersen, J.; Giménez, A. 2010; A&ARv; 18; 67T

Townsend; R. H. D.; Teitler; S. A. 2013; MNRAS; 435; 3406

Ulrich, Roger K. 1970; ApJ; 162; 993U.

Ulrich, R. K. 1986; ApJ; 306; L37

Valenti, J. A., Piskunov; N. 1996; A&AS 118; 595

Valenti, Jeff A., Fischer; Debra A. 2005; ApJS; 159; 141

van Leeuwen, F. 2009; A&A; 497; 209

Verma, Kuldeep; Antia, H. M.; Basu, Sarbani; Mazumdar, Anwesh 2014; ApJ; 794; 114V

Vorontsov, S. V. 1989; ESASP; 286; 475V

Vorontsov, S. V.; Zharkov, V. N. 1989; ASPRv; 7; 1V

Vrard, M.; Mosser, B.; Samadi, R. 2016; A&A; 588; 87

White, T. R.; Bedding, T. R.; Stello, D.; et al. 2011; ApJ; 743; 161

White, T. R.; et al. 2013; MNRAS; 433; 1262